

Dissertation

submitted to the
Combined Faculties for the Natural Sciences and for Mathematics
of the Ruperto-Carola University of Heidelberg, Germany
for the degree of
Doctor of Natural Sciences

presented by
Diplom-Physiker Thorsten Ratzka
born in Wertheim am Main

Oral examination: 11th May 2005

High Spatial Resolution Observations of Young Stellar Binaries

Referees: Prof. Dr. Christoph Leinert
Prof. Dr. Immo Appenzeller

Zusammenfassung

Im ersten Teil dieser Arbeit wird die Durchmusterung von 158 jungen stellaren Objekten im Ophiuchus Sternentstehungsgebiet beschrieben, deren Ziel es war, die *Doppelsternhäufigkeit* in dieser Region zu bestimmen. Die beugungsbegrenzte Auflösung der Speckle-Beobachtungen erlaubt es, alle Begleiter mit Abständen zwischen $0.13''$ und $6.4''$ und einem Flußverhältnis von ≥ 0.1 im K-Band zu identifizieren. Die prozentuale Häufigkeit der Begleiter liegt mit $29.1\% \pm 4.3\%$ nur knapp über dem Wert von $23.5\% \pm 4.8\%$, der im gleichen Abstandsbereich für sonnenähnliche Sterne in Sonnenumgebung gefunden wurde. Die Folgerungen aus diesem Ergebnis werden diskutiert.

Sowohl Beobachtungen mit Speckle-Kameras als auch mit Adaptiven Optiken werden anschließend benutzt, um unsere Kenntnis der *dynamischen Masse* der beiden Begleiter des sonnennahen M-Zwergs LHS 1070 zu verbessern.

Im dritten Teil schließlich werden Beobachtungen mit dem im mittleren Infrarot arbeitenden Instrument MIDI am VLTI beschrieben. Die Reduktion der interferometrischen Daten mit der sogenannten *Fourierspektrum-Analyse* wird gezeigt, und die Interpretation der Resultate praktisch an dem Doppelstern Z CMA und dem Dreifachsystem T Tau demonstriert. Im Falle von Z CMA kann der Positionswinkel, der Abstand und die relative Helligkeit des Infrarotbegleiters, im Falle von T Tau das Flußverhältnis zwischen den beiden südlichen Komponenten und deren projizierter Abstand abgeleitet werden. Mit Hilfe separater Spektren von T Tau N und T Tau S wird der Nachweis einer Silikatabsorption in Richtung von T Tau S und die Berechnung eines räumlich aufgelösten Spektrums der nördlichen Komponente ermöglicht.

Abstract

In the first part of this work a volume-limited *multiplicity survey* with magnitude cutoff ($m_K \leq 10.5$ mag) of 158 young stellar objects located in the Ophiuchus molecular clouds is presented. All companions in the separation range $0.13''$ to $6.4''$ with flux ratios ≥ 0.1 at the diffraction limit could be detected by using speckle techniques. The degree of multiplicity is $29.1\% \pm 4.3\%$ and thus only marginally higher than the value $23.5\% \pm 4.8\%$ derived for the given separation range for the main-sequence solar-like stars in the solar neighbourhood. The implications of these findings will be discussed.

Afterwards observations with both speckle-cameras and adaptive optics systems are used to improve our knowledge of the *dynamical mass* of the two companions of the M-dwarf LHS 1070 located in the solar neighbourhood.

In the third part observations in the mid-infrared with the interferometric instrument MIDI at the VLTI are described. The reduction of the data with the *Fourierspectrum analysis* is explained and the interpretation of the results is demonstrated for the binary Z CMA and the triple system T Tau. In the case of Z CMA the position angle, the separation, and the relative brightness of the infrared companion could be determined. From the T Tau data the projected separation between the southern components and their flux ratio is derived. Separate spectra of T Tau N and T Tau S that reveal a silicate absorption towards T Tau S and a spatially resolved spectrum of T Tau N are shown.

May Astronomy Humble Mankind
By Bringing to Mind
The Creation, Evolution, and Destruction of Worlds.

Meiner Mutter Gewidmet

Contents

1	Introduction	15
1.1	Sensitivity and Resolution	15
1.2	High-Resolution Techniques	17
1.3	Resolving Young Binaries	18
1.4	Binary Frequency	19
1.5	Dynamical Masses	20
1.6	Infrared Companions	20
2	A Stellar Census	23
2.1	The Cloud Complex	23
2.2	Identification of Young Stellar Objects	25
2.3	The Sample	26
3	The Turbulent Atmosphere	39
3.1	Kolmogorov-Obukhov Turbulence	39
3.2	Taylor Hypothesis	40
3.3	Phase Shifts	41
3.4	The Fried Parameter	41
3.5	Coherence Time	43
3.6	Anisoplanatism	43
3.7	Scintillation	44
4	Speckle-Interferometry	47
4.1	Imaging Through the Atmosphere	47
4.2	Speckle Images	47
4.3	Reduction Methods	48
4.3.1	Amplitude Reconstruction	49
4.3.2	Phase Reconstruction	51
4.3.3	Shift-and-Add	53
4.4	Observations	53
4.4.1	Wavelength Range	53
4.4.2	Instruments	55
4.4.3	The Reference Source	56
4.5	Data Reduction	57
4.5.1	Prereduction	57

4.5.2	Visibility and Phases	60
4.5.3	Determination of the Binary Parameters	63
4.5.4	Undetected Companions	64
5	Multiplicity of the ρ Oph Cloud	67
5.1	Results	67
5.1.1	Uncorrected Data	67
5.1.2	Completeness	67
5.1.3	Lower Separation Limit	70
5.1.4	Background	74
5.1.5	Surface Density	75
5.1.6	Wide companions	77
5.1.7	Number of Systems After Background Subtraction	77
5.1.8	The Restricted Sample	78
5.2	Discussion	78
5.2.1	Comparison to Main-Sequence Stars	78
5.2.2	Comparison to Previous Surveys	80
5.2.3	Implications for the Formation Process	81
5.3	Previously Known Binaries	88
5.4	Additional Sources	91
5.5	Summary	93
6	The Triple System LHS 1070	95
6.1	Properties of a Cosmic Neighbour	95
6.2	Adaptive Optics	96
6.3	Data Reduction	101
6.4	Orbital Motion	102
6.5	Dynamical Mass Determination	104
7	MIDI at the VLTI	107
7.1	The Mid-Infrared	107
7.2	The Very Large Telescope Interferometer	108
7.2.1	The Site	110
7.2.2	The VLTI Grid	112
7.2.3	Feeding the Instruments	112
7.3	MIDI - VLTI's First Science Instrument	113
7.3.1	The Warm Optical Bench	114
7.3.2	The Cold Optical Bench	115
7.3.3	The Intermediate Focus	116
7.3.4	The Photometric Beams	117
7.3.5	The Beamcombiner	117
7.3.6	Filters and Dispersive Elements	118
7.3.7	The Three Cameras	118
7.3.8	The Detector	119
8	Long-Baseline Interferometry	121
8.1	The Basic Idea	121
8.2	Resolution of an Interferometer	123
8.3	Interferometric Beam Combination	123
8.3.1	Image-Plane or Fizeau Interferometers	124

8.3.2	Pupil-Plane or Michelson Interferometers	124
8.4	Polychromatic Sources	125
8.5	Extended Sources	126
8.6	Source Morphologies	128
8.6.1	Point Source	128
8.6.2	Binary Star	128
8.6.3	Uniform Circular Disk	129
8.6.4	Gaussian Disk	129
8.6.5	Rectangular Distribution	130
9	Obtaining Visibilities with MIDI	133
9.1	Observations	133
9.1.1	Pointing	133
9.1.2	The Nasmyth Adapter	134
9.1.3	Coudé Guiding	135
9.1.4	Delayline Adjustment	136
9.1.5	The Switchyard	136
9.1.6	Acquisition	137
9.1.7	Fringe Search	140
9.1.8	Fringe Track	140
9.1.9	Photometry	144
9.2	Analysis	145
9.2.1	Masking the Windows	145
9.2.2	The Fourier Amplitude	146
9.2.3	Interferometric Flux	151
9.2.4	Photometric Flux	152
9.2.5	Raw Visibility	152
9.2.6	Instrumental Visibility	153
9.2.7	Calibrated Visibility	154
9.3	Planning an Observation	155
9.3.1	Science Targets	155
9.3.2	Calibrators	156
9.4	Application I: The Binary Z CMa	157
9.4.1	Introduction	157
9.4.2	Journal of Observations	158
9.4.3	Results	158
9.4.4	Fitting a Binary Model	160
9.5	Application II: The Triple T Tau	167
9.5.1	Introduction	167
9.5.2	The Southern Component	168
9.5.3	The Northern Component	171
9.5.4	Individual Spectra	173
9.5.5	Correlated Flux of T Tau N	175
9.6	Summary	175
10	The Future - Imaging with MIDI	177
	Bibliography	179

Chapter 1

Introduction

1.1 Sensitivity and Resolution

The dilemma of an astronomer is that its laboratory is incredible huge, but the door is closed and a small window is the only link between him and the big experiment running inside for billions of years. Indeed, astronomy is unique when compared with other natural sciences. All discoveries are solely based on observations. Only a clever selection of targets can help to answer the open questions. The results of these observations are interpreted within a theoretical framework developed with the help of experiences very often collected in other fields of physics, like mechanics, electrodynamics etc. New questions arising from these interpretations have to be answered again by observations. Only a few samples collected during space missions can be actively manipulated either in situ or in laboratories on earth.

From this point of view it is not surprising that the primary task of engineers working in the field of astronomy is the improvement of the devices used to observe the targets either by increasing their sensitivity or resolution. The

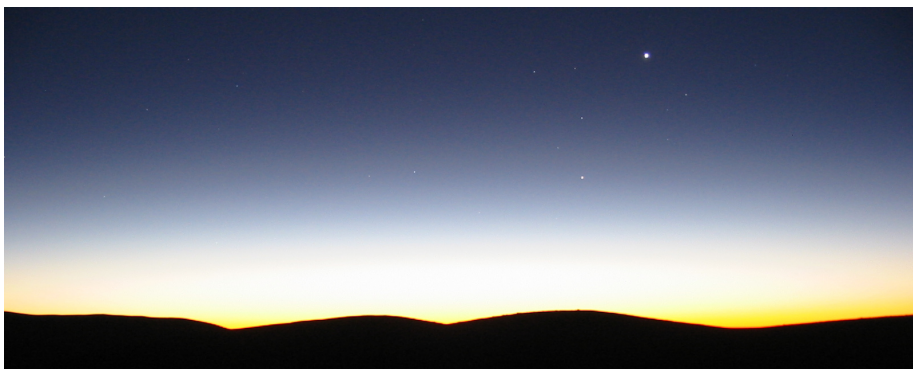


Figure 1.1: Mercury and Venus in the constellation Sagittarius as seen in the evening of 11th December 2003 from Paranal.

sensitivity S of a telescope equipped with a detector is given by

$$S = \pi \left(\frac{D}{2} \right)^2 \eta, \quad (1.1)$$

where D is the diameter of the primary mirror and η the quantum efficiency of the detector, i.e. the efficiency of converting infalling photons into a signal that can be measured. Today detectors are available for many wavelength ranges with high efficiencies. In the visual the progress is intriguing. Modern *Charged Coupled Devices* (CCDs) reach efficiencies close to unity. The human eye – the first astronomical detector – is limited to $\eta \approx 0.03$ for the dark-adapted or scotopic vision. Another advantage of technical detectors like semiconductor chips or previously used photographic plates is their ability to integrate the signal over time. While this can be done for hours, the integration of the human eye is limited to a maximum of approximately 0.1 s.

The resolution θ_R , i.e. the ability to distinguish two point sources separated by an angle θ_R from each other, is related to the wavelength λ of the observed photons and again the diameter of the primary mirror. After applying the *Rayleigh criterion* that two point sources can be resolved when the separation between the central peaks of their diffraction patterns is larger than the distance between the central peak and the first minimum, one finds

$$\sin \theta_R \approx \theta_R = f \cdot \frac{\lambda}{D}, \quad (1.2)$$

with $f = 1.22$ for round apertures. The resolution of a telescope with 10 cm diameter is thus approximately one arcsecond in the visual wavelength range. This is at least 100 times higher than the resolution of the unaided human eye. When watching through this telescope, the sensitivity of the eye is improved approximately by a factor of 150, i.e. stars of 12 mag in the visual can be recognised under a rural sky.

Equations (1.1) and (1.2) favour the strategy to build telescopes with diameters as large as possible. Indeed large efforts have been made to increase the size of the aperture. One breakthrough came in the 1990 when the *New Technology Telescope* (NTT, ESO, La Silla, Chile) pioneered active optics. This technique allows to build thin mirrors that are actively controlled to preserve their shape at all positions. The NTT also was one of the first telescopes residing on an alt-azimuthal mount within a completely rotating building tightly fitted to the telescope. Although carrying only a 3.5 m collecting mirror, the NTT is a cornerstone towards the big facilities, like the *Very Large Telescope* (VLT, 4×8.2 m, Cerro Paranal, Chile), the *Large Binocular Telescope* (LBT, 2×8.4 m, Mt. Graham, Arizona, USA), or the *Keck* telescopes (2×10 m, Mauna Kea, Hawaii, USA). The situation is nicely described by Hellemans (2000):

“On remote mountain tops across the world, a new breed of optical and infrared telescopes stands sentry, watching the heavens. They are the colossi of modern astronomy. Twice the size of their predecessors, they are giants equipped with primary mirrors measuring up to ten meters across.”

Currently, ESO studies the feasibility to construct an even larger telescope named OWL (*Overwhelmingly Large* telescope) with an aperture of 6000 m²!

Unfortunately, the situation is not as easy as it may look like. Although the sensitivity increases with growing apertures according to (1.1), the resolution is limited above a certain threshold by the atmosphere. In the visual wavelength regime this threshold corresponds under medium conditions to the resolution of the 10 cm telescope described above. How the atmospheric influence can be explained and quantified is described in Chapter 3.

1.2 High-Resolution Techniques

Large efforts have been made during the last four decades to overcome the seeing-limited resolution. The probably most spectacular solution is to launch telescopes into space. Similar to satellites are balloons or airplanes that carry for a limited time telescopes into the stratosphere. Since such telescopes are very expensive and available only to a limited number of astronomers, they have to remain very special devices. Fortunately, techniques to improve the resolution of ground-based telescopes have been successfully developed over the last decades. They are briefly described below. However, satellites are the only possibility to observe those parts of the electromagnetic spectrum that are blocked by the atmosphere.

Lunar Occultations This method uses the occultation of an astronomical source by the moon to derive spatially resolved one-dimensional informations on the structure perpendicular to the lunar limb (Leinert, 1994). Therefore, the lightcurve of the source during its disappearance at the eastern or its reappearance at the western limb is recorded. Under ideal conditions the lightcurve of a point source varies like a Fresnel diffraction pattern. If the object is extended, the pattern becomes smeared out. Since the telescope acts as a mere light collector, the only limitations introduced by the atmosphere are the sky background, the sky background noise, and the variations of the stellar flux called scintillation (Section 3.7). Therefore, lunar occultations are preferably performed in the near-infrared. The resolution that can be achieved here for a bright object and an appropriate sampling rate of the lightcurve is approximately 0.001 arcsec! A disadvantage of this method is the limited number of targets located close enough to the ecliptic and the rareness of such occultation events.

Speckle Interferometry This method overcomes the limited resolution of ground-based telescopes by using special cameras providing short integration and readout times (Chapter 4). Since the resulting images do not show the blurring introduced by the temporal evolution of the atmospheric turbulences, they are snapshots of the distorted wavefront and can be analysed afterwards to reconstruct the structure of the observed target. Speckle interferometry has been developed in the near-infrared due to the more stable atmosphere when compared with the visual regime.

Adaptive Optics While speckle imaging is passive, i.e. it virtually ‘freezes’ the atmosphere by taking images with a short integration time, adaptive optics systems (Section 6.2) correct the atmospheric distortions of the wavefront. This active method needs a real-time analysis of the incoming light and a real-time

adaptation of the mirror correcting the distortions. Therefore, adaptive optics systems require not only quick cameras, but also fast adjustable mirrors and modern microcomputers.

Long-Baseline Interferometry This technique combines the light coming from two or more telescopes (Chapter 8). Here the individual telescopes represent subapertures of a virtual telescope with a diameter D_{vir} corresponding to the separation between the two telescopes, i.e. the *baseline*, or when more than two apertures are used to the largest baseline offered. The sensitivity is still limited to the sensitivity of the single telescopes, but the resolution is determined by the virtual diameter D_{vir} when the relative optical path difference between the telescopes is removed. Although long-baseline interferometry is a common tool in radio astronomy, its application at infrared or even visual wavelengths is still challenging. When looking at modern astronomical observatories one fact is noticeable. Many of them are designed with two or more equal telescopes to offer the astronomical community the possibility to tap the full potential of long-baseline interferometry.

1.3 Resolving Young Binaries

The search and study of binaries is one of the topics in astronomy, where resolution plays a crucial role. Although Aitken & Doolittle (1932) already published a catalogue of 17181 double stars, this huge number of detected companions just reflects the large separation range covered by main-sequence stars. It extends over more than seven decades (Mathieu, 1994). The search for companions around young stars residing within their parental clouds at typical distances ~ 150 pc is more challenging and requires high resolution techniques. A short historical review on the detection of companions around T Tauri stars shows this impressively.

Joy & van Biesbroeck (1944) detected five companions around the eleven at that time known members of this new class of irregularly variable, low-mass, young stellar objects (Joy, 1945). They used a spectrograph mounted at the 100-inch telescope on Mount Wilson. Afterwards, the position angles, separations ($0.8''$ - $5.7''$), and relative fluxes in the visual (< 0.3) were determined with micrometer measurements at the McDonald Observatory. Two decades later Herbig (1962) could add 24 T Tauri binaries to this list. Cohen & Kuhi (1979) increased serendipitously the number of known multiple systems to 61. They counted the companions on the TV acquisition system of the Lick 3 m reflector during their spectroscopic survey of more than 500 sources. This system was limited to a flux ratio of 0.01 ($\lambda = 800$ nm) at the detection limit of $1''$ - $2''$.

The advent of high-resolution observations of young stellar objects may be marked deeply symbolic by the finding that the prototype of low-mass pre-main-sequence stars, T Tau itself, is a binary with a separation of $0.7''$. The companion was resolved by Dyck et al. (1982) with the then new technique of speckle imaging. Large surveys exploring the subarcsecond range either with speckle techniques (Ghez et al., 1993; Leinert et al., 1993) or lunar occultations (Simon et al., 1995) in the near-infrared were published in the following years. Leinert et al. (1993) found in their diffraction-limited speckle survey of 104 T Tauri stars in the Taurus-Auriga complex 51 companions and thus almost

doubled their known number in that star-forming region. In the separation range between 0.13" and 1" 28 companions could be resolved. Moreover, the surveys of Leinert et al. (1993), Ghez et al. (1993), and Köhler & Leinert (1998) revealed an overabundance by a factor of two of binaries among the young stars in Taurus-Auriga when compared to the binary frequency of the solar-like main-sequence stars in the solar neighbourhood (Duquennoy & Mayor, 1991).

1.4 Binary Frequency

This result made it very clear that binarity indeed is the dominant mode of star formation. Consequently, in the years after these studies both theoretical and observational work on binaries among young stars and binary formation was intensified. Observationally, two main routes were followed: studying the fraction of binaries in associations and in young clusters, both with the aim to learn about the conditions which influence the preference of binary over single star formation. The study of associations, all of which are about at the same distance of ~ 150 pc and all which are about equally young (several million years) has so far not given a clear picture, see e.g. the summary by Duchêne (1999): the duplicity is high in *Taurus-Auriga*, *Coronae Australis* (Ghez et al., 1997; Reipurth & Zinnecker, 1993) and *Scorpius-Centaurus* (Köhler et al., 2000b), while it almost corresponds to main-sequence values or is even lower in *Chamaeleon* and *Lupus* (Brandner et al., 1996; Reipurth & Zinnecker, 1993; Köhler, 2001). Identifying the reason for this different behaviour will need further observational studies and continued discussions on the interpretation, although Durisen & Sterzik (1994) proposed a possible explanation, namely that fragmentation should lead to lower fractions of binaries for higher initial cloud temperatures.

The situation is somewhat more settled in the case of clusters. The advantage here is that clusters of different age can be studied in order to get information on the temporal evolution. The result is that even the youngest of them, the *Trapezium*, does not show an overabundance of binaries (Prosser et al., 1994; Petr et al., 1998; Padgett et al., 1997). It is true that N-body simulations, e.g. Kroupa (1995) indicate that in dense clusters the fraction of binaries could be reduced by gravitational interactions within 1 million of years from 'high' to 'normal'. But the assumption that the lower fraction of binaries in dense clusters may be intrinsic and determined by the density as a parameter remains a very attractive hypothesis (Duchêne et al., 1999).

However, revealing correlations between the binary frequency and the environmental conditions will improve our knowledge of the underlying physical processes of star-formation. The ρ Ophiuchi star-forming region with its relatively young stellar population within a quite dense environment is a very promising candidate to reveal differences with respect to the somewhat older and less denser Taurus-Auriga aggregate. Since the ρ Ophiuchi molecular cloud complex is located at a distance comparable to that of Taurus-Auriga, biases resulting from different observable separation ranges play no role. Unfortunately, although also indicating an overabundance of binary systems when compared to the main-sequence, the significance of the currently available statistical results (Ghez et al., 1997; Simon et al., 1995; Duchêne, 1999) is limited due to the small number of observed targets. Consequently, the aim of the first part of this thesis is to derive an enlarged survey for the ρ Ophiuchi cloud complex that is

comparable to that of Taurus-Auriga (Leinert et al., 1993; Köhler & Leinert, 1998). Therefore, a magnitude-limited sample based on several previous works that determined the cloud membership of the sources has been created (Chapter 2). With exception of some well-studied objects the complete sample was observed by using speckle techniques at 3.5 m telescopes (Chapter 4). To reduce the data a software package developed in our group during the last years has been used. After the correction of the raw data the results in terms of age and density effects will be discussed (Chapter 5).

1.5 Dynamical Masses

Mass is the most important parameter of a star. However, the knowledge of accurate masses of objects below one solar mass is still very limited. The result is that the initial mass function essential for theories of star-formation is not precisely known. Especially the high duplicity found both for main-sequence and even more pronounced for pre-main-sequence stars is one of the important uncertainties which bias spectroscopic or photometric studies.

Otherwise, resolved binaries historically play an important role in astrophysics for the determination of stellar masses. These so-called *dynamical masses* are solely based on the orbital elements found by fitting astrometric measurements of the position of the companion relative to the primary. Therefore, these masses are not influenced by theoretical predictions and are powerful tools to test evolutionary models of stellar objects.

The determination of the dynamical mass requires a good sampling of the orbital motion. This sets an upper boundary to the periods of the orbits. Since the squared period is proportional to the third power of the semi-major axis of the orbit and the reciprocal system mass, small semi-major axis are crucial especially for the low-mass binaries. High-resolution techniques are thus required even for systems located not far from the sun. An example is shown in Chapter 6 where data taken with adaptive optics systems and speckle interferometric methods (partly assisted by adaptive optics systems) are used to refine the orbit and thus the dynamical mass of the evolved triple system LHS 1070 located in the solar neighbourhood.

1.6 Infrared Companions

About 10% of all T Tauri stars probably harbour so-called *infrared companions*. They are characterised by bright infrared and faint visible radiation (Koresko & Leinert, 2001). When compared with their T Tauri primaries infrared companions show a more extreme infrared excess and a higher photometric variability. It is still unclear, what causes their unusual properties. A different evolutionary status, a special viewing geometry, or active accretion either from a circumstellar or circumbinary disk are discussed. The influence of the primary may also play a role by triggering the active accretion due to gravitational interactions.

The binary system Z CMa and the triple system T Tau, both harbouring an infrared companion were observed in the mid-infrared with the interferometric instrument MIDI operated by ESO at the VLTI (Chapter 7). Long-baseline interferometry with MIDI allows to investigate the circumstellar environment

of these unusual systems in the thermal infrared with a resolution that cannot be reached with currently available single-dish telescopes. The determination of the binary parameters, the individual spectra of the northern and the southern component of T Tau, and the spatially resolved spectrum of T Tau N will demonstrate the unique possibilities offered by this new and challenging technique (Chapter 9).

Chapter 2

A Stellar Census

‘But if you look for a companion, be careful in choosing!’

In this chapter the selection of a statistically significant sample of young stellar objects residing within the ρ Ophiuchi molecular clouds will be described. It is the basis of a multiplicity survey (Chapter 5) that is comparable to those of Taurus-Auriga (Leinert et al., 1993; Köhler & Leinert, 1998).

2.1 The Cloud Complex

The ρ Ophiuchi Dark Cloud (L1688, Fig. 2.1) is the densest part of a complex of vast dark nebulae and molecular clouds that extends in galactic coordinates from $l \approx 345^\circ$ to 10° and from $b \approx 0^\circ$ to $+25^\circ$. While the ρ Oph cloud is located in the western part, the eastern part of this complex is dominated by so-called *streamers*, i.e. long elongated filaments. A scenario presented by de Geus (1992) describes the formation of the complex. The precursor of the ρ Oph cloud seen today was a bigger cloud that was a ‘clump’ in the general Ophiuchus gas. Early-type stars located in the Upper-Scorpius OB association ($l \approx 360^\circ \dots 343^\circ$, $b \approx +10^\circ \dots +30^\circ$) produced a shock-wave that encountered the dense ρ Oph clump from behind, swept away material and deposited it in the present day filaments. This encounter may also have triggered the continuing low-mass star formation within this cloud resulting in an extremely young population of stars with a median age of ≈ 0.3 Myr (Greene & Meyer, 1995; Luhman & Rieke, 1999).

Sartori et al. (2003) investigate the star-formation process on a larger scale. They found that the pre-main-sequence stars within the Ophiuchus, Lupus and Chamaeleon molecular cloud complexes follow a similar spatial distribution as the early-type stars in the subgroups of the Scorpius-Centaurus OB association and a newly found OB association in Chamaeleon. Furthermore, the young objects form an almost uniform group with respect to their kinematics and ages. The most natural scenario to explain the measurements is a spiral arm passing close to the Sun. The global distribution of HII regions (Lépine et al., 2001) supports this hypothesis.

Nevertheless, the distance to the ρ Oph cloud is still subject of discussions, but it has been possible to derive a reliable distance range with the Hipparcos and Tycho catalogues. A lower limit was published by Knude & Hog (1998) who found a steep increase of reddening at 120 pc. For this, they used class V and class III stars in the vicinity of the cloud. Otherwise an upper limit of 145 ± 2 pc has been derived by de Zeeuw et al. (1999). They determined the distance of the Scorpius-Centaurus OB association in the background of the ρ Oph cloud by analysing positions, proper motions, and parallaxes of its members. Here a value of 140 pc is assumed. This distance has been measured for the Taurus-Auriga association and was used by Köhler & Leinert (1998) for their multiplicity survey. So, a direct comparison of the results is possible.

2.2 Identification of Young Stellar Objects

Infrared Observations in our Galaxy have revealed that the formation of stars takes place in dense molecular clouds like the cloud complex near ρ Oph described in Section 2.1. Therefore, a significant part of the luminous energy is radiated over a wide range of infrared wavelengths (1...100 μ m). So it is the most obvious way to search for these embedded sources by infrared observations. Unfortunately, it is not possible to distinguish between cloud members and reddened background stars without performing mid-infrared photometry or near-infrared spectroscopy. A very common alternative used by many authors is to determine the slope a of the spectral energy distribution (SED) over a wavelength range as wide as possible. This spectral index is given by

$$a = \frac{d \log (\lambda F_{\lambda})}{d \log \lambda} \quad (2.1)$$

as defined in Lada (1987). Depending on (2.1) infrared sources are divided up into three classes representing their evolutionary state (Bontemps et al., 2001):

Class I: rising SEDs resulting from (evolved) protostars ($a \gtrsim 0$)

Class II: decreasing SEDs, but broader than stellar blackbodies indicate T Tauri stars with at most optically thick circumstellar disks ($-2 \lesssim a \lesssim 0$)

Class III: weak T Tauri stars with at most optically thin disks show SEDs consistent with (or only slightly broader than) reddened stellar blackbodies ($a \lesssim -2$)

Moreover, young submillimetre protostars in an early accretion phase are designated as Class 0 (André et al., 1993).

X-ray While Class I and Class II objects are easy to identify at infrared wavelengths, the confusion between Class III objects and background main-sequence solar-type or giant stars still remains a problem. Here X-ray-observations play an important role, since it has been shown that most T Tauri stars are X-ray emitters (Montmerle et al., 1983). Responsible for this X-ray emission is an enhanced solar-like magnetic activity at the stellar surface. Casanova et al. (1995) reported for the first time X-ray sources in the dense core region of the ρ Oph molecular cloud with an IR-counterpart not detected in the visible and

thus revealed a close link between young stellar objects and X-ray emission. This result strengthens the role of X-ray observations as a criterion for cloud membership.

Other Indicators In addition other indicators of young stellar object status can be used in areas of lower extinction, e.g. broad $H\alpha$ equivalent width resulting from hot accreting gas, photospheric Lithium absorption, associated nebulosity, and high optical polarisation (Barsony et al., 2003).

2.3 The Sample

The sample of 158 young stellar objects (YSOs) recruits from surveys at optical, infrared, and X-ray wavelengths (Table 2.1). From these surveys objects were selected that can be considered as cloud members using the criteria commonly applied in distinguishing young stars from background or foreground stars (Section 2.2). The most convincing are detailed studies of optical spectra (Herbig & Bell, 1988; Bouvier & Appenzeller, 1992), infrared spectral energy distributions (Wilking et al., 1989; Greene et al., 1994), mid-infrared colour-magnitude relations (Bontemps et al., 2001), and X-ray detections combined with optical/infrared informations (Casanova et al., 1995). A sample as complete as possible down to magnitude $m_K = 10.5$ mag has been combined and observed. It includes objects for which preferably more than one of the criteria infrared excess, X-ray detection, and $H\alpha$ emission applied. The criteria are indicated in Table 2.3 together with the number of the catalogue from which a source was initially chosen. If the criteria did not appear strong, the sources are marked with an ‘U’. Our sample may be characterised as volume-limited with a magnitude cutoff. It was intended to be larger in size and more statistically complete than earlier surveys.

The coordinates and the magnitudes in the K-band presented in Table 2.2 and Table 2.3 are taken from the *Two Micron All-Sky-Survey* (2MASS) Catalog of Point Sources. The coordinates have been verified for all objects. For those sources that are also included in Barsony et al. (1997) additional K-band magnitudes are provided. At the time of the preparation of the survey, the K-band magnitudes of Greene & Young (1992) and Barsony et al. (1997) were available and were used to determine the magnitude cutoff. In practice the magnitude cutoff was uncertain due to variability of the young sources and non-uniformity of the catalogues. In some cases, sources close to the cutoff magnitude could not be included into the survey, because there was no time left to observe them.

We started to build the sample with the then new list of 87¹ confirmed cloud members presented in Casanova et al. (1995). These authors analysed a deep ROSAT image of the central part of the ρ Oph star-forming region and compared the sources with confirmed members mainly derived from the infrared surveys of Wilking et al. (1989) and Greene et al. (1994). This list was completed by including ROXs 4, SR 2 and VLA 1623. Since in Casanova et al. (1995) 67% of the found X-ray sources and 42% of the candidate X-ray sources are common with the list of confirmed cloud members, hitherto unconfirmed cloud members coinciding with the remaining (candidate) X-ray sources are probable new cloud

¹To allow easier comparison of different papers the wide binaries SR 12, SR 24, ROXs 31, ROXs 43 are always counted as one object.

Table 2.1: Contributions of the different papers to the survey (column 7). Given are the number of sources in the individual papers (column 3), the number of sources with $m_K = m_{2\text{MASS}} < m_{\text{lim}} = 10.5$ mag therein (column 4), the number of targets not included in the previously listed papers (column 5), and the number of targets finally observed (column 6). The two targets additionally contributed by Casanova et al. (1995) (Table 2) are slightly fainter than 10.5 mag. The regions covered by the individual papers (column 8), the criteria used to determine the membership of the sources (column 9), and the quality of the criteria (column 10) are also listed.

#	Paper	sources	$m_K < m_{\text{lim}}$			survey	region	criterion	member
			total	new	obs				
1	Casanova et al. (1995) (Table 2)	87	61	61	59	61	core	X-ray + NIR, visual	bona fide
2	Casanova et al. (1995) (Table 1)	19	8	8	7	7	core	X-ray + NIR	probable
3	Casanova et al. (1995) (Table 3)	22	2	2	2	2	core	X-ray + NIR	candidate
4	Wilking et al. (1989) (Table 4)	74	56	5	5	5	L1688	visual to FIR SED	bona fide
5	Greene et al. (1994)	47	37	14	14	14	L1688, L1689, L1709	visual to MIR SED	bona fide
6	Bouvier & Appenzeller (1992)	30	30	13	13	13	whole complex	visual spectra	bona fide
7	Grosso et al. (2000)	54	46	9	7	7	core	Xray + NIR, MIR	bona fide
8	Bontemps et al. (2001)	212	98	20	15	15	L1688, L1689	MIR excess	bona fide
9	Herbig & Bell (1988)	24	24	6	6	6	whole complex	visual spectra	bona fide
10	Wilking et al. (1987)	57	53	19	15	15	whole complex	H α	probable
11	Elias (1978)	26	26	3	3	3	whole complex	NIR to MIR SED	bona fide
12	Wilking et al. (1989) (Table 6)	38	24	13	10	10	L1688	visual to FIR SED	candidate
				Σ		158			

members and thus also targets of our survey. After deleting all sources fainter than 10.5 mag in the K-band to comply with the sensitivity of our companion search and after the removal of the background giant VSSG 6 (Luhman & Rieke, 1999) we are left with 61 certain and 10 probable cloud members (see Table 2.1). For the catalogue differences just mentioned IRS 46 and IRS 54, bright enough in 2MASS, did not make it into our sample, while WL 5 and WL 6 were observed.

From the table of cluster members in Wilking et al. (1989), H α 38, H α 60, SR 20 and H α 63 are missing in the list of Casanova et al. (1995) due to their position outside the investigated core region, as well as the objects IRS 7, IRS 8, IRS 14 where the IRAS association was uncertain. Also the source VSSG 12 was ignored for inconsistencies in the coordinates². With exception of the spurious source VSSG 12 and the faint objects IRS 7 and IRS 14 we reinserted these sources.

While the sources presented in Wilking et al. (1989) only cover the densest part of the cloud complex (L1688), the multicolour infrared study by Greene et al. (1994) includes also sources in L1689 and L1709. We removed VSSG 13, VSSG 15, and VSSG 16, because they had been identified by Elias (1978) as field stars. Also the background giants GY 45, GY 65, GY 232, GY 411, and VSSG 6 (Luhman & Rieke, 1999) have been deleted. From the remaining 37 sources brighter than $m_K = 10.5$ mag 14 were new and became part of our sample.

Bouvier & Appenzeller (1992) searched for counterpart candidates of X-ray sources detected with the *Einstein* satellite in the direction of the ρ Oph molecular clouds. Studying 46 optically visible stars lying in the error circles of 29 ROX sources with spectroscopic and photometric methods resulted in the identification of 29 certain and one probable (ROXs 45D = DoAr 48) cloud member. Of these, we added the 13 until now unaccounted cloud members to our list.

The link between X-ray emitting sources and their counterparts at longer wavelengths is particularly evident in the work of Grosso et al. (2000). Out of 63 sources found with the *ROSAT High Resolution Imager* Grosso et al. (2000) could identify 54 with optical, infrared and radio sources. This emphasises again the usefulness of X-ray emission as criterion for membership. Eight of the sources in Grosso et al. (2000) do not match the brightness criterion and 37 of the remaining were already in our list. Finally, we observed seven of the nine new targets, omitting two which were close to the brightness limit.

Recently (Bontemps et al., 2001) presented an extensive mid-infrared survey of L1688, L1689N and L1689S performed with the ISOCAM camera on board the ISO satellite at 6.7 μm and 14.3 μm . Due to the high sensitivity and the good spatial resolution they have been able to detect 425 point sources. A catalogue of 212 sources detected at both wavelengths and classified as cloud members on the basis of colour-magnitude relations is now available. This catalogue includes 114 objects fainter than $m_K = 10.5$ mag. Twenty out of the remaining 98 sources were not already included in our list. With exception of five sources close to the brightness limit all could be observed. If a source of our survey is included in this catalogue, the number therein is given in the second column of Table 2.3.

²Although SIMBAD identifies VSSG 12 with GSS 30-IRS 2 Wilking et al. (1989) give coordinates north of GSS 29.

Table 2.2: The eleven sources well observed by Ghez et al. (1993) and/or Simon et al. (1995). The last column indicates from which survey the results are taken.

Object	<i>J</i> 2000.0		<i>K</i> _{2MASS} [mag]	Observed by
	α	δ		
Haro 1-4	16 25 10.52	-23 19 14.6	7.509	G
SR 4	16 25 56.16	-24 20 48.2	7.518	G
DoAr 21	16 26 03.02	-24 23 36.0	6.227	G
DoAr 24	16 26 17.06	-24 20 21.6	8.063	G
DoAr 24E	16 26 23.36	-24 20 59.8	6.571	G
SR 24	16 26 58.51	-24 45 36.9	7.057	S
IRS 32b	16 27 13.82	-24 43 31.7	9.978	S
SR 12	16 27 19.51	-24 41 40.4	8.408	S
SR 20	16 28 32.66	-24 22 44.9	6.850	G
V 853 Oph	16 28 45.28	-24 28 19.0	7.997	G
Haro 1-16	16 31 33.46	-24 27 37.3	7.610	G

In the third edition of their catalogue Herbig & Bell (1988) listed 24 sources towards the ρ Oph molecular clouds. All are bright enough to satisfy our requirements. In our complete field six sources were new and thus added to our list. Other targets in the neighbourhood of L1688 can be found in the catalogue of Wilking et al. (1987). They used objective-prism plates to survey 40 square degrees toward the Sco-Cen OB association including much of the ρ Oph cloud complex for H α emission and found 86 sources. The entries #1 to #15, #17, #36, #43, #55, #56, #66, #70, #79 and #81 to #86 are too far from the central cloud. The remaining 57 objects include 53 that fall below our brightness limit. Nineteen of them were not yet included in our sample. They are mainly located in the western portion of the complex. All sources of this catalogue that have been observed are indicated by their number in the third column of Table 2.3. From the sources in Elias (1978) we removed all objects too far from the clouds: #1 to #5, #39, #40, #43, and #46 to #50. The remaining 26 candidates contain 3 new sources: Elias 12, Elias 41, and Elias 45.

Finally, we added objects from the list of unidentified sources given in Wilking et al. (1989). Out of the 38 objects 24 are brighter than 10.5 mag in the K-band. Thirteen sources are new and we could observe 10 of them.

The full list of sources brighter than 10.5 mag in the K-band would include 173 objects spread over L1688 and its environment with a natural concentration in L1688 (Fig. 2.1). Our multiplicity survey covers 156 of these and 2 slightly fainter young stellar objects. Eleven well known sources among them have been already observed in the last decade by Ghez et al. (1993) and Simon et al. (1995) with speckle imaging and during lunar occultations (Table 2.2), i.e. with sufficient resolution and sensitivity. So, there was no necessity to observe these sources again. They are marked in Table 2.3 with an ‘O’.

Table 2.3: The 158 sources of our survey

Object	ISO No.	H α No.	J2000.0		B1950.0		K ₂ MASS [mag]	K _{BKLT} [mag]	Selection #	Note crit.	Other Designation	
			α	δ	α	δ						
H α 16	–	16	16 23 34.83	-23 40 30.3	16 20 34.46	-23 33 35.0	8.552	–	10	- v -	U	-
H α 18	–	18	16 24 59.74	-24 56 00.8	16 21 57.68	-24 49 11.1	9.441	–	10	- v -	-	-
H α 19	–	19	16 25 02.09	-24 59 32.3	16 21 59.95	-24 52 42.8	9.220	–	10	- v -	-	-
Haro 1-4	–	20	16 25 10.52	-23 19 14.6	16 22 10.51	-23 12 25.7	7.509	–	9	- v -	O	HBC 257
H α 21	–	21	16 25 15.22	-25 11 54.1	16 22 12.80	-25 05 05.4	9.642	–	10	- v -	U	-
H α 22	–	22	16 25 17.27	-25 11 05.5	16 22 14.87	-25 04 16.9	9.911	–	10	- v -	-	-
SR 2	–	–	16 25 19.24	-24 26 52.6	16 22 17.79	-24 20 04.2	7.798	–	1	x - i	A	Elias 6
SR 22	–	23	16 25 24.34	-24 29 44.3	16 22 22.83	-24 22 56.2	9.446	–	1	x v i	-	V852, HBC 258
SR 1	–	–	16 25 24.31	-24 27 56.6	16 22 22.83	-24 21 08.5	4.582	–	1	x - i	AE	Elias 9
ROXs 2	–	–	16 25 24.35	-23 55 10.3	16 22 23.57	-23 48 22.3	8.379	–	6	x v -	B	HBC 635
SR 8	–	–	16 25 26.87	-24 43 09.0	16 22 25.06	-24 36 21.1	8.662	8.72	2	x - -	-	-
IRS 2	1	–	16 25 36.74	-24 15 42.4	16 22 35.51	-24 08 55.2	8.380	8.36	1	x - i	-	-
Elias 12	–	–	16 25 37.81	-24 13 43.6	16 22 36.62	-24 06 56.5	6.867	6.95	11	- - i	-	-
J162538-242238	2	–	16 25 38.12	-24 22 36.3	16 22 36.75	-24 15 49.1	9.545	9.68	7	x - i	-	-
IRS 3	3	–	16 25 39.58	-24 26 34.9	16 22 38.12	-24 19 47.9	8.954	8.93	2	x - i	-	-
H α 24	–	24	16 25 42.89	-23 25 26.1	16 22 42.73	-23 18 39.3	9.204	–	10	- v -	-	-
IRS 8	–	–	16 25 47.69	-24 18 31.1	16 22 46.39	-24 11 44.6	9.701	9.69	4	- - i	-	-
IRS 9	–	–	16 25 49.05	-24 31 39.1	16 22 47.48	-24 24 52.7	9.487	9.41	1	x - i	-	-
ROXs 3	–	–	16 25 49.64	-24 51 31.9	16 22 47.64	-24 44 45.5	8.784	8.78	6	x v -	-	HBC 636
VSS 23	5	–	16 25 50.53	-24 39 14.5	16 22 48.78	-24 32 28.2	8.331	8.24	1	x v i	-	IRS 10, ROXs 4
ROXs 5	–	–	16 25 55.83	-23 55 10.0	16 22 55.02	-23 48 24.0	8.383	–	6	x v -	B	-
IRS 11	–	–	16 25 56.10	-24 30 14.9	16 22 54.54	-24 23 28.9	9.764	9.76	12	- - i	U	-

Table 2.3: (continued)

Object	ISO No.	H α No.	J2000.0		B1950.0		K _{2MASS} [mag]	K _{BKLT} [mag]	Selection #	Note crit.	Other Designation	
			α	δ	α	δ						
SR 4	6	25	16 25 56.16	-24 20 48.2	16 22 54.81	-24 14 02.3	7.518	7.25	1	x v i	O	ROXs 6, HBC 259, Elias 13
GSS 20	7	–	16 25 57.52	-24 30 31.7	16 22 55.96	-24 23 45.9	8.319	8.37	1	x v i	-	ROXs 7
Chini 8	–	–	16 25 59.65	-24 21 22.3	16 22 58.28	-24 14 36.6	9.531	9.52	2	x – –	-	-
ROXR1-12	8	–	16 26 01.61	-24 29 45.0	16 23 00.06	-24 22 59.4	9.629	9.55	7	x – i	-	J162601-242945
DoAr 21	10	–	16 26 03.02	-24 23 36.0	16 23 01.60	-24 16 50.6	6.227	6.16	1	x v i	O	ROXs 8, HBC 637, Elias 14
VSSG 19	11	–	16 26 03.29	-24 17 46.5	16 23 02.00	-24 11 01.0	9.115	9.07	5	x – i	-	-
Chini 11	–	–	16 26 08.01	-24 14 39.2	16 23 06.77	-24 07 54.1	9.812	9.79	12	– – i	U	-
SR 3	16	–	16 26 09.31	-24 34 12.1	16 23 07.66	-24 27 27.1	6.504	6.42	1	x – i	A	Elias 16
GSS 26	17	–	16 26 10.33	-24 20 54.8	16 23 08.96	-24 14 09.8	8.475	9.38	1	x – i	-	-
SKS 1-7	18	–	16 26 15.81	-24 19 22.1	16 23 14.47	-24 12 37.5	10.031	9.98	8	– – i	-	-
GSS 29	19	–	16 26 16.84	-24 22 23.2	16 23 15.44	-24 15 38.6	8.201	8.19	1	x – i	-	Elias 18
DoAr 24	20	27	16 26 17.06	-24 20 21.6	16 23 15.70	-24 13 37.1	8.063	8.09	1	x v i	O	GSS 28, ROXs 10A, HBC 638, Elias 19
H α 26	–	26	16 26 18.40	-25 20 55.7	16 23 15.73	-25 14 11.2	8.934	–	10	– v –	-	DoAr 23
VSSG 1	24	–	16 26 18.87	-24 28 19.7	16 23 17.33	-24 21 35.3	8.072	8.68	1	x – i	-	Elias 20
DoAr 22	–	–	16 26 19.32	-23 43 20.5	16 23 18.75	-23 36 36.2	9.018	–	9	– v –	-	HBC 260
H α 28	27	28	16 26 20.97	-24 08 51.9	16 23 19.85	-24 02 07.6	9.502	9.48	7	x v i	C	-
J162621-241544	28	–	16 26 21.02	-24 15 41.5	16 23 19.75	-24 08 57.2	9.273	9.27	8	– – i	-	-
Elias 21	29	–	16 26 21.38	-24 23 04.1	16 23 19.96	-24 16 19.8	8.835	8.32	1	x – i	CE	GSS 30 - IRS 1
GSS 30 - IRS 2	34	–	16 26 22.39	-24 22 52.9	16 23 20.96	-24 16 08.8	9.957	9.60	1	x – i	-	-

Table 2.3: (continued)

Object	ISO No.	H α No.	J2000.0		B1950.0		K ₂ MASS [mag]	K _{BKLT} [mag]	Selection		Note	Other Designation
			α	δ	α	δ			#	crit.		
DoAr 24E	36	30	16 26 23.36	-24 20 59.8	16 23 21.98	-24 14 15.7	6.571	6.44	1	x v i	O	GSS 31, HBC 639, ROXs 10B, Elias 22
LFAM 3	37	–	16 26 23.58	-24 24 39.5	16 23 22.12	-24 17 55.4	10.224	9.94	1	x – i	-	GY 21
DoAr 25	38	29	16 26 23.68	-24 43 13.9	16 23 21.82	-24 36 29.8	7.847	7.57	1	x v i	A	-
GSS 32	39	–	16 26 24.04	-24 24 48.1	16 23 22.58	-24 18 04.0	7.324	7.20	1	x – i	C	Elias 23, GY 23, S 2
Elias 24	40	31	16 26 24.07	-24 16 13.5	16 23 22.79	-24 09 29.4	6.685	6.77	1	x v i	-	-
H α 33	–	33	16 26 26.06	-23 44 02.6	16 23 25.46	-23 37 18.7	9.928	–	10	– v –	U	-
GY 33	43	–	16 26 27.54	-24 41 53.5	16 23 25.70	-24 35 09.7	9.983	9.83	8	– – i	-	-
ROXs 12	–	32	16 26 27.75	-25 27 24.7	16 23 24.93	-25 20 40.8	9.211	–	6	x v –	-	-
VSSG 27	46	–	16 26 30.47	-24 22 57.1	16 23 29.04	-24 16 13.5	9.977	10.72	1	x – i	-	-
S1	48	–	16 26 34.17	-24 23 28.3	16 23 32.72	-24 16 44.9	6.317	6.32	1	x v i	-	ROXs 14, Elias 25
H α 35	–	35	16 26 34.90	-23 45 40.6	16 23 34.26	-23 38 57.3	8.834	–	10	– v –	-	-
J162636-241554	51	–	16 26 36.83	-24 15 51.9	16 23 35.54	-24 09 08.7	9.589	9.38	7	x – i	-	-
H α 37	56	37	16 26 41.26	-24 40 18.0	16 23 39.44	-24 33 35.0	9.273	9.20	1	x v i	-	-
WL 8	58	–	16 26 42.02	-24 33 26.2	16 23 40.35	-24 26 43.4	9.578	9.44	8	– – i	-	-
GSS 37	62	–	16 26 42.86	-24 20 29.9	16 23 41.47	-24 13 47.1	7.878	8.00	1	x – i	-	VSSG 2, Elias 26
VSSG 11	64	–	16 26 43.76	-24 16 33.3	16 23 42.45	-24 09 50.6	9.604	9.58	1	x – i	-	-
GY 112	66	–	16 26 44.30	-24 43 14.1	16 23 42.42	-24 36 31.4	9.573	9.54	2	x – i	-	-
GSS 39	67	–	16 26 45.03	-24 23 07.7	16 23 43.58	-24 16 25.1	8.955	8.88	1	x – i	-	Elias 27
ROXs 16	68	38	16 26 46.43	-24 12 00.1	16 23 45.22	-24 05 17.5	7.485	7.51	4	x v i	-	VSS 27
Haro 1-8	–	39	16 26 47.42	-23 14 52.2	16 23 47.42	-23 08 09.7	8.619	–	9	– v –	B	HBC 261
H α 40	–	40	16 26 48.65	-23 56 34.2	16 23 47.76	-23 49 51.8	8.449	–	10	– v –	-	-

Table 2.3: (continued)

Object	ISO No.	H α No.	J2000.0		B1950.0		K _{2MASS} [mag]	K _{BKLT} [mag]	Selection		Note	Other Designation
			α	δ	α	δ			#	crit.		
WL 18	72	–	16 26 48.98	-24 38 25.2	16 23 47.20	-24 31 42.8	9.977	9.82	1	x – i	E	-
VSSG 3	73	–	16 26 49.23	-24 20 02.9	16 23 47.85	-24 13 20.5	8.687	8.62	1	x – i	-	-
VSSG 10	–	–	16 26 51.69	-24 14 41.6	16 23 50.41	-24 07 59.3	9.713	9.77	12	– – i	U	-
VSSG 5	78	–	16 26 54.44	-24 26 20.7	16 23 52.92	-24 19 38.7	10.014	9.88	1	x – i	-	-
GY 156	80	–	16 26 54.97	-24 22 29.7	16 23 53.53	-24 15 47.7	10.163	10.19	3	x – i	-	-
VSSG 7	81	–	16 26 55.31	-24 20 27.8	16 23 53.91	-24 13 45.8	9.789	9.69	8	– – i	-	-
J162656-241353	83	–	16 26 56.77	-24 13 51.6	16 23 55.51	-24 07 09.7	9.251	9.57	8	– – i	-	-
SR 24	88	41/42	16 26 58.51	-24 45 36.9	16 23 56.56	-24 38 55.1	7.057	7.08	1	x v i	CO	HBC 262, Elias 28
VSSG 8	91	–	16 27 01.62	-24 21 37.0	16 24 00.19	-24 14 55.5	9.389	9.32	8	– – i	-	-
H α 44	–	44	16 27 02.37	-23 09 59.2	16 24 02.46	-23 03 17.8	9.435	–	10	– v –	U	-
WL 16	92	–	16 27 02.34	-24 37 27.2	16 24 00.57	-24 30 45.7	8.064	7.92	1	x – i	-	-
VSSG 9	–	–	16 27 02.85	-24 18 54.7	16 24 01.48	-24 12 13.2	10.116	10.07	12	– – i	U	-
GY 193	96	–	16 27 04.52	-24 42 59.7	16 24 02.62	-24 36 18.3	9.837	9.80	2	x – i	-	-
GY 194	97	–	16 27 04.56	-24 42 14.0	16 24 02.69	-24 35 32.6	9.809	9.82	2	x – i	-	-
VSSG 21	–	–	16 27 05.16	-24 20 07.7	16 24 03.76	-24 13 26.4	9.374	9.27	12	– – i	U	-
J162708-241204	106	–	16 27 09.07	-24 12 00.8	16 24 07.84	-24 05 19.7	9.800	9.76	8	– – i	-	-
WL 10	105	–	16 27 09.10	-24 34 08.1	16 24 07.40	-24 27 27.1	8.915	8.85	1	x – i	-	-
Elias 29	108	–	16 27 09.43	-24 37 18.8	16 24 07.66	-24 30 37.7	7.140	7.54	1	x – i	-	-
Elias 30	110	–	16 27 10.28	-24 19 12.7	16 24 08.89	-24 12 31.8	6.719	6.30	1	x – i	C	SR21
GY 224	112	–	16 27 11.18	-24 40 46.7	16 24 09.33	-24 34 05.7	10.196	10.79	1	x – i	-	-
IRS 32	113	–	16 27 11.68	-24 23 42.0	16 24 10.20	-24 17 01.1	10.107	10.06	5	– – i	-	-
VSSG 24	116	–	16 27 13.73	-24 18 16.9	16 24 12.36	-24 11 36.1	9.287	9.32	8	– – i	-	-

Table 2.3: (continued)

Object	ISO No.	H α No.	J2000.0		B1950.0		K _{2MASS} [mag]	K _{BKLT} [mag]	Selection #	Note crit.	Other Designation	
			α	δ	α	δ						
IRS 32b	117	–	16 27 13.82	-24 43 31.7	16 24 11.91	-24 36 50.9	9.978	10.13	8	--i	O	-
ROXs 20A	–	45	16 27 14.49	-24 51 33.5	16 24 12.40	-24 44 52.8	10.381	10.39	5	xvi	-	HBC 640
ROXs 20B	–	46	16 27 15.13	-24 51 38.8	16 24 13.05	-24 44 58.1	9.392	9.51	5	xvi	-	HBC 641
WL 20	121	–	16 27 15.88	-24 38 43.4	16 24 14.07	-24 32 02.8	9.590	9.21	1	x-i	CE	-
H α 47	–	47	16 27 17.08	-24 47 11.2	16 24 15.08	-24 40 30.6	9.487	9.47	10	-v-	-	-
WL 5	125	–	16 27 18.17	-24 28 52.7	16 24 16.57	-24 22 12.2	10.558	10.28	1	x-i	L	-
WL 4	128	–	16 27 18.49	-24 29 05.9	16 24 16.88	-24 22 25.5	9.683	9.13	1	x-i	-	-
SR 12	130	–	16 27 19.51	-24 41 40.4	16 24 17.64	-24 35 00.0	8.408	8.41	1	xvi	O	ROXs 21, HBC 263
IRS 42	132	–	16 27 21.47	-24 41 43.1	16 24 19.59	-24 35 02.8	8.483	8.41	1	x-i	-	-
WL 6	134	–	16 27 21.80	-24 29 53.4	16 24 20.18	-24 23 13.1	10.827	10.04	1	x-i	L	-
VSSG 22	135	–	16 27 22.91	-24 17 57.4	16 24 21.54	-24 11 17.2	9.454	9.41	1	x-i	-	-
H α 49	–	49	16 27 22.97	-24 48 07.1	16 24 20.95	-24 41 27.0	9.390	9.30	1	xvi	-	-
GY 262	140	–	16 27 26.49	-24 39 23.1	16 24 24.66	-24 32 43.2	9.952	9.77	1	x-i	-	-
IRS 43	141	–	16 27 26.94	-24 40 50.8	16 24 25.07	-24 34 10.9	9.745	9.46	1	x-i	-	YLW 15A
VSSG 25	142	–	16 27 27.38	-24 31 16.6	16 24 25.72	-24 24 36.7	9.316	9.30	1	x-i	-	Elias 31
IRS 44	143	–	16 27 28.03	-24 39 33.5	16 24 26.19	-24 32 53.7	10.379	9.65	1	x-i	-	YLW 16A
VSSG 18	144	–	16 27 28.45	-24 27 21.0	16 24 26.87	-24 20 41.3	10.101	9.39	1	x-i	C	Elias 32
VSSG 17	147	–	16 27 30.18	-24 27 43.4	16 24 28.59	-24 21 03.7	9.024	8.95	1	x-i	C	Elias 33
GY 284	151	–	16 27 30.84	-24 24 56.0	16 24 29.32	-24 18 16.4	10.070	10.04	3	x-i	-	-
J162730-244726	149	–	16 27 30.84	-24 47 26.8	16 24 28.83	-24 40 47.2	9.502	9.44	7	x-i	-	-
GY 292	155	–	16 27 33.11	-24 41 15.3	16 24 31.23	-24 34 35.8	7.806	7.92	1	x-i	-	-
H α 50	156	50	16 27 35.26	-24 38 33.4	16 24 33.44	-24 31 54.1	9.668	9.64	5	-vi	-	GY 295

Table 2.3: (continued)

Object	ISO No.	H α No.	<i>J</i> 2000.0		<i>B</i> 1950.0		K ₂ MASS [mag]	K _{BKLT} [mag]	Selection #	Note crit.	Other Designation	
			α	δ	α	δ						
IRS 48	159	–	16 27 37.19	-24 30 35.0	16 24 35.54	-24 23 55.8	7.582	7.42	1	x – i	-	-
IRS 50	–	–	16 27 38.13	-24 30 42.9	16 24 36.47	-24 24 03.8	9.658	9.59	1	x – i	-	-
IRS 49	163	–	16 27 38.32	-24 36 58.6	16 24 36.53	-24 30 19.5	8.271	8.31	1	x – i	-	-
ROXs 30B	–	51	16 27 38.33	-23 57 32.4	16 24 37.38	-23 50 53.3	7.940	–	6	x v –	-	DoAr 32
ROXs 30C	–	53	16 27 39.01	-23 58 18.7	16 24 38.05	-23 51 39.7	8.206	–	6	x v –	-	-
H α 52	166	52	16 27 39.43	-24 39 15.5	16 24 37.59	-24 32 36.5	8.464	8.35	1	x v i	-	GY 314
IRS 51	167	–	16 27 39.83	-24 43 15.1	16 24 37.90	-24 36 36.0	8.991	8.93	1	x – i	-	-
SR 9	168	54	16 27 40.29	-24 22 04.0	16 24 38.81	-24 15 25.0	7.207	7.20	1	x v i	-	ROXs 29, HBC 264, Elias 34
GY 371	178	–	16 27 49.78	-24 25 22.0	16 24 48.23	-24 18 43.6	10.161	10.17	8	– – i	-	-
VSSG 14	180	–	16 27 49.87	-24 25 40.2	16 24 48.31	-24 19 01.9	7.301	7.32	1	x – i	-	Elias 36
IRS 56	–	–	16 27 50.74	-24 48 21.6	16 24 48.69	-24 41 43.3	8.337	8.23	12	– – i	U	-
ROXs 31	184	–	16 27 52.09	-24 40 50.4	16 24 50.20	-24 34 12.2	8.126	8.09	1	x v i	-	IRS 55, HBC 642
SR 10	187	57	16 27 55.58	-24 26 17.9	16 24 54.00	-24 19 39.9	8.896	8.74	1	x v i	-	HBC 265
GY 410	188	–	16 27 57.83	-24 40 01.8	16 24 55.95	-24 33 24.0	9.866	9.78	1	x – i	-	-
H α 58	–	58	16 27 59.97	-24 48 19.3	16 24 57.91	-24 41 41.6	9.269	9.26	2	x v –	U	-
J162800-245340	–	–	16 28 00.11	-24 53 42.7	16 24 57.94	-24 47 05.1	9.651	9.63	7	x – –	U	-
H α 59	–	59	16 28 09.21	-23 52 20.5	16 25 08.35	-23 45 43.5	9.075	–	10	– v –	U	-
VSS 35	–	–	16 28 10.22	-24 16 01.0	16 25 08.85	-24 09 24.0	7.965	7.89	12	– – i	U	-
J162812-245043	–	–	16 28 12.28	-24 50 44.6	16 25 10.16	-24 44 07.7	9.555	9.36	7	x – –	CU	-
J162813-243249	194	–	16 28 13.79	-24 32 49.4	16 25 12.06	-24 26 12.7	10.096	10.04	8	– – i	-	-
H α 60	196	60	16 28 16.51	-24 36 58.0	16 25 14.68	-24 30 21.4	9.316	9.43	4	– v i	-	-

Table 2.3: (continued)

Object	ISO No.	H α No.	J2000.0		B1950.0		K ₂ MASS [mag]	K _{BKLT} [mag]	Selection #	Note crit.	Other Designation	
			α	δ	α	δ						
ISO-Oph 195	195	—	16 28 16.73	-24 05 14.3	16 25 15.59	-23 58 37.7	8.860	—	8	--i	-	-
SR 20 W _(GWAYL)	—	—	16 28 23.33	-24 22 40.6	16 25 21.81	-24 16 04.5	8.623	8.55	5	--i	-	-
SR 20	198	61	16 28 32.66	-24 22 44.9	16 25 31.13	-24 16 09.4	6.850	7.16	4	xvi	O	ROXs 33, HBC 643
V 853 Oph	199	62	16 28 45.28	-24 28 19.0	16 25 43.61	-24 21 44.4	7.997	7.88	6	xvi	O	ROXs 34, HBC 266
VSS 38	—	—	16 28 45.98	-24 47 55.3	16 25 43.89	-24 41 20.7	5.960	6.14	12	--i	U	-
H α 63	—	63	16 28 54.07	-24 47 44.2	16 25 51.98	-24 41 10.2	8.905	8.96	4	-vi	-	-
VSS 42	—	—	16 29 12.73	-24 23 55.3	16 26 11.14	-24 17 22.6	5.825	6.27	12	--i	U	-
IRAS 64a	—	—	16 29 23.39	-24 13 56.9	16 26 22.00	-24 07 24.8	7.020	6.45	5	--i	-	-
VSS 41	—	—	16 29 45.12	-24 19 50.5	16 26 43.59	-24 13 19.9	8.664	—	12	--i	U	-
Elias 41	—	—	16 30 02.41	-23 51 09.1	16 27 01.47	-23 44 39.7	6.905	—	11	--i	-	-
H α 67	—	67	16 30 23.40	-24 54 16.2	16 27 21.08	-24 47 48.1	9.293	—	10	-v-	-	-
ROXs 39	—	—	16 30 35.63	-24 34 18.9	16 27 33.74	-24 27 51.7	8.025	—	5	xvi	B	-
Haro 1-14/c	—	—	16 31 04.37	-24 04 33.1	16 28 03.09	-23 58 07.8	7.784	—	9	-v-	B	HBC 644
Haro 1-14	—	69	16 31 05.17	-24 04 40.1	16 28 03.89	-23 58 14.9	8.576	—	9	-v-	B	HBC 267
ROXs 42B	—	—	16 31 15.02	-24 32 43.7	16 28 13.13	-24 26 19.1	8.671	—	6	xv-	B	-
ROXs 42C	—	—	16 31 15.75	-24 34 02.2	16 28 13.83	-24 27 37.7	7.129	—	6	xv-	-	-
ROXs 43A/B	—	—	16 31 20.12	-24 30 05.2	16 28 18.29	-24 23 41.0	6.729	—	5	xvi	C	GWAYL 1
H α 71	—	71	16 31 30.88	-24 24 40.0	16 28 29.15	-24 18 16.4	7.900	—	5	-vi	BC	GWAYL 2
Haro 1-16	—	72	16 31 33.46	-24 27 37.3	16 28 31.67	-24 21 13.9	7.610	—	5	xvi	O	GWAYL 3, ROXs 44, HBC 268
IRS 63	—	—	16 31 35.66	-24 01 29.5	16 28 34.42	-23 55 06.3	9.219	—	5	--i	-	GWAYL 4
L1689-IRS 5	204	—	16 31 52.11	-24 56 15.7	16 28 49.68	-24 49 53.6	7.557	—	5	--i	-	GWAYL 5

Table 2.3: (continued)

Object	ISO No.	H α No.	J2000.0		B1950.0		K _{2MASS} [mag]	K _{BKLT} [mag]	Selection #	Note crit.	Other Designation
			α	δ	α	δ					
H α 73	206	73	16 31 54.42	-25 03 49.3	16 28 51.82	-24 57 27.4	9.899	—	8	- v i	-
H α 74	207	74	16 31 54.73	-25 03 23.8	16 28 52.14	-24 57 01.9	7.749	—	8	- v i	-
ROXs 45D	—	—	16 31 57.68	-25 29 33.7	16 28 54.51	-25 23 11.9	9.865	—	6	x v -	-
ROXs 45E	—	—	16 32 00.59	-25 30 28.7	16 28 57.39	-25 24 07.1	9.478	—	6	x v -	-
ROXs 45F	—	—	16 32 01.61	-25 30 25.3	16 28 58.41	-25 24 03.8	9.395	—	6	x v -	-
H α 75	—	75	16 32 05.52	-25 02 36.2	16 29 02.94	-24 56 15.0	9.947	—	10	- v -	U
DoAr 51	—	76	16 32 11.79	-24 40 21.4	16 29 09.69	-24 34 00.6	7.929	—	6	x v -	ROXs 47A, HBC 647
L1689-IRS 7	212	—	16 32 21.05	-24 30 35.8	16 29 19.15	-24 24 15.7	8.620	—	5	- - i	B
Haro 1-17	—	77	16 32 21.93	-24 42 14.8	16 29 19.77	-24 35 54.7	9.151	—	9	- v -	HBC 648
Elias 45	—	—	16 33 21.54	-23 50 21.4	16 30 20.46	-23 44 05.3	6.345	—	11	- - i	-

Names adopted from Barsony et al. (1997) are given without the leading ‘BKLT’ and thus start with ‘J16’.

A: observed with ADONIS/SHARP II+ B: observed with BlackMagic C: companion in 2MASS
E: 2MASS photometric quality flag E L: $m_K > 10.5$ (see text) O: well observed

Selection criteria: X-ray detection (x), visual spectra/H α -emission (v), infrared excess (i) – Selection # refers to Table 2.1

Chapter 3

The Turbulent Atmosphere

‘The night was clear, cool, and starry,
but smoke-like wisps of mist were creep-
ing up the hillsides from the streams
and deep meadows.’

The resolution of astronomical images obtained with ground-based telescopes is limited by the atmosphere above the observatory. A fundamental knowledge of the underlying processes is thus crucial for the understanding of the techniques that help to overcome this limitation. A detailed description can be found in Quirrenbach (1999) and Roddier (1999) from where most of the formulas given below have been adapted.

3.1 Kolmogorov-Obukhov Turbulence

Flows in the earth’s atmosphere with length scales of several meters to kilometres and wind speeds of a few meters per second are almost always turbulent. The turbulent energy is generated by eddies on a large scale. The characteristic size ρ_{out} of this *outer scale* is still discussed and may be a few tens to hundreds of meters in most cases. The large-scale cells spawn a hierarchy of smaller cells (see Fig. 3.1). While the dissipation of kinetic energy plays no role for large-scale eddies, it becomes important in small scale eddies of a characteristic size ρ_{in} . This *inner scale* is of the order of a few millimetres.

Kolmogorov and Obukhov developed a astonishingly simple model to describe the strength of the turbulence. In the *inertial range* between ρ_{in} and ρ_{out} the turbulence only depends on the size of the eddies ρ , their spatial frequency κ , respectively. The one-dimensional powerspectrum of the *Kolmogorov-Obukhov turbulence* is

$$P(\kappa) \propto \kappa^{-\frac{5}{3}}. \quad (3.1)$$

In three dimensions one finds

$$P(|\vec{\kappa}|) \propto |\vec{\kappa}|^{-\frac{11}{3}}. \quad (3.2)$$

In one dimension (3.2) reduces to The multi-scale turbulences mix layers of different temperatures and are thus responsible for inhomogeneities in the air temperature. Fluctuations in the air temperature are essentially proportional to the fluctuations in the air refractive index n . For observations mainly the relative refractive index between one point \vec{r} and a nearby point $\vec{r}' = \vec{r} + \vec{\rho}$ in the atmosphere

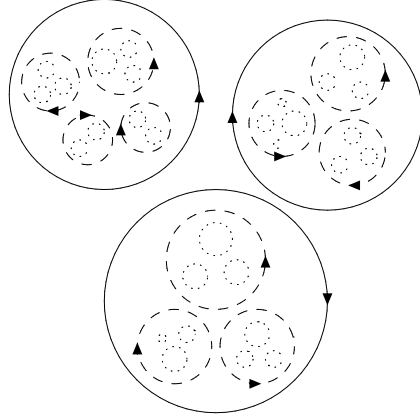


Figure 3.1: Schematic representation of turbulent eddies.

Equation (3.4) fully describes the statistical properties of the refractive index fluctuations on length scales between ρ_{in} and ρ_{out} . At longer distances, i.e. $\rho > \rho_{\text{out}}$, the fluctuations may eventually become uncorrelated and the simple description breaks down.

is relevant. The variance of the difference between the two values of the refractive index is given by

$$D_N(\vec{\rho}) = \langle |n(\vec{r}) - n(\vec{r} + \vec{\rho})|^2 \rangle, \quad (3.3)$$

where $\langle \rangle$ represents an ensemble average. $D_N(\vec{\rho})$ is called *index structure function*. When considering a homogeneous (at least locally) and isotropic random process, (3.1) can be expressed as

$$D_N(\vec{\rho}) = C_N^2 \rho^{\frac{2}{3}} \quad (3.4)$$

(Quirrenbach, 1999) with $\rho = |\vec{\rho}|$. The *index structure coefficient* C_N^2 describes the local amount of inhomogeneities and varies only over distances much larger than the scale of the inhomogeneities.

3.2 Taylor Hypothesis

The temporal evolution of the air refractive index can be described similar to the spatial distribution of the inhomogeneities (3.3). The variance between the time t and the later time $t + \tau$ is thus given by

$$D_N(\tau) = \langle |n(\vec{r}, t) - n(\vec{r}, t + \tau)|^2 \rangle, \quad (3.5)$$

the so-called *temporal structure function*. For open air turbulences under most wind conditions the lifetimes of inhomogeneities are much larger than the time it takes for a wind-driven inhomogeneity to cross the line of sight. According to the *Taylor hypothesis* a turbulence caused by a single layer can be modelled by a ‘frozen’ pattern that is transported across the aperture by the wind in that layer. With the wind speed \vec{v} this hypothesis can be expressed by

$$n(\vec{r}, t + \tau) = n(\vec{r} - \vec{v}\tau, t). \quad (3.6)$$

Inserting (3.6) into (3.5) yields

$$D_N(\tau) = \langle |n(\vec{r}, t) - n(\vec{r} - \vec{v}\tau, t)|^2 \rangle. \quad (3.7)$$

Finally, one finds by substituting ρ in (3.3) with $|\vec{v}\tau|$

$$D_N(\tau) = C_N^2 |\vec{v}\tau|^{\frac{2}{3}}. \quad (3.8)$$

3.3 Phase Shifts

When a wavefront ψ with amplitude A and phase ϕ represented by

$$\psi(\vec{x}) = Ae^{i\phi(\vec{x})} \quad (3.9)$$

propagates through a turbulent layer of thickness Δh at the height h , the variations in the refractive index cause a shift of the phase that can be mathematically described as

$$\Delta\phi(\vec{x}) = k \int_h^{h+\Delta h} n(\vec{x}, z) dz, \quad (3.10)$$

where k is the wave number defined by

$$k = \frac{2\pi}{\lambda}. \quad (3.11)$$

The absolute phase shift of the wavefront is not important, because only relative phase shifts between different parts of the wavefront contribute to the distortion. Therefore, only the relative phase shift between a point \vec{x} and a nearby point $\vec{x}' = \vec{x} + \vec{r}$ is investigated. The variance of the differences, i.e. the *phase structure function* is given similar to (3.3) by

$$D_\phi(\vec{r}) = \langle |\phi(\vec{x}) - \phi(\vec{x} + \vec{r})|^2 \rangle. \quad (3.12)$$

It is easy to show that (3.12) can be rewritten as

$$D_\phi(\vec{r}) = k^2 \Delta h \int_{-\infty}^{+\infty} [D_N(\vec{r}, z) - D_N(0, z)] dz \quad (3.13)$$

(Quirrenbach, 1999). Here the boundaries of the integration have been expanded by assuming that the thickness of the layer Δh is much larger than the correlation scale of the fluctuations. Inserting (3.4) leads to

$$\begin{aligned} D_\phi(r) &= k^2 \Delta h C_N^2 \int_{-\infty}^{+\infty} \left[(r^2 + z^2)^{\frac{1}{3}} - |z|^{\frac{2}{3}} \right] dz \\ &= 2.914 k^2 \Delta h C_N^2 r^{\frac{5}{3}}, \end{aligned} \quad (3.14)$$

where $r = |\vec{r}|$.

3.4 The Fried Parameter

An easy way to quantify this phase variations exist. Starting with the coherence function B of the wavefront $\psi(\vec{x})$ given in (3.9) after it passed through a layer at height h

$$B_h(\vec{r}) \equiv \langle \psi(\vec{x}) \psi^*(\vec{x} + \vec{r}) \rangle \quad (3.15)$$

one finds with the amplitude A set to unity

$$\begin{aligned} B_h(\vec{r}) &= \left\langle e^{i[\phi(\vec{x}) - \phi(\vec{x} + \vec{r})]} \right\rangle \\ &= e^{-\frac{1}{2} \langle |\phi(\vec{x}) - \phi(\vec{x} + \vec{r})|^2 \rangle}, \end{aligned} \quad (3.16)$$

where it has been assumed that $[\phi(\vec{x}) - \phi(\vec{x} + \vec{r})]$ has Gaussian statistics with a mean value of zero. This is true for layers with a thickness Δh much larger than the size of the individual turbulence cells, because then many independent variables contribute to the phase shift. Such Gaussian variables with zero mean β follow the relation

$$\langle e^{\alpha\beta} \rangle = e^{\frac{1}{2}\alpha^2\langle\beta^2\rangle} \quad (3.17)$$

that has been used in (3.16). Since the exponent in (3.16) is the phase structure function, we can substitute it by (3.14):

$$B_h(r) = \exp \left[-\frac{1}{2} \left(2.914 k^2 \Delta h C_N^2 r^{\frac{5}{3}} \right) \right]. \quad (3.18)$$

When C_N^2 depends only on the height in the atmosphere, an integration over the whole atmosphere can be easily performed. With the zenith distance ζ , the airmass $(\cos \zeta)^{-1}$, respectively, this integration yields

$$B(r) = \exp \left[-\frac{1}{2} \left(2.914 k^2 (\cos \zeta)^{-1} r^{\frac{5}{3}} \int C_N^2(h) dh \right) \right]. \quad (3.19)$$

With the *Fried parameter*

$$r_0 \equiv \left[0.423 k^2 (\cos \zeta)^{-1} \int C_N^2(h) dh \right]^{-\frac{3}{5}} \quad (3.20)$$

the phase-coherence function $B(r)$ can be written as

$$B(r) = \exp \left[-3.44 \left(\frac{r}{r_0} \right)^{\frac{5}{3}} \right] \quad (3.21)$$

and thus the phase structure function $D_\phi(r)$ given in (3.14) as

$$D_\phi(r) = 6.88 \left(\frac{r}{r_0} \right)^{\frac{5}{3}}. \quad (3.22)$$

The quantity r_0 is well suited to describe the influence of the atmosphere above a telescope on the observations, because

- it quantifies the turbulent atmosphere by one single parameter.
- the mean-square phase variation over an aperture of D is $1.03 (D/r_0)^{5/3}$ (Fried, 1965; Noll, 1976), i.e. approximately 1 rad^2 over an aperture of r_0 .
- although the size of the turbulence cells spawns a range between ρ_{in} and ρ_{out} , the atmosphere can be described as a sample of patches of size r_0 . Each of these patches has a constant phase. The phases of the various patches are not correlated, i.e. from one patch to another a random phase change occurs.
- a telescope with a diameter D smaller than r_0 is diffraction-limited, i.e. the resolution is proportional to λ/D , while a telescope with a diameter larger than r_0 is seeing-limited, i.e. the resolution is proportional to λ/r_0 . In the visual r_0 can reach values up to 20 cm, i.e. ground-based telescopes larger than 20 cm are always seeing-limited in this wavelength range!

As can be seen from (3.11) and (3.20) the Fried parameter r_0 is a function of the wavelength λ :

$$r_0 \propto \lambda^{\frac{6}{5}}. \quad (3.23)$$

Therefore, the *full-width-half-maximum* (FWHM) σ of a seeing-limited *point-spread-function* (PSF), i.e. of a seeing-limited image of a point-source, varies only slowly with the wavelength according to

$$\sigma \propto \frac{\lambda}{r_0} = \lambda^{-\frac{1}{5}}. \quad (3.24)$$

Another quantity that influences the Fried parameter is the zenith distance ζ of an object. From (3.20) follows

$$r_0 \propto (\cos \zeta)^{\frac{3}{5}}. \quad (3.25)$$

While the wavelength and the zenith distance can be more or less directly influenced by an astronomer by choosing appropriate instruments and observing times, the atmospheric conditions represented in (3.20) by the index structure coefficient C_N^2 change from night to night and are somewhat random. Nevertheless, it is typical for most sites that C_N^2 decreases with height, i.e. the main contributions come from a ground layer influenced by the diurnal temperature cycle. During a seeing campaign at La Silla, Chile, 75% of the fluctuations were caused by air in the altitude range 30 m to 800 m (Leinert, 1994). However, another significant contribution to C_N^2 may be turbulent layers at altitudes between 9 and 12 km, where in the earth's atmosphere the highest wind speeds occur that frequently cause wind shears.

3.5 Coherence Time

In Section 3.2 the Taylor hypothesis describing the atmospheric turbulence in a single layer by a ‘frozen’ pattern has been introduced. The last section made clear that the single patches of this pattern are of the size of the Fried parameter r_0 . The crossing time of such a patch is thus given by

$$\tau_0 \equiv \frac{r_0}{v} \propto \lambda^{\frac{6}{5}}, \quad (3.26)$$

where v is the wind speed. A long exposure, i.e. an exposure with an integration time much longer than τ_0 averages over the atmospheric random process and the ratio between the Fried parameter and the telescope diameter determines whether the image is diffraction-limited or seeing-limited. Otherwise, an exposure with an integration time much shorter than the *coherence time* τ_0 can always reveal diffraction-limited informations by ‘freezing’ the atmospheric pattern. This informations can be derived by the *speckle* algorithms described in Chapter 4.

3.6 Anisoplanatism

Two wavefronts from two sources separated by an angle θ on the sky may pass through two different areas of the turbulent atmosphere and thus experience

different phase variations. The knowledge of the phase difference between the two wavefronts, i.e. the *anisoplanatism*, is important when one of the sources is used as a wavefront reference for the other source (Section 6.2).

To quantify this effect, the separation r in (3.22) has to be substituted by the angle θ multiplied by the distance of the contributing layer $h (\cos \zeta)^{-1}$. In practice, several turbulence layers contribute to the image degradation. Therefore, one has to use a weighted average of the layer altitudes, i.e. the so-called *mean effective turbulence height* (Quirrenbach, 1999), defined by

$$\bar{h} \equiv \left[\frac{\int C_N^2(h) h^{\frac{5}{3}} dh}{\int C_N^2(h) dh} \right]^{\frac{3}{5}}. \quad (3.27)$$

This finally leads to

$$D_\phi(\theta) = 6.88 \left(\frac{\theta \bar{h}}{r_0 \cos \zeta} \right)^{\frac{5}{3}}. \quad (3.28)$$

Similar to the Fried parameter r_0 (3.20) an isoplanatic angle θ_0 can be found, over which the mean-square phase variation is 1 rad²:

$$\theta_0 = (6.88)^{-\frac{3}{5}} \cdot \frac{r_0 \cos \zeta}{\bar{h}} = 0.314 \cdot \frac{r_0 \cos \zeta}{\bar{h}}. \quad (3.29)$$

Reinserting the Fried parameter (3.20) results in the definition of the *isoplanatic angle*:

$$\theta_0 \equiv \left[2.914 k^2 (\cos \zeta)^{-\frac{8}{3}} \int C_N^2(h) h^{\frac{5}{3}} dh \right]^{-\frac{3}{5}}. \quad (3.30)$$

This definition shows that the isoplanatic angle θ_0 is mostly affected by turbulences at high altitudes. As can be seen from (3.29) θ_0 depends on the zenith angle of the object ζ more than the Fried parameter r_0 , while both θ_0 and r_0 scale with $\lambda^{\frac{6}{5}}$.

For two stars separated by an angle larger than θ_0 the short-exposure point-spread-functions are different. In contrast the long-exposure point-spread functions, which represent averages over many realizations of the atmospheric turbulence, are nearly identical even over angles much larger than θ_0 (Quirrenbach, 1999).

3.7 Scintillation

Until now we have integrated the refractive index fluctuations along the line of sight. This *near-field* or *geometric approximation* neglects the refraction and diffraction of light and is true as long as the propagation pathlength is shorter than the *Fresnel propagation length* d_F defined by

$$d_F \equiv \frac{r_0^2}{\lambda} \propto \lambda^{\frac{7}{5}}, \quad (3.31)$$

where (3.23) has been used for the right side. In the visual ($r_0=10$ cm, $\lambda=500$ nm) one finds $d_F = 20$ km, i.e. even in this wavelength regime the near-field approximation is a good first-order approach.

The situation changes when an astronomical object is observed close to the horizon, because at an high airmass the propagation pathlength increases, while d_F decreases, see (3.20) and (3.27). Now interference effects cause fluctuations in the brightness of the source. Since these effects are highly chromatic, the brightness varies with wavelength. Watching Sirius in a clear night makes this phenomenon called *scintillation* obvious. Sirius changes its brightness and colour on time scales of seconds.

Chapter 4

Speckle-Interferometry

‘One felt as if there was an enormous well behind them, filled up with ages of memory and long, slow, steady thinking; but their surface was sparkling with the present: like sun shimmering on the outer leaves of a tree, or on the ripples of a very deep lake.’

In Chapter 5 the multiplicity of the ρ Ophiuchi molecular clouds will be studied. The data are derived by using speckle-interferometric observation methods. Founding on the description of the atmospheric turbulence in Chapter 3 an introduction of this technique that provides diffraction-limited resolution will be given on the following pages. A more mathematical description can be found in Haas (1989).

4.1 Imaging Through the Atmosphere

The *observed* image I of an astronomical object is the result of the convolution of the *object brightness distribution* O , i.e. the *true* image, with the *point-spread-function* P :

$$I(\vec{x}) = \int O(\vec{x}') \cdot P(\vec{x}, \vec{x}') d\vec{x}'. \quad (4.1)$$

The point-spread-function or PSF is defined as the brightness distribution of an point-like source after the light has passed through the atmosphere. It represents thus a complete description of the atmospheric distortions.

4.2 Speckle Images

If the integration time of an exposure is longer than the coherence time τ_0 (Section 3.5), the resolution is limited to the seeing (Fig. 4.1, left). Diffraction limited informations can be obtained when using integration times much

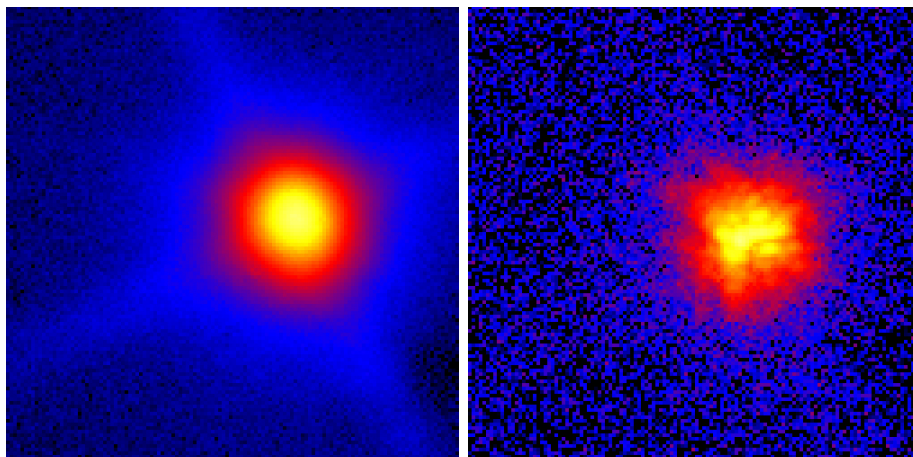


Figure 4.1: Left: This image produced from a stack of speckle images of the single star VSS 42 by calculating the mean is similar to a typical exposure with an integration time much larger than the coherence time τ_0 . The field-of-view is about $6'' \times 6''$. Right: This image is a typical speckle image extracted from the fitscube used for the left image. The images have been taken with SHARP I at the NTT in the K-band.

shorter than τ_0 , because such short integration times ‘freeze’ the atmospheric turbulences.

The ‘frozen’ distortions are responsible for the *speckles* that are visible in those short integrated images (Fig. 4.1, right). Speckles can be explained as interference patterns in the presence of large phase differences in the wavefront. In an extremely simplified picture patches of the size of the Fried parameter r_0 (Section 3.4) with intrinsic phase shifts smaller than 1 rad^2 fill the aperture of the telescope. Between these patches large phase shifts occur. Light rays passing through a single patch interfere in a constructive way, while light rays passing through two different patches interfere destructively. Therefore, the number of speckles is

$$N \propto \left(\frac{D}{r_0} \right)^2, \quad (4.2)$$

where D is the diameter of the primary mirror. Since not only the number of speckles, but also the collecting area scales with D^2 the number of photons per speckle is constant for all telescopes. Each speckle carries high spatial frequency informations and represents a noisy diffraction-limited image of the source. Its size is thus

$$d = \frac{\lambda}{D}. \quad (4.3)$$

4.3 Reduction Methods

According to the *convolution theorem* the convolution given in (4.1) transforms into a simple multiplication in the Fourier space:

$$\mathcal{I}(\vec{u}) = \mathcal{O}(\vec{u}) \cdot \mathcal{P}(\vec{u}). \quad (4.4)$$

The calligraphic letters \mathcal{I} , \mathcal{O} , and \mathcal{P} indicate the Fourier transformations of the corresponding quantities I , O , and P in the image space. To derive the true image from a speckle image one may think about simply calculating

$$\mathcal{O}(\vec{u}) = \frac{\mathcal{I}(\vec{u})}{\mathcal{P}(\vec{u})} \quad (4.5)$$

and transforming the result back into the image space. Unfortunately, it is in many cases not possible to determine the point-spread-function directly, because it is unlikely that a second source is located within the isoplanatic patch around the object (see Section 3.6). Furthermore, \mathcal{P} is very noisy ($S/N \approx 1$) and thus probably exhibits zeros for high spatial frequencies. This low signal-to-noise ratio is also problematic when trying to detect faint structures or companions. Thus the low sensitivity has to be compensated by taking over many minutes several hundreds of frames that can be analysed. This time-sequence showing the temporal evolution of the speckle pattern (Fig. 4.2) is archived as a so-called *fitscube*. However, a simple average over the frames would only lead to a seeing-limited image again.

4.3.1 Amplitude Reconstruction

Labeyrie Process This method has been introduced by Labeyrie (1970) and is also called *powerspectrum analysis*. It is based on the finding that the diffraction-limited resolution is preserved when using the average of the powerspectrum $\langle |\mathcal{I}|^2 \rangle$ instead of the average of the image frames $\langle I \rangle$ or the average of their Fourier transformations $\langle \mathcal{I} \rangle$.

This fundamental result can be easily explained in the image space. When taking an image of a single star with a short integration time, a randomly distributed speckle pattern appears. Calculating the autocorrelation - the Fourier transformation of the powerspectrum - for many frames thus results in a more or less flat continuum. When a second star is present all speckles are doubled with respect to the separation and the flux ratio of the stars. The averaged autocorrelation now clearly indicates this duplicity above the continuum due to the maxima in the two speckle patterns.

When assuming that the object brightness distribution is constant during the observation, (4.4) can be rewritten with the powerspectra as

$$\langle |\mathcal{I}_{\text{Obj}}|^2 \rangle = |\mathcal{O}_{\text{Obj}}|^2 \cdot \langle |\mathcal{P}_{\text{Obj}}|^2 \rangle, \quad (4.6)$$

where $\langle \rangle$ indicates averaged values. Furthermore, the averaged powerspectrum of the point-spread-function exhibits only a moderate spatial variability. A reference, i.e. a single star used to determine the point-spread-function can be separated by up to a few degrees from the target. Also the temporal variations are slow. The averaged powerspectrum can be considered to be constant up to a few hours. A reference thus can be safely observed before or after the target. The corresponding equation to (4.6) for a reference is

$$\langle |\mathcal{I}_{\text{Ref}}|^2 \rangle = 1 \cdot \langle |\mathcal{P}_{\text{Ref}}|^2 \rangle \approx 1 \cdot \langle |\mathcal{P}_{\text{Obj}}|^2 \rangle. \quad (4.7)$$

Herein it has been taken into account that the object brightness distribution of a single star is a delta function. The Fourier transformation of a delta function

is a constant. In (4.7) this constant is set to unity, because the absolute value, i.e. the absolute brightness is not required for the binary search. After dividing (4.6) by (4.7) one gets

$$|\mathcal{O}_{\text{Obj}}|^2 \approx \frac{\langle |\mathcal{I}_{\text{Obj}}|^2 \rangle}{\langle |\mathcal{I}_{\text{Ref}}|^2 \rangle}. \quad (4.8)$$

Under observing conditions noise originating in the read-out electronics and the sky background is introduced in the data. This noise can be determined by taking simultaneously with the frames containing the object, the reference, respectively, frames of the background. If the source does not fill the whole detector, another area of the detector can be used to extract the background. When subtracting it from the data this leads to

$$|\mathcal{O}_{\text{Obj}}|^2 \approx \frac{\langle |\mathcal{I}_{\text{Obj}}|^2 \rangle - \langle |\mathcal{I}_{\text{Obj,Sky}}|^2 \rangle}{\langle |\mathcal{I}_{\text{Ref}}|^2 \rangle - \langle |\mathcal{I}_{\text{Ref,Sky}}|^2 \rangle}. \quad (4.9)$$

Finally, the visibility V defined as the modulus of the Fourier transformation of the object brightness distribution can be derived by simply calculating the

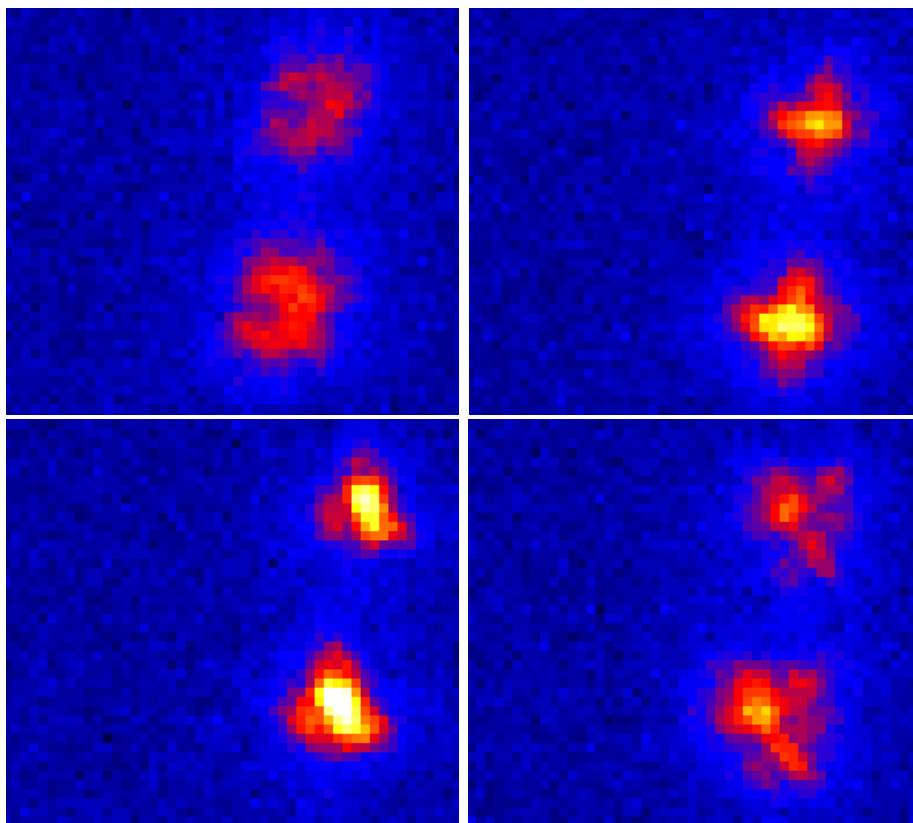


Figure 4.2: The speckle frames #272, #273, #274, and #275 of the fitscube of the binary star H α 18. Between two images 500 ms passed. These images show the rapid change in the distortions. Since the separation between the stars is small and thus both sources reside within the same isoplanatic patch, the distortion of both brightness distributions is similar. The images have been taken with SHARP I at the NTT in the K-band.

square root of (4.9):

$$V = |\mathcal{O}_{\text{Obj}}| = \sqrt{\frac{\langle |\mathcal{I}_{\text{Obj}}|^2 \rangle - \langle |\mathcal{I}_{\text{Obj, Sky}}|^2 \rangle}{\langle |\mathcal{I}_{\text{Ref}}|^2 \rangle - \langle |\mathcal{I}_{\text{Ref, Sky}}|^2 \rangle}} . \quad (4.10)$$

4.3.2 Phase Reconstruction

Speckle-interferometric observations of binaries allow the determination of their structure very precisely (Fig. 4.9): the position angle of the companion, the separation between the two components, and the flux ratio defined as ratio between the flux of the primary and that of the companion. In the visibility all these informations are contained, but the position angle suffers from a 180° ambiguity. To solve this problem the phase ϕ of the complex visibility has to be determined.

Knox-Thompson Algorithm To calculate the phase Knox & Thompson (1974) proposed to average not the powerspectrum, but the cross-spectrum of the frames. One finds

$$\begin{aligned} \langle \mathcal{I}_{\text{Obj}}(\vec{u}_1) \cdot \mathcal{I}_{\text{Obj}}^*(\vec{u}_2) \rangle &= |\mathcal{O}_{\text{Obj}}(\vec{u}_1)| \cdot |\mathcal{O}_{\text{Obj}}(\vec{u}_2)| \cdot e^{i[\phi(\vec{u}_1) - \phi(\vec{u}_2)]} \cdot \\ &|\mathcal{P}_{\text{Obj}}(\vec{u}_1)| \cdot |\mathcal{P}_{\text{Obj}}(\vec{u}_2)| \cdot e^{i[\psi(\vec{u}_1) - \psi(\vec{u}_2)]} \end{aligned} \quad (4.11)$$

for the astronomical object and

$$\langle \mathcal{I}_{\text{Ref}}(\vec{u}_1) \cdot \mathcal{I}_{\text{Ref}}^*(\vec{u}_2) \rangle = |\mathcal{P}_{\text{Ref}}(\vec{u}_1)| \cdot |\mathcal{P}_{\text{Ref}}(\vec{u}_2)| \cdot e^{i[\psi'(\vec{u}_1) - \psi'(\vec{u}_2)]} \quad (4.12)$$

for the reference star. Since the correlation in the pupil plane extends over the range of the size of the Fried parameter r_0 , differences in the spatial frequencies satisfying the relation

$$|\vec{u}_1 - \vec{u}_2| < \frac{r_0}{\lambda} \quad (4.13)$$

lead to small and constant differences in the phases of \mathcal{P}_{Obj} , \mathcal{P}_{Ref} , respectively:

$$\psi(\vec{u}_1) - \psi(\vec{u}_2) \approx \psi'(\vec{u}_1) - \psi'(\vec{u}_2) . \quad (4.14)$$

Dividing (4.11) by (4.12) then results in a cancellation of the terms originating in the point-spread-functions. After normalising the cross-spectra one gets

$$\frac{\langle \mathcal{I}_{\text{Obj}}(\vec{u}_1) \cdot \mathcal{I}_{\text{Obj}}^*(\vec{u}_2) \rangle}{|\mathcal{I}_{\text{Obj}}(\vec{u}_1) \cdot \mathcal{I}_{\text{Obj}}^*(\vec{u}_2)|} \cdot \frac{|\mathcal{I}_{\text{Ref}}(\vec{u}_1) \cdot \mathcal{I}_{\text{Ref}}^*(\vec{u}_2)|}{\langle \mathcal{I}_{\text{Ref}}(\vec{u}_1) \cdot \mathcal{I}_{\text{Ref}}^*(\vec{u}_2) \rangle} = e^{i[\phi(\vec{u}_1) - \phi(\vec{u}_2)]} . \quad (4.15)$$

Therefore, the phase can be reconstructed recursively by using the formula

$$\phi(\vec{u}_1) = \langle \phi(\vec{u}_2) + [\phi(\vec{u}_1) - \phi(\vec{u}_2)] \rangle , \quad (4.16)$$

where the average $\langle \rangle$ is performed over all representations of \vec{u}_2 for which (4.13) and $|\vec{u}_1| < |\vec{u}_2|$ are fulfilled. The fact that the image of the source is real in the image space can be used to find a boundary condition for the recursion:

$$\phi(\vec{u}) = -\phi(-\vec{u}) \rightarrow \phi(0) = 0 . \quad (4.17)$$

For real data the contributions of the phase distortions introduced by the point-spread-function do not cancel out. These structures can be found in the phase of both the object and the reference source. Therefore, subtracting the phase of the reference star from the phase of the object helps to reduce the noise:

$$\phi(\vec{u}) = \phi_{\text{Obj}}(\vec{u}) - \phi_{\text{Ref}}(\vec{u}) . \quad (4.18)$$

Bispectrum Method This method has been originally developed by Weigelt (1977) under the name *speckle-masking*. The idea was to artificially create a reference source image with the same point-spread-function as the object. This would simulate the presence of a reference source within the isoplanatic patch. Such a desirable point-spread-function allows to deconvolve the image directly as it is done in *speckle holography*. To create this intrinsic point-spread-function Weigelt created masks by multiplying each speckle image of the object with itself, after shifting one of the image copies in such a way that a point-source is produced, e.g. shifting the speckle image of a binary by the vectorial separation of the components.

Lohmann et al. (1983) formulated under the name *triple correlation* the today used and mathematical more elegant form of this algorithm. Instead of two images they used three. The corresponding function in the Fourier space is the bispectrum \mathcal{B} named due to the two spatial frequencies used. It is defined as

$$\begin{aligned}\mathcal{B}(\vec{u}_1, \vec{u}_2) &= \langle \mathcal{I}(\vec{u}_1) \cdot \mathcal{I}(\vec{u}_2) \cdot \mathcal{I}^*(\vec{u}_1 + \vec{u}_2) \rangle \\ &= \mathcal{O}(\vec{u}_1) \cdot \mathcal{O}(\vec{u}_2) \cdot \mathcal{O}^*(\vec{u}_1 + \vec{u}_2) \langle \mathcal{P}(\vec{u}_1) \cdot \mathcal{P}(\vec{u}_2) \cdot \mathcal{P}^*(\vec{u}_1 + \vec{u}_2) \rangle.\end{aligned}\quad (4.19)$$

After dividing (4.19) by a reference source one finds

$$\begin{aligned}|\mathcal{B}(\vec{u}_1, \vec{u}_2)| \cdot e^{i\beta(\vec{u}_1, \vec{u}_2)} &= |\mathcal{O}(\vec{u}_1)| \cdot e^{i\phi(\vec{u}_1)} \cdot |\mathcal{O}(\vec{u}_2)| \cdot e^{i\phi(\vec{u}_2)} \cdot \\ &\quad |\mathcal{O}(\vec{u}_1 + \vec{u}_2)| \cdot e^{-i\phi(\vec{u}_1 + \vec{u}_2)}.\end{aligned}\quad (4.20)$$

Thus a recursive formula to calculate the phase of the averaged bispectrum can be derived

$$\beta(\vec{u}_1, \vec{u}_2) = \phi(\vec{u}_1) + \phi(\vec{u}_2) - \phi(\vec{u}_1 + \vec{u}_2) \quad (4.21)$$

or

$$\phi(\vec{u}_1 + \vec{u}_2) = \phi(\vec{u}_1) + \phi(\vec{u}_2) - \beta(\vec{u}_1, \vec{u}_2), \quad (4.22)$$

where $\beta(\vec{u}_1, \vec{u}_2)$ can be measured and the first two terms on the right side have been calculated earlier in the recursion. For two-dimensional images the bispectrum is a four-dimensional quantity. Therefore, three boundary conditions are needed. Besides that given in (4.17), the first non-zero spatial frequency \vec{u}_0 is set to zero, i.e.

$$\phi(\vec{u}_0) = 0. \quad (4.23)$$

This can be realized by shifting the photometric centre, because shifts of the image only contribute a linear term to the phase (4.33). The recursion can be performed along different combinations of spatial frequencies with the same sum $\vec{u} = \vec{u}_1 + \vec{u}_2$. Averaging over all possibilities

$$\phi(\vec{u}) = \arg \left\{ \sum_{|\vec{u}_1| < |\vec{u} - \vec{u}_1|} e^{i[\phi(\vec{u}_1) + \phi(\vec{u} - \vec{u}_1) - \beta(\vec{u}_1, \vec{u} - \vec{u}_1)]} \right\} \quad (4.24)$$

leads to the final result. For this method huge computing power is required, but it has the advantages that it gives a reliable reconstruction of the phase, probably slightly superior to the Knox-Thompson reconstruction (Leinert, 1994). The bispectrum method is very similar to the determination of the *closure phase* used in long-baseline interferometry (Chapter 8). The difference is that there

the three spatial frequencies in (4.19) are defined by the separations of three telescopes from each other, i.e. the baselines, divided by the wavelength. The three phases can thus be determined independently from each other by analysing signals coming from each pair of telescopes. Phase shifts originating in the atmosphere (Section 3.3) are cancelled out by the summation in (4.21).

4.3.3 Shift-and-Add

This method is not a true speckle-interferometric one. It takes advantage of the fact that each individual speckle is a diffraction-limited, but noisy image of the source. According to its name, this method reduces the noise by adding up the individual frames, after they have been shifted in such a way, that the brightest pixel in each frame is brought to the same position. Instead of the brightest pixel the calculated mean of the brightness distribution can be used. The result is a diffraction-limited source that is surrounded by a seeing-limited halo. The quality of the final image is comparable to that of an image obtained with an adaptive optics system with merely tip/tilt correction. An additional gain in resolution can be achieved when deconvolving this image with an image of a nearby reference star created with the same method.

The advantages of this procedure are the directly accessible results and the moderate requirement of computing power, because neither Fourier transformations nor the storage of intermediate results is necessary. However, although this method works quite well for point-like or only slightly extended sources, it produces ambiguous results for extended sources, because the brightest speckle can occur everywhere in the object. Also double sources with equally bright components are problematic due to the fact that each of the components can contribute the brightest speckle.

4.4 Observations

4.4.1 Wavelength Range

The speckle observations of the young stellar objects have been performed in the K-band. The brief discussion below shows that this wavelength was indeed a good choice.

Scientific Rationale

When planning to detect young stars within their parental molecular cloud the most promising wavelength range is the near-infrared between $1\ \mu\text{m}$ and $5\ \mu\text{m}$. At shorter wavelengths the dense molecular gas extinguishes the stellar light very efficiently. At wavelengths longwards of $5\ \mu\text{m}$ only a limited number of the present stars is detectable and the dust in the vicinity of the young stars becomes a main contributor to the emitted light.

Atmospheric Transmission

The transmission of the earth's atmosphere in the near-infrared region offers several windows named X (centred around $1\ \mu\text{m}$), J ($1.25\ \mu\text{m}$), H ($1.65\ \mu\text{m}$), K ($2.2\ \mu\text{m}$), L ($3.6\ \mu\text{m}$), and M ($4.8\ \mu\text{m}$). The absorptions bordering and thus

Table 4.1: Characteristic parameters for different wavelengths, a zenith distance of $\zeta = 0^\circ$, a wind speed of $v = 10 \text{ ms}^{-1}$, and a telescope diameter of $D = 4 \text{ m}$.

		$0.55 \mu\text{m}$	$2.2 \mu\text{m}$	$10 \mu\text{m}$
Fried parameter	r_0	10 cm	60 cm	$\approx 4 \text{ m}$
seeing limit	λr_0^{-1}	$1.1''$	$0.76''$	$0.52''$
coherence time	$r_0 v^{-1}$	10 ms	60 ms	400 ms
diffraction limit	λD^{-1}	$0.028''$	$0.11''$	$0.52''$

defining the windows and influencing especially the M-band are mostly due to water and carbon dioxide. They vary with zenith distance and the amount of water vapour in the air. The background is different for wavelengths below and above $2.2 \mu\text{m}$. In the short-wavelength regime the background is mainly caused by OH emission that originates at an altitude of $\approx 80 \text{ km}$. At wavelengths longwards of $2.2 \mu\text{m}$ the thermal background both from the sky and the telescope is dominating.

Atmospheric Turbulence

Further restrictions come from the turbulent atmosphere (see Tab. 4.1). As has been shown in Section 3.4 the most important quantity to describe the influence of the turbulent atmosphere is the Fried parameter r_0 . The coherence time τ_0 introduced in Section 3.5 that limits the integration time and thus the sensitivity of speckle images is directly proportional to it. While r_0 is about 10 cm in the visual, it is about 60 cm in the K-band. In principle, the fact that r_0 is proportional to $\lambda^{6/5}$ favours longer wavelengths. Otherwise, the diffraction limited resolution λ/D reached with speckle-interferometry favours shorter wavelengths.

Table 4.2: Journal of observations

Camera	Telescope	Date
SHARP I	NTT, La Silla	2000, June 17 - 22
		2001, June 28 - July 4
BlackMAGIC	3.5m, Calar Alto	2000, June 22
SHARP II+ / ADONIS	3.6m, La Silla	2000, June 5 - 6
Ω -Cass (background)	3.5m, Calar Alto	2001, May 31 - June 1

4.4.2 Instruments

The main part of the observations (Table 4.2) was carried out with the near-infrared speckle camera SHARP I (*System for High Angular Resolution Pictures*, see Fig. 4.3) of the Max-Planck-Institute for Extraterrestrial Physics (Hofmann et al., 1992) mounted exclusively on the ESO *New Technology Telescope* (NTT, see Fig. 4.4) at La Silla, Chile. Further our program has been promoted by observations with BlackMAGIC (Herbst et al., 1993) on the MPIA 3.5 m telescope at Calar Alto, Spain and with SHARP II+ that has been specially designed for the use with the adaptive optics system ADO-NIS on the ESO 3.6 m telescope at La Silla. In Table 2.3 objects observed with BlackMAGIC are marked with a ‘B’ while those observed with ADO-NIS/SHARP II+ are indicated by ‘A’. All observations have been performed in the K-band at $2.2 \mu\text{m}$.

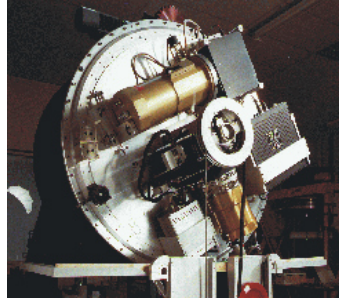


Figure 4.3: SHARP I



Figure 4.4: The ESO New Technology Telescope (NTT) at La Silla, Chile

The cameras are equipped with 256×256 pixels NICMOS3 CdHgTe arrays. To derive the exact pixelscale and orientation of the chips images of the Galactic Center and/or the Orion Trapezium have been taken during each observing campaign. The instrumental positions of the stars have been compared with the very accurate coordinates given in Genzel et al. (1996), Menten et al. (1997) and McCaughrean & Stauffer (1994) by using the astrometric software *ASTROM*. In the case of the observations with BlackMAGIC no such calibration frames are available and thus the position angle and separation of $\text{H}\alpha$ 71 given in Koresko (2002) have been compared with the new results to derive the characteristic parameters of the camera.

For each of the scientific targets between 500 and 1000 frames have been taken to create the two fitscubes required for the data analysis (Section 4.5). Therefore, the primaries have been centred in one of the four quadrants of the detector and after half of the frames were taken the targets

Figure 4.5: The star SAO 184405 on an image from the Digitized Sky Survey II taken in the R-band. This star has been used in most cases as PSF-reference. The southern wing of L1688 can be seen in the upper part of the image as area without stars.



have been shifted to another quadrant. If no companion was visible below the primary, normally the lower two quadrants were used (Fig. 4.6). The advantage of this method is the exact measurement of the background, both at the same time in different areas of the chip, and in the same area at a different time. The exposure time of a single frame varies with respect to the brightness of the target between 200 and 500 ms. This is longer than the expected coherence time τ_0 in the K-band (Tab. 4.1), but these exposure times help to improve the signal-to-noise ratio, while widely preserving the speckle structure.

4.4.3 The Reference Source

To analyse the data speckle images of stars that have no companions are needed as PSF-references. In most cases time series of the star HD 148352 located at a position of $\alpha_{2000} = 16^h28^m25^s16$, $\delta_{2000} = -24^\circ45'01''.0$, and $\pi = 13.33 \pm 0.93$ mas (Perryman et al., 1997) with a spectral type of F2V (Houk & Smith-Moore, 1988) and a K-band magnitude of 6.511 ± 0.018 mag (2MASS) were obtained. Another reference is the high proper-motion star HD 148428 with a spectral type of K0III+G (Houk & Smith-Moore, 1988) and a K-band magnitude of 5.925 ± 0.024 mag (2MASS) located at $\alpha_{2000} = 16^h28^m59^s00$, $\delta_{2000} = -24^\circ32'16''.8$, and $\pi = 15.25 \pm 1.05$ mas (Perryman et al., 1997). These two references are located in the foreground of the southern wing of L1688 and they are comparable to the brightest targets in the K-band. An additional reference only used during the observations with BlackMAGIC is the G1 main-sequence star HD 147681 at $\alpha_{2000} = 16^h24^m12^s93$, $\delta_{2000} = -23^\circ30'01''.4'$, and $\pi = 13.74 \pm 1.23$ mas (Perryman et al., 1997). Its brightness is 7.508 ± 0.023 mag in the K-band (2MASS). The references for the objects observed with SHARP II+ are the targets that have been found to be single stars.

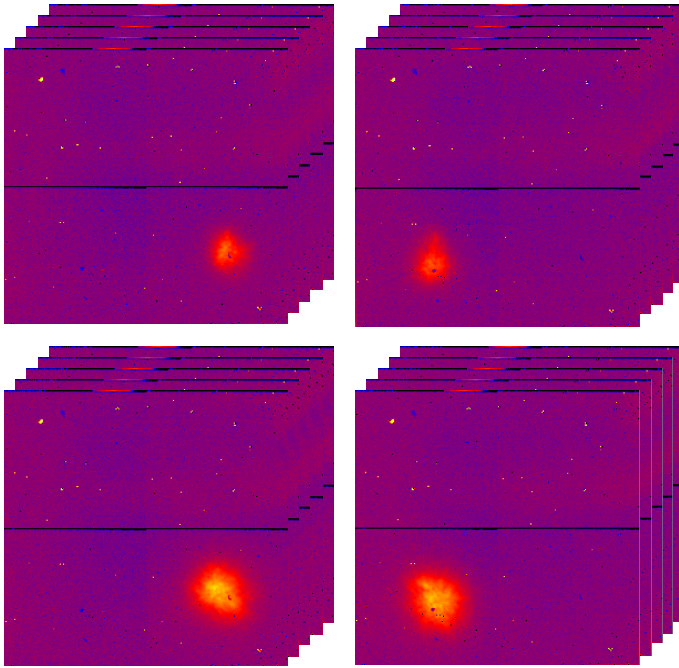


Figure 4.6: A typical set of raw speckle data consisting of four fitscubes with several hundred images each. Two of these fitscubes are taken for the scientific target and two for the PSF-reference.

4.5 Data Reduction

4.5.1 Prereduction

In the last sections the theoretical framework and the observational methods for the speckle-interferometric search for young low-mass stars in the ρ Ophiuchi molecular clouds were described. On the following pages a step by step description of the way that has been used to reduce the obtained data will be presented. A software package named `speckle` that has been developed in our group in Heidelberg performs all the reduction steps described below.

Raw Data

A typical set of raw speckle data is presented in Fig. 4.6. Two fitscubes are taken with the scientific target and two additional with the PSF-reference. Since the upper half of the detector is much more contaminated by areas of so-called *badpixels*, i.e. pixels that show an unusual response, the lower two quadrants are used in most cases. Exceptions are those sources that showed wide companions on the control monitor. Then the appropriate quadrants have been chosen both for the target and the reference.

Automatic Preprocessing

In a first step the fitscubes with 256×256 pixels are divided into four *subcubes* with 128×128 pixels each corresponding to the four quadrants of the detector. Only those subcubes of the quadrants containing a source during the observation will be included into the reduction process. Each large fitscube is thus reduced

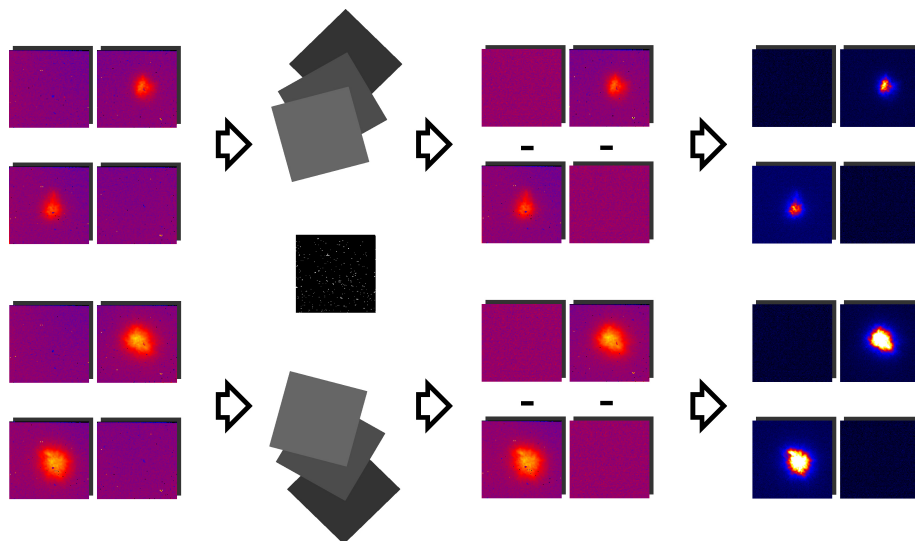


Figure 4.7: Prereduction of the speckle data (part I). On the left side the eight subcubes extracted from the four fitscubes, i.e. the two object-cubes with their corresponding sky-cubes (upper half) and the two reference-cubes with their corresponding sky-cubes (lower half) are schematically drawn. After determining the badpixels and removing the corrupted frames, the average of each sky-cube is calculated. When subtracting these averages from the corresponding object-cubes, reference-cubes, respectively, and the sky-cubes themselves one is left with the eight subcubes drawn on the right side.

to one so-called *object-cube*, *reference-cube*, respectively, and one *sky-cube* (see Fig. 4.7).

Afterwards, the frames in each cube are removed that are corrupted by readout errors or an incorrect positioning of the source on the detector. The criterion to decide between ‘good’ and ‘bad’ frames is the integrated signal over one frame. It can be compared with the average of all integrated signals within one cube. In general only a few frames have to be removed.

Detectors suffer from single pixels that deliver a signal different from the correct one. Two kinds of such badpixels exist. On the one hand, the *dark pixels* are caused by a low quantum efficiency or even no response to infalling photons. On the other hand, the so-called *hot pixels* show always a high signal independent of the illumination. All badpixels have to be identified by comparing their value with the mean of the surrounding pixels, marked in a *badpixel-mask*, and replaced by the median of the neighbouring pixels. At this stage the programme only identifies the badpixels. This is done in the averaged sky-cubes. This recursive process excludes in each step the previously identified badpixels from the following checks. The routine can incorporate a predefined badpixel-mask created in advance for a certain detector.

In the next step the average of each sky-cube is created to determine the background. Such a background image is subtracted from the corresponding object-cube, reference-cube, respectively, and the sky-cube itself. It is important to use a background frame created from the same detector array that was used to record the subcubes from which it is subtracted, because then also the *dark-*

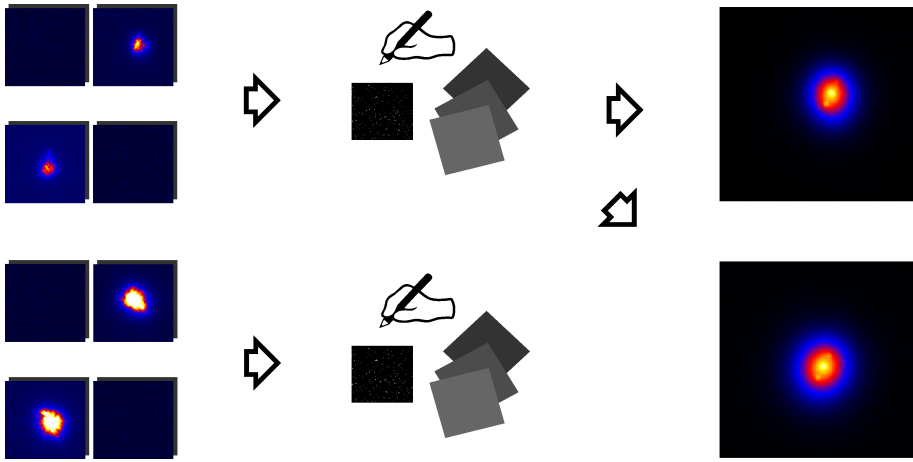


Figure 4.8: Prereduction of the speckle data (part II). The eight subcubes are manually controlled to find the badpixels and corrupted frames not found by the automatic procedures. After their correction the subcubes are reduced by using the Labeyrie process, the Knox-Thompson algorithm, and the Bispectrum method. Additionally, the corrected objects-cubes are coadded by using the shift-and-add algorithm to identify wide companions (right side).

current, i.e. the signal measured by an detector without illumination can be removed. Additional flatfielding is possible with the software, but according to our experience it is in general not necessary.

Quality Control

The simple algorithms used in the preprocessing require a check of the resulting data to prove the quality of the corrections (Fig. 4.8). This can be done with our software package for both the identification of the badpixels and the selection of the corrupted frames.

Badpixels with a signal not very different from the background may have been missed by the search algorithm. To identify them the program displays the averages of the object-cubes, reference-cubes, respectively, in which the previously found badpixels have been corrected. Then the remaining badpixels can be marked interactively. The program updates the badpixel-mask with the new informations and corrects the displayed frames. After the correction in these frames is satisfying, the badpixels indicated by the badpixel-mask are substituted by the median of the neighbouring pixels in all frames of the subcubes and thus do not effect the reduction algorithms any more.

A small additional tool provides the possibility to watch the cubes as movie. Therein frames that are corrupted and have not been found by the automatic search can be marked and deleted. For example, if the telescope vibrates the star is smeared out over a large area while the integrated signal of all pixels used as an indicator by the automatic search procedure is not significantly changed. A similar effect is also visible when the source is shifted from one quadrant of the camera to another. Other events, like impacts of cosmic particles, can cause unwanted effects too.

Finally, the frames of the object-cubes are coadded by using the shift-and-

add algorithm described in Section 4.3.3. Although this algorithm is not very powerful in detecting close companions, especially companions that are fairly bright and well separated can be detected on first sight. Besides giving a first impression, the shift-and-add images are necessary to find faint companions at large separations with standard software packages. For such large separations the spatial frequency becomes too high to be well sampled in the Fourier space with the limited number of pixels provided by the detectors.

Fourier Transformation

To apply the reduction methods described in Section 4.3 the *Fast Fourier Transform* (FFT) of each frame has to be calculated. Therefore, two last steps are necessary to reduce the signal-to-noise ratio of the final results:

- **Subtracting the Baseline** This ensures that the background of each frame is zero by subtracting from each frame the mean of its own background. The area used to determine the remaining background can be selected interactively in the averaged frames. The main reason for a non-vanishing background may be different weather conditions during the observations of the object, the reference, respectively, and the sky.
- **Making the Frames Periodic** Periodic boundary conditions can be realized by modifying the border region of each single frame in such a way that pixels on opposite sides have the same non-zero values. The software does this step automatically. A periodic structure is important, because the FFT is limited to discrete frequencies for a detector image consisting of discrete pixels and thus reconstructed images are always periodic.

4.5.2 Visibility and Phases

Now the visibilities and phases can be calculated by using the methods described in Section 4.3. In Fig. 4.9 some instructive examples are shown.

A binary with a flux ratio between the two components of f and an absolute brightness 1 of the primary can be described by the following object brightness distribution

$$O(\vec{x}) = \delta\left(\vec{x} + \frac{\vec{s}f}{1+f}\right) + f \delta\left(\vec{x} + \frac{\vec{s}}{1+f}\right) \quad (4.25)$$

when assuming that the photometric centre is located in the origin of the coordinate system and that the separation vector \vec{s} is parallel to the x-direction (Köhler, 1997). After calculating the Fourier transformation

$$\mathcal{O}(\vec{u}) = \exp\left(2\pi i \vec{u} \vec{s} \frac{f}{1+f}\right) + f \exp\left(-2\pi i \vec{u} \vec{s} \frac{1}{1+f}\right) \quad (4.26)$$

the visibility V , i.e. the normalised modulus of the Fourier transformation, can be determined. One gets

$$V(\vec{u}) = \sqrt{\frac{1 + 2f \cos(2\nu) + f^2}{1 + 2f + f^2}}, \quad (4.27)$$

where (4.10) and $\nu = \pi \vec{u} \vec{s}$ has been used. The second term in the nominator of (4.27) explains why

- the position angle is perpendicular to the stripes,
- the separation is given by the ‘wavelength’ of the stripes,
- the amplitude of the visibility reflects the flux ratio.

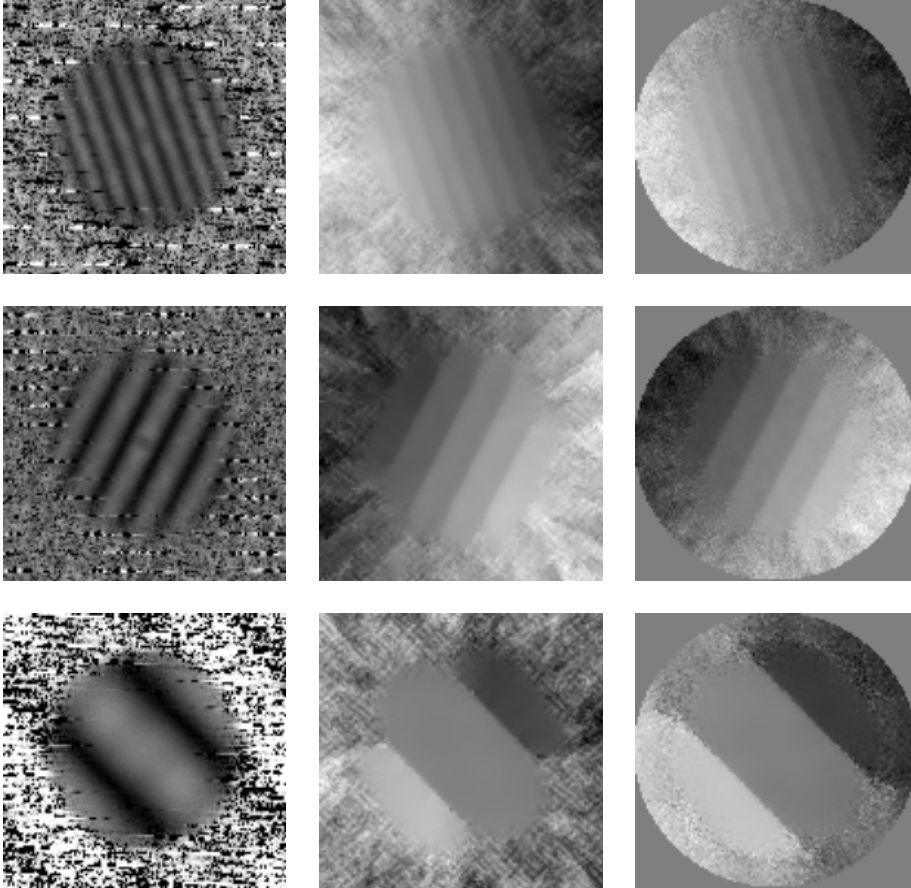


Figure 4.9: The visibility, the Knox-Thompson phase, and the bispectrum phase (from left to right) as reconstructed by our software for the sources IRS 3, ROXs 31, and VSSG 5 (from top to bottom). They are the mean of the results for the two object cubes analysed for each source. The circular area in the individual images is determined by the resolution of the telescope and the bispectrum is only calculated within this area to reduce the computing time. The increasing gap between the maxima in the visibility and the decreasing number of steps in the phases clearly indicate a decrease in separation from top to bottom: $0.663''$, $0.396''$, and $0.148''$. The spatial vector between the two components of a binary is perpendicular to the stripes in the visibility and the phases. The overall gradient of the phases eliminates the 180° ambiguity. Position angles of 115.5° , 251.3° , and 133.9° have been derived. The flux ratio (0.323, 0.655, and 0.873) can be determined by the amplitude of the sinusoidal wave in the visibility and the transition between the steps in the phases. The smaller the flux ratio the smaller the height of the steps. The equally spaced horizontal stripes in the visibilities are artefacts, probably caused by an interference with the readout electronics.

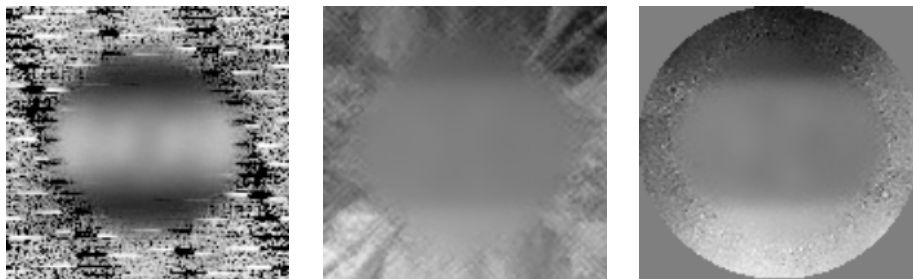


Figure 4.10: The results for the source VSSG 11 (180.1° , $0.107''$, and 0.584). This is an example of an object falling below the diffraction limit of the telescope, i.e. it is not possible to decide whether it is a binary or an elongated structure. No full sinusoidal wave can be seen in the visibility, because the diffraction limit corresponds to the highest spatial frequency directly accessible (outer radius).

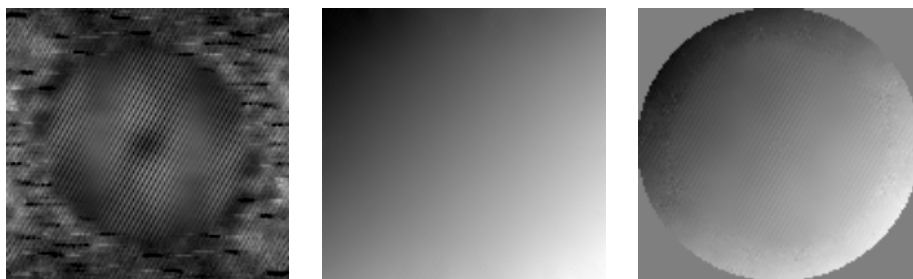


Figure 4.11: The reconstructed visibility and phases of the hierarchical triple system L1689-IRS 5. The visibility clearly shows a wide pair (narrow stripes) and a superimposed close pair almost at the diffraction limit (two wide stripes).

The equation for the phase is more complicated. One finds

$$\tan \phi = \frac{\Im(\mathcal{O})}{\Re(\mathcal{O})} = \frac{2 \sin(\nu) \cos\left(\frac{1-f}{1+f} \nu\right) - (1+f) \sin\left(2 \frac{1}{1+f} \nu\right)}{2 \sin(\nu) \sin\left(\frac{1-f}{1+f} \nu\right) + (1+f) \cos\left(2 \frac{1}{1+f} \nu\right)}. \quad (4.28)$$

The phase thus looks like being build up by plateaus (see Fig. 4.12). At spatial frequencies corresponding to the middle of the n th plateau, i.e. $\nu = n\pi$, the visibility (4.27) is unity, while (4.28) reduces to

$$\tan \phi = -\tan\left(\frac{2\nu}{1+f}\right). \quad (4.29)$$

When taking the periodicity of the tangent into account, this leads to

$$\phi = \pi k - \frac{2\pi n}{1+f}, \quad (4.30)$$

where k is an integer. The phase difference between different plateaus is thus inverse proportional to the total flux of the binary.

When the photometric centre is not located in the origin of the coordinate system, but $\Delta\vec{x}$ away from it, then the object brightness distribution (4.25)

turns into

$$O'(\vec{x}) = O(\vec{x} + \Delta\vec{x}) \quad (4.31)$$

and the Fourier transformation (4.26) exhibits an additional term:

$$\mathcal{O}'(\vec{u}) = \mathcal{O}(\vec{u}) \exp(2\pi i \vec{u} \Delta\vec{x}) . \quad (4.32)$$

Therefore, the visibility is not affected by such an offset, but the phase:

$$\phi' = \phi + 2\pi \vec{u} \Delta\vec{x} . \quad (4.33)$$

4.5.3 Determination of the Binary Parameters

One may think now of calculating ‘real’ images of the sources by combining the visibilities and the phases. Otherwise, the last subsection showed that the characteristic parameters of a binary (separation, position angle, and flux ratio) can be easily determined in the Fourier space. So we decided to avoid the inverse Fourier transformation that would introduce new errors.

Six parameters are needed to describe a binary: the absolute position (two coordinates) and the absolute brightness of both components. When using alternatively the relative position and flux ratio, the position of the photometric centre and the total flux are needed for a complete set of parameters.

If the object turns out to be a binary or multiple star, the position angle, separation and brightness ratio of the components are obtained from a multidimensional least-square fit. Therefore, the program `binplot` tries to minimise the difference between the observational data and the modulus and phase computed

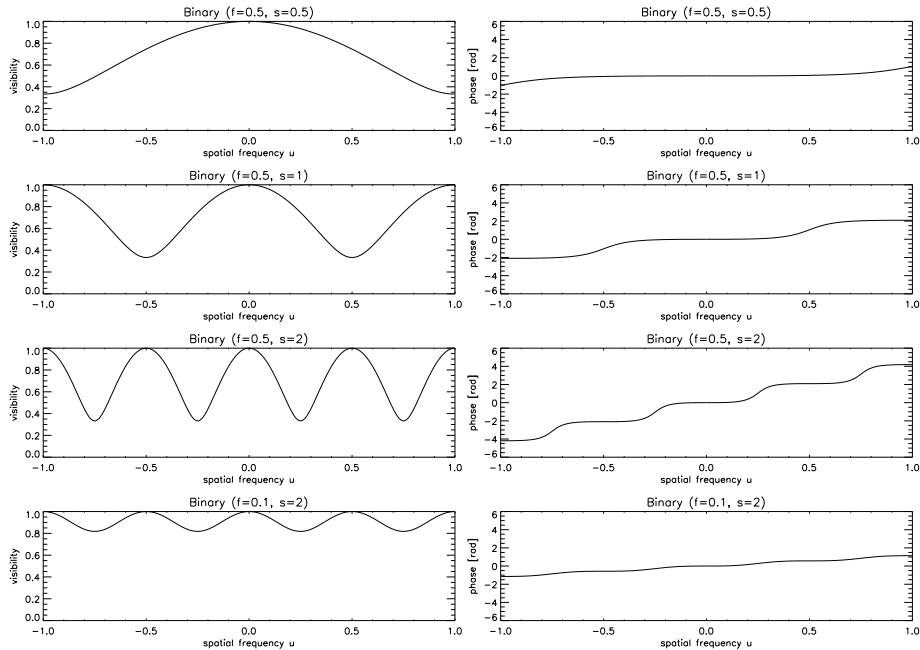


Figure 4.12: The normalised visibilities and the phases calculated along the separation vector of binaries with different flux ratios and separations.

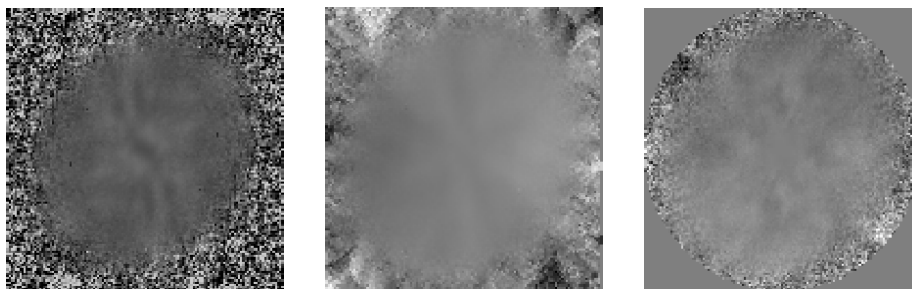


Figure 4.13: The results for the source Haro 1-8. No significant binary structures can be recognised.

from a model binary by varying the binary parameters. It uses the modulus of the Fourier transformed object brightness distribution to estimate the total flux of the binary (4.26) and the phase to estimate the position of the photometric centre (4.33). Fits to different subsets of the data give an estimation of the standard deviation of the binary parameters.

4.5.4 Undetected Companions

If the object appears unresolved (Fig. 4.13), the maximum brightness ratio of a companion that could be hidden in the noise of the data is computed with the

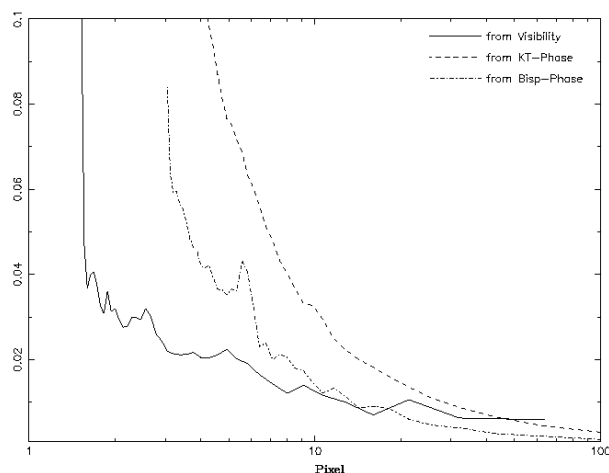


Figure 4.14: The flux ratio of an undetected companion plotted vs. its separation for the source Haro 1-8.

programme `maxbright`. The principle is to determine how far the data deviate from the nominal result for a point source (modulus=1, phase=0) and to interpret this deviation as caused by a companion. For a certain radius range in the Fourier space this procedure is repeated for different position angles and the maximum is used as an upper limit for the brightness ratio of an undetected companion (Leinert et al., 1997).

As can be seen in Fig. 4.14 the flux ratio of a hidden companion strongly depends on the spatial frequency, i.e. the separation of the undetected companion. The wider the separation of the companion the lower the upper limit of the flux ratio. It is typical that for small separations the maximum flux ratio determined from the visibility is well below the value derived from the phases. Only at very large separations the latter value is smaller. This is an intrinsic effect, because the

limits derived with the help of the phases are determined from the ‘plateaus’ at spatial frequencies two times larger than those of the minima in the visibilities (Fig. 4.12) used to derive the upper flux limit there. However, a local maximum in one of the curves indicate that a companion is probably hidden in the data.

In Table 5.1 the values at separations larger than 0.15” (diffraction limit) and 0.50” from the primary are listed. After subtraction of the companion(s) the first value is also calculated for double or multiple stars as an indicator for the quality of the fit (Table 5.2).

Chapter 5

Multiplicity of the ρ Oph Cloud

‘And yet in your speech together I have learned the names and purpose of all thy companions.’

5.1 Results

5.1.1 Uncorrected Data

In Table 5.1 and Table 5.2 the results derived for our 158 targets within the ρ Ophiuchi molecular clouds are listed. Objects also observed in other near-infrared high-resolution studies are identified. In total 45 binaries, 5 triple systems (ROXs 16, WL 20, ROXs 42B, L1689-IRS 5, and SR 24), and no quadruples have been found up to separations of 6.4". The flux ratio or magnitude difference versus the separation of these systems is plotted in Fig. 5.1.

5.1.2 Completeness

The sensitivity of the survey, i.e. the maximum brightness ratio of a possible undetected companion as a function of the separation (see Fig. 5.1) depends on factors such as atmospheric conditions at the time of the observations or the brightness of the target star. Since for each dataset the maximum brightness ratio of a possible undetected companion has been derived by our reduction method, a continuous monitoring of the data quality is possible. At the diffraction limit 85% of the observations reached our quality criterion of a flux ratio ≤ 0.1 (≥ 2.5 mag) in the K-band. Twenty-two observations are not quite sensitive enough to fit this request. In these cases the maximum brightness of an undetected companion at the diffraction limit varies between 0.11 and 0.19. In the case of IRS 44 where the data are very noisy, we provide in Table 5.2 the flux ratio of the detected companion at a separation of 0.26" as upper limit for the brightness of an undetected companion.

CHAPTER 5. MULTIPLICITY OF THE ρ OPH CLOUD

Table 5.1: Upper limits for the relative brightness of an undetected companion to the unresolved stars in our survey, measured at 0.15" and 0.50".

Object	Date	0.15"	0.50"	References*
H α 16	2001, July 4	0.09	0.03	A1
H α 22	2001, July 4	0.08	0.03	
SR 22	2000, June 17	0.07	0.07	B2
SR 1	2000, June 6	0.09	0.03	
SR 8	2001, July 4	0.14	0.07	
Elias 12	2000, June 17	0.03	0.02	
H α 24	2001, July 4	0.12	0.05	
IRS 8	2000, June 21	0.05	0.02	
IRS 9	2000, June 20	0.09	0.06	C
ROXs 3	2000, June 17	0.06	0.04	S2
VSS 23	2000, June 17	0.05	0.05	B2
IRS 11	2001, July 3	0.09	0.04	
SR 4	1990, Aug. 7	0.05	0.04	C, G2, S2
GSS 20	2000, June 17	0.05	0.04	A1, C
Chini 8	2001, June 30	0.16	0.04	
DoAr 21	1990, July 9	0.06	0.06	A1, C, G2, S2
VSSG 19	2000, June 21	0.09	0.04	
Chini 11	2001, July 3	0.13	0.06	
SR 3	2000, June 6	0.05	0.04	C, S2
GSS26	2000, June 20	0.06	0.03	C
SKS 1-7	2001, June 30	0.05	0.02	
GSS29	2000, June 17	0.04	0.04	C, S2
DoAr 24	1990, Aug. 7	0.09	0.07	B2, C, G2
VSSG1	2000, June 20	0.04	0.03	C
J162621-241544	2001, June 29	0.08	0.03	
Elias 21	2000, June 20	0.04	0.02	C
GSS 30 - IRS 2	2000, June 20	0.10	0.06	
LFAM 3	2001, June 30	0.10	0.04	C
DoAr 25	2000, June 6	0.05	0.03	C
GSS 32	2000, June 18	0.03	0.03	R3, S2
Elias 24	2000, June 17	0.10	0.03	C
H α 33	2001, July 4	0.06	0.03	
GY 33	2001, June 30	0.06	0.02	
S1	2000, June 21	0.05	0.02	A1, C, S2**, R3**
J162636-241554	2001, July 3	0.12	0.05	
WL 8	2001, June 29	0.09	0.04	
GY 112	2001, June 30	0.19	0.05	
GSS39	2000, June 20	0.06	0.03	C
Haro 1-8	2000, June 22	0.04	0.02	
H α 40	2001, July 3	0.06	0.03	
VSSG 10	2001, July 3	0.10	0.05	
VSSG 7	2001, June 30	0.14	0.03	
J162656-241353	2001, June 30	0.04	0.02	

Table 5.1: (continued)

Object	Date	0.15''	0.50''	References*
VSSG 8	2001, June 29	0.06	0.03	
H α 44	2001, July 4	0.10	0.06	
WL16	2000, June 18	0.06	0.03	C, S2
VSSG 9	2001, July 3	0.06	0.03	
GY 193	2001, June 30	0.09	0.03	
GY 194	2001, June 30	0.10	0.04	
VSSG 21	2001, July 3	0.12	0.05	
J162708-241204	2001, June 30	0.05	0.02	
WL 10	2000, June 21	0.08	0.03	
Elias 29	2000, June 21	0.03	0.02	C, S2
	2000, June 21	0.09	0.04	
GY 224	2000, June 22	0.09	0.05	
IRS 32	2000, June 22	0.08	0.04	
VSSG 24	2001, June 29	0.07	0.03	
IRS 32b	'91, Aug./'92, July	0.5 (0.02'')		S2
ROXs 20A	2000, June 20	0.10	0.10	
ROXs 20B	2000, June 20	0.09	0.07	
H α 47	2000, June 21	0.09	0.04	
WL 5	2000, June 20	0.18	0.13	
IRS 42	2000, June 21	0.06	0.03	C, S2
WL 6	2001, July 1	0.11	0.05	
VSSG 22	2000, June 20	0.05	0.04	C
H α 49	2000, June 20	0.06	0.06	
GY 262	2000, June 21	0.10	0.04	
IRS 43	2001, June 29	0.07	0.07	C, S2
VSSG 18	2000, June 20	0.12	0.06	
GY 284	2001, July 1	0.08	0.04	
J162730-244726	2001, June 29	0.07	0.05	
GY 292	2000, June 20	0.03	0.03	B2
H α 50	2000, June 21	0.05	0.02	
IRS 48	2000, June 20	0.07	0.02	C, S2
IRS 50	2000, June 20	0.10	0.04	C
IRS 49	2000, June 21	0.04	0.02	C, S2
ROXs 30B	2000, June 21	0.07	0.03	A1, B2
ROXs 30C	2000, June 21	0.08	0.02	A1
H α 52	2000, June 21	0.04	0.02	B2, S2
IRS 56	2001, July 3	0.11	0.06	S2
SR 10	2000, June 21	0.04	0.02	C, R3, S2
H α 58	2001, June 29	0.12	0.03	
J162800-245340	2001, June 30	0.05	0.03	
VSS 35	2001, July 4	0.10	0.05	R3**
J162813-243249	2001, July 1	0.09	0.04	
H α 60	2000, June 21	0.03	0.02	S2
ISO-Oph 195	2001, June 29	0.05	0.04	

Table 5.1: (continued)

Object	Date	0.15''	0.50''	References*
SR 20 W <small>(GWAYL)</small>	2001, July 3	0.08	0.04	
VSS 38	2000, June 17	0.03	0.02	
H α 63	2000, June 17	0.07	0.05	S2
VSS 42	2001, July 4	0.07	0.02	R3
IRAS 64a	2000, June 21	0.06	0.02	
VSS 41	2001, July 4	0.04	0.03	
Elias 41	2001, July 3	0.19	0.06	
H α 67	2001, July 4	0.14	0.04	S2
ROXs 39	2000, June 22	0.09	0.06	A1
Haro 1-14/c	2000, June 22	0.06	0.06	B2
Haro 1-14	2000, June 22	0.05	0.03	B2,G2
	2001, July 4	0.07	0.04	
Haro 1-16	1990, Aug. 6	0.05	0.05	B2, G2, R3, S2
IRS 63	2001, July 4	0.08	0.03	
H α 73	2001, July 2	0.09	0.07	S2
H α 74	2001, July 2	0.07	0.04	B2
ROXs 45D	2001, July 2	0.07	0.02	
ROXs 45E	2001, July 2	0.10	0.04	
ROXs 45F	2001, July 2	0.08	0.04	
H α 75	2001, July 1	0.06	0.02	
L1689 - IRS 7	2000, June 22	0.05	0.04	
Haro 1-17	2001, July 2	0.05	0.02	
Elias 45	2001, July 3	0.13	0.05	

Names adopted from Barsony et al. (2003) are given without the leading ‘BKLT’ and thus start with ‘J16’.

*: references are given in Table 5.2

**: additional lunar occultation companions

Based on the surface density of companions found in Fig. 5.1 at separations larger than 0.13'' in the range between the requested flux ratio of 0.1 and the detection limits of the twenty-two measurements described above, the probability to have missed one companion is 40%. Since the real sensitivity deficit is only relevant for separations below 1'', this estimate represents an upper limit. We are thus confident that all companions with a magnitude difference ≤ 2.5 mag have been found.

5.1.3 Lower Separation Limit

The lower limit of 0.13'' is given by the diffraction limit λ/D of a 3.5 m telescope in K. At this limit one period of the modulus of the complex visibility fits in the radius where the optical transfer function of the telescope is non-zero (Fig. 4.10). Nevertheless, it is possible to detect under good circumstances com-

Table 5.2: The double and multiple stars in our sample. Given are the position angles, the separations, and the flux ratios. The upper limit for the relative brightness of an additional undetected companion at the diffraction limit is provided in the sixth column.

Object	Date	PA [deg]	Separation ["]	Flux Ratio	0.15"	Remarks
H α 18	2001, July 4	82.3 ± 0.1	1.083 ± 0.002	0.737 ± 0.018	0.15	
H α 19	2001, July 4	262.9 ± 0.1	1.491 ± 0.020	0.462 ± 0.017	0.05	
Haro 1-4	1990, July 9	27 ± 1	0.72 ± 0.01	0.238 ± 0.011	0.05	G2
H α 21	2001, July 4	57.6 ± 1.6	0.161 ± 0.019	0.740 ± 0.081	0.07	
SR 2	2000, June 5	122.4 ± 0.6	0.222 ± 0.006	0.874 ± 0.112	0.06	G2
ROXs 2	2000, June 22	345.5 ± 1.4	0.424 ± 0.007	0.598 ± 0.032	0.05	B2, C
IRS 2	2000, June 17	78.6 ± 0.4	0.426 ± 0.006	0.132 ± 0.013	0.10	B2, C
J162538-242238	2001, July 4	170.2 ± 0.5	1.788 ± 0.013	0.084 ± 0.010	0.06	
IRS 3	2001, June 29	115.5 ± 0.6	0.663 ± 0.004	0.323 ± 0.017	0.04	
ROXs 5	2000, June 22	327.3 ± 1.7	0.176 ± 0.005	0.408 ± 0.029	0.03	A1
ROXR1-12	2001, June 30	18.5 ± 2.9	0.102 ± 0.009	0.672 ± 0.108	0.12	
H α 26	2001, July 4	25.8 ± 0.5	1.135 ± 0.004	0.846 ± 0.037	0.11	
DoAr 22	2001, July 2	258.9 ± 0.2	2.297 ± 0.004	0.005 ± 0.000	0.03	
H α 28	2001, June 29	357.8 ± 0.1	5.209 ± 0.013	0.047 ± 0.004	0.09	
DoAr 24E	1990, July 9	150 ± 1	2.03 ± 0.04	0.179 ± 0.029	0.05	A1, C, G2, S2
ROXs 12	2001, July 2	10.3 ± 0.1	1.747 ± 0.002	0.005 ± 0.000	0.06	
VSSG 27	2000, June 20	66.8 ± 0.5	1.222 ± 0.010	0.244 ± 0.043	0.05	C
H α 35	2001, July 4	132.2 ± 0.1	2.277 ± 0.007	0.272 ± 0.115	0.10	
H α 37	2000, June 20	65 ± 2	0.16 ± 0.01	0.108 ± 0.007	0.10	not seen by C, PA mod 180°
GSS 37	2000, June 18	69.5 ± 0.3	1.438 ± 0.012	0.299 ± 0.006	0.05	C
VSSG 11	2001, July 1	180.1 ± 0.6	0.107 ± 0.001	0.584 ± 0.017	0.04	

Table 5.2: (continued)

Object	Date	PA [deg]	Separation ["]	Flux Ratio	0.15"	Remarks
ROXs 16	Aa-Ab	2000, June 21	24.2 ± 7.5	0.098 ± 0.017	0.357 ± 0.061	0.05
	Aa-B		105.4 ± 0.6	0.577 ± 0.003	0.186 ± 0.019	A1, C
WL18		2000, June 22	292.4 ± 0.2	3.617 ± 0.001	0.162 ± 0.001	0.04
VSSG 3		2000, June 21	53.8 ± 0.5	0.243 ± 0.002	0.801 ± 0.052	0.07
VSSG 5		2001, June 30	133.9 ± 1.3	0.148 ± 0.001	0.873 ± 0.053	0.04
GY 156		2000, June 21	201.9 ± 1.8	0.161 ± 0.012	0.248 ± 0.030	0.07
SR 24	S-N	1999, Apr. 17	349.4 ± 1.3	5.065 ± 0.086	0.636 ± 0.033	0.06
	Na-Nb	1991, Aug. 19	84	0.197 ± 0.020	0.21	G2, S2 (flux limit at 0.02") C, S2
Elias 30		2000, June 21	175.6 ± 0.2	6.388 ± 0.013	0.063 ± 0.002	0.06
WL 20	A-B	2001, July 1	269.9 ± 0.1	3.198 ± 0.000	0.877 ± 0.010	0.06
	A-C		232.3 ± 0.1	3.619 ± 0.001	0.071 ± 0.003	
WL 4		2000, June 20	284.2 ± 2.3	0.176 ± 0.005	0.602 ± 0.062	0.06
SR 12		'86, Jan. / '91, Aug.	85	0.300 ± 0.030	0.91	0.33
VSSG 25		2000, June 20	173.3 ± 0.3	0.468 ± 0.003	0.887 ± 0.113	0.10
IRS 44		2001, June 30	246.6 ± 5.1	0.256 ± 0.005	0.204 ± 0.021	0.2
VSSG 17		2000, June 21	260.2 ± 0.8	0.242 ± 0.009	0.644 ± 0.072	0.04
IRS 51		2000, June 20	9.6 ± 0.3	1.645 ± 0.005	0.039 ± 0.001	0.07
SR 9		2001, July 3	353.3 ± 0.5	0.638 ± 0.006	0.057 ± 0.010	0.17
GY 371		2001, June 30	198.1 ± 0.3	0.347 ± 0.001	0.643 ± 0.010	0.06
VSSG 14		2000, June 18	83.6 ± 1.5	0.130 ± 0.004	0.296 ± 0.010	0.04
ROXs 31		2001, June 29	251.3 ± 0.2	0.396 ± 0.002	0.655 ± 0.029	0.05
GY 410		2000, June 20	277.0 ± 1.4	0.196 ± 0.024	0.143 ± 0.013	0.05

Table 5.2: (continued)

Object	Date	PA [deg]	Separation ["]	Flux Ratio	0.15"	Remarks
H α 59	2001, July 4	103.2 ± 2.4	0.100 ± 0.030	0.258 ± 0.029	0.07	
J162812- 245043	2001, July 3	101.7 ± 0.1	3.591 ± 0.001	0.428 ± 0.003	0.15	
SR 20	1990, July 9	225 ± 5	0.071 ± 0.001	0.125 ± 0.016	0.03	G2, R3, S2, not seen by C
V 853 Oph	1990, Aug. 7	96 ± 2	0.399 ± 0.008	0.238 ± 0.028	0.14	C, G2, S2 (triple*)
ROXs 42B	Aa-Ab A-B	2001, July 1	157.9 ± 1.7 268.0 ± 0.3	0.083 ± 0.002 1.137 ± 0.014	0.350 ± 0.049 0.002 ± 0.001	0.06 R3, S2, not seen by A1
ROXs 42C	2001, July 1	151.0 ± 0.7	0.277 ± 0.003	0.220 ± 0.040	0.05	B2, G2
ROXs 43A/B	2001, July 4	11.9 ± 0.1	4.523 ± 0.004	0.445 ± 0.004	0.07	A1, G2, S2 (quadruple*)
H α 71	2000, June 22	35.0 ± 1.4	3.560 ± 0.006	0.151 ± 0.056	0.04	S2
L1689 - IRS 5	A-Ba Ba-Bb	2001, July 2	241.2 ± 0.1 84.4 ± 6.1	3.006 ± 0.009 0.140 ± 0.011	0.277 ± 0.018 0.946 ± 0.137	0.05
DoAr 51	2001, July 2	79.3 ± 0.2	0.784 ± 0.003	0.228 ± 0.008	0.06	B2

Names adopted from Barsony et al. (1997) are given without the leading ‘BKLT’ and thus start with ‘J16’.

A1: Ageorges et al. (1997) B2: Barsony et al. (2003) C: Costa et al. (2000)
G2: Ghez et al. (1993) R3: Richichi et al. (1994) S2: Simon et al. (1995)

*: additional spectroscopic or lunar occultation companions

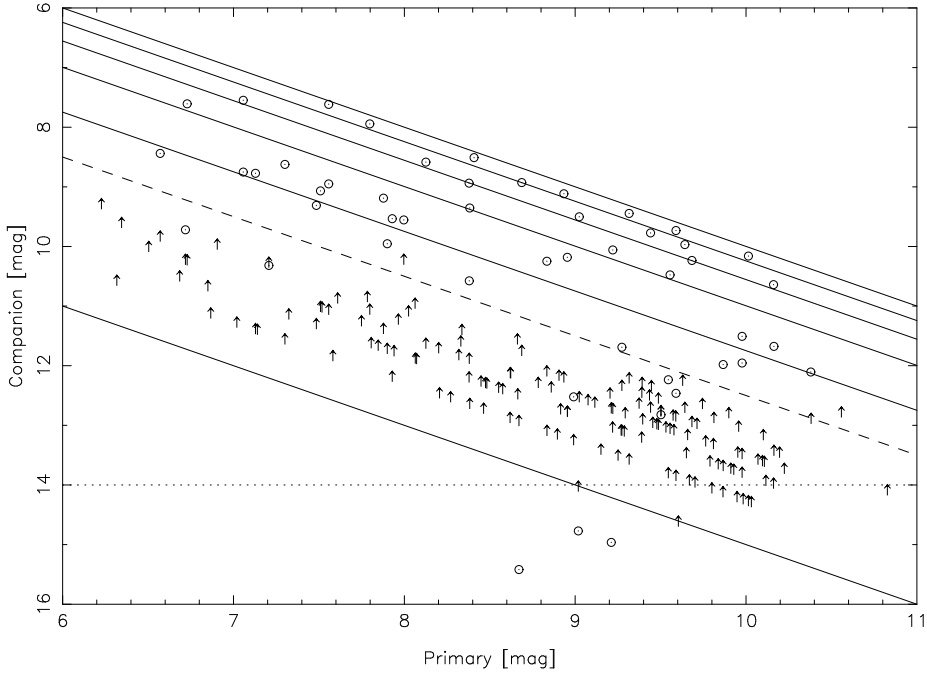


Figure 5.2: The brightness of detected (\odot) and the upper limit for non-detected companions at a separation of $0.5''$ (\uparrow) vs. the brightness of the primaries. The diagonal lines indicate flux ratios of 0.01, 0.1 (=completeness, dashed), 0.2, 0.4, 0.6, 0.8, and 1.0. The dotted horizontal line gives the magnitude used for the background determination.

Although three companions with a K-band magnitude around 15 (see Fig. 5.2) have been detected, they have been found in the shift-and-add images and are thus not very representative for the upper detection limit of our survey. The upper flux limit provided by the speckle software for non-detected companions at a separation of $0.5''$ from the primary is much better suited for this purpose. As shown in Fig. 5.2 this upper limit lies slightly above $m_K = 14$ mag.

The results of counting the stars down to the 14th magnitude in each field is plotted in Fig. 5.3. The histogram can be fitted by a Poisson distribution with a mean value of ≈ 3.5 that corresponds to an absolute value of $1.5 \cdot 10^{-4} \text{ arcsec}^{-2}$. Defining the area within $16^h 25^m \dots 16^h 30^m$ in right ascension and $-25^\circ \dots -24^\circ$ in declination as centre and the remaining area as periphery, one can find from the associated fields no significant difference between the centre and the periphery. Besides, a background density of $1.5 \cdot 10^{-4} \text{ arcsec}^{-2}$ is in good agreement with the value $1.6 \dots 1.7 \cdot 10^{-4} \text{ arcsec}^{-2}$ derived from the survey of Barsony et al. (1997)¹.

5.1.5 Surface Density

Another interesting property of a star forming region is the surface density $\Sigma(\theta)$ of companions (see Fig. 5.4). Over the separation range $0.13'' \leq \theta \leq 6.4''$ a

¹To obtain this value the number of stars brighter than $m_K = 14$ mag in Barsony et al. (1997) has been divided by the covered area. The uncertainty in the resulting background density is caused by the determination of the area.

Figure 5.3: Background statistics: In the 104 fields all stars down to a brightness limit of 14 mag are included. The dots represent a Poisson distribution with the mean value of ≈ 3.5 .

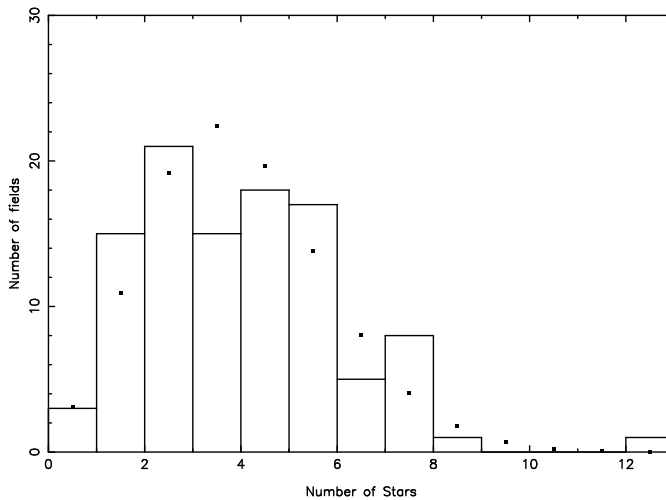
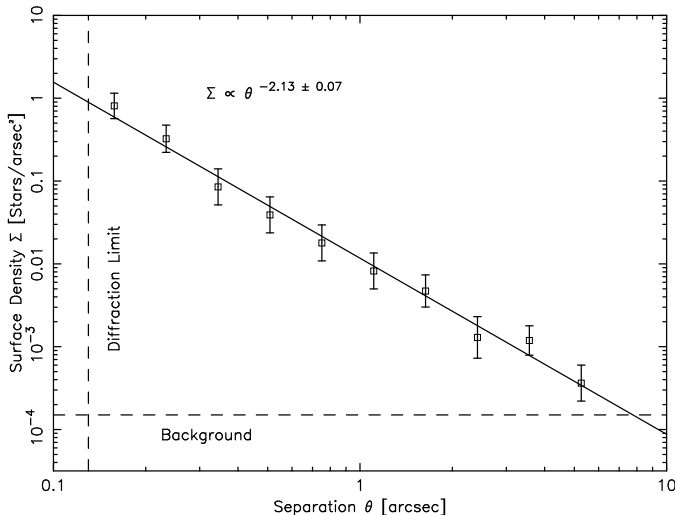


Figure 5.4: Surface density of the companions, compared to the surface density of the background stars.



linear regression of the surface density leads to

$$\Sigma(\theta) \propto \theta^{-2.13 \pm 0.07}, \quad (5.1)$$

which means that the number of companions is almost constant per logarithmic separation interval (see Fig. 5.1). This is nearly the same value as derived for the Taurus star forming region (Köhler & Leinert, 1998). Due to the enlarged samples both results put the conclusion of Simon (1997) on a firmer footing. He found that the surface density of companions in the binary regime in different star forming regions (Taurus, Ophiuchus, Orion Trapezium) can be approximately described by θ^{-2} .

The surface density of the companions is used to provide an upper limit for the separations in our survey. We choose 6.4" (half the field of view of the SHARP cameras), because chance projections of background or foreground objects would become important at larger separations.

5.1.6 Wide companions

The field of view of the SHARP I and the SHARP II+ camera is 12.8". Usually, we centred the object in one of the lower quadrants, where the number of bad pixels was lowest. All companions out to 3.2" should thus have been detected in these measurements. For the wider companions the 2MASS database has been checked and eleven infrared sources with a second source detected in the K-band within the separation range covered by our survey have been found. These objects are marked with a ‘C’ in Table 2.3. The companions of H α 28 ($m_K^{\text{comp}} = 11.869$ mag), Elias 30 (9.465 mag), BKLT J162812-245043 (10.378 mag), ROXs 43A/B (7.089 mag) and H α 71 (9.927 mag) as well as the in the 2MASS database unresolved companions in the triple system WL 20 (9.484 mag) have been already detected with our reduction methods. The coordinates given in 2MASS for the south and the north (7.549 mag) component of SR 24 are not consistent with the relative positions reported in Simon et al. (1995). We decided to adopt the values from the 2MASS All-Sky Catalog of Point Sources for the wide pair S-N and used the values given in Simon et al. (1995) for the close pair Na-Nb.

The ‘wide companions’ of the sources Elias 21 ($m_K^{\text{comp}} = 11.015$ mag), VSSG 18 (12.284 mag) and VSSG 17 (13.291 mag) are indicated in the 2MASS All Sky Catalog as point sources falling within the elliptical boundary of an extended source. This implies that the point sources are extractions of pieces of underlying nebulae. A visual inspection of the 2MASS images strengthens this suspicion. A similar case is the spurious source 5.5" west of GSS 32 with a brightness of $m_K^{\text{comp}} = 13.339$ mag. It is probably an artifact. Although Simon et al. (1995) found GSS 32 single, they did not reach the necessary sensitivity to falsify the wide companion ($m_K \leq 9.2$ mag). Finally, Terebey et al. (2001) and Haisch et al. (2002) classified GSS 32 as a single star. In our fitscubes of LFAM 3 GSS 32 appears in the upper, i.e. eastern quadrants of the chip. No companions are visible. However, all of the ‘real’ companions found in 2MASS have been already detected with our reduction method and thus are already included in Table 5.2.

5.1.7 Number of Systems After Background Subtraction

In our sample of 158 targets 49 fully resolved companions in the separation range $0.13'' \leq \theta \leq 6.4''$ have been found. It thus contains 112 single stars, 43 binaries, 3 triples, and no quadruples. In addition one has to take into account that the probability p to detect a background star close to a surveyed star is (Section 5.1.4)

$$p = \pi \cdot (6.4 \text{ arcsec})^2 \cdot 1.5 \cdot 10^{-4} \text{ arcsec}^{-2} \approx 0.019 \quad (5.2)$$

or ≈ 3 companions in the whole sample. Therefore, three of the companions should be chance projections. This leads to a companion star frequency of 0.29 ± 0.04 . To correct the number of single, binary, and triple systems, one has to consider that, e.g. ‘false’ triple systems can be produced with a probability of p by the ‘true’ binaries and with a probability of p^2 by ‘true’ single star. Otherwise, e.g. the number of ‘true’ single systems is increased when compared to the number of ‘observed’ single systems by a factor $1/(1 - p + \mathcal{O}(p^2))$, because

projected companions reduce their number. A brief calculation leads to 114.2 ‘real’ single stars, 41.7 binaries, and 2.2 triple systems.

5.1.8 The Restricted Sample

For statistical purposes we also define a restricted sample, excluding all targets with uncertain association (‘U’ in Table 2.3) and including only companions with brightness ratios ≥ 0.1 where the survey is complete and with separations exceeding the diffraction limit. The brightness ratio of 0.1 for these young stars approximately corresponds to the limit in mass ratio of 0.1 used for the work on solar-like main-sequence stars (Duquennoy & Mayor, 1991). This restricted sample contains 38 companions around 139 primaries. For the restricted sample one finds 103 single stars, 34 binaries, and 2 triple systems. The background density is only $0.6 \cdot 10^{-4} \text{ arcsec}^{-2}$ for a detection limit of 12 mag on average. With $p = 0.008$ this sample thus contains 103.8 ‘real’ single stars, 33.4 binaries, and 1.7 triple systems. The companion star frequency is 0.27 ± 0.04

5.2 Discussion

5.2.1 Comparison to Main-Sequence Stars

To compare the results with the solar-type main-sequence sample surveyed by Duquennoy & Mayor (1991) one has to transform their lognormal period distribution

$$f[\lg(P)] = C \exp \left[-\frac{1}{2\sigma^2} (\lg(P) - \langle \lg(P) \rangle)^2 \right] \quad (5.3)$$

with $\langle \lg(P) \rangle = 4.8$, $\sigma_P = 2.3$, and P measured in days into a lognormal distribution of separations. This is not trivial since our observations are snapshots, i.e. one cannot derive periods by fitting the orbits.

For random distribution of orbital planes the relation between semi-major axis and actual observed separation is given by (Leinert et al., 1993)

$$\langle r \rangle = \frac{\pi}{4} a \left(1 + \frac{e^2}{2} \right). \quad (5.4)$$

The combined reduction of the average separation with respect to the semi-major axis would be by a factor of 0.98, if the eccentricities follow the distribution

$$f(e) = 2e \quad (5.5)$$

(Duquennoy & Mayor, 1991). This allows to convert the orbital periods to average observed separations using Kepler’s third law. With an assumed system mass of $1 M_\odot$ and r in astronomical units $\langle \lg(P) \rangle$ and σ_P transform into $\langle \lg(r) \rangle = 1.48$ and $\sigma_r = 1.53$. The observed separation r scales with the cubic root of the total system mass.

Alternatively, one may use the well-known properties of main-sequence binaries to predict their number within the observed separation range. For Fig. 5.5 a sample of 10^7 systems is simulated for different masses or mass ranges. These systems have orbital elements according to Duquennoy & Mayor (1991), i.e. the periods have the lognormal distribution (5.3) and the distribution of eccentricities is given by (5.5). The inclinations are distributed isotropically and

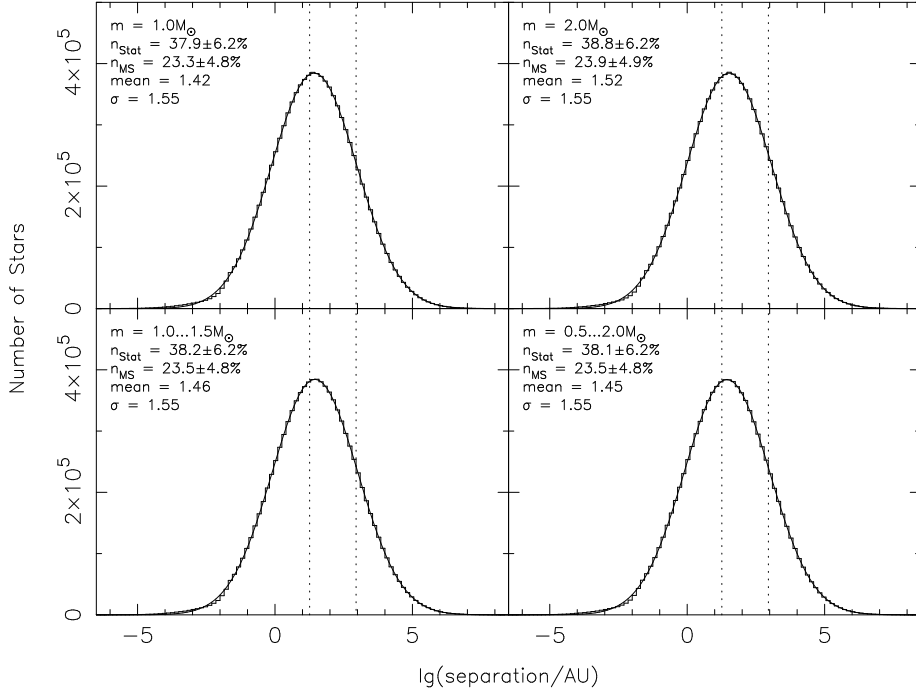


Figure 5.5: Simulated distributions of projected separations for four samples of 10 million main-sequence binaries each with different system masses or mass ranges. The histogram shows the simulated data; the line is a lognormal distribution fitted to the histogram. The dotted vertical lines border the separation range we have observed when assuming a distance of 140 pc to the cloud complex.

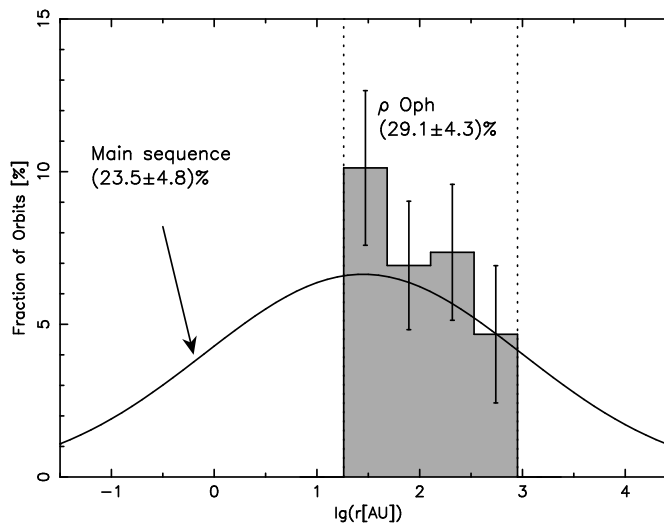
the other parameters uniformly. After binning the results the distribution is fitted with a Gaussian (solid line). For a total system mass of $1 M_{\odot}$ the values are in good agreement with the results above: $\langle \lg(r) \rangle = 1.42$ and $\sigma_r = 1.55$. While σ_r is constant for all masses and mass ranges the mean value increases as expected from lower to higher masses. For the plots in the following sections $\langle \lg(r) \rangle = 1.45$ and $\sigma_r = 1.55$ will be used, i.e the average of the values resulting from the system mass distributions $0.5 M_{\odot} \dots 2.0 M_{\odot}$ and $1.0 M_{\odot} \dots 1.5 M_{\odot}$.

Here a distance of 140 pc to the Ophiuchus Dark Cloud is assumed. The separation range covered by our sample is marked by the vertical dotted lines in Fig. 5.5. n_{Stat} is the percentage of the systems falling within these limits. After multiplying this value with the corrected (Duquennoy & Mayor, 1991) multiplicity of the main-sequence sample (101 companions out of 164 systems) one finds n_{MS} , the number of companions that would have been found if we had observed a sample of main-sequence stars in our survey. Due to the fact that with increasing masses the peak of the Gaussian drifts to larger separations and into our observation range, n_{MS} also increases with the mass of the systems. However, for the mass ranges considered here this effect is negligible. For both plots with variable masses

$$n_{\text{MS}} = (23.5 \pm 4.8)\% \quad (5.6)$$

has been found. This value will be used as a reference.

Figure 5.6: Binary frequency as a function of separation for the total sample. The curve is the distribution of binaries among solar-type main-sequence stars (Duquennoy & Mayor, 1991).



After binning all companions within the separation range $0.13'' \leq \theta \leq 6.4''$ into four bins and subtracting the background the result of our survey is plotted in Fig. 5.6. Four bins are chosen since the original histogram by Duquennoy & Mayor (1991) also contains approximately four bins for the relevant range of separations or periods, respectively. The error is estimated as \sqrt{N} . A comparison of the slope of the distribution with that of the main-sequence stars shows good agreement. An exception is the overabundance of close companions (see Section 5.2.3). A similar agreement has been found for the binary frequency. With a value of

$$n_{\text{Oph}} = (29.1 \pm 4.3)\% \quad (5.7)$$

the multiplicity is only 1.24 ± 0.31 times larger than for the main-sequence stars (5.6). For the restricted sample (see Fig. 5.10) one finds

$$n_{\text{Oph}}^{\text{res}} = (26.6 \pm 4.4)\% \quad (5.8)$$

or 1.13 ± 0.30 times the value for a main-sequence sample (5.6). The multiplicity in Ophiuchus is thus marginally larger than for the main-sequence, but the difference is on the level of one σ only.

5.2.2 Comparison to Previous Surveys

The appraisal of multiplicity among young stars ‘in Ophiuchus’ keeps changing. From the beginning, it has been centred on a comparison to the multiplicity observed in the Taurus-Auriga star-forming region.

Ghez et al. (1993) observed the 24 known young stars brighter than $m_K = 8.5$ mag in Scorpius and Ophiuchus and found no difference with respect to Taurus in the range of separations between 16 AU and 252 AU ($0.1'' - 1.8''$), but a value of duplicity by a factor of 4 greater than that of the solar-type main-sequence stars (Duquennoy & Mayor 1991). Simon et al. (1995) had a sample of 35 sources, selected by the randomness of lunar occultation observations (location of observatories, committee approval, weather, instrumental efficiency). Supplemented by imaging for larger separations, they found that between 3 AU

and 1400 AU ($0.05'' - 10''$) Ophiuchus had a binary frequency of 1.1 ± 0.3 times that of nearby solar-type stars, while for Taurus this number was 1.6 ± 0.3 . These are lower limits because no corrections for incompleteness were applied. Duchêne (1999) added the Gunn z band observations of Reipurth & Zinnecker (1993) to these earlier surveys, corrected for incompleteness and found an enhancement of multiplicity by a factor of 1.5 ± 0.3 (2.0 ± 0.3 , when Simon et al. (1995) is not included) over the main-sequence value, quite the same as for the Taurus-Auriga association.

Barsony et al. (2003) restricted the sample to objects searched by high-resolution near-infrared techniques. Adding new observations of this type for 19 optically selected sources from the environment of the main cloud L1688, they arrived at an overabundance of a factor of 2 ± 1 with respect to the main sequence for their sample of 80 objects, consistent with the values for the Taurus-Auriga star forming region. Duchêne et al. (2004) did a deep ($3 \text{ mag} \leq \Delta m_K^{\text{lim}} \leq 7 \text{ mag}$) near-infrared imaging survey of 63 embedded young stellar objects in Ophiuchus and Taurus, concluding that in the range of 110 – 1400 AU ($0.8'' - 10''$) the multiplicity is about twice as large as for nearby solar-type main-sequence stars, and with no difference between Taurus and Ophiuchus. In this study the most embedded sources showed the highest multiplicity, still by a factor of 1.5 larger than the average. The latter result is similar to the findings in Haisch et al. (2002) on a sample of 19 embedded objects in Ophiuchus and Serpens. Our survey, with a duplicity of young stars in Ophiuchus close to that of the main-sequence sample of Duquennoy & Mayor, is similar in result to the study of Simon et al. (1995) again.

While the studies of Haisch et al. (2002) and Duchêne et al. (2004), performed on small samples, delineate interesting and important trends with age of the objects, the difference of our work to the work of Barsony et al. (2003) needs some explanation. As shown in Section 5.3, the difference will not lie in the different efficiency of the surveys, since binary young stars are consistently found in the overwhelming majority of cases by both surveys with quantitatively good agreement. Differences then should result from the selection of the sample and the angular limits over which duplicity is considered. Barsony et al. (2003) in their survey and compilation of 80 objects, found 0.24 ± 0.11 companions per primary for the range of $0.1'' - 1.1''$. Choosing from their paper companions in the range of $0.13''$ to $6.4''$, as applied in our study, the resulting number of companions per primary would increase to 0.33 ± 0.07 , or 1.4 ± 0.4 above the expectation for the main-sequence sample of solar-type stars. Otherwise, when restricting our sample to separations between $0.13''$ and $1.1''$ one finds a companion star frequency of 0.16 ± 0.03 . The differences are thus within the errors and naturally to be explained by differences in the samples. This just shows again the importance of large samples and to keep the sample by definition as complete as possible. The current survey with the selection criterion to take *all* stars brighter than $m_K = 10.5 \text{ mag}$ that have shown convincing signs of youth compares well with previous works.

5.2.3 Implications for the Formation Process

The general frame in which we are looking at the data is the scenario that stars originally form with a high multiplicity, which then is reduced to the main-sequence value in dense environments by dynamical interactions on a short

time scale. This does not mean that we primarily want to confirm this image, but that we want to check which comments or corrections with respect to this picture result from our study.

Density

Both the Taurus-Auriga and the ρ Ophiuchi molecular clouds are located at a distance of about 140 pc, contain of the order of $10^4 M_\odot$ of gas and dust and harbour several hundreds of young stars with an age of at most a few million years. What causes the smaller binary frequency found in our survey when compared with the result

$$n_{\text{Tau}} = (48.9 \pm 5.3)\% = (1.93 \pm 0.26) n_{\text{MS}}^{13} \quad (5.9)$$

found by Köhler & Leinert (1998) for Taurus-Auriga? n_{MS}^{13} is the main-sequence binary fraction between their diffraction limit of $0.13''$ and their upper limit of $13''$. One finds

$$n_{\text{Tau}}^{\text{res}} = (39.7 \pm 4.8)\% = (1.56 \pm 0.31) n_{\text{MS}}^{13} \quad (5.10)$$

after all companions with a flux ratio less than 0.1 have been removed.

Taurus-Auriga is the prototypical site of low-mass star-formation. Various studies of the large-scale structure have revealed a complex, irregular, and filamentary appearance. Embedded along this filamentary structures small (≈ 0.1 pc) and dense ($\geq 10^4 \text{cm}^{-3}$) cores have been identified in which the young stars are forming. Their typical mass is $1 M_\odot$ and their kinetic temperature about 10 K. Typical visual extinctions are between 5 and 10 mag. The whole Taurus-Auriga aggregate covers an area of 300pc^2 and thus the stellar surface density is a few stars pc^{-2} . Only weak clustering is apparent.

Similar conditions are found when studying the outer regions of the ρ Oph complex. Loose filamentary and clumpy structures can be easily identified. A different environment is present in the main cloud L1688. This westernmost cloud contains in an area of only $1 \times 2 \text{pc}$ a centrally condensed core of $600 M_\odot$ with active star formation. A large fraction of all young stellar objects in the ρ Oph molecular clouds are concentrated in this cluster. Stellar surface densities one or two orders of magnitudes higher than the values found in Taurus-Auriga are the result. Peak values of $5 \cdot 10^3$ stars pc^{-3} within the densest cores (Allen et al., 2002) are almost comparable to the values that are found in the Orion nebula cluster, although there the high densities extend over larger scales. The high star-formation efficiency in L1688 suggests that the cluster may remain gravitationally bound and thus survive as an open cluster (Lada et al., 1993). The visual extinction can reach values between 50 and 100 mag. While the radiation field caused by massive stars plays a minor or even no role for the Taurus-Auriga complex (Zinnecker et al., 1993), the ρ Ophiuchi molecular clouds are highly influenced by the nearby Upper Scorpius-Centaurus OB-association. This may be reflected by the cometary shape of the complex and the high density reached within L1688. The influence of nearby massive stars may have also triggered the rapid rise of star-formation about 1 million years ago in the central cloud L1688 (Palla & Stahler, 2000). Therefore, the ρ Oph Dark Cloud with its embedded cluster seems to be an important link between loose T associations and dense clusters at larger distances.

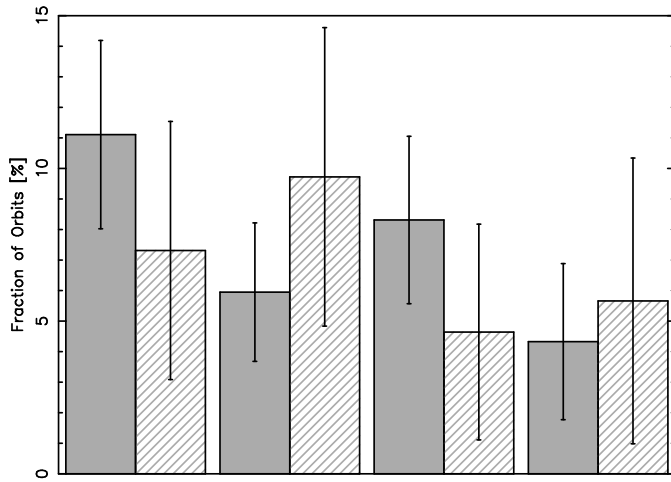


Figure 5.7: The four bins plotted in Fig. 5.6, but plotted for both the 117 primaries in the centre (solid) and the 41 primaries in the periphery (hatched).

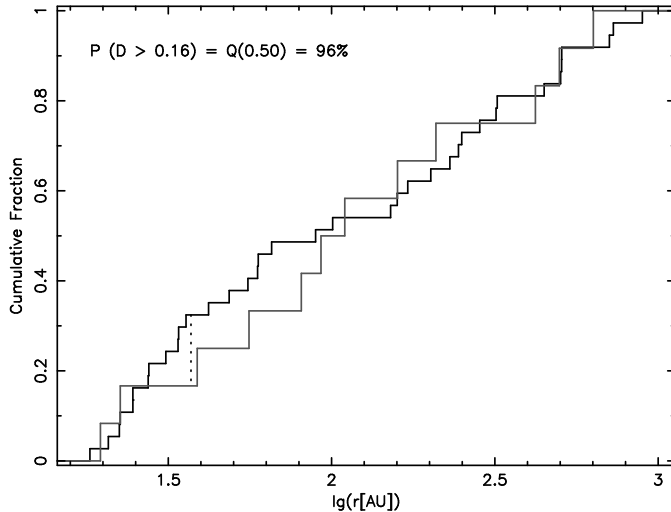


Figure 5.8: The Kolmogorov-Smirnov test for the two datasets (centre: black, periphery: grey). With a probability of 96% the two datasets are from the same sample.

Duchêne (1999) in his quantitative comparison of various multiplicity surveys found that all dense clusters have binary fractions compatible with the main-sequence, while all the regions with a binary excess are loose associations. This favours a tight correlation between the density or a related parameter and the multiplicity of a star forming region. The new results presented here seem to fit very well in this picture with a duplicity value lying between those of Taurus-Auriga and the main-sequence and hence dense clusters, both for the full and the restricted sample. In the context of dependence of duplicity on density of the star-forming region this would be a plausible result, more plausible than the large overabundance of companions found in some of the earlier surveys with smaller samples.

One consequence of this density hypothesis would be a difference between the multiplicity of the dense central region (L1688) and that of the less dense outer regions. Recalculating the companion frequency of the total sample for both the 117 sources within L1688 ($16^h25^m \dots 16^h30^m$, $-25^\circ \dots -24^\circ$) and for the 41 sources in the periphery reveals that the multiplicity of both is very

similar:

$$n_{\text{Cen}} = (29.7 \pm 5.0)\% = (1.26 \pm 0.34) n_{\text{MS}}, \quad (5.11)$$

$$n_{\text{Per}} = (27.3 \pm 8.2)\% = (1.16 \pm 0.42) n_{\text{MS}}. \quad (5.12)$$

Replotting the four bins displayed in Fig. 5.6 shows that the distribution of the separations of both subsamples differ only slightly from each other (Fig. 5.7). A Kolmogorov-Smirnov test (Fig. 5.8) also favours a common distribution. The corresponding values for the restricted sample with 104 targets in the centre and 38 targets in the periphery are

$$n_{\text{Cen}}^{\text{res}} = (26.2 \pm 5.0)\% = (1.11 \pm 0.31) n_{\text{MS}}, \quad (5.13)$$

$$n_{\text{Per}}^{\text{res}} = (27.8 \pm 8.9)\% = (1.18 \pm 0.45) n_{\text{MS}} \quad (5.14)$$

with a probability of 29% that the two distributions are drawn from the same sample.

This means that locally we cannot see a density effect of duplicity within the errors. The sources in the surroundings appear older on average than those within L1688 and part of them could have formed in a denser environment now dissolved. However, this is nothing more than a somewhat vague possibility. The conclusions therefore are not as clear as one might want it to be.

Although density or a related parameter seems to play a crucial role in the formation of binaries on a global scale, there is no statistical significance within the ρ Oph molecular cloud complex that areas with different densities show different multiplicities.

Temporal Evolution

Star forming regions with a main-sequence binary fraction are found at all ages, e.g. IC 348 (Duchêne et al., 1999), Orion (Petr et al., 1998) with an age of a few million years, the Pleiades (Bouvier et al., 1997) with 120 Myr, and the Praesepe (Bouvier et al., 2001) with 700 Myr. This suggests that dynamic interactions, if responsible for reducing an originally high duplicity to much lower values, act very quickly in dense clusters, while little future effect has to be expected for low-density regions like Taurus-Auriga. Thus temporal evolution of the binary frequency is not in general responsible for the difference between the overabundance of companions found in Taurus-Auriga when compared to the main-sequence. The fact that in the young but not too dense Ophiuchus star-forming region there remains an overabundance of companions, with the most embedded sources showing the highest degree of multiplicity (Duchêne et al., 2004), would be compatible with the dynamical evolution of binarity in cluster environments (Kroupa, 1995).

We tried to see this effect in our sample with respect to the age of the different objects and thus searched for their infrared classes in the literature. Although this classification scheme is more a morphological description than a direct indicator of the age, it provides the best approach when no spectroscopic data are available. To avoid systematic errors from different surveys only the classification provided by the mid-infrared survey of Bontemps et al. (2001) and the near-infrared study of Greene et al. (1994) has been taken into account. To be consistent with the classification in Bontemps et al. (2001) we decided to classify in Greene et al. (1994) objects with a spectral slope $a > 0.55$ as class I

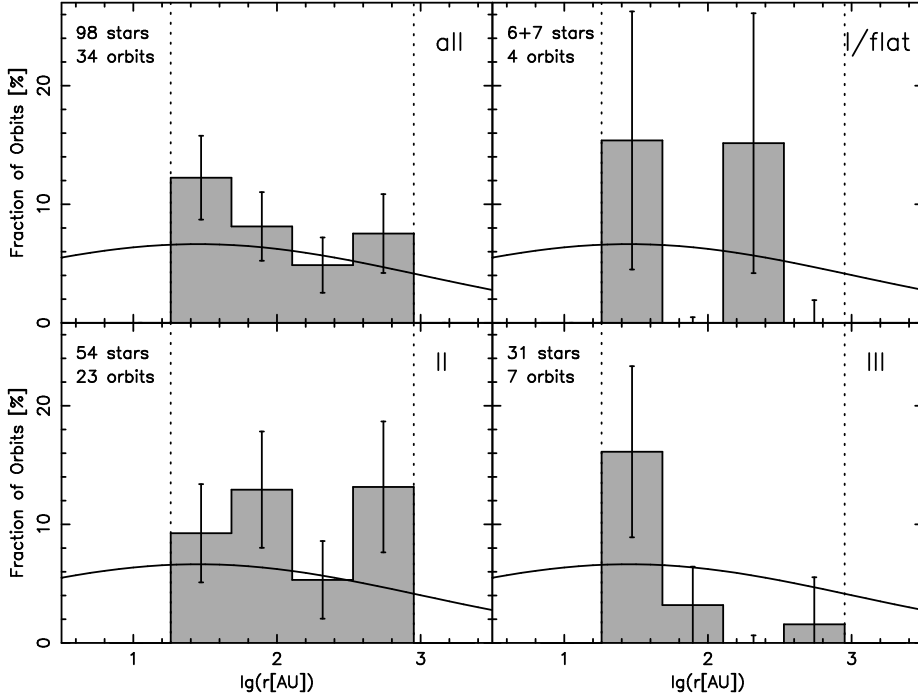


Figure 5.9: Binary frequency as a function of separation and class. The upper left panel shows the distribution for all classified sources. The remaining panels display the combined sample of flat spectrum and class I sources, the class II, and the class III samples. The curve is the distribution of binaries among solar-type main-sequence stars (Duquennoy & Mayor, 1991).

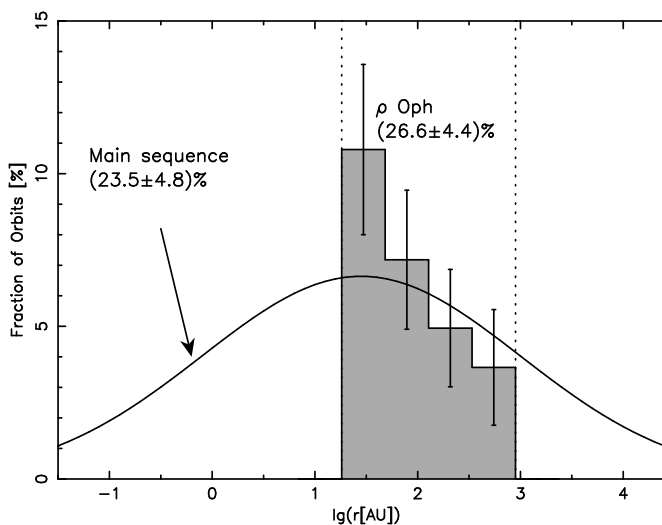
and those with $a > -0.05$ as flat spectrum sources. To distinguish between more evolved class II and class III objects in Greene et al. (1994) $a = -1.6$ has been applied as limit. WL 5 is an exception, since it is classified as a heavily reddened class III source. This conclusion is in agreement with the result in Bontemps et al. (2001). All sources included in both samples are classified consistently with exception of L1689-IRS 5 and LFAM 3 that are according to Greene et al. (1994) flat spectrum sources, but are classified as class II sources in Bontemps et al. (2001). Since LFAM 3 lies only marginally below the limit in Bontemps et al. (2001) we decided to classify it as flat spectrum source. Otherwise, L1689-IRS5 is only slightly above the limit in Greene et al. (1994) and well below in Bontemps et al. (2001). We thus classified it as class II object. Class I and class II sources in Greene et al. (1994) with an upper limit for a are ignored. This leads to a sample of 6 class I, 7 flat spectrum, 54 class II, and 31 class III sources. The multiplicity of this subsample is

$$n_{\text{I-III}} = (32.8 \pm 5.8)\% = (1.39 \pm 0.38) n_{\text{MS}} \quad (5.15)$$

and thus compatible with the result found in (5.7) and (5.8) within the errorbars. After separating the different evolutionary states one is left with subsamples that are no longer free from small number statistics (see Fig. 5.9):

$$n_{\text{I/flat}} = (29 \pm 15)\% = (1.2 \pm 0.7) n_{\text{MS}}, \quad (5.16)$$

Figure 5.10: Binary frequency as a function of separation for the restricted sample. The curve is the distribution of binaries among solar-type main-sequence stars (Duquennoy & Mayor, 1991).



$$n_{\text{II}} = (41 \pm 9)\% = (1.7 \pm 0.5) n_{\text{MS}}, \quad (5.17)$$

$$n_{\text{III}} = (21 \pm 8)\% = (0.9 \pm 0.4) n_{\text{MS}}. \quad (5.18)$$

There appears to be a trend that class III systems (WTTS) have fewer companions and at smaller separations than their class II (CTTS) counterparts. This was not found in Taurus. Ghez et al. (1993) suggested from a similar result on a smaller sample that close companions may help to clear circumstellar disks earlier and therefore appear more frequently in WTTS.

Temporal evolution may be important in dense environments at early stages. Our sample of stars mostly older than 1 Myr and located in a cluster of medium density is not sensitive to such an effect, if it exists. However, the difference in the multiplicity and separation distribution between class II and class III sources and with respect to Taurus could show real changes, maybe temporal evolution. In general one fundamental problem remains. The parameters used to determine the age of the systems are influenced by the multiplicity.

Another possibility is a biasing of the sample by a yet not distinguished older population of lower multiplicity. In the last section a strong influence of such a population in the periphery could be excluded. Nevertheless, if the stars reside instead in the foreground, they could mimic the here discussed difference between the classes. Precise measurements, e.g. with GAIA of the parallaxes will test this yet just vague idea.

Although temporal evolution seems to be not responsible for the reduction of the binary frequency in general except for the earliest stages, our survey indicates statistical differences between the infrared classes with respect to their companion frequencies and separation distributions.

Missing Companions

Two possible explanations have been discussed by Duchêne (1999) for the low multiplicity of the Ophiuchus star forming region when compared to Taurus-Auriga:

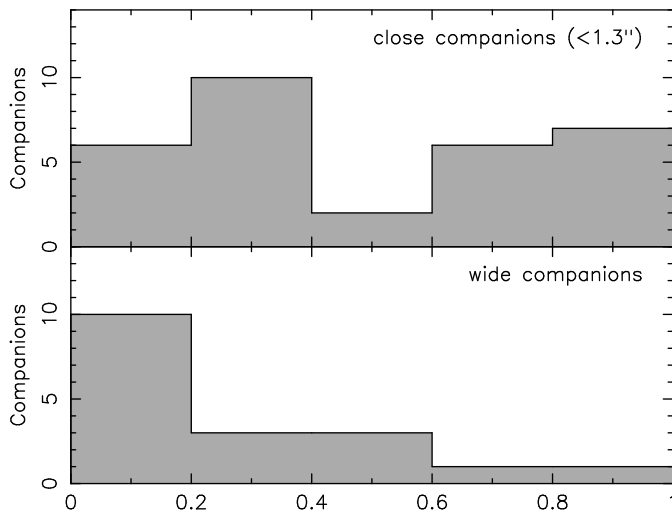


Figure 5.11:
Flux ratio for close (<1.3'') and wide companions.

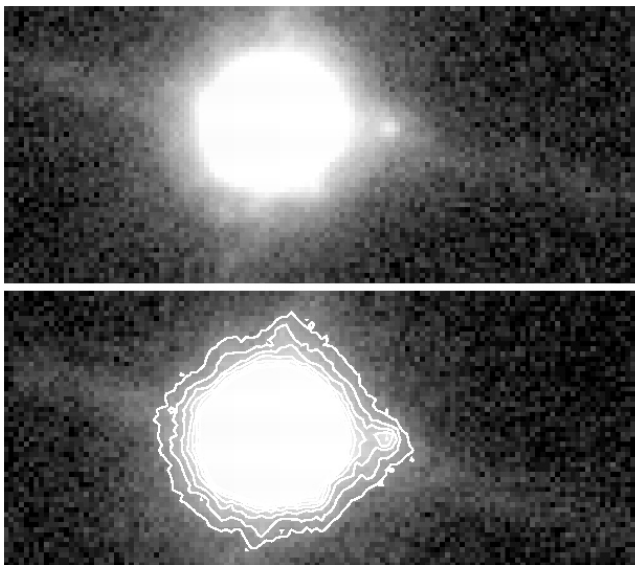
1. The distribution of the projected separations can be shifted to lower values, i.e. the ‘missing’ companions are *too close* to be resolved and are hidden from our survey below the diffraction limit.
2. The flux ratio of the companions is smaller for Ophiuchus, i.e. the ‘missing’ companions are *too faint* to be detected.

To conclude on the first possibility, very high resolution observations (lunar occultations or interferometry) would have to be available for most of the sources of our survey, which is not yet the case. From Simon et al. (1995) and Barsony et al. (2003) there is at least evidence that no overabundance of stars for very close companions is present. However, both studies suffer from poor statistics. Fig. 5.10 that displays the multiplicity as function of the separation for our restricted sample shows a contrary trend. The sample is dominated by close companions. This overabundance is more apparent in the restricted sample than in the total sample (Fig. 5.6 and Fig. 5.10).

Concerning the second suggestion, Duchêne (1999) found from Ghez et al. (1993) that 73% of the binaries in Taurus, but only 23% of the binaries in Ophiuchus exhibit a magnitude difference between companion and primary of $\Delta m_K < 1.5$ mag. To check whether this also holds for our larger sample, the flux ratios of our companions in the total sample are displayed in Fig. 5.11. Indeed, the whole sample is dominated by small flux ratios. About 59% of the systems show flux ratios below 0.4 and 33% below 0.2.

This tendency to favour small flux ratios is introduced by the wide pairs. When defining binaries with a separation of $\theta_w \geq 1.3''$ as wide binaries like in Köhler & Leinert (1998) 72% of the wide companions are below 0.4 and 56% show flux ratios smaller than 0.2. This leads to the significant overabundance of close binaries in the restricted, i.e. also flux-limited sample (see Fig. 5.10). The close companions are almost equally distributed. Also a decrease of θ_w does not lead to a domination of high or low flux ratios. When varying θ_w Kolmogorov-Smirnov tests show that the probability that the two distributions have a common origin is below 10% over a wide range.

Figure 5.12: The faint companion of ROXs 42B as seen in the shift-and-add images of the two fitscubes. The images are printed in logarithmic scale. Linear contours are overlaid on the second image. The flux ratio is 0.002.



In Köhler & Leinert (1998) wide pairs ($>1.3''$) are also dominated by small flux ratios, similar to the result displayed in Fig. 5.11. On the other hand there is a clear tendency in Taurus-Auriga for close binaries to exhibit a large fraction of equally bright systems probably caused by a lack of close binaries with small flux ratios present in Ophiuchus. This population may be the reason for the finding in Duchêne (1999).

A combination of the two results, i.e. the high fraction of close binaries and the presence of close companions with low flux ratios, leads to the conclusion that ‘missing’ companions may play a role with the implication that the full binary fraction over all separations would be more clearly enhanced than the binarity in the restricted sample.

5.3 Previously Known Binaries

Barsony et al. (2003) compiled a list of all known binary and multiple systems associated with the ρ Ophiuchi molecular clouds. In Table 5.3 all sources of this compilation with a separation in the range $0.05'' \leq \theta \leq 6.7''$ that have been newly observed within the scope of our survey are listed. The first column gives the name used in our survey. If Barsony et al. (2003) used another designation it appears in the last column. The second column gives their references. The references printed in bold font are those that have been used to derive the values for the position angles, the separations and the flux ratios in the columns 4, 5, and 6. The date of observation in this reference is given in column 3. For comparison our results are listed in the subsequent columns.

Only one companion was not detected in our survey. This is probably caused by the small separation below the diffraction limit of our telescopes. Otherwise, additional companions of ROXs 42B and L1689-IRS 5 transforming these objects into triple systems have been detected. The new companion of ROXs 42B (Fig. 5.12) is a faint knot west of the primary. In the case of L1689-IRS 5 (Fig. 5.13) the previously known companion splits up into two point sources

Table 5.3: Comparison to previously known binary and multiple systems

Object	Ref	Observation Date	PA _{Lit} [deg]	θ_{Lit} ["]	K ₂ /K _{1,Lit}	PA [deg]	θ ["]	K ₂ /K ₁	Remark
H α 18	K R1	1999, June 1/2	339.55 ^m	$\approx 0.1004^d$	≈ 0.505	-	-	-	undetected
			80.4	1.08	0.7	82.3	1.083	0.737	
H α 19	K R1	1999, June 1/2	260.7	1.53	0.5	262.9	1.491	0.462	
SR 2	A2 G2	1990, July 8	156	0.236	0.80	122.4	0.222	0.874	ROX 1
ROXs 2	B2 C	2002, May 24	347.1	0.42	0.57	345.5	0.424	0.598	
WLY 2-2	B2 C	2002, May 24	77.6	0.42	0.13	78.6	0.426	0.132	
ROXs 5	A1	1993 / 1994	≈ 130	≈ 0.13	≈ 0.5	327.3	0.176	0.408	H-band
H α 26	K R1	1999, June 1/2	23.8	1.15	0.9	25.8	1.135	0.846	
H α 28	R1	1991 / 1992	358	5.1	0.06	357.8	5.209	0.047	Gunn z
VSSG 27	C	1995 / 1996	68	1.22	0.24	66.8	1.222	0.244	
H α 35	K R1	1999, June 1/2	130.3	2.29	0.3	132.2	2.277	0.272	
GSS37	C K R1	1999, June 1/2	67.0	1.44	0.3	69.5	1.438	0.299	
ROXs 16	A1 C	1995 / 1996	-	-	-	24.2	0.098 ^d	0.357	VSS II-27, triple?
			106	0.57	0.06	105.4	0.577	0.186	
WL 18	B1	1988, June 2/3	293	3.55	0.2	292.4	3.617	0.162	rel. pos. B2
VSSG 3	C	1995 / 1996	47	0.25	0.38	53.8	0.243	0.801	
Elias 30	M1 S2	1992, June 13	175	6.700	0.030	175.6	6.388	0.063	SR 21
WL 20	R2	1990 / 1998	270.1	3.17	0.70 ⁿ	269.9	3.198	0.877	phot. 1990, pos. 1998, mid-IR
			232.2	3.66	0.07 ⁿ	232.3	3.619	0.071	
VSSG 25	C	1995 / 1996	356	0.46	0.5	173.3	0.468	0.887	WL 13
WLY 2-44	CHS2 T	1997	81	0.27	-	246.6	0.256	0.204	

Table 5.3: (continued)

VSSG 17	C	1995 / 1996	269	0.25	0.2	260.2	0.242	0.644	
SR 9	B2 G1 G2	1990, July 9	350	0.59	0.09	353.3	0.638	0.057	
VSSG 14	S2	1992, June 13	89 ^P	0.101 ^{d,P}	0.5	83.6	0.130	0.296	
ROXs 31	A1 C S1 S2	1986 / 1991	262	0.480	0.8	251.3	0.396	0.655	
ROXs 42B	S2	1992, June/July	89 ^P	0.056 ^{d,P}	0.8	157.9	0.083 ^d	0.350	new triple
			-	-	-	268.0	1.137	0.002	
ROXs 42C	B2 G2 M2	1990, July 8	135	0.157	0.25	151.0	0.277	0.220	
ROXs 43 A/B	A1 M1 R1 S2	1992, July 11	7	4.800	0.44	11.9	4.523	0.445	
H α 71	K S2	1999, June 1/2	35.0	3.56	0.17	35.0	3.560	0.151	calibrator
L1689 - IRS 5	H	2001, July 11	240.3	2.92	0.61	241.2	3.006	0.277	new triple
			-	-	-	84.4	0.140	0.946	
DoAr 51	B2	2002, May 24	80.8	0.79	0.2	79.3	0.784	0.228	ROXs 47A
A1: Ageorges et al. (1997)		A2: Aitken & Doolittle (1932)			B1: Barsony et al. (1989)				
B2: Barsony et al. (2003)		C: Costa et al. (2000)			G1: Geoffray & Monin (2001)				
G2: Ghez et al. (1993)		H: Haisch et al. (2002)			K: Koresko (2002)				
M1: 2MASS		M2: Mathieu et al. (1989)			R1: Reipurth & Zinnecker (1993)				
R2: Ressler & Barsony (2001)		R3: Richichi et al. (1994)			S1: Simon et al. (1987)				
S2: Simon et al. (1995)		T: Terebey et al. (2001)							
d: below our diffraction limit		m: mod 180 deg							
n: non-photometric conditions		P: projected values							

with equal fluxes. They are visible as a elongated structure in the shift-and-add images and are very prominent in the visibility. Unfortunately, a probable third component of ROXs 16 is too close to distinguish between an elongated structure and a point source. Although the binary parameters derived in our analysis are in general very similar to those provided by the papers used as references in Table 5.3, some important differences exist. The position angles of the binaries ROXs 5, VSSG 25 and IRS 44 have changed approximately 180° since the last observations. Due to the fact that the separations did not change either the flux ratio has changed significantly or the measurements suffer from the 180° ambiguity. Furthermore, some flux ratios have changed at least by a factor of two: ROXs 16 (maybe mainly an effect of the probable new companion), VSSG 3, Elias 30, VSSG 17, and the close companion of ROXs 42B. Finally, the relative positions of the companions orbiting SR 2 and ROXs 42C have changed significantly.

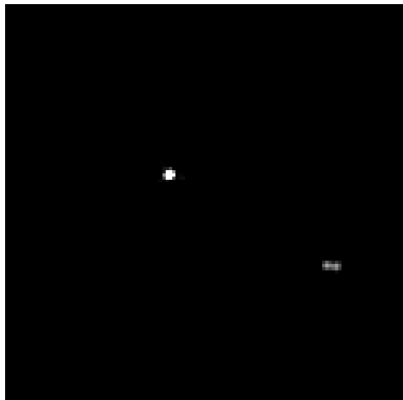


Figure 5.13: The reconstructed image of the newly detected triple system L1689-IRS 5. The known companion has been resolved into two stars.

5.4 Additional Sources

During our speckle observations we recorded 12 sources not part of our sample (see Table 5.4). BKL T J162637-241602 has been observed by chance due to its location close to BKL T J162636-241554. Although VSS 28 is probably not a member of the Ophiuchus molecular clouds, we observed it with speckle techniques, because the area around VSS 28 has been used to determine the background density. While DoAr 58 was listed as HBC 269 in Herbig & Kameswara Rao (1972), it has been removed in the third edition of this catalogue (Herbig & Bell, 1988). The remaining objects are either background giants or foreground dwarves.

VSS 28 is a binary that has been observed with a separation of $0.344'' \pm 0.005''$ at a position angle of $308.3^\circ \pm 0.7^\circ$ in the night following the 4th of July 2001. The flux ratio of the two components is 0.203 ± 0.026 and at a distance of $0.15''$ ($0.50''$) from the main component companions with flux ratios larger than 0.07 (0.04) can be excluded. Another binary is GY 45. The 2MASS images of this source show a very symmetric extension to the south that has been detected in all three wavelength bands. After inspecting the shift-and-add images a shallow glow at the calculated position only 2σ above the background has been found. The parameters of this binary can be derived from the 2MASS survey. The companion resides at a position angle of $168.4^\circ \pm 1.8^\circ$ with a separation of $4.977'' \pm 0.144''$ and a flux ratio of 0.017 ± 0.003 . In our speckle data obtained at the 17th June 2000 companions brighter than 0.04 (0.03) times the flux of the primary can be excluded at a distance of $0.15''$ ($0.50''$) from the main component. All the remaining ten sources are single stars.

Table 5.4: Additional sources

Object	J2000.0		K ₂ MASS [mag]	Date	0.15 [$''$]	0.50 [$''$]	Remarks
	α	δ					
GY 45	16 26 29.98	-24 38 42.8	8.367	2000, June 17	0.04	0.03	binary, background giant (Luhman & Rieke, 1999)
GY 65	16 26 32.91	-24 36 26.4	8.996	2000, June 17	0.08	0.05	background giant (Luhman & Rieke, 1999)
J162637-241602	16 26 37.13	-24 15 59.9	10.757	2001, July 3	0.15	0.08	too faint
VSS 28	16 26 52.80	-23 43 12.7	6.702	2001, July 4	0.07	0.04	binary, not a member, backgr. determination
VSSG 6	16 26 53.86	-24 22 28.0	9.827	2000, June 21	0.09	0.04	background giant (Luhman & Rieke, 1999)
GY 232	16 27 13.26	-24 41 33.7	9.592	2000, June 21	0.10	0.07	background giant (Luhman & Rieke, 1999)
VSSG 13	16 27 46.69	-24 23 22.1	7.270	2000, June 21	0.03	0.02	field star (Elias, 1978)
GY 411	16 27 57.89	-24 37 49.0	9.560	2000, June 21	0.07	0.03	background giant (Luhman & Rieke, 1999)
VSSG 16	16 28 03.73	-24 26 32.0	6.504	2000, June 17	0.04	0.03	field star (Elias, 1978)
VSSG 15	16 28 09.23	-24 23 20.7	7.140	2000, June 21	0.07	0.03	field star (Elias, 1978)
ROXs 47B	16 32 23.28	-24 40 18.5	8.581	2000, June 22	0.04	0.04	foreground (Bouvier & Appenzeller, 1992)
DoAr 58	16 34 26.70	-24 13 43.7	7.707	2001, July 4	0.15	0.04	HBC 269, deleted in Herbig & Bell (1988)

5.5 Summary

- We presented a volume-limited multiplicity survey with magnitude cut-off ($m_K \leq 10.5$ mag) of 158 young stellar objects located within or in the vicinity of the ρ Ophiuchi Dark Cloud (L1688). The survey covers separations between $0.13''$ (diffraction limit) and $6.4''$ (background contamination) and is complete for flux ratios ≥ 0.1 ($\Delta m_K \leq 2.5$) at the diffraction limit. A restricted sample has been defined that is complete and excludes all uncertain cloud members.
- The detection limit is $m_K \approx 14$ mag, and the stellar background density at this brightness is $\approx 1.5 \cdot 10^{-4}$ arcsec $^{-2}$
- Among the 147 targets newly observed with speckle techniques in the K-band we found 48 companions (40 binary and 4 triple systems). Five of these companions are below the diffraction limit of the telescopes and thus only marginally resolved. From the remaining 43 companions (39 binary and 2 triple systems) 14 are new detections including a third component in the previously known binary systems ROXs 42B and the resolution of the previously known companion of L1689-IRS 5 into two sources.
- The surface density of the companions Σ as a function of the separation θ can be well fitted by the power law $\Sigma(\theta) \propto \theta^{-2.13 \pm 0.07}$.
- Within the range $0.13'' \leq \theta \leq 6.4''$ our multiplicity is $(29.1 \pm 4.3)\%$ for the total and $(26.6 \pm 4.4)\%$ for the restricted sample.
- This value is 1.24 ± 0.31 times the main-sequence value, 1.13 ± 0.30 respectively. The close similarity between Taurus and Ophiuchus found in most previous surveys is questioned by our result, which is based on a larger and more complete sample.
- The idea that the observed duplicity in star-forming regions is governed by some process related to the density of the stellar environment gets global support from our observations. This process has been suggested earlier to be related to the formation process or to dynamical interaction afterwards. Observations like those of Duchêne (1999) and Haisch et al. (2002) tend to favour the second scenario. Our data are not sensitive to this alternative.
- There seems to be a relation between infrared classes and binary fraction. Class II objects have a multiplicity twice that of class III objects. This relation has not been found in the Taurus-Auriga survey (Köhler & Leinert, 1998).
- Our results find their place in the paradigm of originally very high multiplicity of young stellar objects that then is reduced by dynamical interactions to different degrees in environments of different densities. This may be the global picture, however, locally within our sample we see no significant difference between the ρ Ophiuchi Dark Cloud (L1688) and its less dense environment. Only the differences between class II and class III sources may point to evolution.

- A population of close binaries with low flux ratios not present in Taurus may be a partial answer to the question why the multiplicity in Taurus-Auriga is higher than in Ophiuchus.

Chapter 6

The Triple System LHS 1070

‘Then there’s a travelling company
of dwarves going West come in this
evening.’

6.1 Properties of a Cosmic Neighbour

Leinert et al. (1994) observed as part of their near-infrared speckle survey for duplicity of nearby southern M dwarves the M5.5V star LHS 1070. By using the SHARP camera mounted on the NTT they detected in 1993 two companions 1.1" and 1.3" north of the primary. In a consecutive measurement the companions exhibited an orbital motion around each other and around the primary while following the proper motion of the system (0.61"/yr). This turned LHS 1070 into a known triple system. The trigonometric parallax has been measured by Altena et al. (1995). They found a value of $0.1353'' \pm 0.0121''$. Due to the proximity of LHS 1070, the orbital periods are about twenty years for the close orbit and about a century for the wide orbit.

When comparing the colours of the components, the companions appear redder than the primary. Based on the absolute brightnesses of the stars in the K-band and the dynamics of the system, first estimations lead to a mass of about $0.10 M_{\odot}$ for the primary and approximately $0.08 M_{\odot}$ for each of the two companions. The masses of LHS 1070 B and C are thus close to the hydrogen burning limit that divides brown dwarves from main-sequence stars. This mass range is characterised by a strong decrease of the effective temperature and the onset of dust formation in the atmospheres. Photometric and spectroscopic measurements with the Hubble Space Telescope in the visual indeed found signatures of dust (Leinert et al., 2000). Also the low masses could be confirmed. The spectral classifications of the companions are M8.5V and M9-9.5V. The main difference between the otherwise very similar components B and C is the higher activity of component B maybe related to the higher temperature or a different rotation period. The primary has an earlier spectral type of M5.5-6V. According to the spectra, the age of the system is several gigayears. Kinematic

measurements (Basri & Marcy, 1995) associate LHS 1070 with the old disk population.

The companions provide the possibility to refine the models of main-sequence stars close to the transition region to brown dwarves. It is thus very important to derive the exact masses of the stars. The short orbital period is very well suited to allow a dynamical mass determination. This method has the advantage of being independent from theoretical models.

6.2 Adaptive Optics

When using ground-based telescopes, speckle techniques (Chapter 4) and/or adaptive optics systems are required to separate the three components of LHS-1070. While speckle observations are *passive* in the sense that the distortions of the wavefront are merely recorded, adaptive optics systems allow an *active* correction of them. This allows integration times that are significantly longer than the coherence time τ_0 (Section 3.5).

Over the last decades adaptive optics systems became very common and are used on almost all observatories today. Their general design is illustrated in Fig. 6.1. The wavefront distortions are measured with a so-called *wavefront sensor*. Very often a *Shack-Hartmann sensor* is used. It consists of a lenslet array that samples the incoming wavefront. Each lenslet forms an image of the object and the displacement of the image gives an estimate of the wavefront slope at that lenslet. Shack-Hartmann sensors work with white light, very faint stars, and moderately extended sources. A real-time computer processes the measurements of the wavefront sensor and adjusts a deformable mirror to compensate the distortions of the incoming wavefront. This is done very often by moving piezoelectric actuators on which the mirror is mounted.

The quality of an image obtained with an adaptive optics system can be mathematically checked by determining the Strehl ratio S , basically the ratio between the peak intensities of an aberrated and a diffraction-limited image of a point-source obtained with the same aperture. For a circular aperture it is defined in spherical coordinates (ρ, θ) by

$$S = \frac{1}{\pi^2} \left| \int_0^1 \int_0^{2\pi} \rho \, d\rho \, d\theta \, e^{ik\psi(\rho, \theta)} \right|^2, \quad (6.1)$$

where the integration is performed over the incoming wavefront. The aberration function $\psi(\rho, \theta)$ describes the wavefront distortion and is measured in units of length (Quirrenbach, 1999). The Strehl ratio varies between 0 and 1. It becomes unity for a constant ψ and is very small for a strongly varying ψ . From (6.1) it becomes clear that the Strehl ratio tends to be larger for longer wavelengths (smaller k). In the case of atmospheric turbulence, only the statistical properties of ψ are known. If the root mean-square wavefront error $D_\phi \equiv kD_\psi$ is smaller than about 2 rad, S can be approximated by the so-called *extended Maréchal approximation* (Quirrenbach, 1999):

$$S = \exp(-D_\phi). \quad (6.2)$$

As described in Section 3.4 the mean-square phase variation D_ϕ over an aperture D is $1.03(D/r_0)$. Thus for a telescope with a diameter equal to the Fried parameter r_0 the Strehl ratio is 36%.

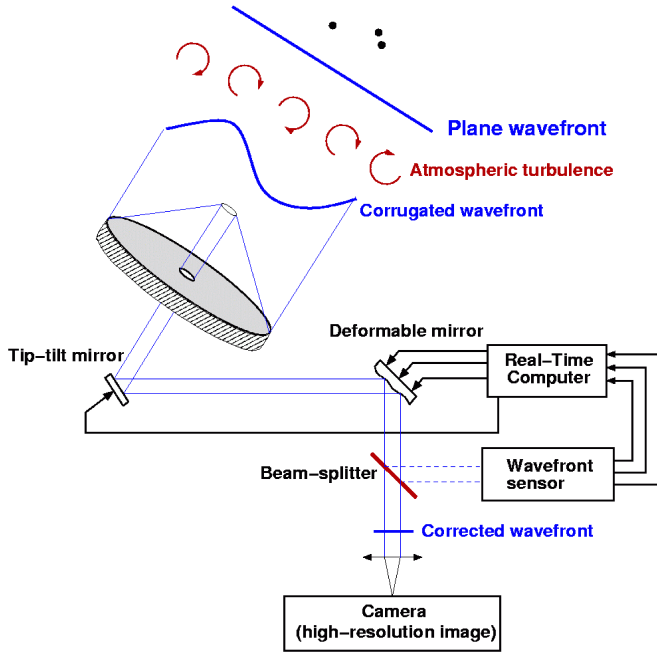


Figure 6.1: Schematic representations of an adaptive optics system (Lidman et al., 2004).

Number of actuators Since there is no need to correct wavefront perturbations on a scale smaller than r_0 , the number of actuators N_0 needed for an adaptive optics system is

$$N_0 \sim \left(\frac{D}{r_0}\right)^2 \propto \lambda^{-\frac{12}{5}} (\cos \zeta)^{-\frac{6}{5}}. \quad (6.3)$$

For the right side (3.20) has been used. Inserting (3.22) into (6.2) and using the above relation leads to

$$S \propto \exp \left[- (N_0/N)^{5/6} \right], \quad (6.4)$$

where N is the number of actuators actually used.

Time Delay The time delay allowed for the measurement, processing, and correction of the distortions is directly proportional to the coherence time τ_0 introduced in Section 3.5:

$$\tau_0 = r_0/v \propto \lambda^{\frac{6}{5}} (\cos \zeta)^{\frac{3}{5}}. \quad (6.5)$$

By using again (3.22) one finds

$$S \propto \exp \left[- (\tau/\tau_0)^{5/3} \right]. \quad (6.6)$$

Reference Source The brightness of the reference source used to determine the wavefront distortion is very important for the performance of an adaptive optics system. If off-axis-guiding is allowed, the separation between the reference

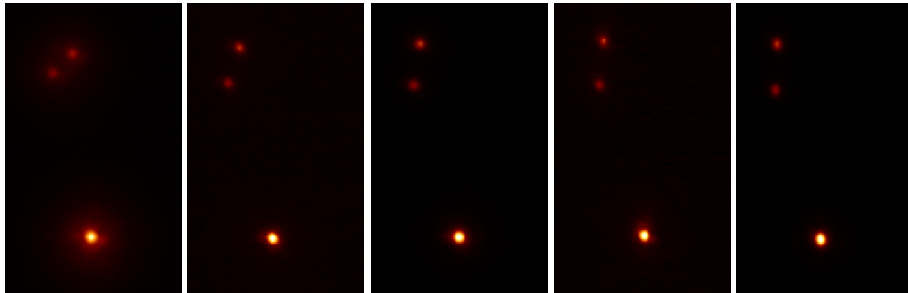


Figure 6.2: The five observations of LHS 1070 performed with the adaptive optics system NAOS/CONICA in the K-band: Dec. 2001, Dec. 2002, Jun. 2003, and Sep. 2003, and Dec. 2003 (from left to right). North is up and east is left.

source and the scientific target should be smaller than the isoplanatic angle described in Section 3.6:

$$\theta_0 \propto \lambda^{\frac{6}{5}} (\cos \zeta)^{\frac{8}{5}}. \quad (6.7)$$

With (3.28) follows

$$S \propto \exp \left[-(\theta/\theta_0)^{5/3} \right]. \quad (6.8)$$

In Fig. 6.2 five images of LHS 1070 obtained in the K-band with the near-infrared adaptive optics system NAOS/CONICA mounted at the Nasmyth focus of *Yepun*, i.e. one of the four 8 m *Unit Telescopes* (UT) at the *Very Large Telescope* (VLT, ESO, Cerro Paranal, Chile), are displayed. NAOS the adaptive optics part that delivers the corrected wavefront to the near-infrared camera system CONICA is equipped with Shack-Hartmann sensors both for the visible and the near-infrared regime. Up to 144 subapertures are available to determine the wavefront distortions and 185 actuators manipulate the deformable mirror. Reference sources with a brightness of up to 16 mag in the visual or 12 mag in the near-infrared and at separations up to 55 arcsec from the science target can be used.

Under moderate seeing conditions ($0.8''$), at an airmass of 1.2, and for an on-axis reference star with $V=10$ mag Strehl ratios of almost 50% can be reached in the K-band (Lidman et al., 2004). Bad seeing conditions of $1.2''$ degrade the Strehl ratio to 32%. When solely decreasing the brightness of the reference source to 13 mag the Strehl ratio is still 26%. The highest influence comes from the isoplanatic angle. A reference source separated by $30''$ leads to a Strehl ratio of only 9%, although a moderate seeing of ($0.8''$) and a bright reference source ($V=10$ mag) has been taken into account.

A small pixel-scale is needed to record the images. Therefore, CONICA offers a $1k \times 1k$ chip with a pixel scale less than 14 mas when using the high resolution camera (Fig. 6.2). The diffraction limit in the K-band is four times larger.

Table 6.1: Relative positions of the three components of LHS 1070 reported in Leinert et al. (2001)

Datum	Telescope	Instrument	d_{AB} ["]	ϕ_{AB} [deg]	d_{AC} ["]	ϕ_{AC} [deg]	d_{BC} ["]	ϕ_{BC} [deg]
29-07-1993	ESO, NTT	SHARP I	1.072 ± 0.010	351.4 ± 0.3	1.322 ± 0.012	346.9 ± 0.3	0.266 ± 0.005	328.5 ± 0.7
01-05-1994	ESO, NTT	SHARP I	1.085 ± 0.004	352.3 ± 0.1	1.425 ± 0.004	351.0 ± 0.1	0.341 ± 0.005	346.9 ± 0.6
15-09-1994	MPIA, 3.5 m	BlueMAGIC	1.092 ± 0.009	352.8 ± 0.4	1.467 ± 0.011	352.8 ± 0.4	0.375 ± 0.004	352.7 ± 0.6
24-09-1994	ESO, 3.6 m	ADONIS/SHARP II	1.095 ± 0.012	353.2 ± 0.4	1.477 ± 0.013	353.4 ± 0.4	0.382 ± 0.005	353.9 ± 0.7
17-01-1995	ESO, 3.6 m	ADONIS/SHARP II	1.094 ± 0.006	353.8 ± 0.3	1.494 ± 0.007	354.4 ± 0.3	0.400 ± 0.008	356.1 ± 0.4
09-07-1995	ESO, NTT	SHARP I	1.119 ± 0.011	353.6 ± 0.1	1.553 ± 0.011	356.3 ± 0.1	0.439 ± 0.004	3.2 ± 0.1
14-07-1995	HST	WFPC2	1.102 ± 0.003	353.9 ± 0.1	1.534 ± 0.003	356.7 ± 0.1	0.436 ± 0.001	3.7 ± 0.2
16-01-1996	ESO, 3.6 m	ADONIS/SHARP II	1.124 ± 0.002	354.4 ± 0.3	1.572 ± 0.003	358.6 ± 0.3	0.459 ± 0.003	9.0 ± 0.3
22-08-1996	ESO, 3.6 m	ADONIS/SHARP II	1.161 ± 0.005	355.0 ± 0.1	1.606 ± 0.006	0.6 ± 0.1	0.465 ± 0.003	14.9 ± 0.1
27-09-1996	MPIA, 3.5 m	BlueMAGIC	1.157 ± 0.008	355.3 ± 0.1	1.603 ± 0.012	1.2 ± 0.1	0.468 ± 0.004	15.8 ± 0.1
15-07-1997	ESO, NTT	SHARP I	1.235 ± 0.014	356.5 ± 0.2	1.656 ± 0.019	3.7 ± 0.3	0.458 ± 0.006	23.4 ± 0.6
25-08-1997	ESO, 3.6 m	ADONIS/COMIC	1.243 ± 0.007	356.5 ± 0.2	1.652 ± 0.010	4.1 ± 0.2	0.450 ± 0.015	25.4 ± 1.0
17-11-1997	MPIA, 3.5 m	BlueMAGIC	1.223 ± 0.005	357.1 ± 0.1	1.620 ± 0.008	4.8 ± 0.1	0.439 ± 0.008	26.5 ± 0.5
02-01-1998	HST	NICMOS	1.260 ± 0.003	357.5 ± 0.1	1.646 ± 0.003	5.2 ± 0.1	0.432 ± 0.003	28.0 ± 0.5
07-05-1998	ESO, NTT	SHARP I	1.281 ± 0.007	358.1 ± 0.1	1.634 ± 0.009	6.2 ± 0.1	0.408 ± 0.008	32.3 ± 0.7
10-10-1998	MPIA, 3.5 m	Ω -Cass	1.332 ± 0.008	359.0 ± 0.1	1.641 ± 0.010	7.3 ± 0.1	0.377 ± 0.019	38.2 ± 0.5
18-06-1999	ESO, NTT	SHARP I	1.404 ± 0.003	0.4 ± 0.1	1.631 ± 0.003	8.9 ± 0.1	0.318 ± 0.002	49.4 ± 0.4
03-08-1999	MPIA, 3.5 m	Ω -Cass	1.407 ± 0.007	1.0 ± 0.3	1.615 ± 0.007	9.4 ± 0.3	0.303 ± 0.007	52.1 ± 0.3
01-09-1999	MPIA, 3.5 m	Ω -Cass	1.414 ± 0.004	1.2 ± 0.2	1.605 ± 0.006	9.6 ± 0.3	0.292 ± 0.008	54.6 ± 1.0
23-11-1999	MPIA, 3.5 m	Ω -Cass	1.437 ± 0.004	1.6 ± 0.1	1.600 ± 0.003	10.2 ± 0.2	0.279 ± 0.005	60.1 ± 0.9
04-06-2000	ESO, 3.6 m	ADONIS/SHARP II					0.240 ± 0.002	76.0 ± 0.4
20-06-2000	ESO, NTT	SHARP I	1.518 ± 0.003	3.6 ± 0.3	1.588 ± 0.004	12.0 ± 0.3	0.237 ± 0.003	80.8 ± 0.7

Table 6.2: New measurements of the relative positions of the three components of LHS 1070

Datum	Telescope	Instrument	d_{AB} ["]	ϕ_{AB} [deg]	d_{AC} ["]	ϕ_{AC} [deg]	d_{BC} ["]	ϕ_{BC} [deg]
31-10-2000	MPIA, 3.5 m	Ω -Cass	1.516 ± 0.003	4.4 ± 0.1	1.543 ± 0.003	12.5 ± 0.1	0.218 ± 0.003	91.1 ± 1.0
01-11-2000	MPIA, 3.5 m	Ω -Cass	1.517 ± 0.003	4.4 ± 0.1	1.546 ± 0.005	12.4 ± 0.3	0.218 ± 0.007	90.8 ± 1.5
09-01-2001	ESO, 3.6 m	ADONIS/SHARP II	1.546 ± 0.006	4.7 ± 0.2	1.540 ± 0.006	12.8 ± 0.2	0.219 ± 0.009	100.4 ± 2.3
29-06-2001	ESO, NTT	SHARP I	1.603 ± 0.003	5.3 ± 0.1	1.524 ± 0.003	13.0 ± 0.1	0.222 ± 0.004	119.8 ± 1.2
02-07-2001	ESO, NTT	SHARP I	1.602 ± 0.003	5.4 ± 0.1	1.522 ± 0.003	13.0 ± 0.1	0.223 ± 0.004	120.1 ± 1.2
05-07-2001	ESO, NTT	SHARP I	1.602 ± 0.003	5.4 ± 0.1	1.520 ± 0.003	13.0 ± 0.1	0.223 ± 0.004	120.7 ± 1.2
06-07-2001	ESO, NTT	SHARP I	1.608 ± 0.004	5.4 ± 0.1	1.526 ± 0.003	13.1 ± 0.1	0.225 ± 0.004	120.6 ± 1.2
06-12-2001	ESO, UT4	NAOS/CONICA	1.632 ± 0.002	6.8 ± 0.2	1.489 ± 0.002	14.1 ± 0.2	0.245 ± 0.001	136.0 ± 0.2
11-12-2001	ESO, 3.6 m	ADONIS/SHARP II	1.633 ± 0.003	7.1 ± 0.2	1.487 ± 0.003	14.4 ± 0.2	0.247 ± 0.006	136.8 ± 1.2
19-10-2002	MPIA, 3.5 m	Ω -Cass	1.709 ± 0.01	9.4 ± 0.5	1.446 ± 0.01	15.4 ± 0.5	0.310 ± 0.02	160.4 ± 3.4
16-12-2002	ESO, UT4	NAOS/CONICA	1.716 ± 0.002	9.6 ± 0.1	1.432 ± 0.001	15.5 ± 0.1	0.329 ± 0.001	162.6 ± 0.1
11-06-2003	ESO, UT4	NAOS/CONICA	1.758 ± 0.007	11.4 ± 0.1	1.414 ± 0.005	16.5 ± 0.1	0.372 ± 0.001	171.3 ± 0.1
05-09-2003	ESO, UT4	NAOS/CONICA ^a	1.771 ± 0.007	11.8 ± 0.1	1.403 ± 0.005	16.5 ± 0.1	0.391 ± 0.001	174.4 ± 0.1
12-12-2003	ESO, UT4	NAOS/CONICA	1.783 ± 0.003	12.4 ± 0.1	1.391 ± 0.002	16.7 ± 0.1	0.409 ± 0.001	177.9 ± 0.1

^a: Orientation and pixel scale have been interpolated.

6.3 Data Reduction

Our astrometric measurements of the relative positions of the individual components are summarised in Tab. 6.1 and Tab. 6.2. They have been performed at various observatories over the last decade by using speckle techniques and/or adaptive optics systems. The speckle data as well as the adaptive optics supported speckle data have been reduced in the same way that was described in Chapter 4. In the adaptive optics images the positions of the three components have been derived by using the IDL programme *Starfinder*. It is designed to determine the positions of stars by fitting a typical point-spread-function of a reference star. This is necessary, because the point-spread-function produced by an adaptive optics system shows an artificial halo caused by the corrections of the distorted wavefront. This halo surrounds the diffraction-limited core. Here always the point-spread-function of LHS 1070 A has been chosen as reference for the programme. It is located close enough to the two other components

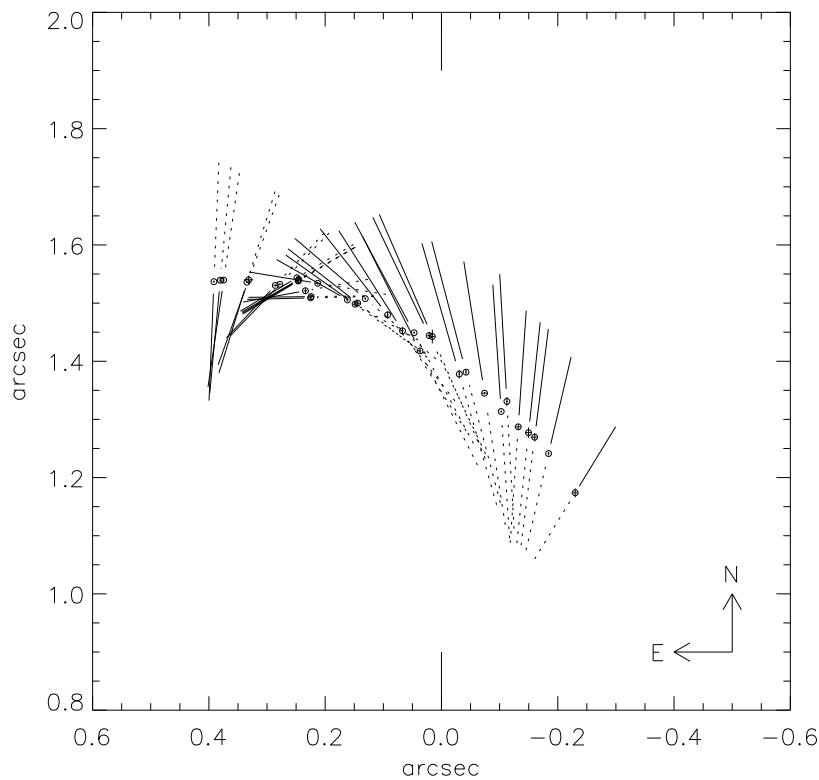


Figure 6.3: The counterclockwise orbital motion of the two low-mass components B and C around each other and around the primary A. The main component has been placed in the origin of the coordinate system. The dotted lines end at the position of component B, while the solid lines end at the position of component C. The lines originate in the photometric (geometric) centres of the BC-system. They are marked by circles with a radius of 5 mas. The very small errorbars are overplotted.

to reside within the same isoplanatic patch, but wide enough to show a single point-spread-function not mixed with those of LHS 1070 B or C. Finally, the orientation and pixelscale of the cameras have been derived by analysing images of the Trapezium or the Galactic Center taken with the same instrument configuration. Again the astrometric software `ASTROM` has been used (Section 4.4.2).

6.4 Orbital Motion

The orbital motions of the individual components of LHS 1070 are visualised in Fig. 6.3, where the proper motion of the whole system has been removed by plotting positions relative to component A. The rapid rotation of the low-mass components around their geometric and probably gravitational centre while co-moving on their orbit around the primary is well sampled.

In Fig. 6.4 the relative positions of component C with respect to component B

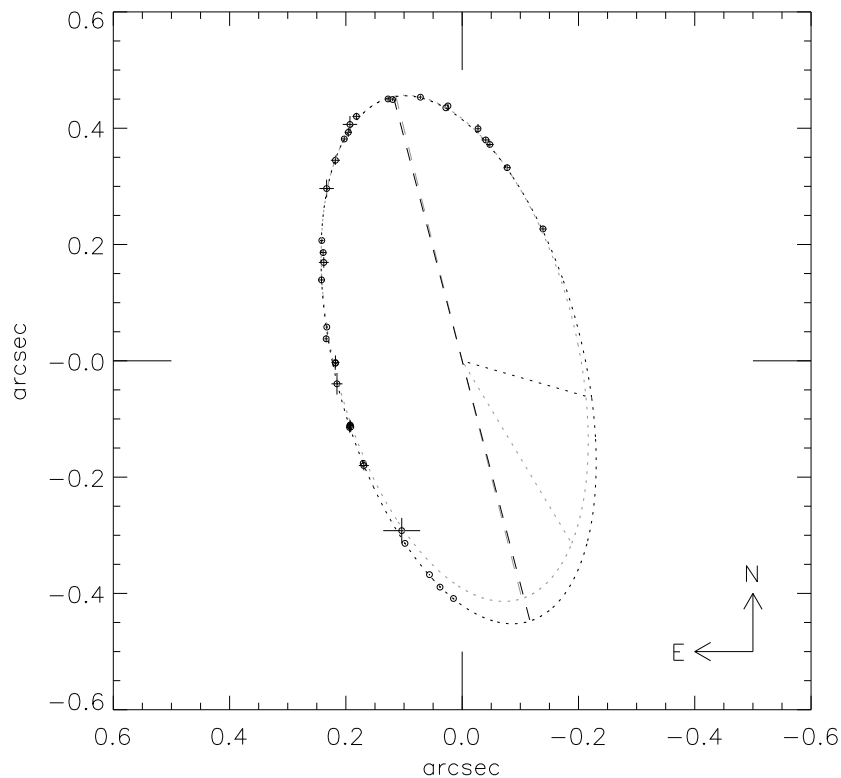


Figure 6.4: The orbit of component C around component B. LHS 1070 B has been put to the origin of the coordinate system. The 36 observations are marked by circles with a radius of 5 mas. Overplotted are the errorbars. The newly fitted orbit is plotted in black. The dotted line from the centre to the orbit marks the position of the periastron. The hatched line represents the line of knots. The previously fitted orbit (Leinert et al., 2001) based on 22 measurements is underlaid in grey to allow a comparison.

are displayed. Now the orbital motion of the low-mass companions around each other is obvious. The gravitational force of the primary can be ignored when assuming that it acts equally strong on both components. Leinert et al. (2001) determined the orbital elements of this close orbit from the first 22 measurements (Tab. 6.1). They found an almost circular, highly inclined orbit (Tab. 6.3 & Fig. 6.4).

After including the new measurements (Tab. 6.2) it seems meaningful to recalculate the orbit, because the recent results with NAOS/CONICA were not covered good enough. Therefore, the astrometric measurements were sent to H. Jahreiß (ARI, Heidelberg), who already did the old fit. The values he derived are given in Tab. 6.4. With exception of the periastron that is not significant for a very small eccentricity, the new values are well within the errorbars found for the old orbital fit. Since the new *jackknife*-errors are smaller than the old ones, we have reduced the allowed parameter space significantly. In Tab. 6.5 the observed positions are compared with the fit.

Table 6.3: Orbital parameters derived from the fit of the first 22 measurements (Leinert et al., 2001). This orbit is plotted in Fig. 6.4 in grey.

Parameter		Value	Error
semi-major axis a	[arcsec]	0.446	0.029
eccentricity e		0.064	0.063
inclination i	[deg]	62.1	1.5
line of knots Ω	[deg]	14.1	0.6
periastron ω	[deg]	213	26
period P	[yr]	16.1	1.4
periastron passage T_0		1990.2	0.7

Table 6.4: New orbital fit derived by H. Jahreiß (ARI, Heidelberg). This orbit is plotted in Fig. 6.4 in black.

Parameter		Value	Error
semi-major axis a	[arcsec]	0.466	0.017
eccentricity e		0.027	0.009
inclination i	[deg]	62.9	0.2
line of knots Ω	[deg]	14.6	0.3
periastron ω	[deg]	255	6
period P	[yr]	17.2	0.2
periastron passage T_0		1991.7	0.3

Table 6.5: Relative cartesian positions of component C with respect to component B. The observed positions are compared with the positions calculated from the new orbital elements.

Epoch	X _{obs}	Y _{obs}	X _{cal}	Y _{cal}	ΔX	ΔY
1993.567	0.227	-0.139	0.232	-0.134	-0.005	-0.005
1994.332	0.332	-0.077	0.332	-0.075	0.000	-0.002
1994.707	0.372	-0.048	0.372	-0.044	0.000	-0.004
1994.732	0.380	-0.041	0.375	-0.042	0.005	0.001
1995.046	0.399	-0.027	0.402	-0.015	-0.003	-0.012
1995.520	0.438	0.025	0.433	0.026	0.005	-0.002
1995.534	0.435	0.028	0.434	0.028	0.001	0.001
1996.033	0.453	0.072	0.452	0.070	0.001	0.002
1996.642	0.449	0.120	0.454	0.118	-0.005	0.001
1996.740	0.450	0.127	0.452	0.126	-0.002	0.002
1997.537	0.420	0.182	0.417	0.179	0.003	0.003
1997.649	0.407	0.193	0.410	0.185	-0.003	0.008
1997.879	0.393	0.196	0.392	0.197	0.001	-0.001
1998.005	0.381	0.203	0.381	0.203	0.000	0.000
1998.348	0.345	0.218	0.348	0.218	-0.003	0.000
1998.775	0.296	0.233	0.299	0.231	-0.003	0.002
1999.463	0.207	0.241	0.207	0.242	0.000	-0.001
1999.589	0.186	0.239	0.189	0.243	-0.003	-0.004
1999.668	0.169	0.238	0.177	0.243	-0.008	-0.005
1999.896	0.139	0.242	0.143	0.242	-0.004	0.000
2000.426	0.058	0.233	0.059	0.234	-0.001	-0.001
2000.470	0.038	0.234	0.052	0.233	-0.014	0.001
2000.832	-0.004	0.218	-0.006	0.222	0.001	-0.004
2000.835	-0.003	0.218	-0.006	0.222	0.003	-0.004
2001.024	-0.040	0.215	-0.037	0.215	-0.003	0.000
2001.492	-0.110	0.193	-0.111	0.194	0.001	-0.001
2001.500	-0.112	0.193	-0.112	0.194	0.001	-0.001
2001.508	-0.114	0.192	-0.114	0.193	0.000	-0.001
2001.511	-0.115	0.194	-0.114	0.193	-0.001	0.001
2001.930	-0.176	0.170	-0.178	0.169	0.002	0.001
2001.944	-0.180	0.169	-0.180	0.168	0.000	0.001
2002.798	-0.292	0.104	-0.297	0.109	0.005	-0.005
2002.957	-0.314	0.099	-0.316	0.097	0.002	0.002
2003.441	-0.368	0.056	-0.367	0.058	-0.001	-0.002
2003.677	-0.389	0.038	-0.388	0.038	-0.001	0.000
2003.945	-0.409	0.015	-0.409	0.015	0.000	0.000

6.5 Dynamical Mass Determination

According to Kepler's third law the dynamical mass of the system

$$M_{BC} = M_B + M_C \tag{6.9}$$

in solar masses M_{\odot} can be simply calculated by

$$M_{BC} = \frac{a^3}{P^2}, \quad (6.10)$$

where the semi-major axis a is measured in astronomical units and the period P in years. The orbital fits only determine a in arcsec. Therefore, (6.10) has to be rewritten as

$$M_{BC} = \frac{a^3 d^3}{P^2} \quad (6.11)$$

with the distance d to the system in parsec. The old orbital fit leads to

$$M_{BC} [M_{\odot}] = (0.144 \pm 0.003) \left(\frac{d[\text{pc}]}{7.5} \right)^3. \quad (6.12)$$

Since the parallax of LHS 1070 is not very precisely known, d is measured in the last equation relative to the value $0.1353'' \pm 0.0121''$ (≈ 7.5 pc) listed in Altena et al. (1995).

The relative error of 2% in equation (6.12) is astonishingly small. One would find from a simple error propagation that the uncertainty of the dynamical mass is 25% when ignoring the error in the distance and 36% when it is included. However, such a calculation assumes that the parameters are uncorrelated. This is not the case. For example, a longer period could fit the data only when the semi-major axis becomes larger. When calculating the mass both changes almost cancel out each other (Leinert et al., 2001). The relations between the different parameters thus have to be taken into account to derive the error given in (6.12). This has been done by calculating the dynamical mass of the system while one of the parameters was fixed at a non-optimal value (Leinert et al., 2001).

For the new orbital fit one finds

$$M_{BC} [M_{\odot}] = 0.144 \left(\frac{d[\text{pc}]}{7.5} \right)^3, \quad (6.13)$$

i.e. exactly the same value as for the old fit. This verifies the small error of the dynamical mass numerically derived for (6.12). Since the new orbital fit resides in a subspace of the parameter space occupied by the old orbital elements, it can be assumed that the error of the dynamical mass is less or equal to the value given in (6.12). Even the nominal error from the error propagation calculation is reduced to 11%, 28%, respectively, when the error in the distance is taken into account.

It should be mentioned here that not yet published new measurements of the parallax of LHS 1070 favour a slightly larger distance of about 8 pc (H. Jahreiß, private communication).

Chapter 7

MIDI at the VLTI

‘He lifted his staff and pointed to a high window. There the darkness seemed to clear, and through the opening could be seen, high and far, a patch of shining sky.’

7.1 The Mid-Infrared

In Fig. 7.1 an atmospheric transmission model for the near- and mid-infrared is shown (Lord, 1992). The transmission is characterised by a number of molecular absorption bands, including water vapour at 2.5, 3.1, 6, and 25 μm , ozone at 9.7 μm , carbon dioxide and oxygen at 4.3 and 15 μm , respectively, and methane and nitric oxide at 7.6 μm (Lawrence, 2004). The four atmospheric windows longwards of 2.5 μm are from left to right the L-, M-, N-, and Q-band.

The mid-infrared wavelength range ($\gtrsim 7 \mu\text{m}$) is also called thermal infrared, because according to Wien’s law a blackbody with a temperature of $\sim 300 \text{ K}$ (room temperature) shows a peak emission around 10 μm . The temperatures characteristic for the mid-infrared are thus well below those expected even for cool stars ($\sim 1500 \text{ K}$). Stars are emitting their light mainly at wavelengths in the visual and the near-infrared. The thermal infrared thus traces photons reprocessed in dusty environments, i.e. the dust absorbs the light from a hot stellar source and reemits it at longer wavelengths.

This explains the importance of the N-band (7–13 μm) for the observation and after all for the improvement of our knowledge of a variety of astronomical objects:

- Circumstellar disks around low- and intermediate-mass young stellar objects: these disks are remnants of the protostellar core from which the stars formed and provide important informations on the star formation process. In many cases the stars still accrete from these reservoirs. In the last years their role as active sites of planet formation has been understood.

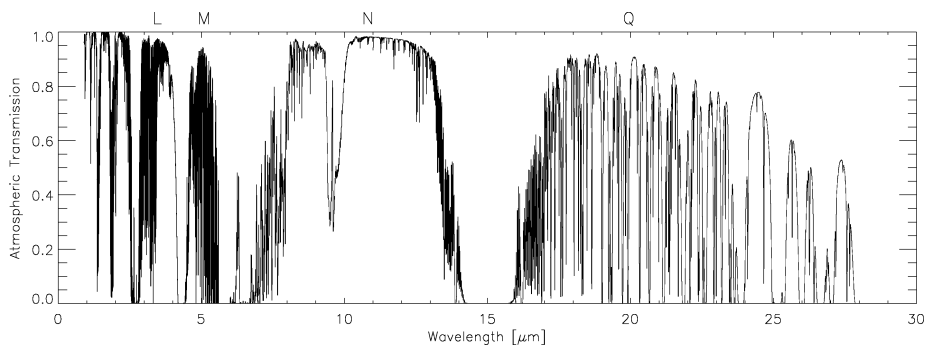


Figure 7.1: Atmospheric transmission in the near- and mid-infrared simulated for Mauna Kea (Hawaii) assuming a water column density of 1.0 mm and an airmass of 1.5 (Lord, 1992). The data are the courtesy of the Gemini Observatory.

- Accretion disks around high mass young stellar objects: while the presence of circumstellar disks around low- and intermediate-mass stars is well established, disks around high-mass stars (spectral type O) are neither theoretically nor observationally proven. It is still unclear, whether the disks can be shielded or shield themselves from the extremely strong stellar winds.
- Envelopes of *Asymptotic Giant Branch* stars: in the ejected envelopes around these evolved stars dust condensates. Since the dust changes the opacity of these outer layers the stars show a strong variability.
- *Active Galactic Nuclei*: The central black holes of *Seyfert galaxies* are surrounded by dusty tori. Different spectral energy distributions occur probably due to different inclination angles of the tori.

Fortunately, the wavelength range of the N-band covers the silicate band and also various bands of polyaromatic carbons. This provides the possibility to study the composition, mineralogy, temperature and the geometrical distribution of the dust (Przygodda, 2004).

On the other hand, there exist some serious limitations in the thermal infrared. The background radiation is a few orders of magnitude higher than the flux from the astronomical object. Each medium that is not totally transparent or perfectly reflecting contributes to it. The atmosphere, the telescope mirror, the support structures, the electronic devices, etc. Furthermore, all optical parts, e.g. windows, filters, and dispersive elements, have to be made of special materials that in some cases seem strange when having their visual properties in mind, e.g. Germanium. Gold is used instead of aluminium to coat the mirrors, because the reflectivity of gold is much higher in the mid-infrared than that of aluminium or silver. Another disadvantage is the limited size and perfection of available detectors for the mid-infrared.

7.2 The Very Large Telescope Interferometer

The list of scientific targets in Section 7.1 shows that their angular diameters are very small. For example the radius of a typical circumstellar disk around a

low-mass young stellar object is of the order of a few AU in the mid-infrared. At the distance of the Taurus or Ophiuchus star forming region (~ 150 pc) this corresponds to a angular diameter of a few tens of milli-arcsec. On the other hand, the resolution of the largest today available telescopes with a diameter of 10 m, i.e. the Keck telescopes at Mauna Kea, Hawaii, is only 200 mas at $10 \mu\text{m}$. The only way to overcome this discrepancy is the usage of telescope arrays that combine the light interferometrically.

Interferometric measurements have been first suggested by Hippolyte Fizeau (Fizeau, 1868). Edouard Stéphan followed this idea and tried to measure stellar diameters at the Marseilles Observatory between 1872 and 1873 (Stéphan, 1873). In close collaboration with Fizeau he found that diameters of stars have to be much smaller than $0.158''$ (Stéphan, 1874). Albert Michelson published the first full mathematical description almost two decades later (Michelson, 1890). Whether this work was done independent from the previous work of Fizeau and Stéphan is still unclear (Lawson, 1999). Afterwards, Michelson performed the first successful measurements when observing the moons of Jupiter (Michelson, 1891). The first measurements of binaries (Schwarzschild, 1896) and the determination of the orbit of Capella (Anderson, 1920) are other important milestones. The first stellar diameter (α Ori) was measured in 1921 with Michelson's famous stellar interferometer at the Mount Wilson observatory (Michelson & Pease, 1921).

Although interferometry has been developed in the visual regime, radio astronomy used it as a well understood standard first. This has been forced by the very limited resolution of single telescopes at radio wavelengths, the moderate requirements on the precision of technical devices used in this regime, and the availability of amplifiers. Today radio astronomers can handle baselines up to the diameter of the earth by recording the signals at different sites independently after synchronising them with a common time basis. Even satellites serving as an additional station can be used. However, in the visual or the infrared regime interferometry remained a tool for experts. Interferometers often designed for a certain kind of astronomical observations never became instruments offered to a broad community.

A first step towards a change of the situation was made when the *Very Large Telescope Interferometer* (VLTI) came into operation in 2001. It is an integral part of the



Figure 7.2: The VLT as seen from a point west of the Residencia.

Very Large Telescope (VLT) built and operated by ESO, the *European Southern Observatory*, at the flattened summit of Cerro Paranal, a mountain with an altitude of 2635 m (Fig. 7.2).

7.2.1 The Site

Cerro Paranal is located in the northern Atacama desert 130 km south of the Chilean city of Antofagasta. Although the Pacific ocean is only at a distance of 12 km from Cerro Paranal and visible by the unaided eye, the Atacama desert is known as one of the regions with the lowest humidity on earth. This is caused by the Humboldt stream transporting cold water from Antarctica to the north. So water vapour in the air coming from the west condensates and the clouds never reach the high altitude parts of the Atacama desert. Another important factor are the Andes serving as a natural barrier to the east. The resulting stable weather conditions with many clear nights of very good seeing make the



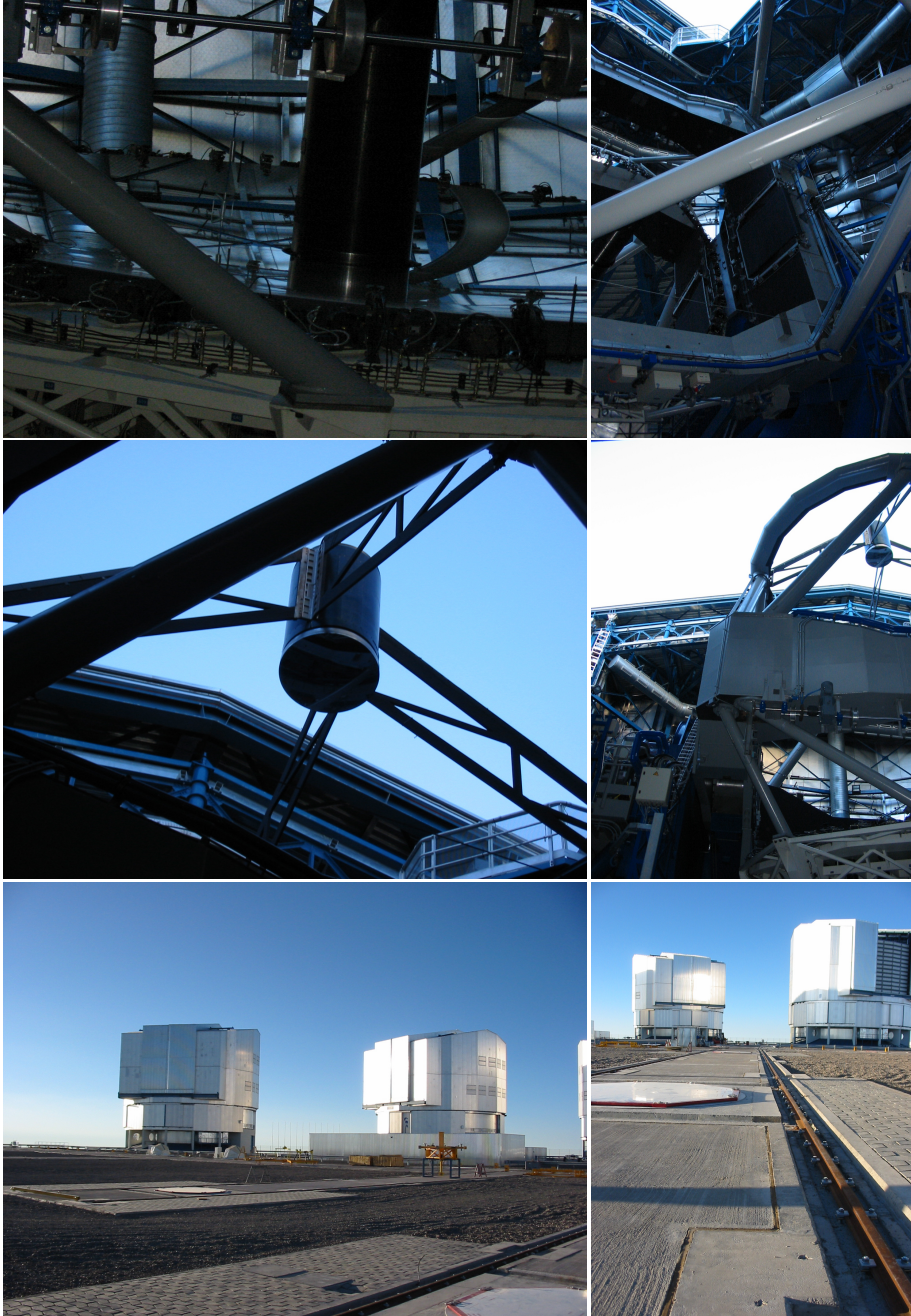
Figure 7.3: The maintenance buildings and the Residencia (white dome) seen from the summit.

Atacama desert to one of the best astronomical sites worldwide. The largest telescopes at southern latitudes are thus located here.

However, due to the hostile conditions in this dry area a large effort is required to support the work of engineers and astronomers. A large maintenance and housing complex thus has been installed below the summit (Fig. 7.3).

Figure 7.4: The images on the right side have been taken during my visit in Dec. 2003. Upper left: The main 8.2 m-mirror of UT4 that is only 175 mm thick. Its shape is actively controlled by 150 actuators. It is made of Zerodur and weights 23 tons. Upper right: The central structure of UT4 with the cover protecting one of the Nasmyth outlets. Middle left: the secondary 1.1 m-mirror of UT4 made of Beryllium. Middle right: The Nasmyth platform of UT4 that is equipped with the adaptive optics system NAOS/CONICA. The structure of the enclosure is visible in the background. Lower left: the enclosures of UT1 and UT2. The interferometric laboratory is shown in front of UT2. Some of the AT-tracks can be identified. The small pyramid-like structures on the left are the covers of the siderostats used for the commissioning of the VLTI. Lower right: This image allows a detailed view of the AT-track in front of UT3 (closed) and UT4 (open). The octagonal cover protects one of the inlets used by the ATs.

7.2. THE VERY LARGE TELESCOPE INTERFEROMETER



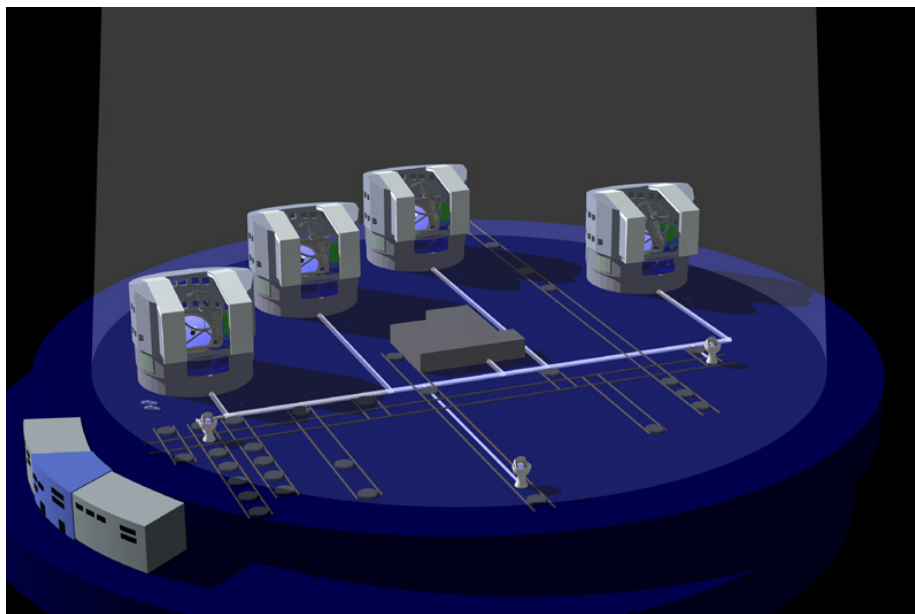


Figure 7.5: Schematic representation of the VLTI components. The VLT control building is located left of the platform (image courtesy of ESO).

7.2.2 The VLTI Grid

A schematic representation of the VLTI grid is given in Fig. 7.5. All telescopes are located on this grid with a spacing of 8 m. The four *Unit Telescopes* (UTs) with their 8.2 m mirrors are fixed at their positions. The six baselines offered by them vary between 47 m and 130 m. The UTs are currently offered to the community both for single telescope and interferometric measurements.

Two *Auxiliary Telescopes* (ATs) with a primary mirror of 1.8 m will become available in 2005. Afterwards, a third and a fourth AT will be integrated. The ATs are dedicated to interferometric measurements only. They are designed to be moved to thirty different positions on the grid. A simple plugging mechanism allows a very fast change of the positions within a few hours. Baseline lengths between 8 m and 200 m will be available.

7.2.3 Feeding the Instruments

The main part of the VLTI is the interferometric laboratory residing underground in the centre of the grid. Although the laboratory is only 20 m \times 7 m to allow a control of the environmental conditions, all interferometric instruments using the light from two or more telescopes are put on optical benches within this laboratory. Also the upcoming second generation of interferometric instruments will be placed here.

The light coming from the *Coudé rooms* (Fig. 7.6) below the telescopes is brought to the central interferometric laboratory by so-called *delaylines*. They are located in the 160 m long and 8 m wide *delayline-tunnel* south of the laboratory. The delaylines do not only transfer the telescope pupils at fixed locations



Figure 7.6: The Coudé room below one of the unit telescopes (image courtesy of ESO).

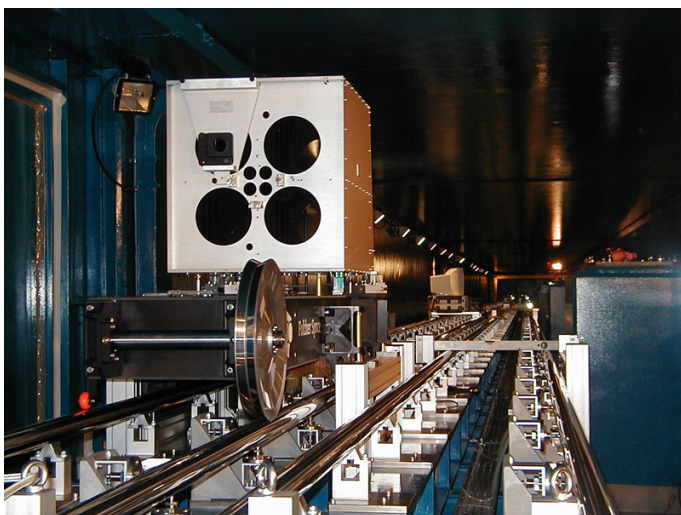


Figure 7.7: A delayline-carriage inside the delayline-tunnel. The retroreflector is mounted inside the white box. The black holes are the inlets and outlets for the beams (image courtesy of ESO).

inside the interferometric laboratory, but also compensate differences in the *optical path lengths* of the beams. Therefore, the *delayline-carriages* (Fig. 7.7) equipped with an retroreflector for two beams can be moved up to 60 m in the delayline-tunnel. So the delaylines cover a range of 120 m in optical path difference each. A velocity of 0.5 m/s allows a fast positioning that can be repeated with an accuracy of $50\ \mu\text{m}$ over the total stroke length, $1\ \mu\text{m}$ over 3 meters of observation stroke length, respectively. This requires a good thermal stability. Nevertheless, a design with evacuated pipes has been rejected due to cost reasons. In the final configuration six delaylines will be available.

7.3 MIDI - VLTI's First Science Instrument

Six years after the first presentation of the instrumental concept to ESO in 1997, the *MID-infrared Interferometric instrument* (MIDI) built by an international collaboration between the Max-Planck-Institute for Astronomy (Heidelberg), ASTRON (Dwingeloo, NL), the Sterrewacht Leiden (NL), the Kiepenheuer-Institute (Freiburg), the Astronomical Institute Amsterdam, DESPA (Meudon, F), and the Observatoire de la Côte d'Azur (Nizza, F) combined successfully two beams coming from two UTs. One year later the observations in the frame of the ESO schedule with objects proposed by the astronomical community started. With this first scientific instrument at the VLTI a new era in astronomy has begun. MIDI operates in the N-band and thus allows an exploration of

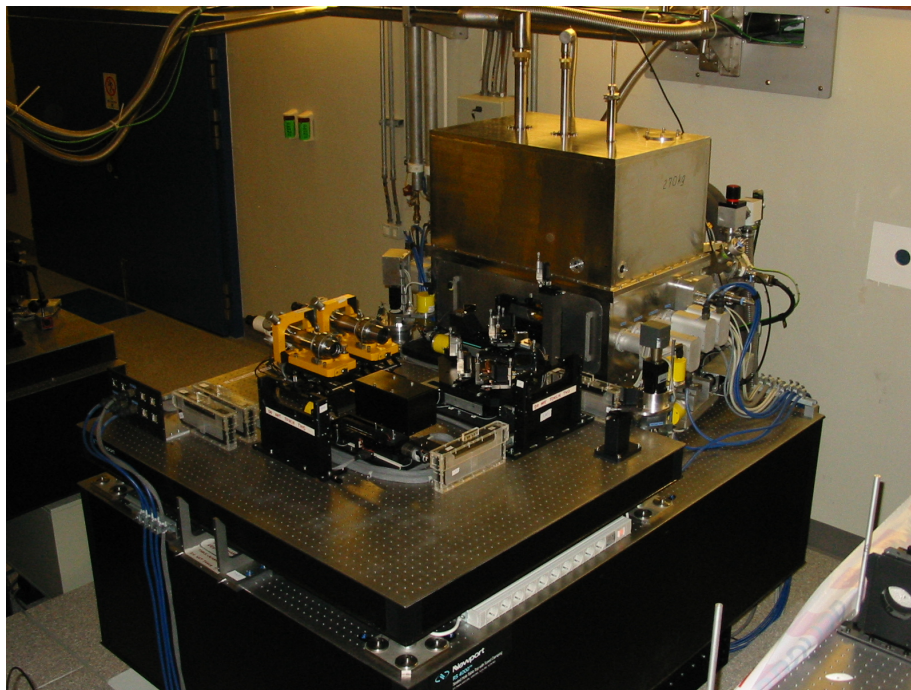


Figure 7.8: MIDI in the interferometric laboratory (image courtesy of ESO).

this wavelength range with an unprecedented resolution. All the science topics discussed in Section 7.1 can now be studied in great detail. Moreover, interferometry at optical wavelengths is turning with MIDI more and more into a standard tool. In this section a short overview of the instrument will be given. How observations are performed will be demonstrated in Chapter 9. The theoretical basis of long-baseline interferometry will be introduced in Chapter 8.

Fig. 7.8 shows MIDI on top of the 60-cm-thick optical bench in the interferometric laboratory. The shining box in the background is a dewar. While the upper half is a tank for liquid nitrogen, the lower half contains those parts of the instrument that are cooled to cryogenic temperatures. These parts are fixed on the *cold optical bench*. In front of the dewar several optical devices can be seen. These parts are mounted on the *warm optical bench*. Both benches can be adjusted to ensure a sufficient alignment of the instrument.

7.3.1 The Warm Optical Bench

The beams from the two telescopes reach the dewar by passing through small delaylines realized by optical elements on the warm optical bench (Fig. 7.9). The two roof mirrors mounted on Piezo stages can be moved by $100\ \mu\text{m}$ each. Since the beams pass two times these delaylines, the optical path length of both beams can be modified by $200\ \mu\text{m}$. If a higher optical delay is needed, one of the Piezo stages can be moved up to 50 mm.

The warm optical bench also offers several possibilities to calibrate the instrument. A blackbody can be moved into the optical path and the light from a CO_2 laser can also be fed to the instrument. The laser itself is mounted out-

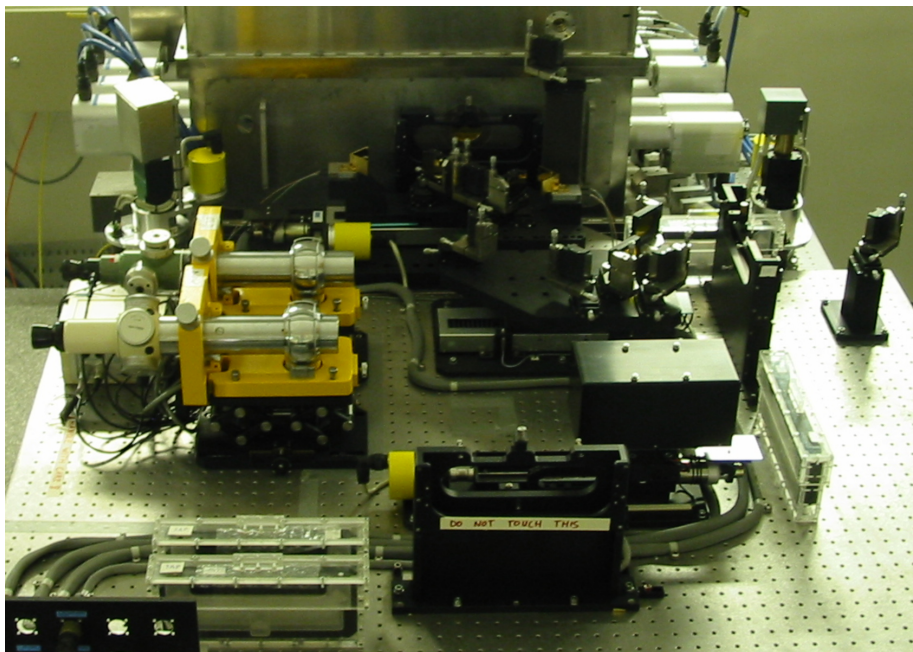


Figure 7.9: Close-up of the warm-optical bench that shows the small golden piezo-mounted roof mirrors (close to the entrance window of the dewar), the alignment telescopes, the blackbody source (black cube), and the CO₂ laser feeding optics (mirrors on the right side). The dewar harbours the cold optics. The closed cycle cooler is attached on the here not visible back side (image courtesy of ESO).

side of the laboratory and the light is brought inside by a window. Two small alignment telescopes are also present on the warm optical bench.

7.3.2 The Cold Optical Bench

After passing the MIDI delaylines the beams enter the dewar through a antireflection-coated ZnSe window. ZnSe has been chosen, because it provides a good transmission between $0.63\ \mu\text{m}$ and $18\ \mu\text{m}$. The visible wavelengths are needed to align the instrument. The dewar is evacuated to 10^{-7} mbar by a turbo molecular pump. An outer radiation shield cooled by liquid nitrogen protects a radiation shield in contact with the cold optical bench. These inner parts are cooled to 40 K by a closed cycle cooler working with helium. The detector operates at an even lower temperature of 5 K. Although the cooling is crucial to reduce the strong background radiation in the mid-infrared, the pump and the closed cycle cooler are serious sources of vibrations that may effect the measurements. A careful design of those parts was thus necessary.

Since all optical elements have to be aligned when the dewar is open, large or differential expansion coefficients of the metal structures have to be avoided. Otherwise, the alignment would get lost during the cooling process. Therefore, the whole optical bench has been manufactured from a single block of a special aluminium alloy.

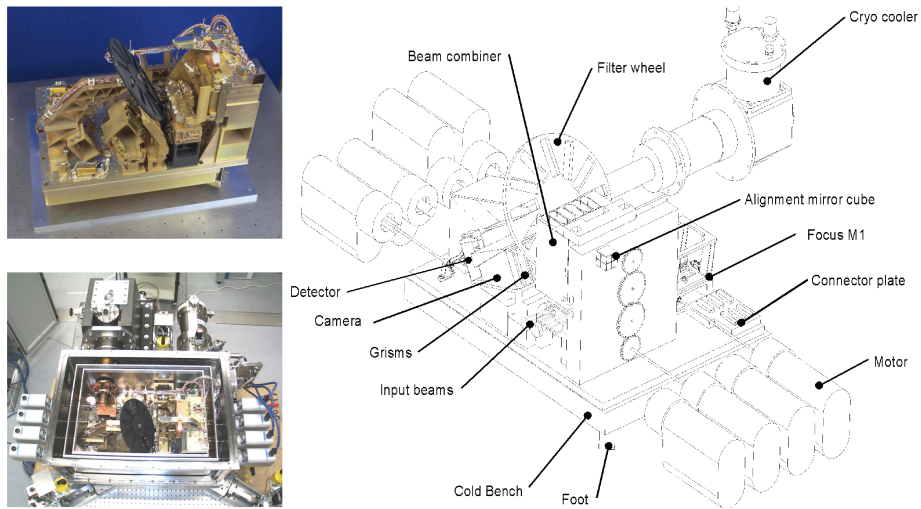


Figure 7.10: The mechanical and optical parts mounted on the cold optical bench inside the dewar (image courtesy of ASTRON). In the upper inset the optical bench in the laboratory of ASTRON is shown. In the lower inset the bench resides in the dewar (image courtesy of F. Przygodda).

7.3.3 The Intermediate Focus

Behind the entrance window a pupil stop called *cold pupil* cuts the outer parts of the beams. This reduces the beam diameter from a nominal value of 18 mm to 17.7 mm. Afterwards, two parabolic mirrors are passed. They are represented in Fig. 7.11 by lenses. While the first mirror focuses the beam, the second mirror recollimates it. The intermediate focus is used to bring slits or pinholes into the

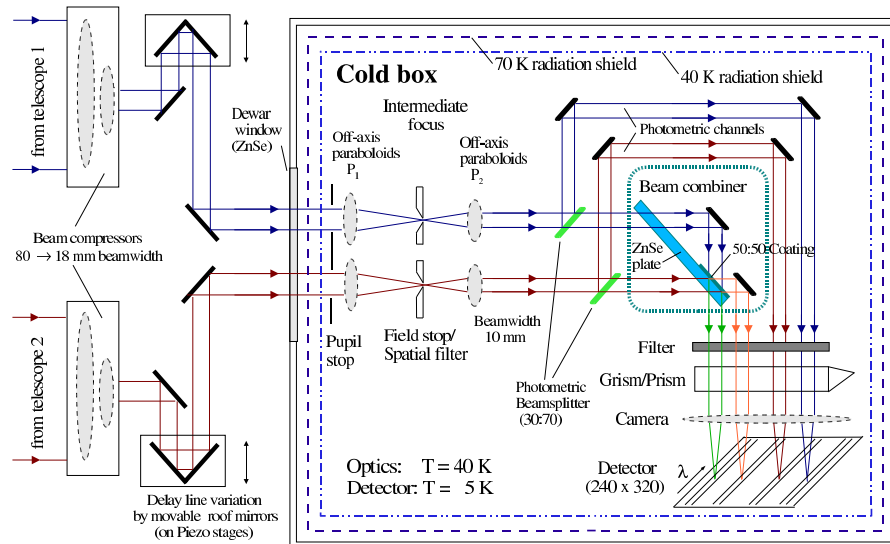


Figure 7.11: Schematic optical layout of MIDI (image courtesy of U. Graser, MPIA).

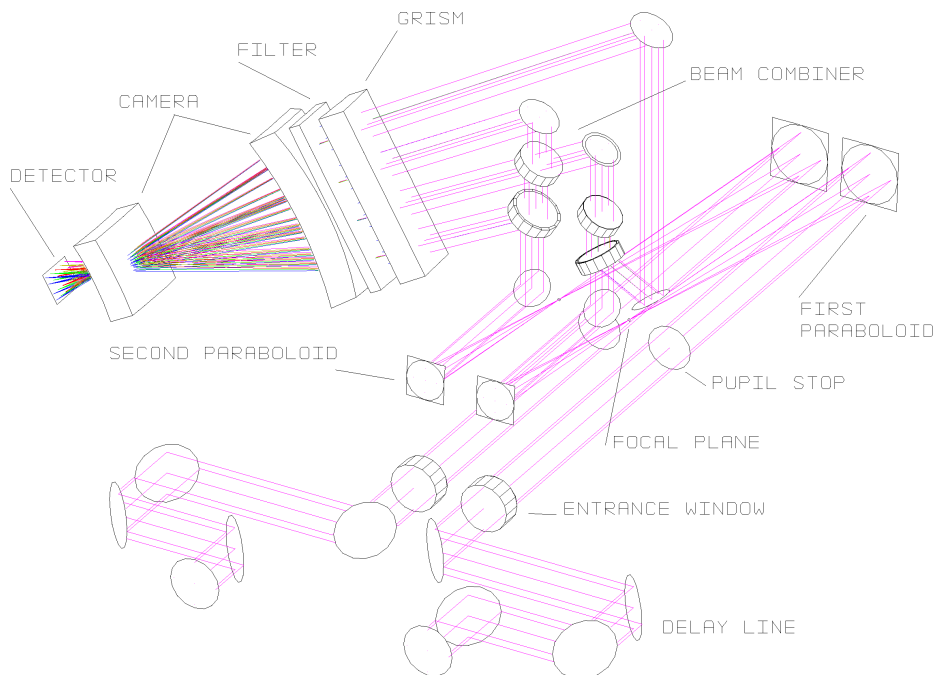


Figure 7.12: Optical layout of MIDI as it has been realized.

optical path. The diameter of the recollimated beams is 10 mm.

7.3.4 The Photometric Beams

Before the light enters the beamcombiner two optional beamsplitters reflecting $\sim 30\%$ of the light into the *photometric beams* can be inserted. The photometric channels are used to determine the position of the beams entering the beamcombiner and to measure the photometric flux simultaneously to the interferometric signal. This instrument mode is thus called *science-phot*. When all photons are entering the beamcombiner, i.e. when not using the photometric beamsplitters, the sensitivity of MIDI is higher. Therefore, this mode is called *high-sense*. Then the photometry has to be recorded after the interferometric measurements. Since the science-phot mode has been successfully tested, it will probably be offered to the community in 2005.

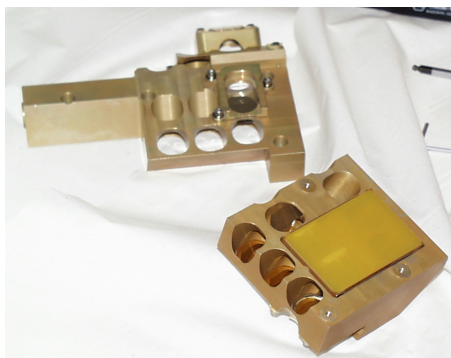


Figure 7.13: The beamcombiner in its slider (image courtesy of ESO).

7.3.5 The Beamcombiner

The central beamcombiner (Fig. 7.13) is realized by a antireflection-coated ZnSe-plate whose one side is half

covered with a 50:50 coating. A plane mirror reflects one of the beams, so that both beams interfere at the same position. Interferometers using this kind of combining the light are known as pupil-plane or Michelson interferometers (Section 8.3). The two beams that are leaving the beamcombiner towards the detector contain all interferometric informations.

7.3.6 Filters and Dispersive Elements

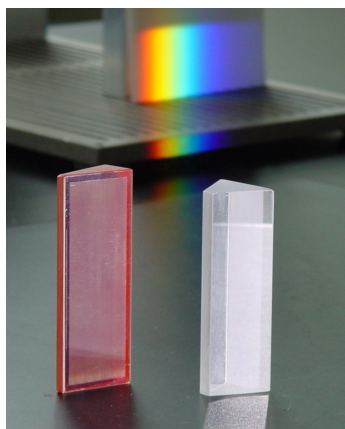


Figure 7.14: The KRS-5 grism and the NaCl prism (image courtesy of ASTRON).

When required one of several filters can be brought into the optical path. This is done by rotating a wheel with a diameter of 25 cm where the 20 mm-filters are mounted (Fig. 7.10).

Moreover, a double prism or a grism, i.e. a prism with a grating, both mounted on a slider allow a spectral dispersion of the interferometric and the photometric beams. The double prism is made of NaCl and Ge. While the wavelength derivative of the refractive index of NaCl is among the highest values at $10.5 \mu\text{m}$ ($0.00996 \mu\text{m}^{-1}$), Germanium has a very low dispersion and ensures that the beams go straight through the prism. The double prism offers a resolution of $\lambda/\Delta\lambda \approx 30$.

The grism provides an even higher resolution of $\lambda/\Delta\lambda \approx 230$. It is made of thallium bromide (KRS-5). This material offers a high transmission between $0.6 \mu\text{m}$ and $40 \mu\text{m}$.

7.3.7 The Three Cameras



Figure 7.15: Ge lenses (image courtesy of ASTRON).

On another slider three cameras are mounted. They are designed to focus the incoming beams onto the detector. Each camera consists of two lenses made of antireflection-coated Germanium. Germanium offers the highest index of refraction (≈ 4.0) of any commonly used infrared transmitting material. In Fig. 7.15 the lenses forming the *spectral camera* are shown. While without a dispersive element or with the prism the so-called *field camera* is used, the spectral camera has been optimised for the grism, because along the dispersion direction the focal length of this camera is two times larger with respect to its focal length along the perpendicular direction. This ensures a appropriate sampling of the spectra with the detector. The third camera is called *pupil camera*. This camera is used to image the pupils.

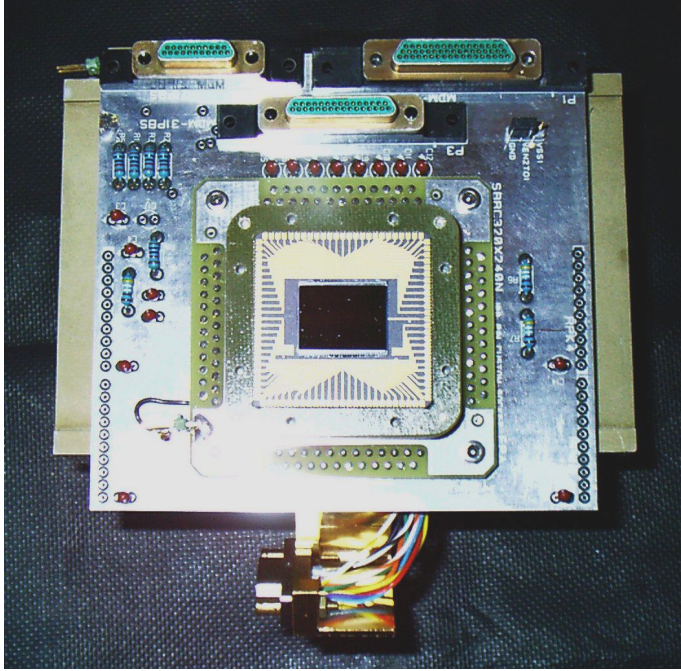


Figure 7.16:
The Raytheon detector in its socket (image courtesy of ESO).

7.3.8 The Detector

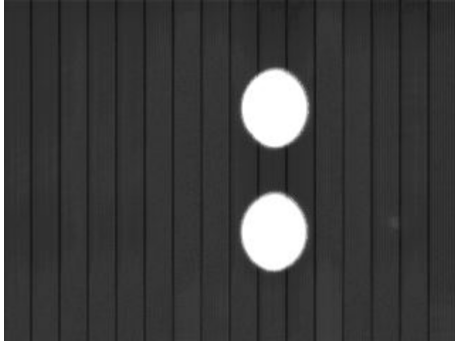


Figure 7.17: An image taken with the background illuminated detector (image courtesy of ESO).

The detector is a Raytheon Si:As Impurity Band Conduction (IBC) array with a size of 320×240 pixels (Fig. 7.16). The physical size of a pixel is $50 \times 50 \mu\text{m}$. The detector is divided into 16 channels consisting of 20×240 pixels each. The vertical stripes in Fig. 7.17 correspond to the readout channels of the detector with slightly different gains. They allow a fast readout of the whole array with frequencies up to 160 Hz ('integrate-then-read' mode). A minimum integration time of 0.2 ms is possible. The detector is operated in the coldest part of the whole MIDI instrument at a temperature of 5 K.

Chapter 8

Long-Baseline Interferometry

‘There was some link between Isengard and Mordor, which I have not yet fathomed. How they exchange news I am not sure; but they did so.’

8.1 The Basic Idea

The geometrical layout of an ideal two telescope interferometer is presented in Fig. 8.1. The telescopes may be located at the positions \vec{x}_A and \vec{x}_B . The separation vector between the two telescopes, i.e. the *baseline* is given by

$$\vec{B} = \vec{x}_B - \vec{x}_A . \quad (8.1)$$

An astronomical source observed with the interferometer may be located at a relative position \vec{a} at an infinite distance. The pointing direction of the telescopes is thus defined by the unit vector

$$\hat{a} = \frac{\vec{a}}{|\vec{a}|} . \quad (8.2)$$

Monochromatic light of frequency ν originating in the astronomical object and propagating towards the telescopes can be described by the electric field vector of a planar wave

$$\begin{aligned} \vec{E}(\vec{x}, t) &= E e^{i(\vec{k}\vec{x} - \omega t)} \\ &= E e^{-i(k\hat{a}\vec{x} + \omega t)} \end{aligned} \quad (8.3)$$

with the wave number $k = 2\pi/\lambda$ and the angular frequency $\omega = 2\pi\nu = kc$. When entering the two telescopes, the fields are given by

$$\vec{E}_A = E_A e^{-i(k\hat{a}\vec{x}_A + \omega t)} , \quad (8.4)$$

$$\begin{aligned} \vec{E}_B &= E_B e^{-i(k\hat{a}\vec{x}_B + \omega t)} \\ &= E_B e^{-i(k\hat{a}\vec{B} + k\hat{a}\vec{x}_A + \omega t)} . \end{aligned} \quad (8.5)$$

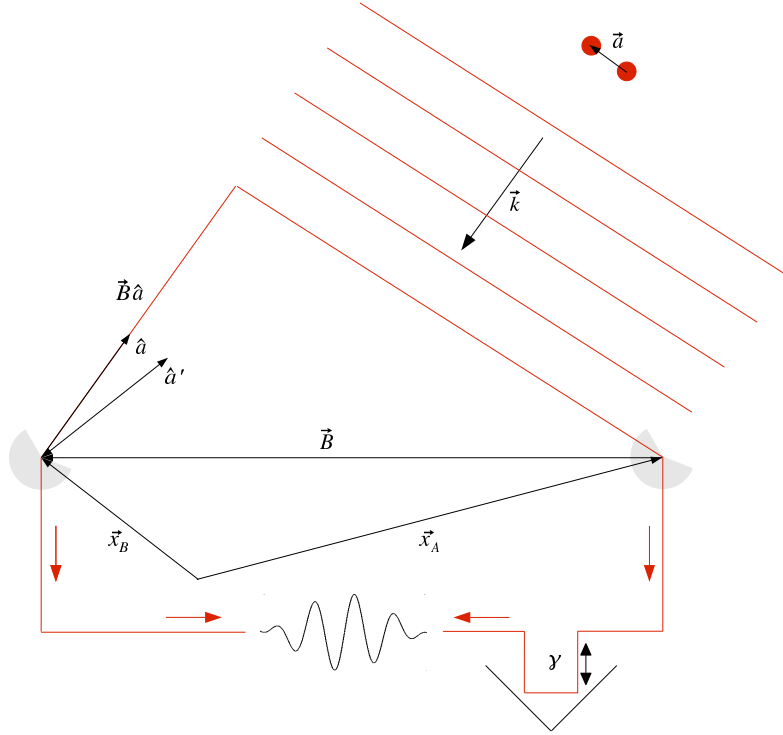


Figure 8.1: Basic geometry of an interferometer

In the last step (8.1) has been used. Without loss of generality one can remove the common time-independent phase factor:

$$\vec{E}_A = E_A e^{-i\omega t}, \quad (8.6)$$

$$\vec{E}_B = E_B e^{-ik\hat{a}\vec{B}} e^{-i\omega t}. \quad (8.7)$$

The phase difference between the two beams is thus solely determined by $\hat{a}\vec{B}$ and the time-averaged signal I measured by an detector is

$$\begin{aligned} I &= \left| \vec{E}_A + \vec{E}_B \right|^2 \\ &= E_A^2 + E_B^2 + E_A E_B e^{-i(k\hat{a}\vec{B})} + E_A E_B e^{i(k\hat{a}\vec{B})} \\ &= I_A + I_B + 2\sqrt{I_A}\sqrt{I_B} \cos(k\hat{a}\vec{B}) \\ &= 2I_{\text{tel}} \left[1 + \cos(k\hat{a}\vec{B}) \right], \end{aligned} \quad (8.8)$$

where in the last step equal intensities of the incoming beams

$$I_{\text{tel}} = I_A = I_B \quad (8.9)$$

have been assumed. A modulation of the signal is possible by using a delayline that introduces an additional phase shift $k\gamma$:

$$\begin{aligned} I &= 2I_{\text{tel}} \left[1 + \cos \left[k \left(\hat{a}\vec{B} + \gamma \right) \right] \right] \\ &= 2I_{\text{tel}} \left[1 + \cos(k\delta) \right]. \end{aligned} \quad (8.10)$$

In the space of relative delay $\delta = \hat{a}\vec{B} + \gamma$ the signal oscillates between zero and two times the total collected signal of the two telescopes. The relative delay is called *optical path difference* or OPD. The oscillations are known as interferometric *fringes*.

8.2 Resolution of an Interferometer

According to the last equation the optical path difference between the two beams cannot only be changed by varying the delay line, but also by varying the pointing of the telescopes, the position of the source, respectively, represented by \hat{a} . This allows an estimation of the resolution offered by an interferometer. A second source located at \hat{a}' is resolved when

$$k(\hat{a}\vec{B} + \gamma) - k(\hat{a}'\vec{B} + \gamma) \geq \pi \quad (8.11)$$

is fulfilled. This relation corresponds to the application of the Rayleigh criterion to interferometric measurements. In this modification it says that two sources are resolved when the peak of one of the fringe signals falls at least in the first minimum of the fringe signal of the other source. With the definition of the wave number this yields to

$$(\hat{a} - \hat{a}')\vec{B} \geq \frac{\lambda}{2}. \quad (8.12)$$

The left side can be rewritten with the *projected baseline* B_{proj} , i.e. the baseline \vec{B} projected on the separation vector $\vec{a} = \hat{a} - \hat{a}'$, and the angular separation of the sources a , i.e. the modulus of the separation vector \vec{a} . Therefore, the resolution of an interferometer is

$$a \geq \frac{\lambda}{2B_{\text{proj}}}. \quad (8.13)$$

Otherwise, when the resolution is defined as the inverse of the spatial frequency of the fringe signal, one finds

$$a \geq \frac{\lambda}{B_{\text{proj}}}. \quad (8.14)$$

In this form it can be directly compared with the resolution of a single telescope λ/D that is determined by the inverse of the highest measurable spatial frequency. The projected baseline B_{proj} of an interferometer thus corresponds to the diameter D of a telescope mirror. The telescopes feeding the interferometer represent in this picture two subapertures located at the edge of a virtual mirror with a diameter B_{proj} . From an observer's point of view it is important to keep in mind that the sensitivity is still limited to the collecting area of the single telescopes.

8.3 Interferometric Beam Combination

Interferometers are divided into two classes according to the method used to combine the beams interferometrically (Traub, 1999).

8.3.1 Image-Plane or Fizeau Interferometers

These interferometers combine the incoming beams formed by two individual telescopes or two different parts of a mirror in the image-plane. In the resulting image the intensity distributions produced by the single telescopes are modulated by the interferometric fringe pattern (8.10). This type of interferometer is named after Fizeau who suggested to create an interferometer by covering the aperture of a telescope with a two-slit mask. Michelson's famous stellar interferometer was an image-plane instrument. It combined the beams coming from two 45° flat mirrors riding on an external rail with a conventional telescope.

When dividing a mirror of a telescope into segments, one may think of each pair of segments as an interferometer. Each telescope thus represents an image-plane interferometer with a full coverage of the spatial frequencies up to that corresponding to the inverse diffraction limit of the telescope. The diffraction-limited point-spread function is a result of the superposition of the different fringe patterns.

8.3.2 Pupil-Plane or Michelson Interferometers

These interferometers superimpose the parallel incoming beams by using a beamsplitter, fibre optics, or similar devices. They are named after Michelson who used an pupil-plane interferometer to measure the speed of light.

MIDI belongs to this group. The central beamsplitter is schematically shown in Fig. 8.2. It has been realized by covering one side of a ZnSe-plate half with a coating that transmits about half of the incoming light and reflects the remaining part. Energy conservation requires a phase shift of $\pi/2$ between the reflected and the transmitted light (Traub, 1999). Therefore, with the incoming beams

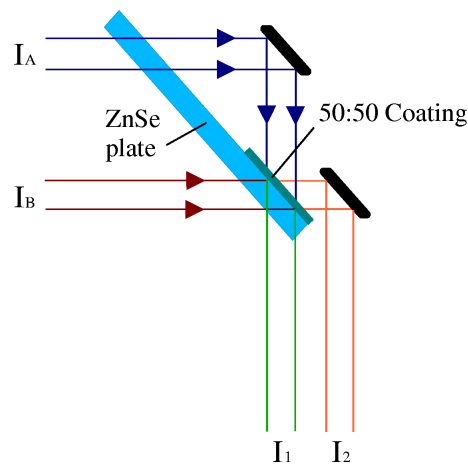


Figure 8.2: Sketch of the central beamsplitter of MIDI.

$$I_A = |\vec{E}_A|^2 \quad \wedge \quad I_B = |\vec{E}_B|^2, \quad (8.15)$$

where \vec{E} is the electric field vector, the outgoing interferometric beams I_1 and I_2 are given by

$$I_1 = |\vec{E}_1|^2 = |\vec{E}_{A,1} + \vec{E}_{B,1} e^{+i\frac{\pi}{2}}|^2, \quad (8.16)$$

$$I_2 = |\vec{E}_2|^2 = |\vec{E}_{A,2} + \vec{E}_{B,2} e^{-i\frac{\pi}{2}}|^2. \quad (8.17)$$

The first indices indicate the origin of the electric field vectors. Calculating this

equations leads to

$$\begin{aligned}
 I_1 &= \left| \vec{E}_{A,1} \right|^2 + E_{A,1} E_{B,1} e^{i(\phi_A - \phi_B + \frac{\pi}{2})} + E_{A,1} E_{B,1} e^{-i(\phi_A - \phi_B + \frac{\pi}{2})} + \left| \vec{E}_{B,1} \right|^2 \\
 &= I_{A,1} + 2E_{A,1} E_{B,1} \cos(\phi_A - \phi_B + \pi/2) + I_{B,1} \\
 &= I_{A,1} - 2E_{A,1} E_{B,1} \sin(\phi_A - \phi_B) + I_{B,1},
 \end{aligned} \tag{8.18}$$

$$\begin{aligned}
 I_2 &= \left| \vec{E}_{A,1} \right|^2 + E_{A,1} E_{B,1} e^{i(\phi_A - \phi_B - \frac{\pi}{2})} + E_{A,1} E_{B,1} e^{-i(\phi_A - \phi_B - \frac{\pi}{2})} + \left| \vec{E}_{B,1} \right|^2 \\
 &= I_{A,1} + 2E_{A,1} E_{B,1} \cos(\phi_A - \phi_B - \pi/2) + I_{B,1} \\
 &= I_{A,1} + 2E_{A,1} E_{B,1} \sin(\phi_A - \phi_B) + I_{B,1}.
 \end{aligned} \tag{8.19}$$

An interesting property of pupil-plane interferometers is that the output beams are complementary. This means, that adding up the two intensities leads to a constant value that is under ideal conditions equal to the input intensities:

$$\begin{aligned}
 I_1 + I_2 &= I_{A,1} + I_{A,2} + I_{B,1} + I_{B,2} \\
 &= I_A + I_B \\
 &\stackrel{(8.9)}{=} 2I_{\text{tel}}.
 \end{aligned} \tag{8.20}$$

The interferometric flux can be determined by subtracting (8.19) from (8.18). With the assumption that the beamsplitter transmits exactly 50% and reflects the remaining light, i.e.

$$I_{A,1} = I_{A,2} = \frac{I_A}{2} \quad \wedge \quad I_{B,1} = I_{B,2} = \frac{I_B}{2}, \tag{8.21}$$

one finds

$$\begin{aligned}
 I_{\text{int}} &= I_2 - I_1 \\
 &= 2 \left(\sqrt{\frac{I_A}{2}} \sqrt{\frac{I_B}{2}} + \sqrt{\frac{I_A}{2}} \sqrt{\frac{I_B}{2}} \right) \sin(\phi_A - \phi_B) \\
 &= 2\sqrt{I_A I_B} \sin(k\delta) \\
 &\stackrel{(8.9)}{=} 2I_{\text{tel}} \sin(k\delta),
 \end{aligned} \tag{8.22}$$

where δ is the optical path delay between the two incoming beams that can be adjusted by changing the delay line.

8.4 Polychromatic Sources

In the last sections it has been assumed that the light emitted by an astronomical source is monochromatic. This is obviously not the case for real objects. They emit light with a wavelength-dependent intensity $I(\lambda)$. Moreover, atmospheric and instrumental restrictions described by a spectral filter function $\eta(\lambda)$ limit the throughput as function of wavelength. To describe this situation one has to modify (8.22):

$$I_{\text{int}} = 2 \int I(\lambda) \eta(\lambda) \sin(k\delta) d\lambda. \tag{8.23}$$

Here the harmonical decomposition of light is used. This is possible, because to an extremely good approximation optical photons do not interact with each other (Boden, 1999). The calculation of (8.23) will be simplified by assuming a wavelength-independent intensity and a filter function of width $\Delta\lambda$ centred at λ_0 that is defined by

$$n(\lambda) = \begin{cases} \eta_0 & , \text{ if } \lambda_0 - \frac{1}{2}\Delta\lambda < \lambda < \lambda_0 + \frac{1}{2}\Delta\lambda \\ 0 & , \text{ else.} \end{cases} \quad (8.24)$$

Integrating (8.23) results then in (Boden, 1999)

$$\begin{aligned} I_{\text{int}} &= 2 I(\lambda_0) \Delta\lambda \eta_0 \frac{\sin(\pi\Delta\lambda/\lambda_0^2\delta)}{\pi\Delta\lambda/\lambda_0^2\delta} \sin(k_0\delta) \\ &= 2 I(\lambda_0) \Delta\lambda \eta_0 \text{sinc}(\pi\Delta\lambda/\lambda_0^2\delta) \sin(k_0\delta) \\ &= 2 I(\lambda_0) \Delta\lambda \eta_0 \text{sinc}(\pi\delta/\Lambda) \sin(k_0\delta) . \end{aligned} \quad (8.25)$$

The sinc function is the Fourier transform of the spectral filter function (8.24) and is best described by a characteristic coherence length

$$\Lambda \equiv \frac{\lambda_0^2}{\Delta\lambda} , \quad (8.26)$$

because the sinc function becomes small for $|\pi\delta| > \Lambda$. It is instructive to compare (8.25) with (8.22). The telescope intensity is now recorded in the bandwidth $\Delta\lambda$ with an efficiency η_0 . The interferometric fringes oscillate with the wave number k_0 like a monochromatic fringe pattern produced by light of the central wavelength λ_0 . The main effect introduced by the polychromatic source is the multiplication with a sinc function centred at $D = 0$. A few examples with Λ varying between $20\lambda_0$ and $2\lambda_0$ are shown in Fig. 8.3.

8.5 Extended Sources

After investigating sources emitting not monochromatically, but over a wide spectral range, here the changes occurring when observing spatially extended sources instead of point sources will be shown. With the assumption that photons from different locations on the source are incoherent, an extended object can be described by a superposition of coherent point sources at positions given by \vec{a} (Section 8.2). With the fractions of light seen through each of the two telescopes

$$f_A = \frac{I_A}{I_A + I_B} \quad \wedge \quad f_B = \frac{I_B}{I_A + I_B} \quad (8.27)$$

one finds by modifying (8.22)

$$\begin{aligned} I_{\text{int}} &= 2\sqrt{f_A f_B} \int I(\vec{a}) \sin \left[k \left(\delta + \vec{a}\vec{B} \right) \right] d\vec{a} \\ &= 2\sqrt{f_A f_B} \int I(\vec{a}) \frac{1}{2i} \left[e^{i(k\delta + k\vec{a}\vec{B})} - e^{-i(k\delta + k\vec{a}\vec{B})} \right] d\vec{a} \\ &= \sqrt{f_A f_B} \left[\frac{1}{i} e^{ik\delta} \int I(\vec{a}) e^{ik\vec{a}\vec{B}} - \frac{1}{i} e^{-ik\delta} \int I(\vec{a}) e^{-ik\vec{a}\vec{B}} \right] . \end{aligned} \quad (8.28)$$

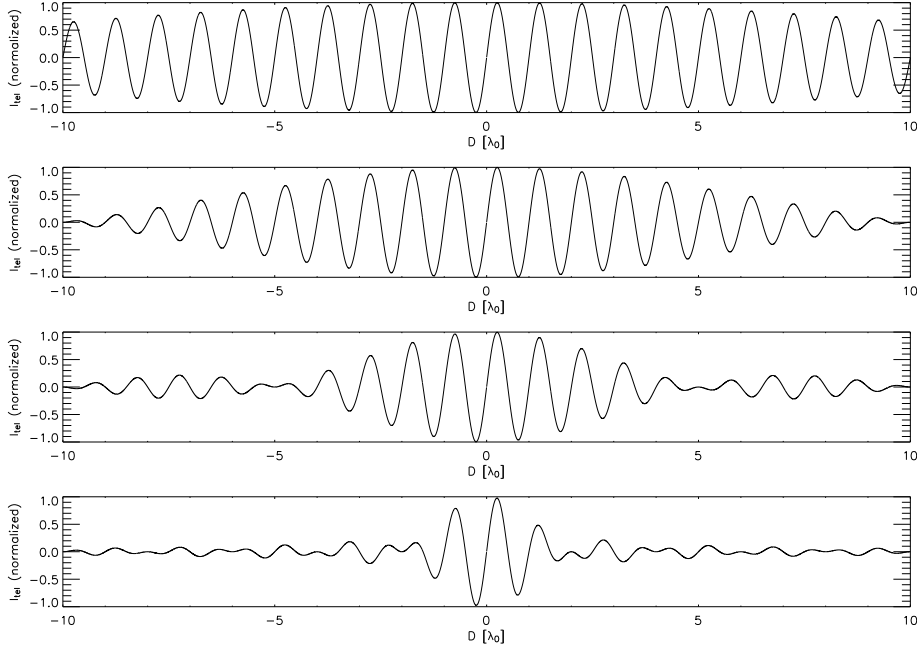


Figure 8.3: Fringe signal for $\Lambda=20 \lambda_0$, $10 \lambda_0$, $5 \lambda_0$, and $2 \lambda_0$ (from top to bottom).

The two integrals can be interpreted as Fourier transforms of the intensity. With the definition of the wave number k and the projected baseline B_λ measured in units of λ they are given by:

$$\int I(\vec{a}) e^{+2\pi i \frac{\vec{a}\vec{B}}{\lambda}} = \mathcal{I}(+B_\lambda) = |\mathcal{I}(B_\lambda)| e^{+i\phi(B_\lambda)}, \quad (8.29)$$

$$\int I(\vec{a}) e^{-2\pi i \frac{\vec{a}\vec{B}}{\lambda}} = \mathcal{I}(-B_\lambda) = |\mathcal{I}(B_\lambda)| e^{-i\phi(B_\lambda)}. \quad (8.30)$$

It has been used in (8.30) that the Fourier transform of real functions like the intensity distribution I is hermitic, i.e. the Fourier transform fulfils

$$\mathcal{I}(-\vec{u}) = \mathcal{I}^*(\vec{u}) \quad \text{or} \quad |\mathcal{I}(-\vec{u})| = |\mathcal{I}(\vec{u})|. \quad (8.31)$$

Now (8.29) and (8.30) have to be inserted into (8.28). This yields

$$\begin{aligned} I_{\text{int}} &= \sqrt{f_A f_B} \left[\frac{1}{i} e^{ik\delta} |\mathcal{I}(B_\lambda)| e^{i\phi(B_\lambda)} - \frac{1}{i} e^{-ik\delta} |\mathcal{I}(B_\lambda)| e^{-i\phi(B_\lambda)} \right] \\ &= \sqrt{f_A f_B} |\mathcal{I}(B_\lambda)| \frac{1}{i} \left[e^{i[k\delta + \phi(B_\lambda)]} - e^{-i[k\delta + \phi(B_\lambda)]} \right] \\ &= 2\sqrt{f_A f_B} |\mathcal{I}(B_\lambda)| \sin[k\delta + \phi(B_\lambda)]. \end{aligned} \quad (8.32)$$

Since no external fringe tracker is yet available, it cannot be determined with MIDI, whether a measured phase ϕ originates in a wrong determination of $k\delta=0$ or the morphology of the source. Nevertheless, the amplitude of the fringe signal can be determined with a high accuracy by, e.g. the *Fourierspectrum analysis*

(Section 9.2). The normalised visibility is calculated with

$$V(B_\lambda) \equiv \frac{|\mathcal{I}(B_\lambda)|}{|\mathcal{I}(0)|} = \frac{|I_{\text{corr}}|}{I_A + I_B}, \quad (8.33)$$

where the ‘true’ correlated flux

$$|I_{\text{corr}}| = \frac{|I_{\text{int}}|}{2\sqrt{f_A f_B}}, \quad (8.34)$$

i.e. corrected for different throughputs of the telescopes (8.32), has to be used instead of I_{int} . Inserting (8.34) into (8.33) and using (8.27) leads to

$$V(B_\lambda) = \frac{|I_{\text{int}}|}{2\sqrt{I_A I_B}}. \quad (8.35)$$

8.6 Source Morphologies

Interferometers are powerful devices to determine the morphology of astronomical objects, because the measured visibility is proportional to the modulus of the Fourier transform of $I(x)$, i.e. of the object brightness distribution projected onto a plane containing the object and the interferometer apertures (Section 8.5). If (x, y) are coordinates on the sky with x measured parallel to the baseline and y normal to it, then

$$I(x) = \int I(x, y) dy. \quad (8.36)$$

Here some instructive and easy examples will be discussed. Very often complex structures can be described by convolving the simple intensity distributions. According to the *Convolution Theorem* the visibilities are then derived by multiplying the visibilities of the basic structures. B_λ is again the length of the projected baseline in units of λ .

8.6.1 Point Source

A point source of intensity I_0 located at a position a can be described mathematically by a δ -function:

$$I(x) = I_0 \delta(a - x). \quad (8.37)$$

The Fourier transform of this function is a constant. The normalised visibility is thus given by

$$V(B_\lambda) \equiv 1, \quad (8.38)$$

i.e. it is unity independent of the spatial frequency B_λ .

8.6.2 Binary Star

A binary is described by two δ -functions. Assuming that the two components are located at $\pm a/2$ the brightness distribution is

$$I(\vec{x}) = I_1 \delta\left(x - \frac{a}{2}\right) + I_2 \delta\left(x + \frac{a}{2}\right). \quad (8.39)$$

With the flux ratio of the components

$$f = \frac{I_1}{I_2} \quad (8.40)$$

the normalised visibility is given by

$$V(B_\lambda) = \sqrt{\frac{1 + f^2 + 2f \cos(2\pi a B_\lambda)}{(1 + f)^2}}. \quad (8.41)$$

This has been already demonstrated in Section 4.5.2.

8.6.3 Uniform Circular Disk

Another important morphology is a uniform circular disk of diameter a . Then the intensity distribution $I(x)$ is a semicircle. If the disk resides in the origin of the coordinate system, the intensity is mathematically described by

$$I(x) = \begin{cases} I_0 \sqrt{1 - \left(\frac{2x}{a}\right)^2} & , \text{ if } -a/2 < x < a/2 \\ 0 & , \text{ else.} \end{cases} \quad (8.42)$$

With the Fourier transform one finds the visibility

$$V(B_\lambda) = \left| \frac{2J_1(\pi d B_\lambda)}{\pi d B_\lambda} \right|, \quad (8.43)$$

where $J_1(\vec{x})$ is the first order Bessel function. Such a uniform circular disk is the easiest approach to model a resolved star. It will be used later for the calibrators that are required to determine the instrumental visibility.

8.6.4 Gaussian Disk

Gaussian disks are characterised by their full-width-half-maximum (FWHM) σ , defined as the width of the disk when measuring at intensity values half of the maximum. In other words, the intensity is reduced to half of the peak value at a distance $\sigma/2$ from the centre. Since the integration given in (8.36) preserves the FWHM along the projected baseline, one finds

$$I(x) = I_0 e^{-\left(\frac{2\sqrt{\ln 2}}{\sigma} x\right)^2}. \quad (8.44)$$

The Fourier transform and thus the visibility is also a Gaussian with a reciprocal FWHM, i.e. wide distributions are narrow in the Fourier space and vice versa:

$$V(B_\lambda) = e^{-\left(\frac{\pi\sigma}{2\sqrt{\ln 2}} B_\lambda\right)^2}. \quad (8.45)$$

Gaussian distributions are often used as an approximation for centrally heated structures like circumstellar disks.

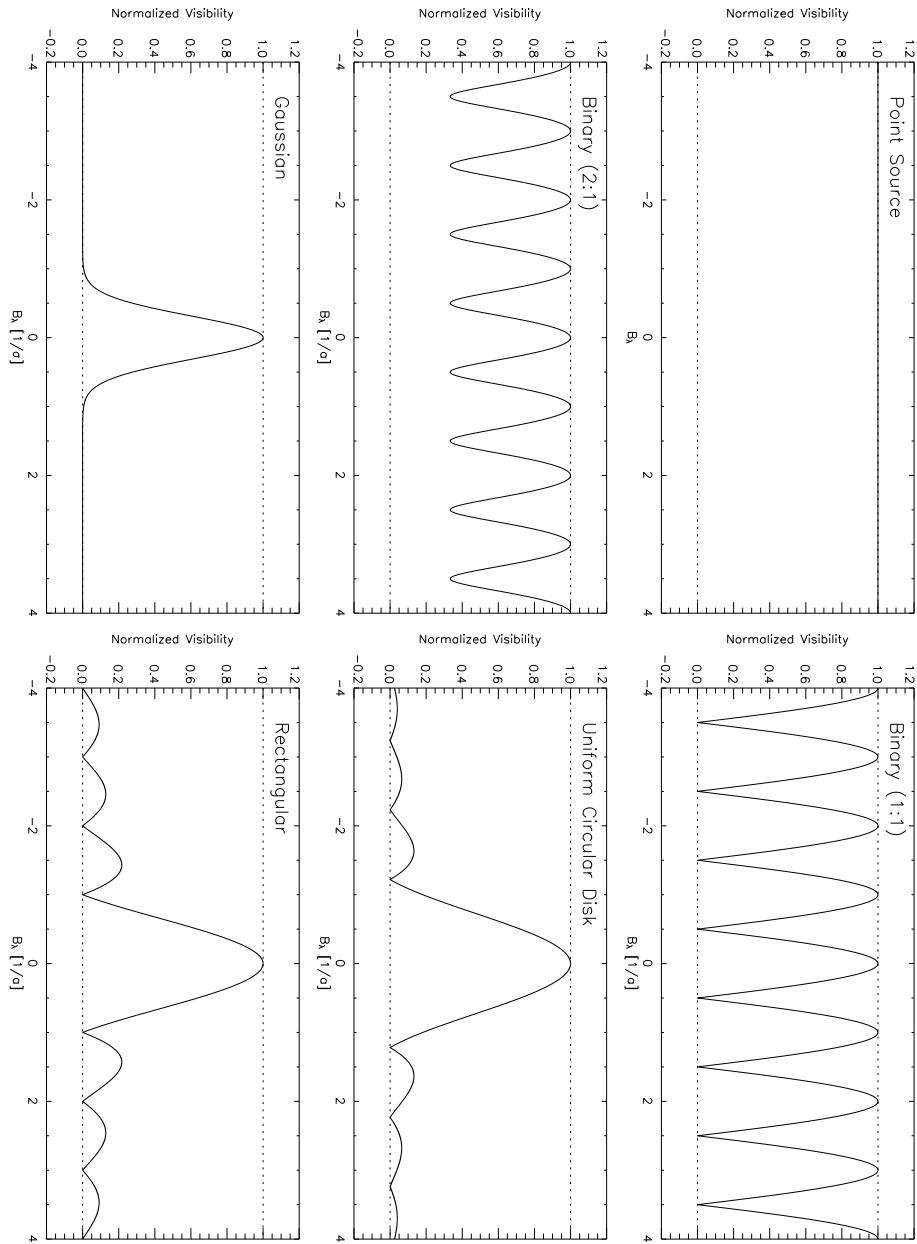


Figure 8.4: The different models described in this chapter. The spatial frequency is scaled in units of distance (binary), diameter (uniform circular disk, rectangular distribution), or FWHM (Gaussian disk).

8.6.5 Rectangular Distribution

A rectangular or top-hat function

$$I(x) = \begin{cases} I_0 & , \text{ if } -a/2 < x < a/2 \\ 0 & , \text{ else} \end{cases} \quad (8.46)$$

that can be found naturally (atmospheric windows, etc.) or is produced artificially (filter, etc.) has been already discussed in Section 8.4. The visibility is a sinc function:

$$V(B_\lambda) = \left| \frac{\sin(\pi a B_\lambda)}{\pi a B_\lambda} \right|. \quad (8.47)$$

Chapter 9

Obtaining Visibilities with MIDI

‘It seemed to him that he had stepped through a high window that looked on a vanished world. A light was upon it for which his language had no name. All that he saw was shapely, but the shapes seemed at once clear cut, as if they had been first conceived and drawn at the uncovering of his eyes, and ancient as if they had endured for ever.’

9.1 Observations

A modern instrument mounted on a modern telescope represents a very complex system with respect to control and handling. For interferometric observations with MIDI this is even more valid (Fig. 9.1): two telescopes collecting the photons, two adaptive optics system cleaning and stabilising the beams, two delay lines bringing the beams to the interferometric laboratory, and last but not least a helium-cooled beam-combining instrument. Although the system is complex, an astronomer preparing observations for MIDI will not have to care about the details. Nevertheless, it is important to understand how a typical observation is performed and how the different subsystems work together.

9.1.1 Pointing

After sending the celestial coordinates of the target to the telescopes, the alt-azimuthal mounts slew into this direction. The unit telescopes can acquire any target between 20° and 89.5° elevation in less than three minutes (ESO, 2003). Obstructions of the UTs due to the enclosures of other UTs play a role only below 30° elevation. If the provided coordinates are precise enough, the pointing can normally be done with an accuracy good enough to bring the source into the MIDI field-of-view of 2×2 arcsec. The pointing model provides after three years



Figure 9.1: The VLTI section in the main control building of the VLT after a night of observations. The telescopes and the adaptive optics systems are controlled by two operators with the consoles on the left side. With the computers in the left central part an operator can control the delaylines and the VLTI laboratory. Sebastien Morel is sitting in front of the MIDI control units watching the Real Time Display. The right side is reserved for the astronomers preparing observations and checking the results.

of operation the absolute pointing coordinates to within 1.5 arcsec root mean square. Offset pointings of 45° and 60° in elevation and azimuth respectively are possible within 35 seconds, to within 0.1 arcsec accuracy relative to the telescope encoders (ESO, 2003).

The incoming wavefront is focused by the primary mirror (M1) and the secondary mirror (M2) reflects the light back towards the primary. The convex, hyperbolic M2 mirror allows the correction of some optical aberration of the telescope (defocus and decentring coma) and the change of the pointing direction by adjusting its position and orientation along five degrees of freedom (ESO, 2003). Afterwards, the flat, elliptical tertiary mirror (M3) mounted on a tower in the centre of the primary guides the light towards the Nasmyth adapter.

9.1.2 The Nasmyth Adapter

Each Nasmyth adapter is equipped with a pick-up mirror that feeds two separate CCD-sensors with the light of a reference star in the peripheral field-of-view of the telescope by using a dichroic beamsplitter. The star selection is done by positioning the pick-up mirror appropriately. One sensor is used for guiding. When using a guide-star the UTs are designed to track better than 0.05 arcsec root mean square over an one hour period (ESO, 2003). The other sensor monitors the image of the reference star and determines how the active optics

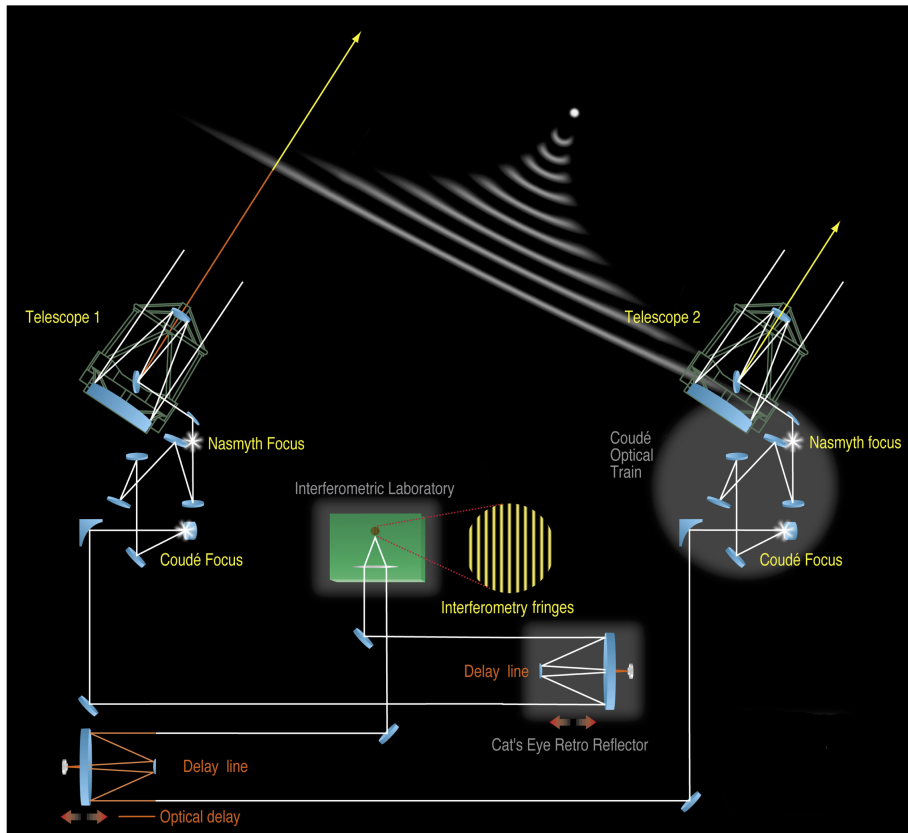


Figure 9.2: Sketch of the VLTI infrastructure (courtesy of ESO).

system can compensate for static or slowly varying optical errors such as those caused by, e.g. manufacturing errors, gravitational or thermal distortions (ESO, 2003). The sky-coverage of suitable stars is not problematic, but the closing of the loop can be highly affected by the nearby moon. Observers should keep this point in mind when planning their observations with MIDI that are not influenced by the moon in general.

9.1.3 Coudé Guiding

A concave, cylindrical mirror (M4) residing in front of the Nasmyth adapter directs the light now to the *Coudé train*. Optics therein with two concave, spherical (M5, M7) and one concave, cylindrical mirror (M6) provide an image of the telescope pupil close to a flat mirror called M8 and an image of the sky in the *Coudé focus* inside the Coudé room (Fig. 7.6). In the beginning a tip/tilt-system (STRAP) with a sensor in the Coudé focus corrected the lowest order of wavefront-distortions introduced by the atmospheric turbulence. Since summer 2004 the flat mirror M8 has been replaced on UT2, UT3, and UT4 by a deformable mirror. This mirror is part of the *Multi-Application Curvature Adaptive Optics* (MACAO). The wavefront-sensor of this system is located in the Coudé focus again. It uses the visible light of the beam that is extracted by a

large dichroic (M9) located between M8 and the wavefront-sensor to compensate the distortions in a 2 arcmin field-of-view. The performance of MACAO thus may be also affected by the close by moon similar to the active optics system.

Since the MACAO units require visible light, mere infrared targets need a guide star ($V < 17$ mag) that is separated by less than 1 arcmin. When observations with adaptive optics are not possible due to a missing guide star, a good overlap of the two beams is not guaranteed. The usage of the photometric beams (Section 7.3.4) may help here. Although MACAO allows a better correction of the wavefront, even the still available STRAP units allow a diffraction-limited imaging of the source in the mid-infrared. However, in this wavelength range the beams are in general diffraction-limited below a seeing of ~ 0.8 arcsec. Therefore, infrared sources without a guide star within 1 arcmin should be observed only under good seeing conditions. Nevertheless, the stability of the background is under all seeing conditions much higher with the full correcting MACAO units.

9.1.4 Delayline Adjustment

Besides the large dichroic (M9) two other mirrors are mounted in the Coudé room below the telescope (Fig. 7.6). The convex spherical mirror M10 reimages the telescope pupil in the tunnel centre and adjusts the lateral position in the interferometric laboratory. The off-axis parabola M11 collimates the beam and sends it towards M12 inside the delayline-tunnel that feeds the carriage of the delayline (Fig. 7.7).

These carriages inside the tunnels will bring the optical path difference between the two delaylines now to nominal zero with an accuracy better than 1mm. To achieve this, empirical models are used that take the pointing directions of the telescopes into account. The delayline-carriages are equipped with three mirrors (M13, M14, and M15). The *Variable Curvature Mirror* (VCM) M13 is very important to reimage the pupil inside the interferometric laboratory. Depending on the optical path length the curvature of this mirror can be changed. It is not in operation yet, i.e. the focal length is fixed. This causes a varying diameter of the beam on the detector when the carriage is moved. According to our experience also the quality of the beam varies. Integrating the variable curvature mirrors is thus one of the most urgent actions during the next time.

The final delayline adjustments and scans required for the search (Section 9.1.7) and the tracking of the fringes (Section 9.1.8) are performed with piezo-mounted mirrors on the warm optical bench (Section 7.3.1) in front of MIDI.

9.1.5 The Switchyard

A mirror (M16) in front of the interferometric laboratory brings the beams now to the so-called *switchyard*. This array of mirrors located inside the laboratory is designed to feed the interferometric instruments with the light from the telescopes. When serving for MIDI the beams are sent to a beamcompressor first that reduces their diameter from 80 cm to 18 cm. Afterwards the compressed beams are reflected back to the switchyard from where they are sent to a feeding mirror in front of the warm optical bench of MIDI (Section 7.3.1).

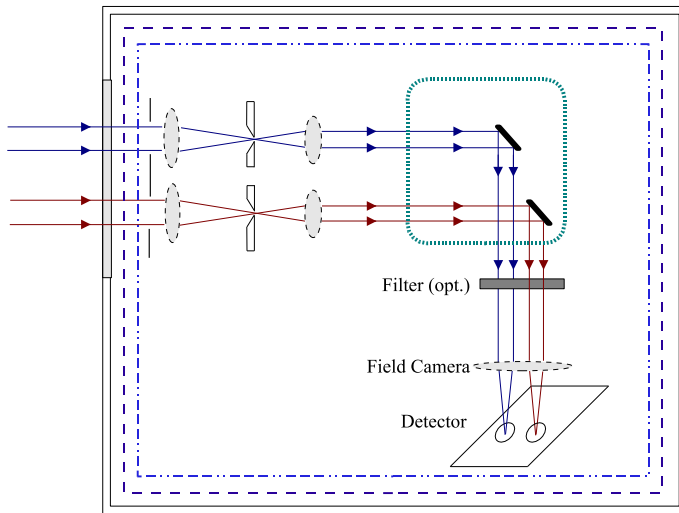


Figure 9.3: Schematic MIDI configuration for the acquisition of a source.

9.1.6 Acquisition

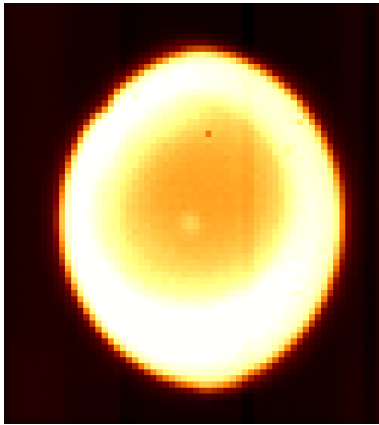


Figure 9.4: Acquisition frame of Z CMa obtained with UT4 on 4. Nov. 2004.

The first recorded data are the acquisition frames used to determine the correct positioning of the images of the target on the chip. This ensures a good overlap of the beams when the beamcombiner is inserted. An example obtained with light coming from UT4 and passing a broad N-band filter is shown in Fig. 9.4. One can clearly distinguish within the circular boundary of the beam between light originating in the delayline-tunnel (broad, bright rim) and light both from the sky and the 23 mirrors feeding MIDI (orange area). With a total reflectivity of $2/3$ the mirrors radiate 10 times stronger than the sky. Since the brightness of Z CMa is high (~ 140 Jy) and the Strehl ratio was good, the source appears in the centre as faint dot. A source with a brightness of a few Jansky would not be visible at

all. The photon noise of the background limits the brightness of a source that can be detected. Since the thermal background and thus its noise does not scale with the telescope diameter, it is important to use telescopes as large as possible to increase the signal from the source.

The integration time of the acquisition frames is only 4 ms to avoid a saturation of the detector by the high thermal background. Therefore, at least 1000 frames are taken with the two telescopes during the acquisition procedure to increase the signal-to-noise ratio when combining them. This requires a fast detector readout and a reduction of the amount of data. Only two 62×69 pixels subarrays located where the two beams illuminate the detector are thus read out (Fig. 7.17).

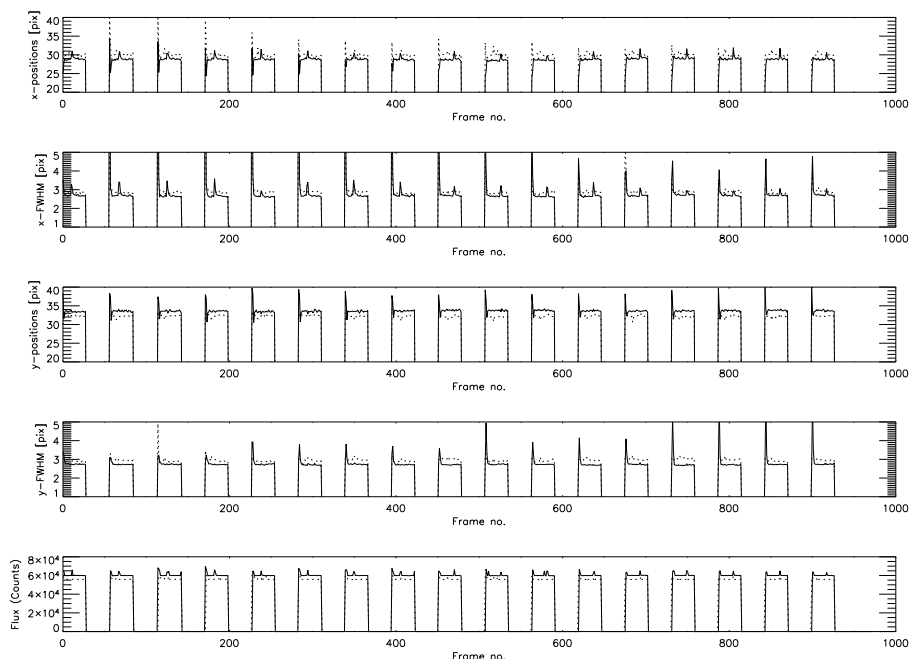


Figure 9.5: The fitted positions and full-width-half-maxima of Z CMa in the frames obtained with UT3 (solid line) and UT4 (hatched line) on 4. Nov. 2004. The flux of the source in a single frame is displayed in the panel at the bottom.

To check the centring of a source with a few Jansky it is necessary to determine the strong and fast varying thermal background. MIDI uses a standard procedure for the mid-infrared called *chopping*, because the two secondary mirrors of the telescopes periodically point to another position. An image of the sky is recorded by MIDI at this offset position that is by default 15 arcsec away from the target. This can be done with a frequency of up to 2 Hz at the UTs. The procedure is illustrated in Fig. 9.5 for the Z CMa observation: a sequence with approximately thirty frames on source indicated by non-zero flux values and thirty frames off source has been repeated continuously until 1000 frames have been recorded for each of the two telescopes. The relative position and full width half maximum of Z CMa has been fitted after subtracting from each target frame the mean of the averages of the blocks of sky frames taken before and after. The peaks at the beginning of each block of target frames are caused by a jittering of the secondary, an unprecise recentring of the source, respectively. Moreover, between the blocks of target and sky frames several frames have been already removed, since they are marked neither as sky nor as target frames. The total number of frames is thus reduced to ~ 930 .

The acquisition images displayed on the *Real-Time Display* (RTD) at the MIDI console look similar to the images on the right side in Fig. 9.6. They have been created by averaging both the target and the sky frames and calculating the difference. If the Coudé guiding is working, automatic tools can be used to centre the source in the MIDI field-of-views. Afterwards the adaptive optics unit will keep the beams centred. If the beams are ‘flat’, i.e. all major background fluctu-

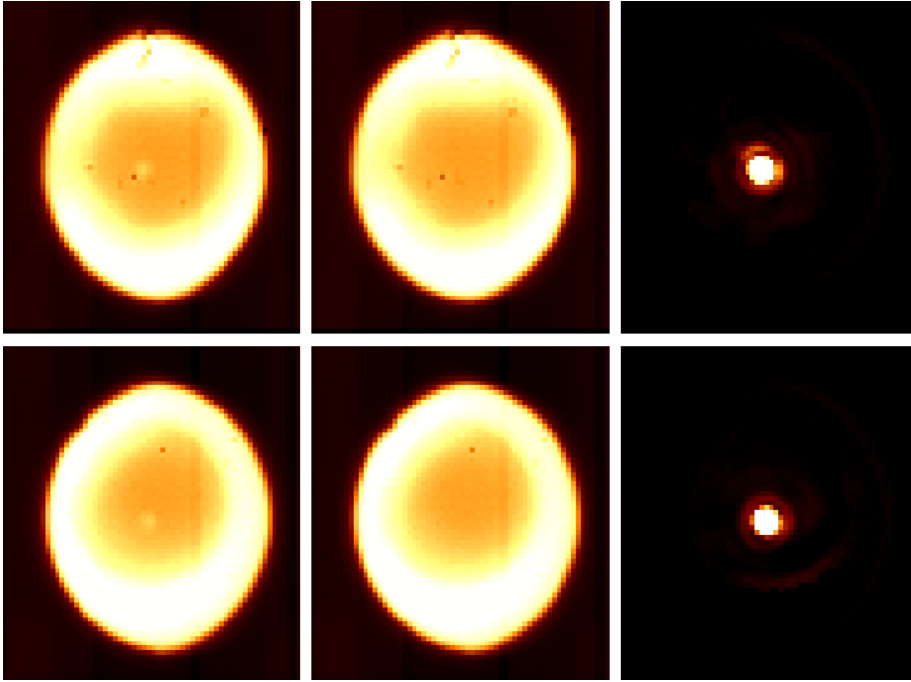


Figure 9.6: In the upper row the mean of the on-source frames (left), the mean of the off-source frames (centre), and their difference (right) obtained during the observation of Z CMa on 4. Nov. 2004 is shown for UT3. In the lower row the same is displayed for UT 4. Three Airy rings are visible in the upper right image.

ations could be eliminated, it is not problematic to find and centre sources, but a careful selection of the filter used for the acquisition is recommended. Without

Coudé guiding a semi-automatic target acquisition with Nasmyth guiding allows the usage of the coordinates of the detector.

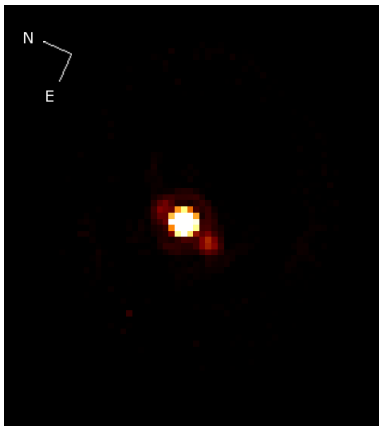
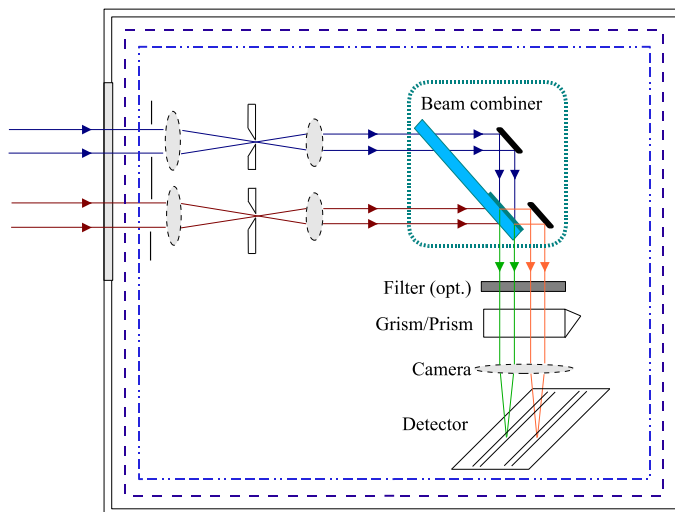


Figure 9.7: Acquisition image of FU Ori obtained with UT3 on 31. Oct. 2004.

As said before, the main purpose of the acquisition images is to centre the beams with a precision high enough to allow an interferometric beam combination. However, the acquisition images are of scientific worth by their own. MIDI provides as first instrument at the VLT diffraction-limited images in the mid-infrared.

An instructive example is shown in Fig. 9.7. This acquisition image of FU Ori has been created by combining 10000 frames with 4 ms integration time each. The companion is clearly visible slightly outside the first Airy ring. The north direction in Fig. 9.7 is rotated counterclockwise by 66.8° .

Figure 9.8:
Schematic MIDI configuration for the search and track of the fringe signal in the high-sense mode.



9.1.7 Fringe Search

Interferometric observations are done up to now with the high-sense mode configuration shown in Fig. 9.8. During these measurements the active optics has to be switched off. Otherwise, adjustments of the actuators could cause jumps in the optical path difference. When searching for fringes (Fig. 9.9), i.e. the typical modulation in the flux difference between the two interferometric beams, one of the piezo-mounted reflectors on the warm optical bench in front of MIDI (Section 7.3.1) is moved in overlapping scans of a few tens of microns from a few millimetres below to a few millimetres above the nominal value for zero OPD. The search range can be adjusted by the operator. If no fringe signals were found in a specified range, another OPD range can be covered with the scans. Under normal circumstances the found position is stable for hours within a fraction of a millimetre.

9.1.8 Fringe Track

With the fringe search procedure a fringe packet, i.e. the interferometric signal convolved by the wavelength-dependent transmission function of the atmosphere and/or a filter (see Fig. 8.3) is recorded when scanning close to zero OPD. This fringe packet theoretically contains all the required informations of the source geometry, especially since the MIDI measurements are performed almost always with a dispersive element and thus several fringe packets for different wavelengths can be recorded simultaneously. Obviously, when using this few measurements the errors are huge, because the statistics are very poor.

It is thus necessary to obtain many thousands of measurements by continuously scanning over or close to the real zero OPD position. To reduce the technical overhead and the amount of data only two subarrays of 171×41 pixels are read out for the prism (261×40 pixels for the grism). For the Z CMA measurements obtained with the prism (Fig. 9.10) the default integration time of 12 ms for each frame has been chosen. With the higher spectral resolution of the grism a three times longer integration time would have been required.

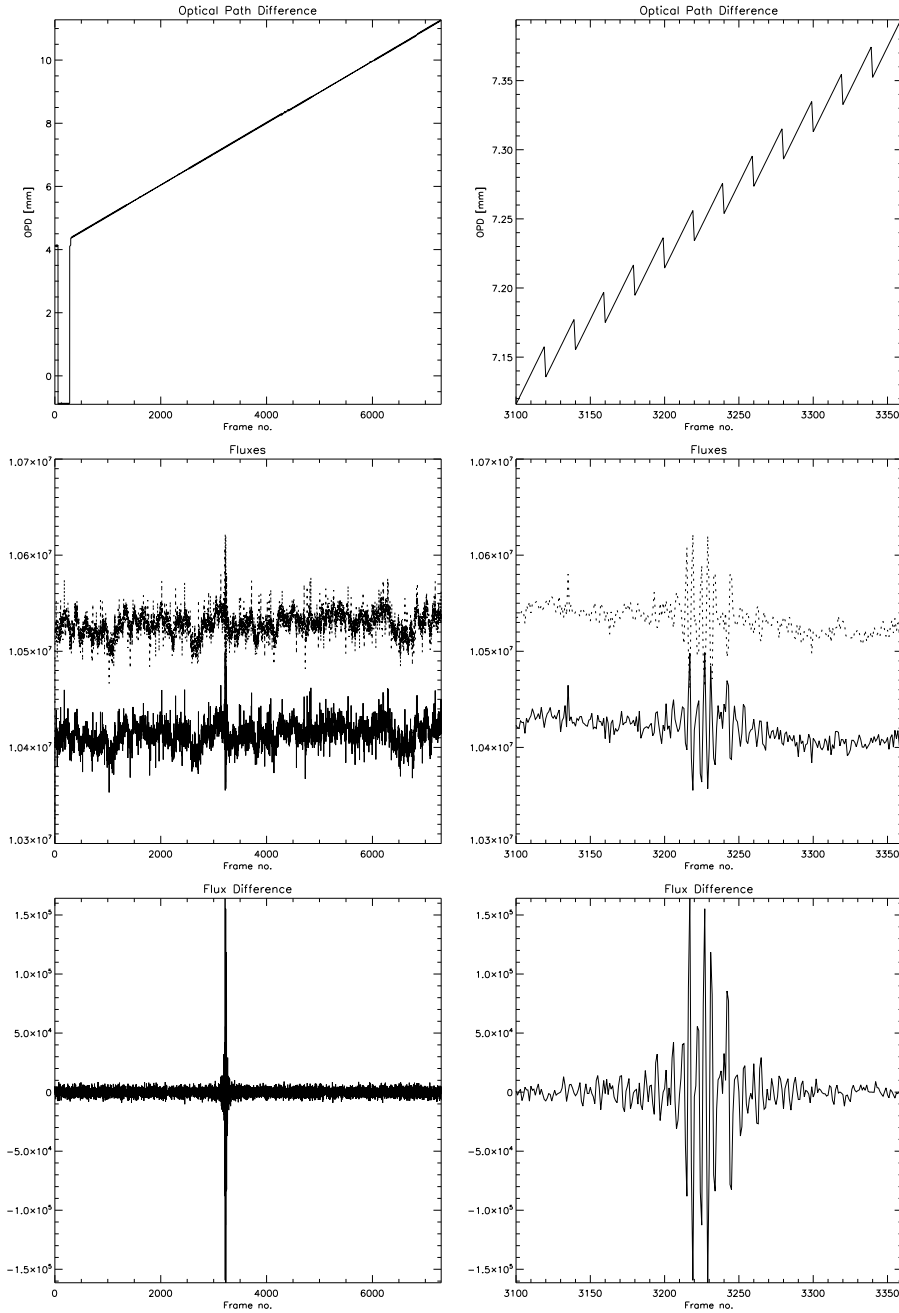


Figure 9.9: Interferometric observation of the source Z CMa on 4. Nov. 2004 to find the fringe signal. From top to bottom the optical path difference relative to nominal zero, the interferometric fluxes according to (8.18), (8.19) respectively, and the difference of the interferometric fluxes (8.22) are plotted versus the frame number. The 7300 frames have been observed within 365 overlapping scans with 20 frames each. The OPD covered by each scan is $41.6 \mu\text{m}$. The three right panels are detailed views of 260 frames (13 scans) centred around real zero OPD.

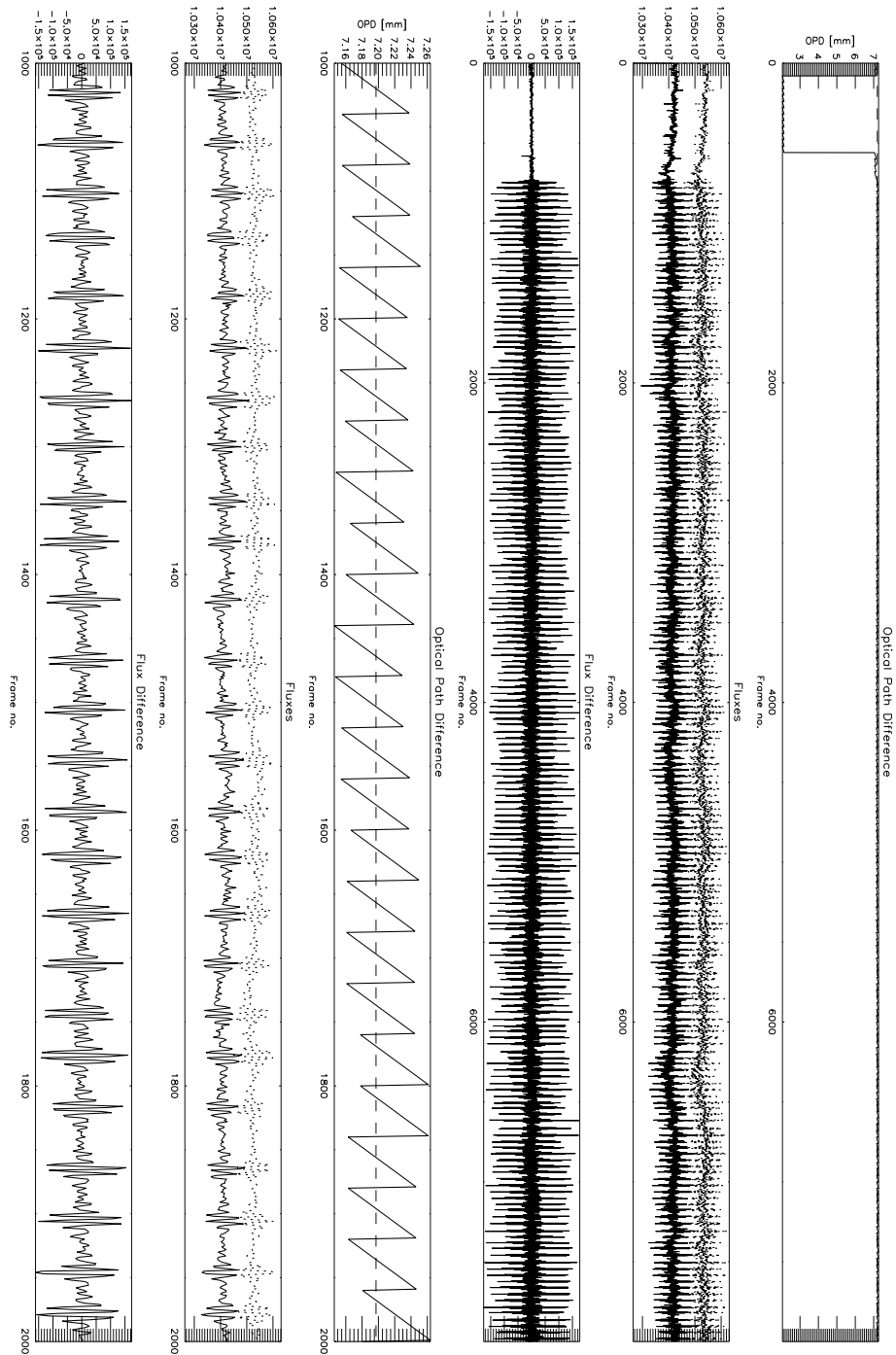


Figure 9.10: Same as the previous figure, but while tracking on average at an OPD-offset of $7197 \mu\text{m}$ relative to the nominal zero OPD. The total number of 8000 frames have been observed within 200 scans with 40 frames each. The OPD covered by each scan is $83.2 \mu\text{m}$. The three lower panels are detailed views of 1000 frames (25 scans).

Since the optical path difference changes due to the influence of the turbulent atmosphere on timescales of 100 ms in the mid-infrared, it is necessary to adjust the internal delaylines of MIDI by analysing the fringe signal. For this *internal fringe tracking* two different methods have been tested:

Undispersed Fringe Tracking searches for zero OPD in the *white light*, i.e. the light integrated over the whole observed wavelength range. In the integrated light only the relative height of the central fringe peak occurring for all wavelengths at zero OPD (Fig. 9.11) is preserved, while all other structures of the envelope (last plot in Fig. 8.4) with a wavelength-dependent position are more or less smeared out. This *white-light fringe* can thus be used as an indicator for zero OPD when bright sources are observed. Problems occur for faint sources. Furthermore, for very bright targets the probability is high that one of the sidelobes is tracked.

Dispersed Fringe Tracking uses the spectral informations of a frame to calculate how far from zero OPD the measurement is actually performed (Fig. 9.11). From several frames within a scan this method is able even to determine in which direction the white-light fringe can be found. The dispersed fringe tracking is thus more efficient than the undispersed mode in finding zero OPD. It is recommended for faint sources to allow a stable tracking, but also for very bright sources to distinguish between the signal at zero OPD and the sidelobes. Moreover, dispersed fringe tracking allows to track at different offsets from zero OPD. The data shown in Fig. 9.10 have been tracked at an offset of 0 from zero OPD ('pseudo' undispersed fringe tracking).

In the future *external fringe trackers* like FINITO (*Fringe tracking Instrument of NIce and TORino*) or PRIMA (*Phase-Referenced Imaging and Microarcsecond Astrometry*) will support or even substitute the internal fringe-tracking modes.

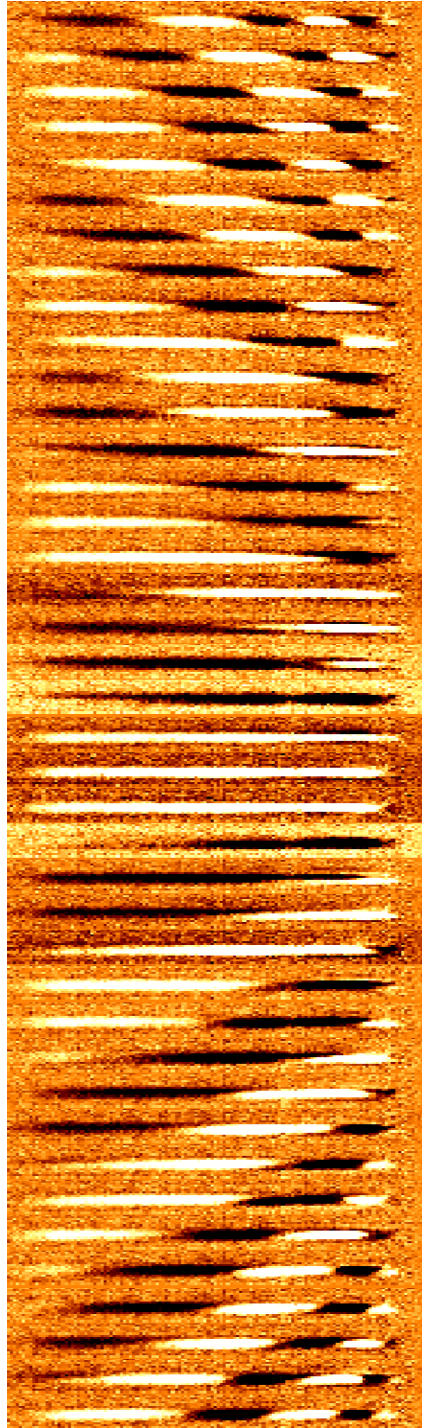


Figure 9.11: Variation in the difference of the flux signal during one scan (frame #1600 to #1639). Shorter wavelengths are plotted on the right.

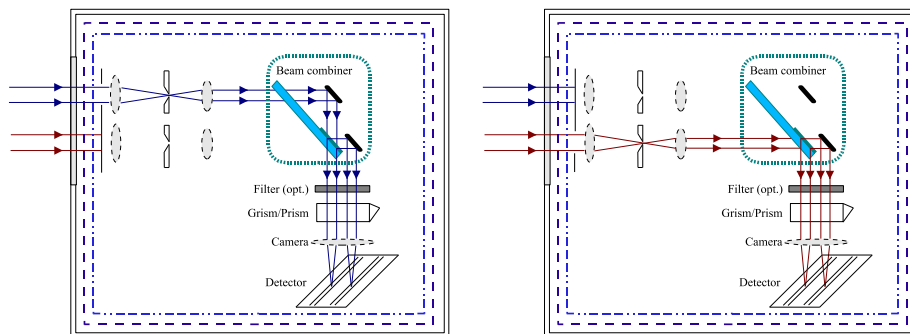


Figure 9.12: Schematic MIDI configurations for the two photometric measurements.

9.1.9 Photometry

Calculating the normalised visibility (8.34) means calculating the ratio of correlated flux to integrated flux. To determine the integrated flux separate photometric measurements of both beams with the beamcombiner inserted are necessary. While measuring beam A, beam B is blocked and vice versa (Fig. 9.12). The integration time should be equal to the integration time used for the interferometric measurements to allow an easy comparison, i.e. 12 ms for the prism data of Z CMa (Fig. 9.13). Since again many thousands of frames have to be obtained for the photometric measurements, only the two subarrays already used for the interferometric measurements are read out. Similar to the acquisition procedure chopping of the secondary mirror has to be used to allow a subtraction of the background. The active optics switched off during the interferometric measurements is now working again.

If a higher precision is needed, the science-phot mode (Section 7.3.4) is required that allows a simultaneous measurement of the photometric and interferometric channels. Besides the then necessary chopping of the telescopes during the fringe-tracking, other difficulties concerning the data reduction are introduced by this mode: the photometric beams pass different optical elements and are recorded in different areas of the detector when compared with the interferometric channels. Therefore, this mode has not been made available to the community yet and will probably be offered in the upcoming semesters only together with additional photometric measurements like those described above.

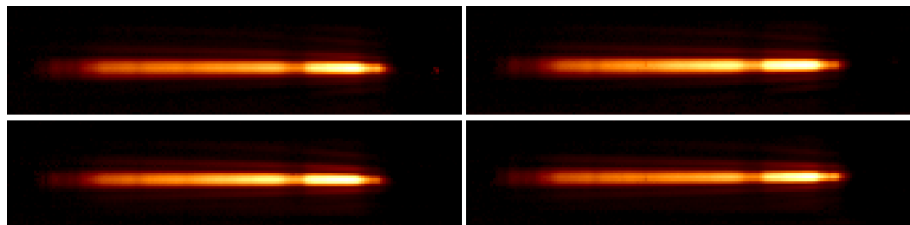


Figure 9.13: Photometric observation of the source Z CMa on 4. Nov. 2004. Shown are the two recorded spectra for the beam coming from UT4 (top) and from UT3 (bottom). Shorter wavelengths are recorded on the right side. The ozone absorption feature can be easily identified.

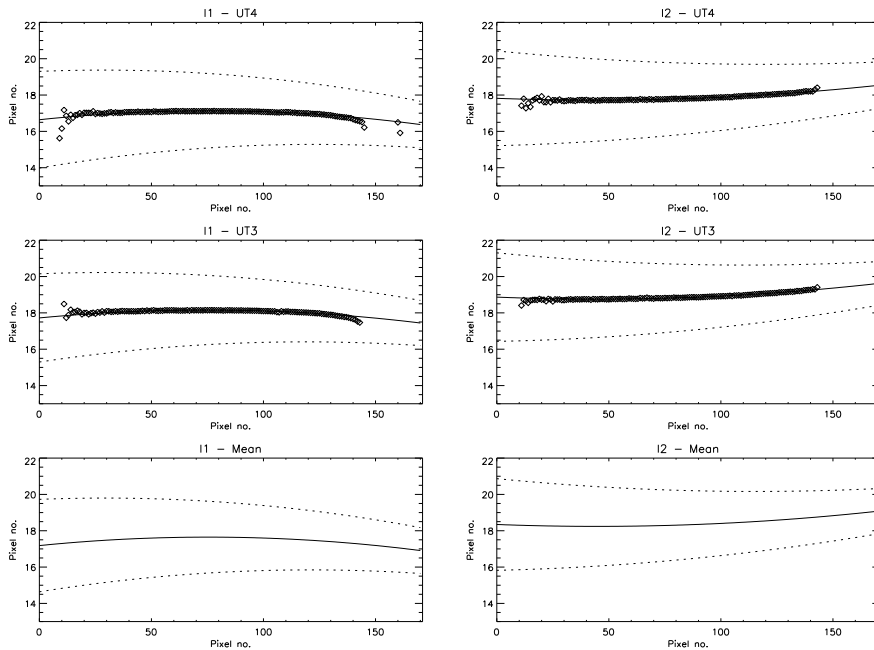


Figure 9.14: The four Gaussian fits and the calculated means for the two beams from UT3 and UT4.

9.2 Analysis

In this section the reduction of the interferometric data with the MPIA software package *MIA* (*MIDI Interactive Analysis*) that analyses the powerspectrum of the fringe signal will be described. A more detailed description of the IDL commands can be found as a tutorial at <http://www.mpia.de/MIDISOFT>. This website also offers a download of the package. It incorporates all the IDL and C routines required for both the analysis and the input/output of the data.

The Z CMA data presented in the last section will be used to illustrate the different steps. They have been obtained on 4. Nov. 2004 while UT3 and UT4 were feeding MIDI. The photometric data have been taken after the interferometric measurements were completed (=high-sense mode).

9.2.1 Masking the Windows

The interferometric and photometric signals are recorded almost in the middle of the subarrays. In a first step two Gaussian masks are created that suppress the areas that lie outside of the central region and are only illuminated by the thermal or tunnel background. It is possible to create the masks either from the interferometric or the photometric frames. We favour the photometric spectra, because in the currently offered high-sense mode they are chopped, while the interferometric frames suffer from the high background.

Methods to derive the masks from the interferometric frames, e.g. by checking which pixels vary rapidly during the scans, have been tested, but the probably best procedure to determine the masks uses Gaussian fits of the photometric

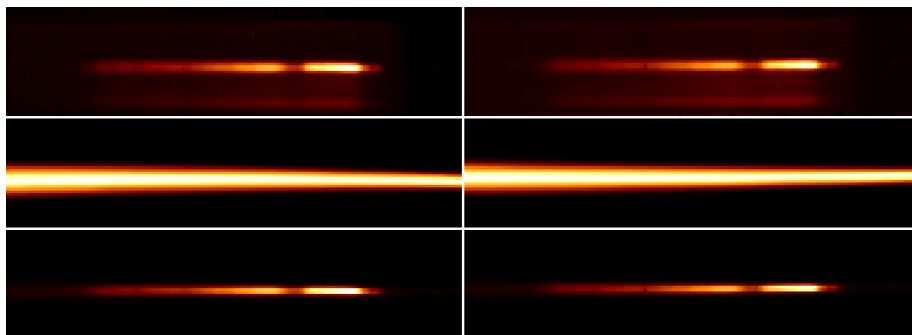


Figure 9.15: RMS of the interferometric data of Z CMa obtained with UT4 and UT3 on 4. Nov. 2004 (top). After a multiplication with the masks (middle) the background is reduced and the signal appears more prominent (bottom).

spectra. The fits for the Z CMa data are shown in the top and middle row of Fig. 9.14 and have been found by the following steps:

1. columnwise median smoothing to remove badpixels
2. columnwise one-dimensional Gaussian fit (centres marked by diamonds)
3. fit to the photo centres (solid line) with a second order polynomial
4. fit to the FWHMs of the Gaussians (dotted lines) with a first order polynomial

Afterwards the Gaussian masks are created from the averages of these Gaussian fits (last row in Fig. 9.14). How a mask influences the data is shown in Fig. 9.15, where for each beam the RMS of the interferometric data is multiplied with the corresponding mask.

9.2.2 The Fourier Amplitude

The next steps after multiplying the n_F interferometric frames of I_1 and the n_F interferometric frames of I_2 with the masks are schematically presented in Fig. 9.16 (the values given below in brackets are valid for the Z CMa data):

Compression The frames are compressed in the y-direction, i.e. the n_F (= 8000) two-dimensional images in both stacks are transformed into n_F one-dimensional arrays.

Flux Difference The one-dimensional arrays originating in beam I_2 are subtracted from those originating in beam I_1 , i.e. the flux difference is calculated.

Sorting The n_F one-dimensional arrays are arranged into the n_S (= 200) scans in which they have been taken, i.e. $n_f = n_F/n_S$ (= 40) arrays belonging to one scan are handled as a unit.

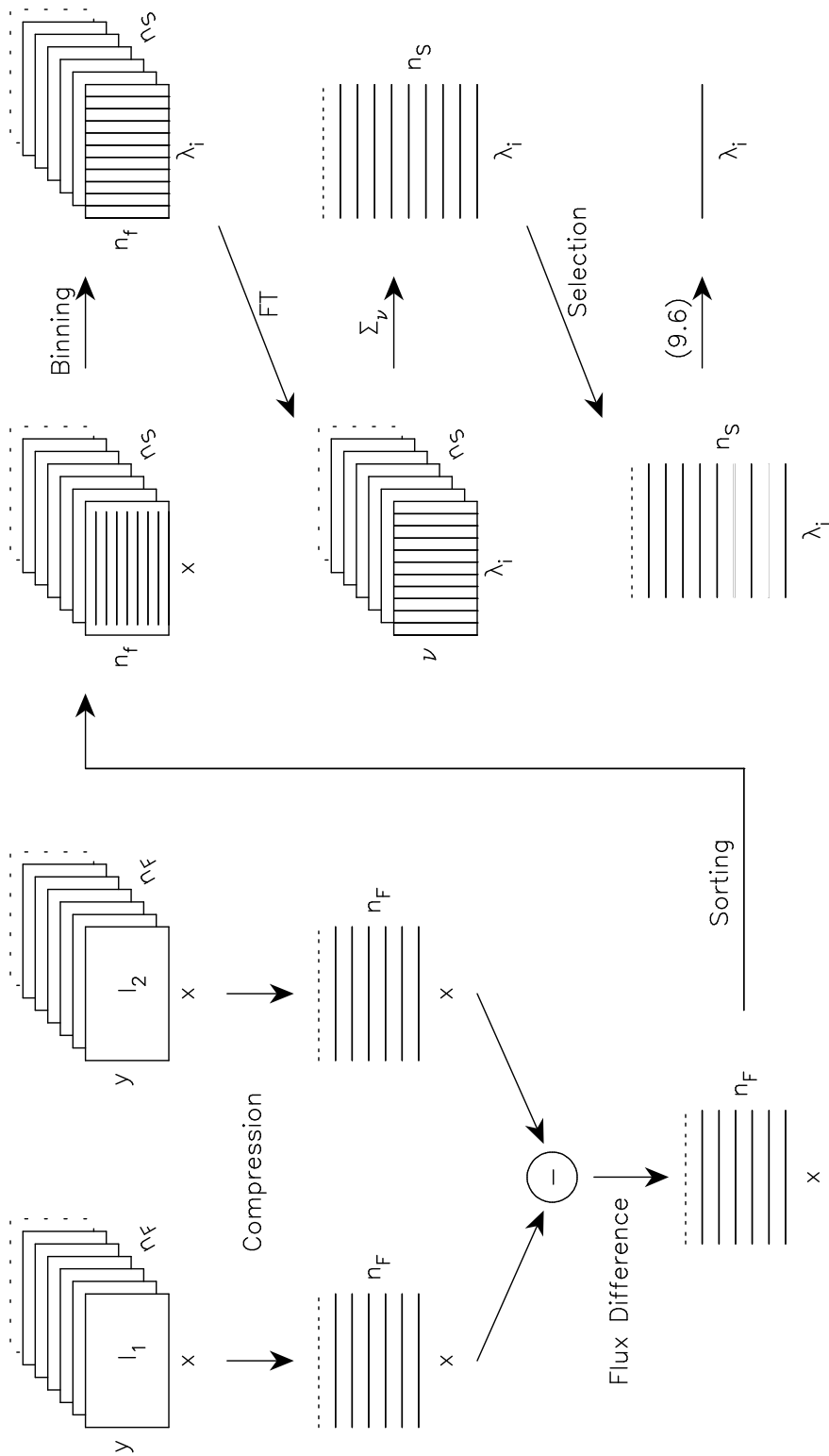


Figure 9.16: Data Flow of the MIA software package

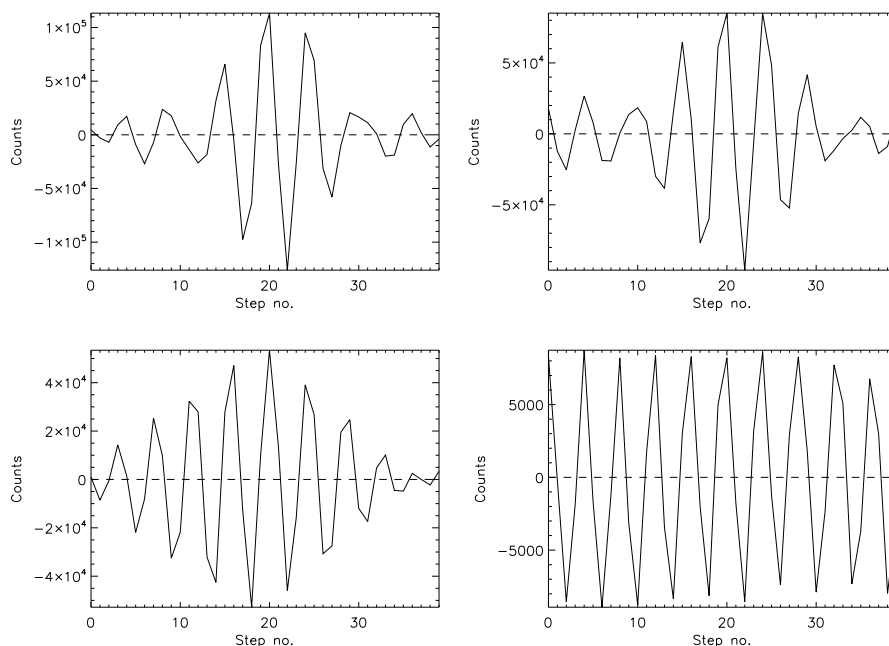


Figure 9.17: Measured interferometric signal in the Z CMa data from Nov. 4 for different bins: 41..133 pix (full wavelength range), 71..130 pix, 101..130 pix, and 127..130 pix. Shown are the detector counts versus the step number within a scan. All scans were averaged after their correlation has been optimised by shifting them in horizontal direction. The maximum is shifted to step number 20. Compare this with Fig. 8.3.

Binning The x-direction, representing the wavelength, is binned by default between $8\ \mu\text{m}$ and the $13\ \mu\text{m}$ into stripes λ_i with a width of 4 pix, i.e. the width of a point source image in undispersed mode. The wavelength calibration for the prism is

$$\lambda(x) = -0.0001539(x + x_0)^2 + 0.009491(x + x_0) + 15.451905, \quad (9.1)$$

where x is the pixel number relative to the left border of the subarray located at pixel number $x_0 = 120$ on the detector. The standard binning (Fig. 9.18) thus corresponds to twenty-three bins between $x = 41$ pix ($13\ \mu\text{m}$) and $x = 133$ pix ($8\ \mu\text{m}$). When a filter is used the wavelength range is further restricted.

Selection The value of the Fourier amplitude of the white-light fringe is used as criterion to decide whether a scan can be used for the determination of the correlated flux. ‘Good’ scans that have been performed at zero OPD show a high amplitude when compared with ‘bad’ scans obtained at another optical path difference or suffering from other errors.

The first step to derive the Fourier amplitude is the summation of the three-dimensional λ -f-S-cubes (Fig. 9.16) over the wavelength range between λ_{low} and λ_{high} . These boundaries are determined by the transmission curve of the inserted filter. When the filter wheel is open like for the Z CMa measurements,

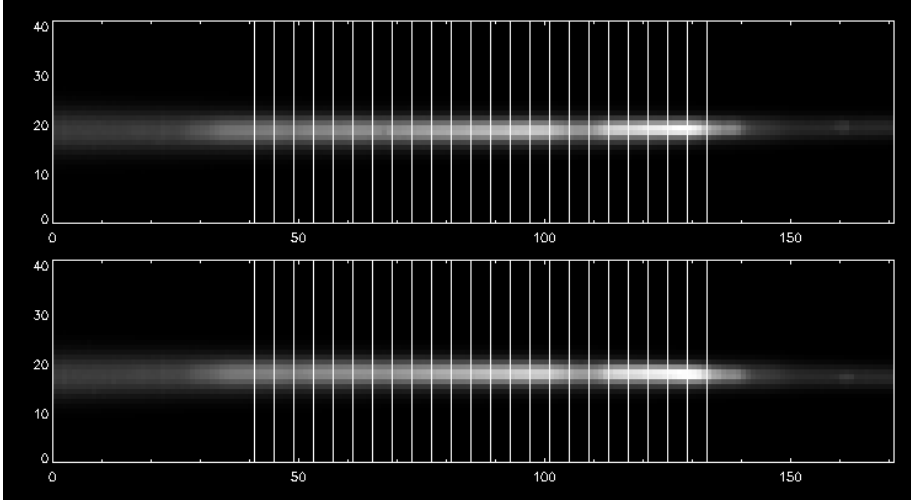


Figure 9.18: Standard binning of the Z CMA data into 23 bins

the transmission is limited by the atmosphere and thus the boundaries are $\lambda_{\text{low}} = 7 \mu\text{m}$ and $\lambda_{\text{high}} = 13 \mu\text{m}$. The summation is mathematically described by

$$I_{\text{int}}(f, s) = \sum_{\lambda_{\text{low}}}^{\lambda_{\text{high}}} I_{\text{int}}(\lambda, f, s), \quad (9.2)$$

where I_{int} is the interferometric flux (8.22) and f ($= 0 \dots n_f - 1$) the number of the frame within the scan s ($= 0 \dots n_s - 1$). Afterwards, the f -direction is transformed into the Fourier space, i.e. the discrete Fourier transform \mathcal{I}_ν for the spatial frequency ν is determined:

$$\mathcal{I}_\nu(\nu, s) = \frac{1}{n_f} \sum_{f=0}^{n_f-1} I_{\text{int}}(f, s) e^{-\frac{2\pi i}{n_f} \nu f}. \quad (9.3)$$

The frequency range, where the fringe signal should occur is given by

$$\frac{\Delta}{\lambda_{\text{high}}} \leq \nu \leq \frac{\Delta}{\lambda_{\text{low}}}, \quad (9.4)$$

where Δ is the change of the optical path difference during a scan. With the scanlength Δ ($= 83.2 \mu\text{m}$) $= n_f \cdot \delta$ ($= 4.16 \mu\text{m}$) the frequencies for the Z CMA data are limited to the range between 6.4 and 11.9. After summing the powerspectrum $|\mathcal{I}_\nu(\nu, s)|^2$ over the appropriate frequency range one can determine the *white-light fringe amplitude* A :

$$A(s) = \sqrt{4 \cdot \sum_{\nu_{\text{low}}}^{\nu_{\text{high}}} |\mathcal{I}_\nu(\nu, s)|^2}. \quad (9.5)$$

The additional pre-factor in the above equation originates in the property of the Fourier transform that real functions like the fringe signal are hermitic in

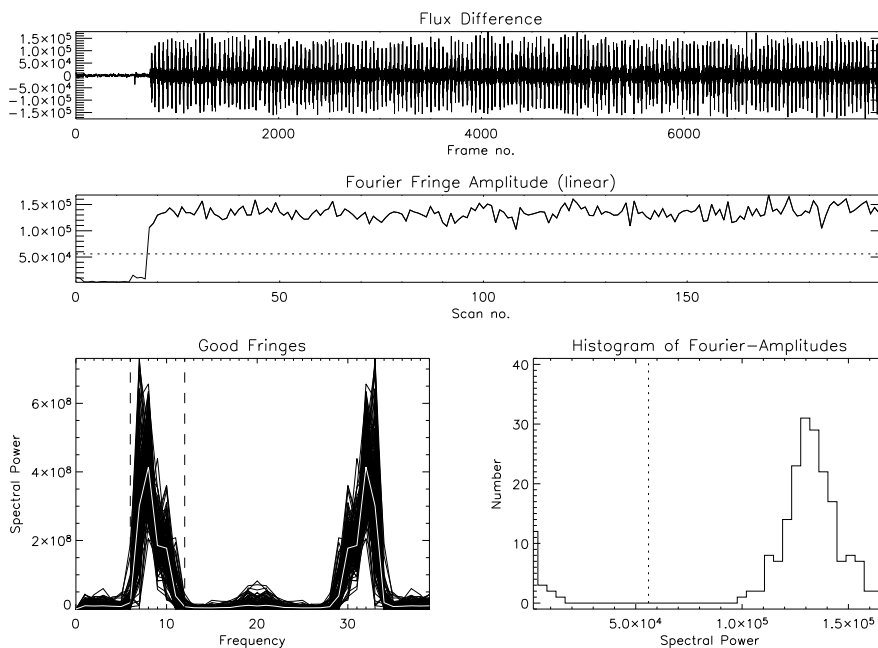


Figure 9.19: Selection of the good scans obtained during the observation of Z CMa. Displayed are the difference of the interferometric fluxes as function of the frame number, the Fourier amplitude of the white-light fringe for each scan, the spectral power of the fringe signal as function of the frequency, and the histogram of the white-light Fourier amplitude measured in the scans. The dotted line divides the few bad scans on the left side from the good scans on the right. It is equivalent to the dotted line in the central plot. In the lower left plot the predicted frequency band (9.4) is marked by dashed lines. The white curve is the mean of the different powerspectra. The Fourier transform is responsible for the symmetry with respect to the central frequency $\nu = 20$.

the Fourier space (8.31). The powerspectrum is thus symmetric around $\nu = 0$ or around the central frequency $\nu = n_f/2$ due to the periodicity of the discrete Fourier transform (lower left plot in Fig. 9.20). The summation of the powerspectrum between ν_{low} and ν_{high} thus takes only one quarter of the squared fringe amplitude into account. This loss is compensated by the additional factor in (9.5).

The results are plotted in Fig. 9.19 as function of the scan number. The threshold that divides the good scans with a high signal from the bad scans with a low signal is marked by the dotted line. How well the good scans are separated from the bad scans is shown in the histogram. There is a huge gap between the nicely distributed well tracked and the other scans.

The situation is more complicated when dispersed fringe tracking with an OPD offset from zero OPD is used, because a compensation of the reduced signal is required. This compensation can be done by dividing the wavelength range $\lambda_{\text{high}} \dots \lambda_{\text{low}}$ into a number of bins. For each wavelength bin (9.5) is performed separately.

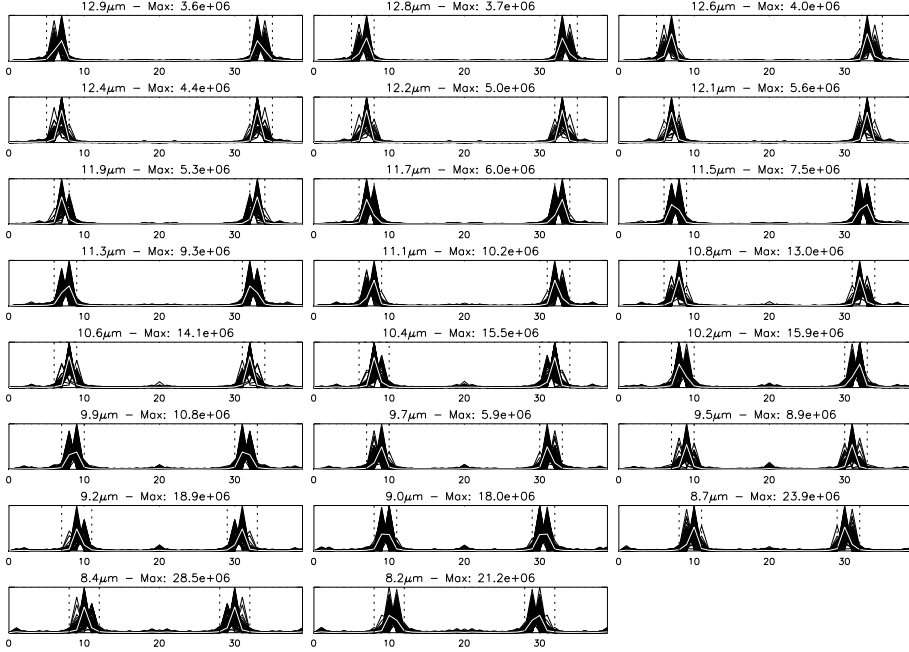


Figure 9.20: The powerspectra of the good scans calculated for the default twenty-three wavelength bins. The central wavelength is given in the title of each plot as well as the peak value (all plots are normalised). The frequency bands are marked by dashed lines and the means by white curves.

9.2.3 Interferometric Flux

In Fig. 9.20 the good scans are calculated for the default twenty-three wavelength bins visualised in Fig. 9.18. Plotted are the powerspectra versus the frequency. Other binnings can be chosen. The interferometric flux $I_{\text{int}}^{\text{good}}$ within one of those wavelength bins between λ_1 and λ_2 is given by

$$I_{\text{int}}^{\text{good}}(\lambda_1, \lambda_2) = \frac{2}{t} \sqrt{\frac{1}{N_{\text{g}}} \sum_{\text{good}} \sum_{\nu_1}^{\nu_2} |\mathcal{I}_{\nu}^{\text{bin}}(\nu, s)|^2}, \quad (9.6)$$

where the sum adds up all N_{g} good scans within a bin and t is the detector integration time not explicitly taken into account up to now. When the background noise contribution cannot be neglected, equation (9.6) transforms into

$$I_{\text{int}}^{\text{good}}(\lambda_1, \lambda_2) = \frac{2}{t} \sqrt{\frac{1}{N_{\text{g}}} \sum_{\text{good}} \sum_{\nu_1}^{\nu_2} |\mathcal{I}_{\nu}^{\text{bin}}(\nu, s)|^2 - \frac{1}{N_{\text{n}}} \sum_{\text{noisy}} \sum_{\nu_1}^{\nu_2} |\mathcal{I}_{\nu}^{\text{bin}}(\nu, s)|^2}. \quad (9.7)$$

The N_{n} noisy scans from which the background can be determined have to be obtained far enough from zero OPD to ensure that no correlated flux has been detected. This is the reason for the big jump in the OPD in Fig. 9.10 that is performed before the tracking starts.

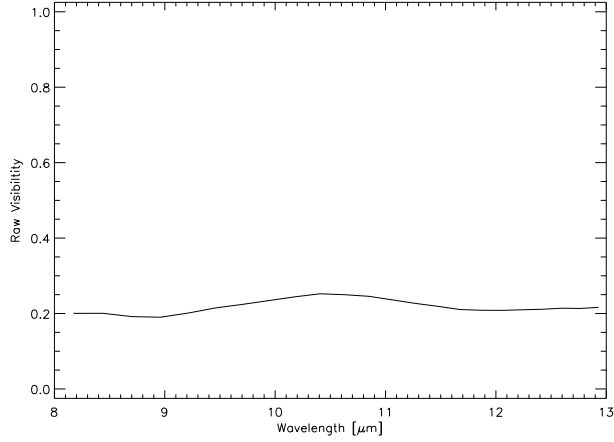


Figure 9.21: The raw visibility of Z CMA.

9.2.4 Photometric Flux

The photometric flux is derived by subtracting the sky frames of the chopped photometric measurements from the on-source frames. This leads to four spectra $P_{A,1}$, $P_{A,2}$, $P_{B,1}$, and $P_{B,2}$ (Fig. 9.13), where the first index represents the incoming beam and the second the detector window. The flux of the spectra as function of the x-coordinate, the wavelength, respectively, is given by

$$I_{i,j}(x) = \frac{1}{t} \sum_y P_{i,j}(x,y) M_j(x,y) \quad , \quad i = A, B, \quad j = 1, 2, \quad (9.8)$$

where t is again the detector integration time. The masks M_1 and M_2 were derived from the photometric frames and have been already used for the interferometric frames. When integrating $I_{i,j}(x)$ along the x-direction one gets the total photometric flux of the beam i in the subarray j . The correction factor $\sqrt{I_A I_B}$ introduced in equation (8.35) for the visibility is calculated by

$$\begin{aligned} \sqrt{I_A(x) I_B(x)} &= \frac{1}{t} \left[\sum_y \sqrt{P_{A,1}(x,y) P_{B,1}(x,y) M_1(x,y)} + \right. \\ &\quad \left. \sum_y \sqrt{P_{A,2}(x,y) P_{B,2}(x,y) M_2(x,y)} \right] \\ &= \sqrt{I_A(\lambda) I_B(\lambda)} . \end{aligned} \quad (9.9)$$

9.2.5 Raw Visibility

After inserting (9.7) and (9.9) into (8.35) one obtains the so-called *raw visibility* in the wavelength range between λ_1 and λ_2 :

$$V(\lambda_c) = \frac{I_{\text{int}}^{\text{good}}(\lambda_1, \lambda_2)}{2 \sum_{\lambda=\lambda_1}^{\lambda_2} \sqrt{I_A(\lambda) I_B(\lambda)}} . \quad (9.10)$$

The central wavelength λ_c is given by

$$\lambda_c = \frac{\lambda_1 + \lambda_2}{2} . \quad (9.11)$$

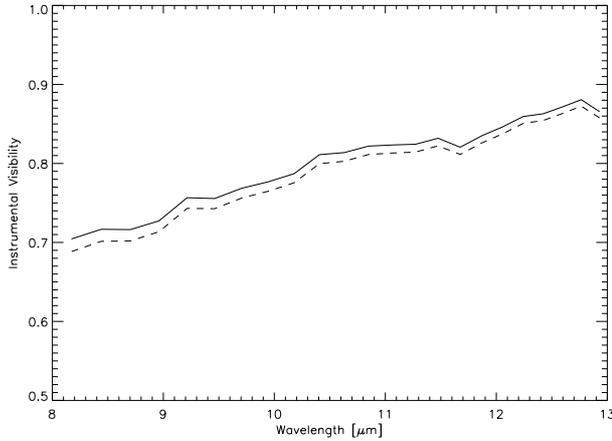


Figure 9.22: The raw visibility (dashed) of HD 50778 and the instrumental visibility (solid) derived from it.

The result for the observation of Z CMa is presented in Fig. 9.21. This visibility is called ‘raw’, because until now it has been assumed that the interferometric measurements are not affected by MIDI and the VLTI, what is obviously not true.

9.2.6 Instrumental Visibility

The efficiency with which a certain spatial frequency $\vec{u} = (u, v)$ is transmitted by an optical instrument is measured by the *Modulation Transfer Function* (MTF), defined as the modulus of the *Optical Transfer Function* (OTF). The MTF is mathematically described by the autocorrelation of the pupil amplitude distribution $G(\xi, \eta)$ that determines the strength of the elementary waves originating in the pupil of the instrument according to the *Fresnel-Huygens principle*:

$$\text{MTF}(\vec{u}) = \int \int G(\xi, \eta) G(\xi + \lambda u, \eta + \lambda v) d\xi d\eta . \quad (9.12)$$

The elementary waves form the image brightness distribution I by interfering in the focal plane. With calligraphic letters indicating Fourier transforms one finds (Leinert, 1994)

$$I(x, y) = \mathcal{G}(x, y) \mathcal{G}^*(x, y) . \quad (9.13)$$

It can be shown that the Fourier transform \mathcal{I} of the image brightness distribution I is equal to the MTF:

$$\text{MTF}(\vec{u}) = \mathcal{I}(\vec{u}) . \quad (9.14)$$

The normalised MTF of a circular aperture with diameter D is given by (Leinert, 1994)

$$\text{MTF}(\vec{u}) = \frac{2}{\pi} \left[\arccos\left(\frac{\lambda \vec{u}}{D}\right) - \frac{\lambda \vec{u}}{D} \cdot \sqrt{1 - \left(\frac{\lambda \vec{u}}{D}\right)^2} \right] \quad (9.15)$$

and thus varies almost linearly between 1 for the largest structures ($\vec{u} = 0$) and 0 for the cut-off frequency ($\vec{u}_c = \frac{D}{\lambda}$). A circular aperture thus operates as a low-pass filter cutting off frequencies $\vec{u} > \vec{u}_c$.

The MTF of the VLTI should follow this general trend, because an interferometer mimics a circular aperture with a diameter given by the projected

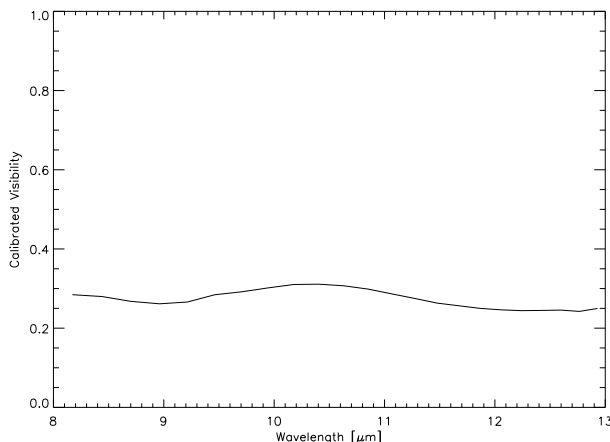


Figure 9.23: The calibrated visibility of Z CMa.

baseline length B . The measured spatial frequency B_λ varies with the wavelength λ like

$$B_\lambda = \frac{B}{\lambda}. \quad (9.16)$$

Therefore, one would expect a decreased visibility when going from longer to shorter wavelengths, i.e. when increasing the spatial frequency B_λ . However, the exact instrumental influence as function of the wavelength can only be determined empirically by observing an astronomical source for which the theoretical visibility is known. The usual way is to observe immediately before or after the science target a star whose diameter has been measured before.

In the case of Z CMa the instrumental visibility is determined by observing the calibrator HD 50778 with a diameter of $d = 3.76 \pm 0.04$ mas immediately after the science target. The dashed line in Fig. 9.22 represents its raw visibility calculated by the same procedure applied to the Z CMa data before. The instrumental visibility displayed as solid line in Fig. 9.22 is derived by dividing the raw visibility by the theoretical visibility of a uniform disk with diameter d according to equation (8.43).

As expected the instrumental visibility shows a more or less constant positive slope. It has been found that this slope is characteristic of the MIDI/VLTI infrastructure and is thus preserved over long periods. Otherwise, the absolute values change even during a night. Since the adaptive optics system MACAO has been installed, the instrumental visibility is higher by ~ 0.2 over the whole wavelength range. The stability has been improved too. Now the instrumental visibility seems to be stable over a whole night for a certain baseline configuration.

9.2.7 Calibrated Visibility

The calibrated visibility V_{cal} of Z CMa (Fig. 9.23) is simply obtained by dividing the raw visibility V_{raw} (Fig. 9.21) by the instrumental visibility V_{ins} (Fig. 9.22):

$$V_{\text{cal}}(\lambda) = \frac{V_{\text{raw}}(\lambda)}{V_{\text{ins}}(\lambda)}. \quad (9.17)$$

9.3 Planning an Observation

9.3.1 Science Targets

Hopefully, the last chapters have demonstrated that observations with a long-baseline interferometer are very complex both from a technical and an observational point of view. However, an observer may never come into contact with many of the discussed details. What has to be considered by an astronomer when planning an observation with MIDI? Here the most important questions that have to be answered are summarised:

- What scientific question can be solved by observing the visibility of the target?
- Allows the declination of the object a reasonable observation at the VLTI ($\delta < +25^\circ$)?
- Is the flux high enough (MIDI requires a correlated flux, i.e. the total flux multiplied by the visibility of the object, higher than 1 Jy in the N-band for the prism, i.e. $m_N \leq 4$ mag, and above 10 Jy for the grism, i.e. $m_N \leq 1.5$ mag, when operated with the UTs)?

Besides these classical constraints that are relevant for all astronomical observations, a positive answer to the question

- Is the target itself or another object within a radius of 1 arcmin around the target brighter than 17 mag in the V-band?

allows the usage of the MACAO units. These adaptive optics systems improve the performance of the VLTI due to an enhanced guiding of the beams. Although observations in the mid-infrared are not affected by the moon, MACAO and the active optics systems of the UTs work in the visible and are thus influenced by lunar straylight. A separation between the science target and the moon below 10° should be avoided. Last but not least the interferometric limitations have to be taken into account.

- Is the length of the projected baseline sufficient to resolve the relevant structures? Are the structures overresolved?
- When offers the chosen baseline the suitable position angle?

It has to be emphasised here that the last questions make interferometric observations time-critical. As an example the changing appearance of the baseline UT3-UT4 as seen from Z CMa located at a declination of $\delta = -11.5^\circ$ is visualised in Fig. 9.24. The images have been created with a Tcl/Tk-based script called `Cheddar`. It calculates the position angle and length of the projected baseline when the coordinates of a target are provided. Since the results can also be displayed as a timeline, this tool is ideally suited to create a detailed schedule of the observations. A tutorial and a download link can be found at <http://www.mpia.de/MIDISOFT>.

As a rule of thumb one hour is necessary to obtain a calibrated visibility, i.e. one observation of the target and another of the calibrator.

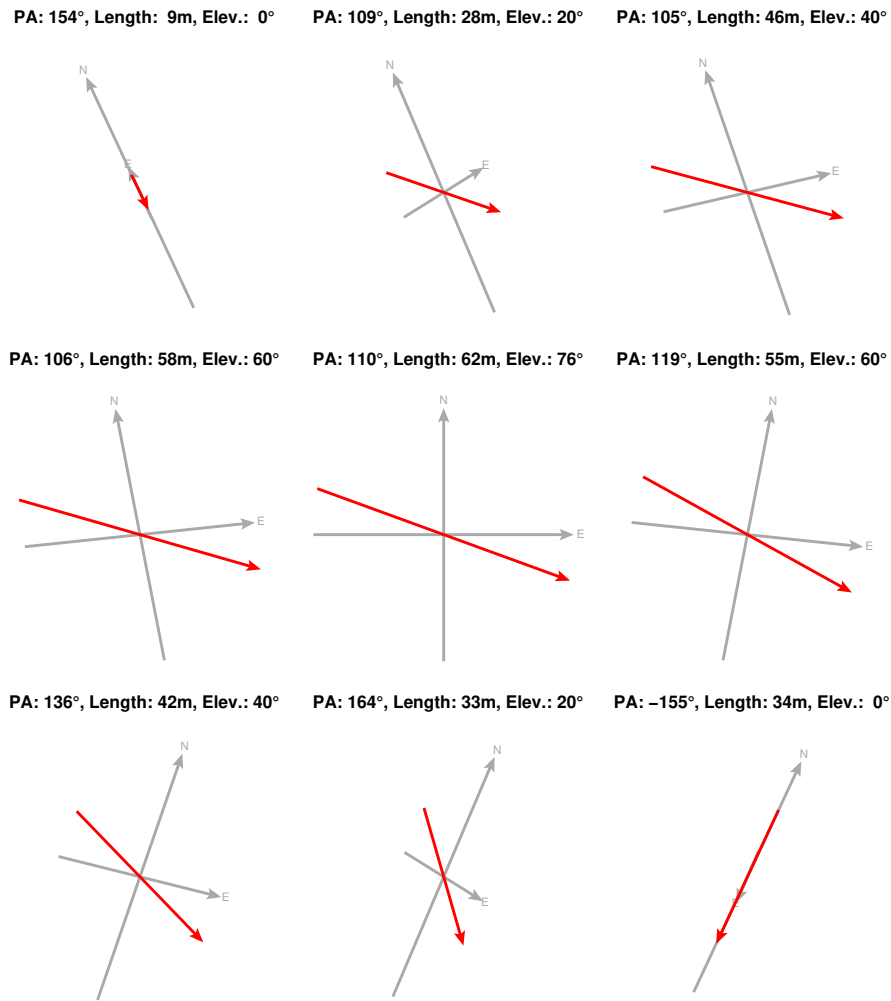


Figure 9.24: The changing appearance of the baseline UT3-UT4 as seen from Z CMa ($\delta = -11.5^\circ$) between rise (top left) and set (bottom right). The time sequence spans more than 12 hours. The numbers in the title give the position angle of the projected baseline, its length, and the elevation of the target. The central image shows the projected baseline, when Z CMa culminates.

9.3.2 Calibrators

The Internet-based tool *CalVin* to select appropriate single stars as calibrators is offered by ESO at <http://www.eso.org/observing/etc>. Calibrators should be chosen with respect to

- their proximity to the science target,
- the error of their measured size (important especially for long baselines),
- their mid-infrared flux, and

- their magnitude in the visual (if the science target has to be observed without MACAO, the calibrator should be observed also without the adaptive optics system, because the influence of MACAO leads to a different instrumental visibility)

None of these selection criteria is really strict. So the rare spectrophotometric calibrators with known diameter can always be included in an observation sequence. They allow a calibration of the flux in the acquisition images and the spectrum in the photometric data of the science targets.

However, all available informations about structures in the environment of the calibrators like companions or disks should be carefully taken into account to avoid calibrators that cannot be appropriately described by uniform disks. For example we found in the literature for some well observed calibrators spectroscopic companions with a critical separation or orbital motions of the photometric centre. The unprecedented resolution offered by MIDI in the mid-infrared will probably reject additional stars from the calibrator list.

9.4 Application I: The Binary Z CMa

9.4.1 Introduction

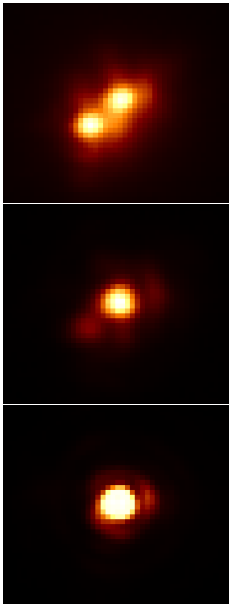


Figure 9.25: Observations with NAOS/CONICA of Z CMa from 15. Dec. 2002. The images have been taken in the J-, Ks-, and L'-band.

Hartmann et al. (1989) suggested that the variable ($m_V \sim 9 - 11$ mag) pre-main-sequence star Z CMa (HD 53179, IRAS 07013-1128) harbours a luminous accretion disk, similar to the FU Ori variables (FUors). These young objects designated after their prototype FU Ori (Fig. 9.9) exhibit optical brightening of several magnitudes caused by a rapid temporal increase of the disk accretion rate. In a scenario presented by Hartmann & Kenyon (1996) the material piles up in the inner disk until its column density becomes high enough to switch on a thermal instability. Observations of the outbursts revealed that both ‘slow’ lightcurves rising over several decades (V1515 Ori, V346 Nor) and ‘fast’ lightcurves increasing over a few months (FU Ori, Z CMa, V1057 Cyg) exist. Since many FUors have been found to be binaries like FU Ori itself (Wang et al., 2004) it is discussed whether a passage of a close companion influences the timescale on which eruptions occur (Reipurth & Aspin, 2004).

The photometric and spectroscopic properties of Z CMa show some similarity with those of the FUors. During the quiescent state an absorption spectrum is dominant and the spectrum can be interpreted as that of an optically thick accretion disk (Hartmann et al., 1989). Otherwise, the spectrum of Z CMa shows many non-typical narrow optical emission lines especially during the outbursts (van den Ancker et al., 2004).

The detection of a close companion separated by only $0.1''$ at a position angle of 120° by Koresko et al. (1991)

can explain this strange finding easily. Three images of the young binary system taken with NAOS/CONICA in December 2002 are shown in Fig. 9.25. Koresko et al. (1991) found that the south-eastern component is brighter in the visible wavelength range. At near-infrared wavelengths the north-western star is dominating. The emission of both stars is characterised by circumstellar material. No signs of stellar photospheres have been detected. The south-eastern component was identified as the FUor inferred by Hartmann et al. (1989), while the north-western component is most likely a Herbig Be star surrounded by an asymmetric dust envelope (Garcia et al., 1999). This star is responsible for the emission lines in the spectrum. Its visible and near-infrared light is escaping from the envelope probably by scattering off the walls of a jet-blown cavity. A linear feature found by Millan-Gabet & Monnier (2002) seems to trace one of this inner walls. Moreover, jets (Poetzel et al., 1989) and bipolar molecular outflows (Evans et al., 1994) have been discovered.

9.4.2 Journal of Observations

During our *Guaranteed Time Observations* (GTO) in November 2004 we recorded fringes of Z CMa at the end of two nights. In the morning of the 2nd November 2004 the baseline UT2-UT4 has been used with a projected baseline length of 85.8m at a position angle of 78.1°. Two days later in the morning of the 4th November UT3-UT4 was in operation. When recording Z CMa the projected baseline had a length of 62.2m at a position angle of 110.4°. A complete journal of the observations of Z CMa and its calibrator HD 50778 is given in Tab. 9.1. Also the other calibrators successfully observed during these two nights are listed therein. The astrophysical properties of the objects are summarised in Tab. 9.2.

9.4.3 Results

In Fig. 9.26 the raw visibilities of the four calibrators successfully observed during the first night are plotted as dashed lines. The instrumental visibilities are derived by correcting the finite size of the stars. They are overplotted as solid lines. The instrumental visibilities of the calibrators observed during the second night are shown in Fig. 9.28. Since the projected baseline was much shorter in the second night the corrections of the raw visibilities of the calibrators are smaller when compared with the first night.

Obviously, there is something wrong with the calibrator HD 188603. Its visibility is too high. Since it is impossible that a spatial structure of the calibrator increases the visibility, probably a problem with the photometry occurred. The remaining ozone feature around 10 μm together with the high airmass (Tab. 9.1) supports this hypothesis. Otherwise, the visibility is much flatter than those of the other calibrators. This different slope of the visibility cannot be explained by the photometry alone. However, this calibrator should not be used unless the quality of the calibrator has been checked. The other calibrators are in good agreement with each other. Also the calibrators HD 31421 and HD 50778 that have been measured in the first night (Fig. 9.26) are consistent with these results. Probably due to an underestimated photometric flux, the slopes of the visibilities of HD 37160 and HD 61935 that have been observed also in the first

Table 9.1: Journal of observations. Listed are all successful observations of Z CMa, T Tau N, T Tau S, and the calibrators in the nights starting on the 1st and 3rd of November 2004. All observations have been performed with the prism and in the high-sense mode.

Universal Time	Object	Baseline*		Airmass*	Acquisition Frames	Interferometric Frames	Photometric Frames
		[m]	[deg]				
1./2. Nov. 2004 (UT2 – UT4)							
05:10 - 05:36	T Tau N	85.0	87.9	1.44	1000×4 ms	16000×12 ms	2×2500×12 ms
06:10 - 06:37	HD 31421	87.7	84.5	1.28	1000×4 ms	16000×12 ms	2×2500×12 ms
07:08 - 07:41	HD 37160	89.1	82.8	1.21	10000×4 ms	16000×12 ms	2×2500×12 ms
07:41 - 08:09	Z CMa	85.8	78.1	1.06	1000×4 ms	16000×12 ms	2×2500×12 ms
08:09 - 08:37	HD 50778	88.6	80.2	1.03	1000×4 ms	16000×12 ms	2×2500×12 ms
08:37 - 09:03	HD 61935	87.2	79.6	1.05	1000×4 ms	16000×12 ms	2×2500×12 ms
3./4. Nov. 2004 (UT3 – UT4)							
00:01 - 00:26	HD 178345	57.0	145.6	1.36	1000×4 ms	20000×12 ms	2×5000×12 ms
02:10 - 02:47	HD 188603	45.5	168.6	2.27	1000×4 ms	16000×12 ms	2×5000×12 ms
02:47 - 03:54**	HD 25604	60.7	117.1	1.81	1000×4 ms	16000×12 ms	2×5000×12 ms
04:36 - 05:04	T Tau S	62.3	111.4	1.50	1000×4 ms	12000×12 ms	2×5000×12 ms
05:04 - 05:29	HD 20644	59.0	101.5	1.69	1000×4 ms	12000×12 ms	2×3000×12 ms
07:18 - 07:36	HD 37160	61.0	107.4	1.21	1000×4 ms	8000×12 ms	2×2000×12 ms
08:36 - 09:00	Z CMa	62.2	110.4	1.03	1000×4 ms	8000×12 ms	2×2000×12 ms
09:00 - 09:23	HD 50778	61.0	112.6	1.04	1000×4 ms	8000×12 ms	2×2000×12 ms
*: at the beginning of the fringe-tracking					**: affected by problems to find zero OPD		

Table 9.2: The objects observed to determine the visibilities of Z CMa.

Object	J2000.0		N**	V	Diameter	Other
	α	δ				
Z CMa	07 03 43.17	- 11 33 06.3	126.6	9.9		
HD 50778	06 54 11.41	- 12 02 18.9	17.3	4.1	3.76 ± 0.04	ϑ CMa
Other Calibrators						
HD 20644	03 20 20.38	+29 02 54.5	14.7	4.5	3.62 ± 0.15	
HD 25604	04 04 41.70	+22 04 55.0	5.1	4.4	1.88 ± 0.05	37 Tau
HD 31421	04 56 22.29	+13 30 52.1	9.3	4.1	2.49 ± 0.06	σ_2 Ori
HD 37160*	05 36 54.39	+09 17 26.2	6.5	4.1	2.02 ± 0.02	ϕ_2 Ori
HD 61935	07 41 14.85	- 09 33 04.1	7.1	3.9	2.21 ± 0.01	α Mon
HD 178345	19 10 01.76	- 39 20 27.0	8.6	4.1	2.46 ± 0.13	β CrA
HD 188603	19 56 56.83	- 27 10 11.6	11.4	4.5	2.86 ± 0.29	

*: spectrophotometric calibrator **: IRAS $12 \mu\text{m}$

night are too steep when compared with those of the other two calibrators of that night.

This brief discussion explains why it is useful to calibrate the raw visibility of a science target with more than one calibrator. Therefore, usually all calibrators of one night are used to find the error introduced by the calibration. The calibrated visibilities derived for Z CMa by following this strategy are plotted in Fig. 9.27 and Fig. 9.29. The upper panels display the results when the raw visibility is divided by the individual instrumental visibilities. In the lower panels the means are plotted. The errorbars represent the standard deviation. In the following discussion the visibility calibrated with HD 188603 that contributes the largest calibration errors will be ignored.

9.4.4 Fitting a Binary Model

In Fig. 9.30 and Fig. 9.31 the calibrated visibilities are plotted after substituting the wavelength by the spatial frequency u_{proj} along the position angle of the projected baseline B_{proj} according to

$$u_{\text{proj}} = \frac{B_{\text{proj}}}{\lambda} . \quad (9.18)$$

The errors of the visibilities are dominated by the calibration errors that are indicated by the errorbars in the both figures. With respect to these errors the photometric errors have been found to be negligible, especially when the sources are fairly bright.

To derive the binary parameters of Z CMa a non-linear least squares fit of the simple function

$$f = (a_0 + a_1 u_{\text{proj}}) \cdot \frac{\sqrt{1 + a_2^2 + 2a_2 \cos(2\pi a_3 u_{\text{proj}})}}{(1 + a_2)} \quad (9.19)$$

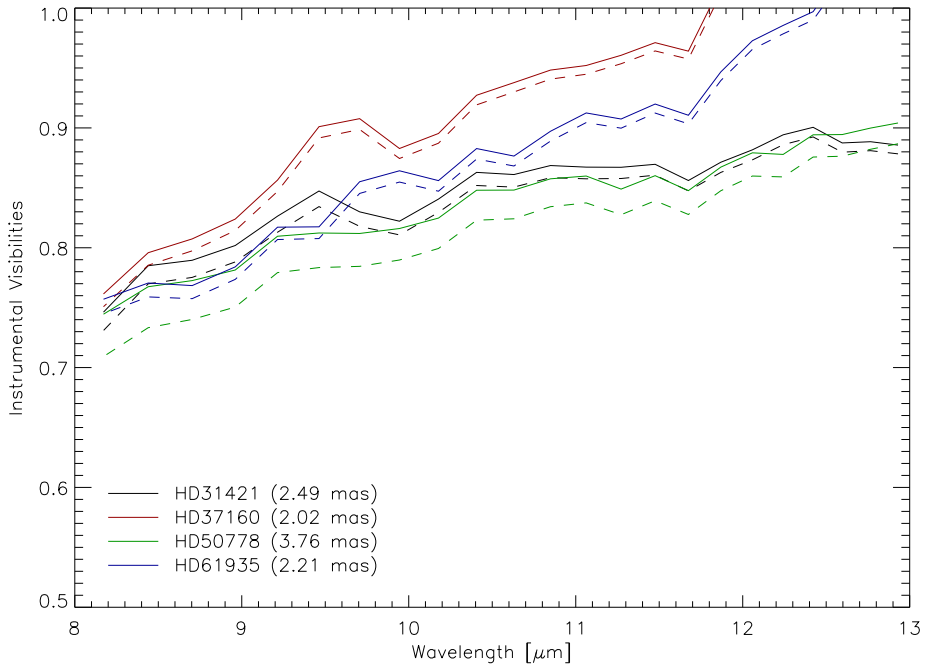


Figure 9.26: The instrumental visibilities (solid lines) derived from the four calibrators observed during the first night. The raw visibilities of the calibrators are also plotted (dashed lines).

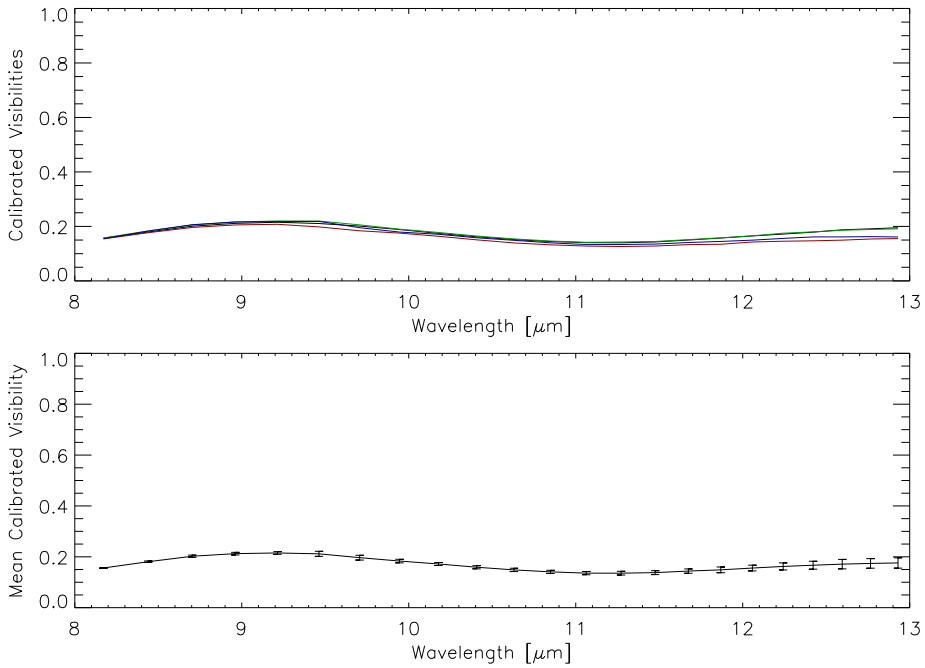


Figure 9.27: The calibrated visibilities (top) and their mean (bottom) for the first night. The errorbars represent the standard deviation of the calibrated visibilities.

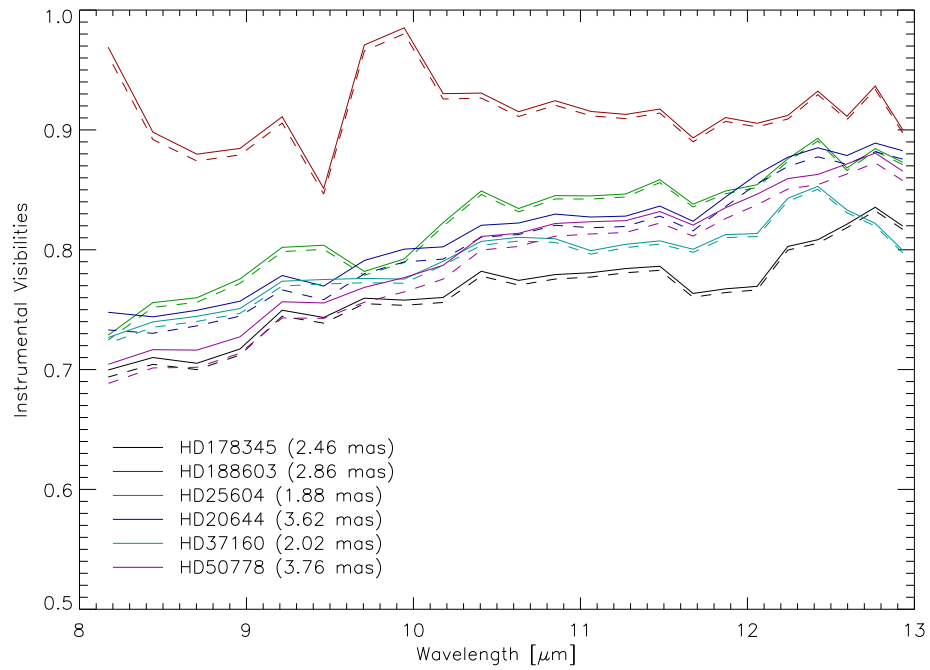


Figure 9.28: The instrumental visibilities (solid lines) derived from the six calibrators observed during the second night. The raw visibilities of the calibrators are overplotted (dashed lines).

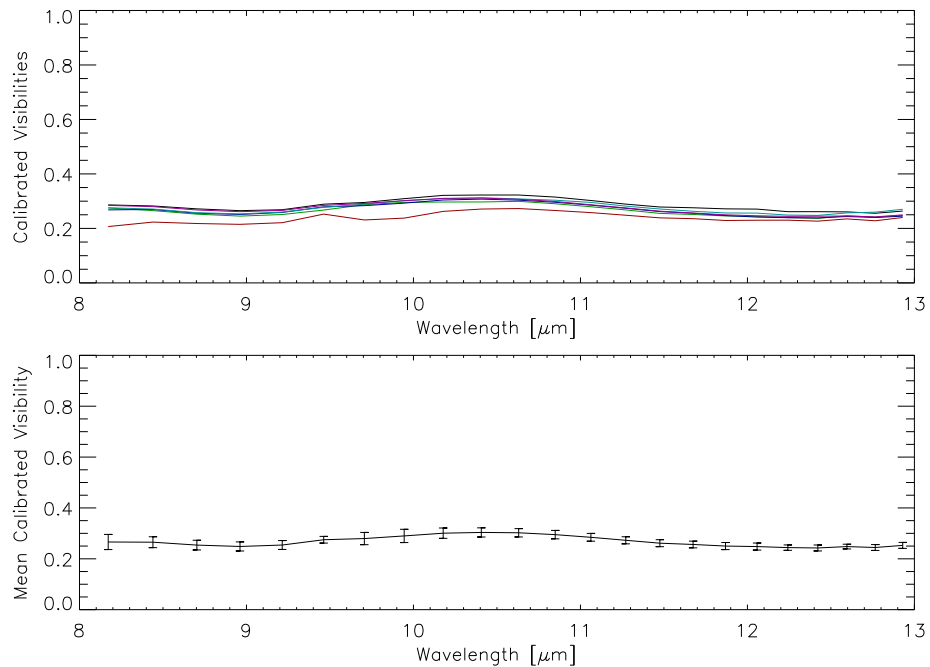


Figure 9.29: The calibrated visibilities (top) and their mean (bottom) for the second night. The errorbars represent again the standard deviation.

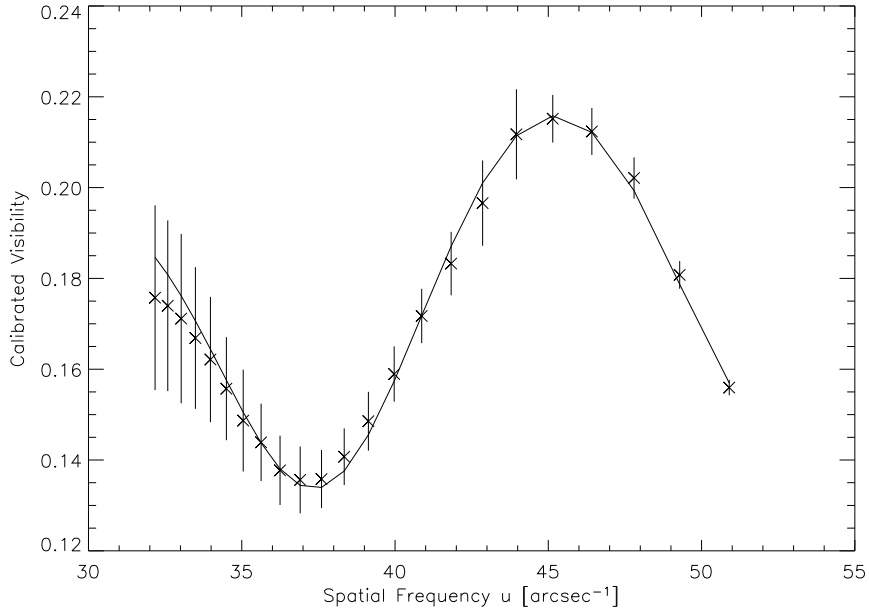


Figure 9.30: The calibrated visibility, the calibration errors, and the best fits for the data of Z CMA taken in the first night.

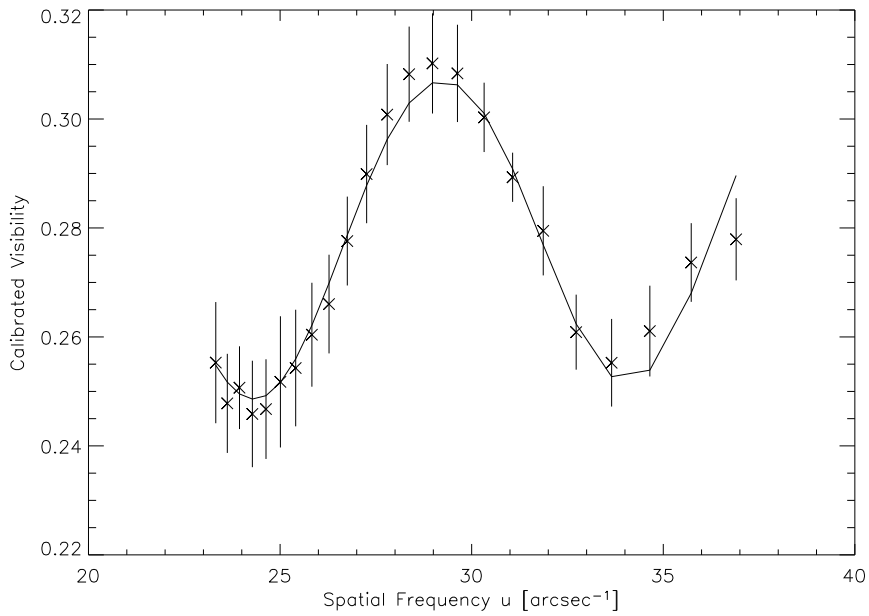


Figure 9.31: The calibrated visibility, the calibration errors, and the best fits for the data of Z CMA taken in the second night.

Table 9.3: The results of the two binary fits. The errors are the standard deviations of the fitted parameters.

Parameter	1./2. Nov.		3./4. Nov.	
	Value	Error	Value	Error
Offset a_0	0.1467	0.0160	0.2959	0.0161
Slope a_1	0.0015	0.0004	0.0004	0.0005
Flux Ratio a_2	0.2083	0.0020	0.1022	0.0027
Separation a_3 [arcsec]	0.0667	0.0002	0.1027	0.0004
χ^2 -Test	2.91		5.61	

has been performed. The linear part just compensates the visibility loss due to extended structures around the stars, e.g. disks or envelopes. While in the image space the brightness distribution of the binary is convolved with the brightness distribution of the extended structure, this contribution is according to the *convolution theorem* just a multiplicative term in the Fourier space.

A fit with a Gaussian or a uniform disk is hard to derive from the visibilities shown in Fig. 9.30 and Fig. 9.31, because they are dominated by the binary signal. Another difficulty is that the spectrally resolved visibilities obtained with MIDI are the products of two contrary effects. On the one hand, the offered instrumental resolution is proportional to the wavelength, i.e. the visibility increases towards longer wavelengths when the size of the emitting region is fixed. On the other hand, a usual source shows cold outer layers surrounding hot inner parts. Since these cold structures are larger, the visibility might decrease from shorter to longer wavelengths. The slope of the visibility of a resolved structure thus reflects whether the growing size of the structure at longer wavelengths can compensate the lower obtained resolution. The usage of a linear fit to describe the extended structure is thus a good approximation that avoids the introduction of new errors resulting from the wavelength-dependent size of the circumstellar structures.

The non-linear part of equation (9.19) fits the binary parameters according to equation (8.41). The flux ratio of the both components is given by a_2 , while the separation of the components is given by a_3 . This is valid as long as the projected intensity distributions (8.36) of the two components of the binary are both centrosymmetric along the projected baseline at all wavelengths.

The results of the fits to the two measurements are listed in Tab. 9.3.

Symmetry

A first important result is given by the offsets a_0 and the slopes a_1 . Although both measurements overlap in a significant spatial frequency range, the offsets and slopes are different. This shows that the structures in the environment of the stars are not radial symmetric. In general the emission seems to be more extended along the position angle 78.1° of the first measurement, when compared with the result along the position angle 110.4° of the second measurement. However, it is not possible to distinguish between the contributions of the two

individual sources with this simple model.

Position

Another property is the position of the companion relative to the primary. The separations listed in Tab. 9.3 represent the projected separations r_i ($i=1,2$) along the position angles ϕ_i , $\phi_i \pm 180^\circ$, respectively, of the projected baselines used to determine the visibilities. They are indicated by the dashed lines in Fig. 9.32, where the primary is located in the origin of the coordinate system. The possible positions of the companion (red squares) are determined by the intersections of the lines of constant projected separations (dotted lines) that are perpendicular to the projected separation vectors.

The position of the companion can be derived by a simple trigonometric calculation explained in Fig. 9.33. Here the position angles are rotated in such

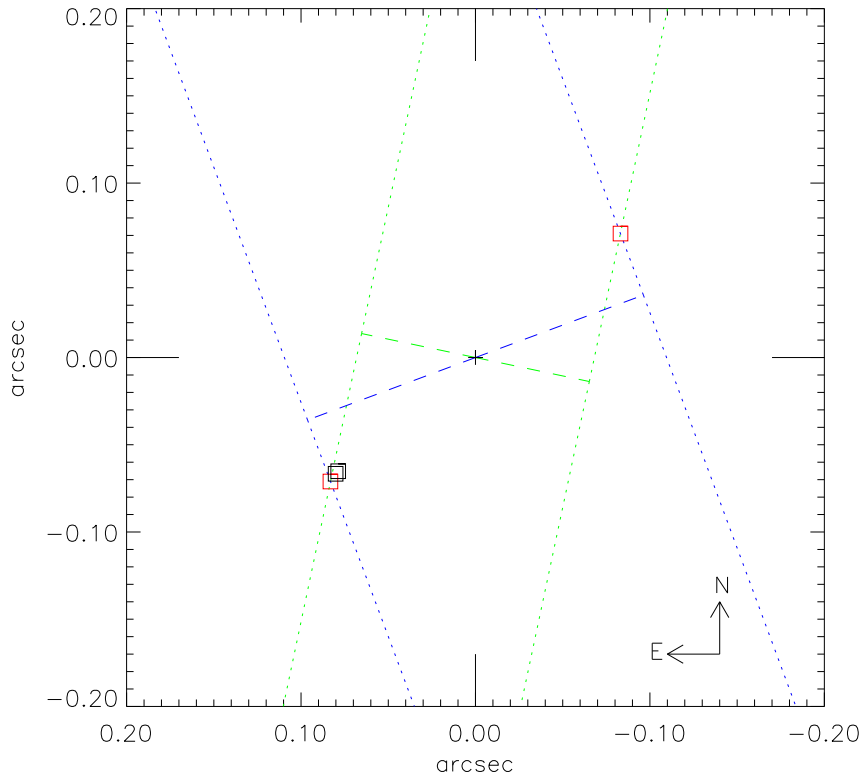


Figure 9.32: Reconstruction of the position of the companion (red squares) based on the two projected separations. The primary is centred in the origin of the coordinate system. The measurements are visualised by the green (2. Nov.) and blue (4. Nov) lines. The two intersections of the dotted lines of constant projected separation from the primary are the possible solutions. Without the phase information one is not able to decide, whether the correct position is at 130.4° or 310.4° . The results of the NAOS/CONICA measurements are plotted with black squares.

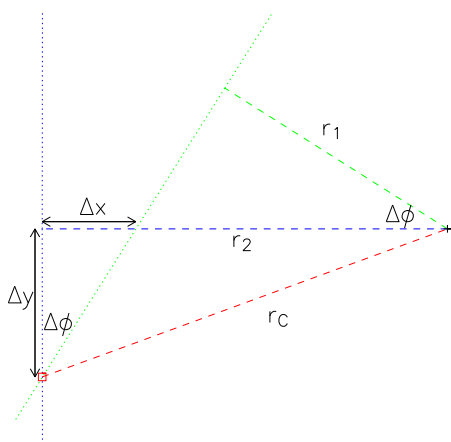


Figure 9.33: Sketch of the quantities necessary to determine the separation and position angle of the companion (red).

a way that the projected separation vector r_2 is parallel to the x-axis. The only quantity that is necessary to determine the real separation

$$r_c = \sqrt{r_2^2 + \Delta y^2} \quad (9.20)$$

and the position angle

$$\phi_c = \phi_2 + \text{atan} \left(\frac{\Delta y}{r_2} \right) \quad (9.21)$$

of the companion is the relative offset along the y-axis

$$\Delta y = \Delta x \tan^{-1} (\Delta \phi) . \quad (9.22)$$

To solve equation (9.22) the difference between the two position angles

$$\Delta \phi = \phi_2 - \phi_1 \quad (9.23)$$

and the offset along the x-axis

$$\Delta x = r_2 - r_1 \cos^{-1} (\Delta \phi) \quad (9.24)$$

are needed. Finally, one finds for the Z CMa measurements

$$r_c = 0.109 \pm 0.001 \text{ arcsec} , \quad (9.25)$$

$$\phi_c = 130.5^\circ \pm 0.3^\circ \text{ (mod } 180^\circ) . \quad (9.26)$$

A resolved observation of this companion in the mid-infrared would require a single-dish telescope with a diameter of approximately 20m when working diffraction-limited.

The ambiguity in the position angle can be solved by analysing, e.g. the images taken with NAOS/CONICA shown in Fig. 9.25. A position angle of $129.7^\circ \pm 0.7^\circ$ has been derived from the J-band image and $129.6^\circ \pm 0.7^\circ$ from those obtained in the Ks-band. These results are consistent with our visibility fits. In the L'-band images obtained with NAOS/CONICA the companion is not detectable.

We found in the J-band image taken with NAOS/CONICA a separation of the companion of 0.104 ± 0.001 arcsec and in the Ks-band image 0.102 ± 0.001 arcsec. The NAOS/CONICA positions are thus consistent with the near-infrared measurements by Millan-Gabet & Monnier (2002). The separation in the near-infrared is slightly smaller than the separation derived from the fits of the visibilities (Fig. 9.32). At the given distance to Z CMa of 1150 pc (Skinner et al., 1993) the difference corresponds to 6 AU when compared with the J-band and 8 AU when compared with the Ks-band measurements.

What causes this difference between the near-infrared and the mid-infrared position? A natural explanation may be given by the fact that the mid-infrared radiation does not solely trace the stars like the near-infrared light, but originates in the warm dust surrounding them. However, no verification of this explanation can be given yet, because the simple model used is not sensitive to this effect.

Flux Ratio

The flux ratio is not consistent between the two MIDI measurements. We thus derive a large errorbar:

$$\frac{I_2}{I_1} = 0.155 \pm 0.075 . \quad (9.27)$$

The error can be explained by the simple fit algorithm used and the fact that it has been assumed that the flux ratio between the sources is constant over the N-band. Detailed wavelength-dependent simulations have to be done to reduce the errors. However, this result fits into the trend described by Koresko et al. (1991). They found a flux ratio of 4.8 in the J-, 2.7 in the H-, 0.45 in the Ks-, 0.19 in the L-, and 0.15 in the M-band. Millan-Gabet & Monnier (2002) reported a shift of the wavelength range where the flux ratio reaches unity from the Ks-, to the H-band due to an increased flux of the Herbig Be star after an outburst. Unfortunately, our measurements with NAOS/CONICA have been performed with a neutral density filter that is not ‘neutral’ in the near-infrared. Therefore, the found flux ratios of 0.81 in the J-, and 0.12 in the Ks-band underestimate the flux of the visual brighter component systematically.

When applying the total flux of the system in the N-band determined by Przygodda (2004) with TIMMI 2 (*Thermal Infrared MultiMode Instrument*) one finds an absolute flux of 119 Jy for the primary and 19 Jy for the secondary.

9.5 Application II: The Triple T Tau

9.5.1 Introduction

T Tau has grown more and more complex as observations improve. The optical visible northern component T Tau N (Fig. 9.34) is the prototype of a classical T Tauri star. A close companion named T Tau S was detected by Dyck et al. (1982). It is located 0.7" south of T Tau N. It is a prototypical infrared companion deeply embedded ($A_V \approx 35$ mag) and not detectable in the visual (Stapelfeldt et al., 1998). Two different routes to explain the higher extinction have been discussed (Koresko et al., 1997). One the one hand, it may be caused by a special geometry of the system like viewing T Tau S through an edge-on disk or viewing a background T Tau S through the foreground face-on disk of T Tau N. Then T Tau S can be a normal T Tau star coeval to its northern neighbour. On the other hand, a different evolutionary status of T Tau S may be the reason. Interpretations range from a less evolved pre-main-sequence star still deeply embedded to a true protostar or a low-luminosity embedded accretion disk similar to those of FU Ori variables.

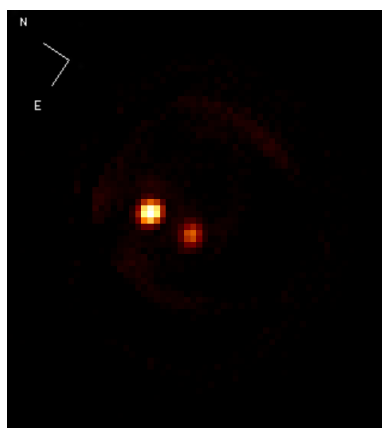


Figure 9.34: Acquisition image of T Tau obtained with UT4 on 4. Nov. 2004.

T Tau S has been resolved by Koresko (2000) and Duchêne et al. (2002) into two components named T Tau Sa and T Tau Sb,

with a separation of about 0.05" in 1997 and about 0.09" in 2002. T Tau Sb appears to be a 'normal' active low-mass pre-main-sequence star with an extinction of $A_V > 8$ mag. It cannot be buried within the same material obscuring T Tau Sa.

The northern component has shown neither in the K-, nor in the L'-band a significant brightness variation (Beck et al., 2004). Even its visual flux seems to be constant (Ghez et al., 1991). The southern component shows a variability with a total amplitude of ~ 2 mag in the K-, and ~ 3 mag in the L'-band. Beck et al. (2004) explained the variations by changes in the amount of obscuring material. In its bright state T Tau S dominates the flux of the system longwards of $3 \mu\text{m}$. According to Ghez et al. (1991) the flux ratio between the southern and the northern component in the N-band is ~ 0.4 in the minimum and ~ 2.6 in the maximum. Both components forming T Tau S have been identified as being variable. The flux ratio of T Tau Sb with respect to T Tau Sa varies between ~ 0.1 (Koresko, 2000) and ~ 3.6 (Beck et al., 2004) in the K-band.

The southern binary appears fainter in the acquisition images (Fig. 9.34) taken with MIDI in the default acquisition filter (N8.7 = lower N-band, $\lambda_0 = 8.7$, $\Delta\lambda = 1.5 \mu\text{m}$). The flux ratio derived from the aperture photometry of two consecutive images where either the northern or the southern component is centred to avoid vignetting effects is

$$\frac{I_S}{I_N} = 0.47 \pm 0.02 . \quad (9.28)$$

T Tau S thus has been probably observed in its minimum, i.e. in a state of high obscuration. After multiplying (9.28) with the absolute flux measured by Przygodda (2004) in the N8.9-filter ($\lambda_0 = 8.7$, $\Delta\lambda = 1.6 \mu\text{m}$) of TIMMI2 one finds

$$I_N = 7.07 \pm 0.42 \text{ Jy} \quad (9.29)$$

for the northern and

$$I_S = 3.33 \pm 0.21 \text{ Jy} \quad (9.30)$$

for the southern component.

9.5.2 The Southern Component

In Fig. 9.35 the calibrated visibilities for the southern component observed on Nov. 4. are plotted. They have been derived from the calibrators measured during this night (Fig. 9.28). After excluding the erroneous instrumental visibility of HD 188603 the mean of the calibrated visibilities versus the spatial frequency is displayed in Fig. 9.36. The errors are determined by the standard deviation of the calibrated visibilities.

The signature of the southern binary Sa-Sb is clearly visible. Therefore, equation (9.19) has been fitted again to the data to derive the binary parameters, i.e. the flux ratio together with the projected separation (only one measurement). The data point in brackets has been ignored due to its doubtful value probably affected by the ozone band. Since a fit to the whole spatial frequency range (solid line) is difficult, the lower (dashed line) and upper (dotted line) ranges have been fitted separately. While the offsets and slopes differ significantly from each other the flux ratio and the separation is consistent (Tab. 9.4).

9.5. APPLICATION II: THE TRIPLE T TAU

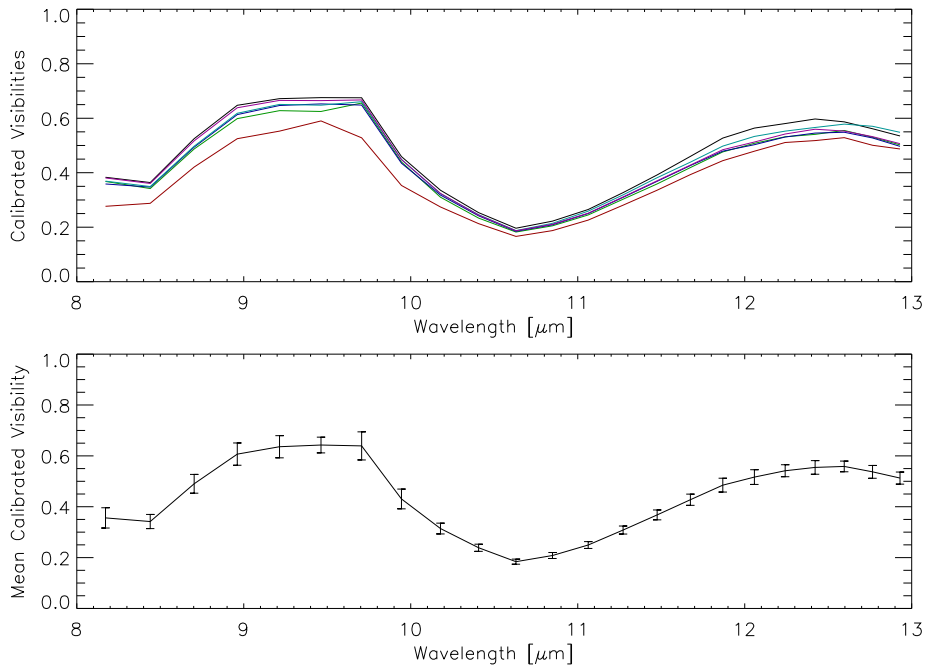


Figure 9.35: The calibrated visibilities (top) and their mean (bottom) for the observation of T Tau S. The errorbars represent again the standard deviation.

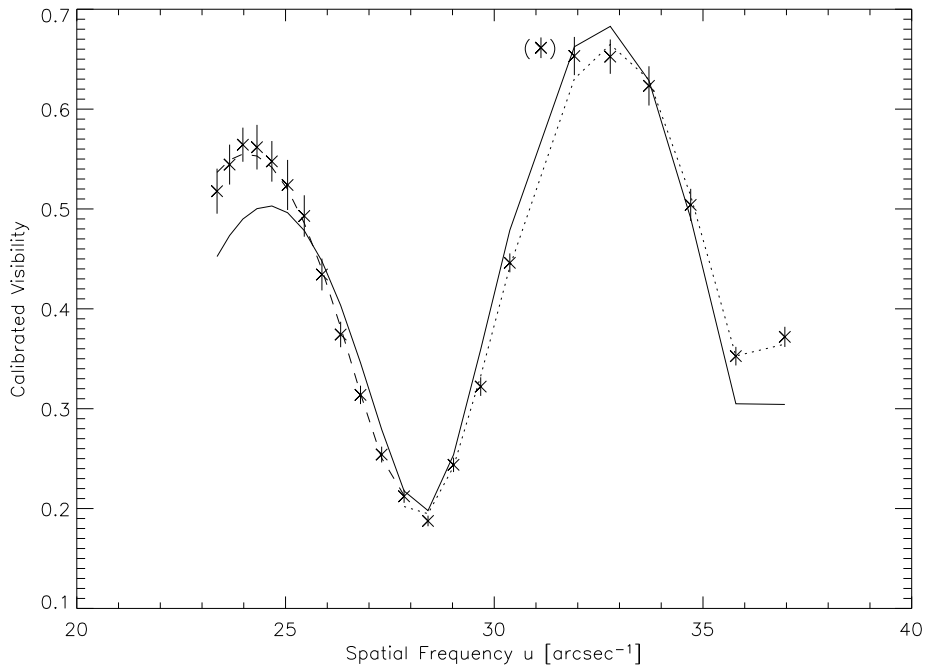


Figure 9.36: The calibrated visibility, the calibration errors, and the best fits for the data of T Tau S.

Table 9.4: The results of the three binary fits.

Parameter	all		u_{low}		u_{high}	
	Value	Error	Value	Error	Value	Error
Offset a_0	-0.0466	0.0328	0.3476	0.4280	-0.6235	0.0718
Slope a_1	0.0225	0.0012	0.0087	0.0177	0.0395	0.0022
Flux Ratio a_2	0.5011	0.0036	0.4705	0.0161	0.4406	0.0047
Separ. a_3 ["]	0.1236	0.0001	0.1252	0.0006	0.1236	0.0001
χ^2 -Test	192		2.11		8.68	

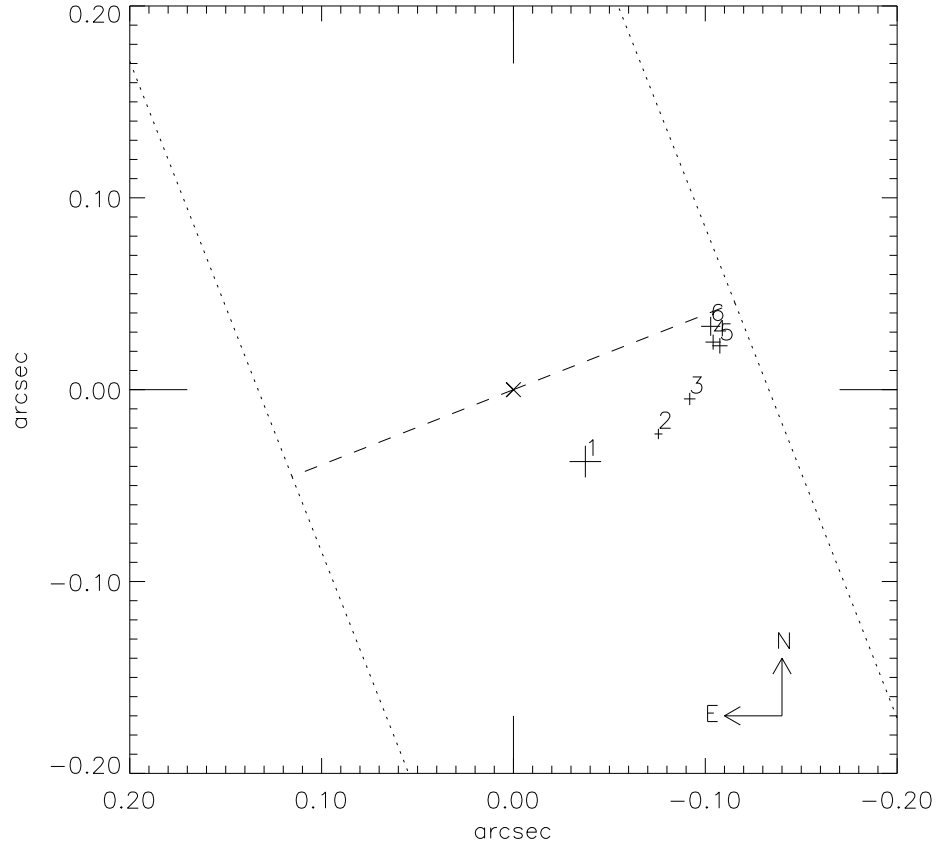


Figure 9.37: The near-infrared measurements of the positions of T Tau Sb with respect to T Tau Sa. The labelled positions are adopted from 1: Koresko (2000), measured in Dec. 1997, 2: Köhler et al. (2000a), Feb. 2000, 3: Duchêne et al. (2002), Nov. 2000, 4: Beck et al. (2004), Oct. 2002, 5: Beck et al. (2004), Dec 2002, 6: Furlan et al. (2003), Dec. 2002. The crosses correspond to the errorbars. Overplotted is the projected separation derived from our mid-infrared interferometric measurement.

From the two fits to the subsets of the data one finds

$$I_2/I_1 = 0.456 \pm 0.021 , \quad (9.31)$$

$$r_{\text{proj}} = 0.124 \pm 0.001 \text{ arcsec} , \quad (9.32)$$

where the projected separation r_{proj} is measured along the position angle 111.4° of the projected baseline.¹ In Fig. 9.37 the published infrared positions are visualised together with our projected separation. The component T Tau Sb resides west of the infrared companion T Tau Sa. Unfortunately, we cannot determine without a phase, whether the flux ratio (9.31) is measured with respect to T Tau Sa or T Tau Sb.

Beck et al. (2004) discussed orbits with semi-major axis of $\sim 0.10''$ and $\sim 0.12''$ with periods of ~ 20 yr, ~ 40 yr, respectively. However, they found that the numeric results are uncertain, because the χ^2 surface is broad and flat in the region of the minimum. It also remains unclear, why the lunar occultation of T Tau S observed by Simon et al. (1996) with a spatial resolution of 21 mas could not reveal the companion separated at that time by ~ 70 mas from the primary in both orbits. At least in the wide orbit T Tau Sb should have been also detected in the speckle data of Ghez et al. (1991). In the wide orbit it was separated at the time of the observation by ~ 120 mas. Either the companion was actually closer to T Tau Sa than the predicted values and thus below the spatial detection limit or it was just too faint to be detected. In the orbits presented by Beck et al. (2004) the westernmost parts are represented by the positions 4, 5, and 6. Since the here derived projected separation is a lower limit to the true separation, our data favour an even wider orbit.

9.5.3 The Northern Component

The calibrated visibility obtained on Nov. 1./2. for T Tau N is plotted in Fig. 9.38. Again all calibrators measured during that night have been used to estimate the calibration errors. The calibrated visibility is well below unity and thus indicates that the circumstellar structure around the northern component could be resolved with MIDI.

To allow an estimation of the size of the circumstellar structure it will be assumed here that the material can be described by a Gaussian disk. In Fig. 9.39 Gaussian disks with different FWHMs are overplotted on the calibrated visibility. The loss of resolution towards longer wavelengths according to (8.13) is reflected by the increasing visibilities of the Gaussian disks. The decreasing visibility of T Tau N thus indicates a growing apparent size of the circumstellar material that overcompensates this degraded resolution.

The calculated FWHMs and their errors for the different wavelengths are plotted in Fig. 9.40. They can be fitted with a constant slope of

$$\frac{\Delta\sigma}{\Delta\lambda} = 1.97 \pm 0.05 \frac{\text{mas}}{\mu\text{m}} . \quad (9.33)$$

If this simple model describes the reality, the FWHM of the circumstellar structure around T Tau N varies between 7 mas at $8 \mu\text{m}$ and 16 mas at $13 \mu\text{m}$. This corresponds to 1.0 AU, 2.2 AU, respectively, when assuming a distance of 140 pc to the Taurus-Auriga star-forming region.

¹An additional visibility observed at 30./31. Oct. 2004 with a projected baseline of 43.9 m at a position angle of 48.9° shows no signs of a binary.

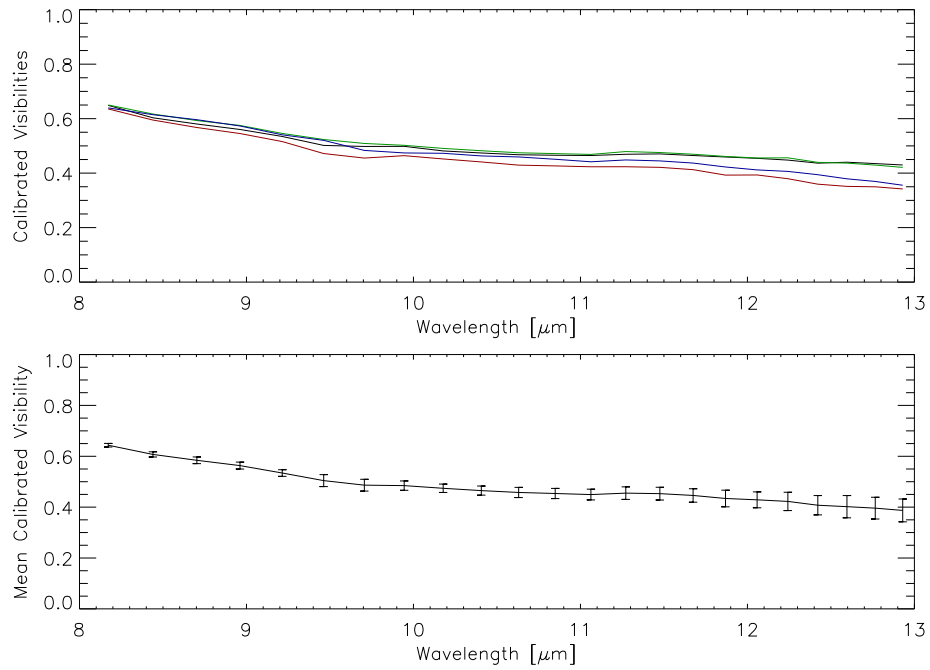


Figure 9.38: The calibrated visibilities (top) and their mean (bottom) for the observation of T Tau N. The errorbars represent the standard deviation.

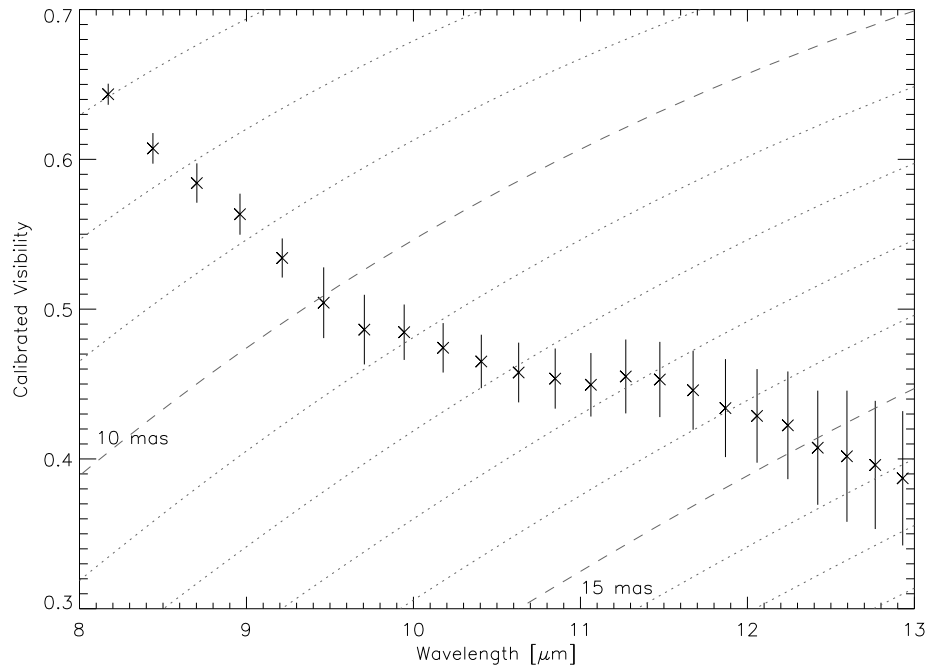


Figure 9.39: The calibrated visibility plotted versus the wavelength. The lines represent Gaussian disks with different FWHMs. The dashed lines mark those with a FWHM of 10 mas and 15 mas.

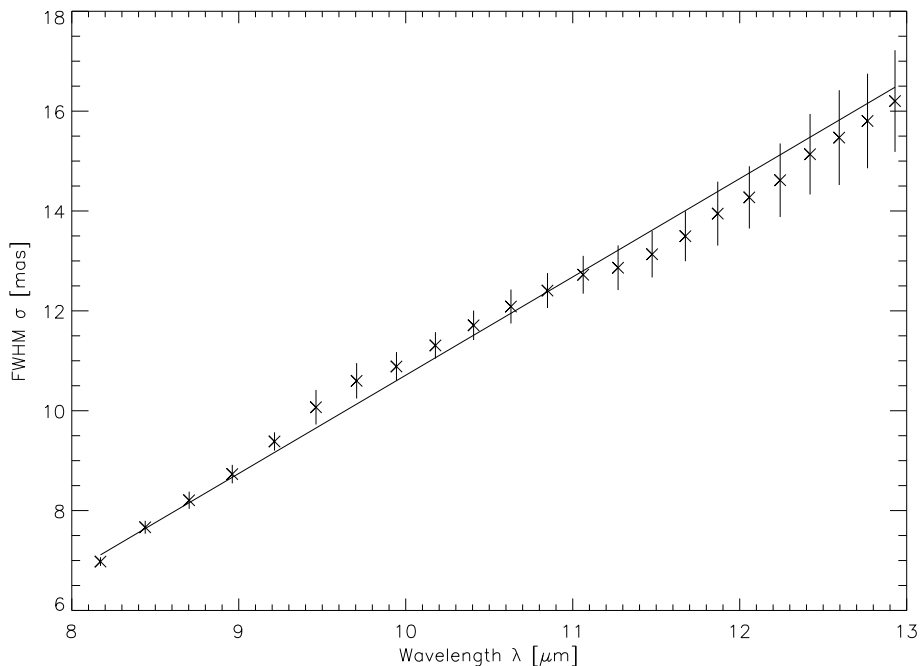


Figure 9.40: The FWHMs of the Gaussian disks, their errors, and the best linear fit.

9.5.4 Individual Spectra

The spectra obtained during the photometric measurements with the prism are plotted in Fig. 9.41. The spectrum of T Tau N has been calibrated with the spectrophotometric standard HD 37160 (blue). The southern companion was calibrated both with the spectrophotometric calibrator HD 178345 (red, dashed) and HD 37160 (red, solid). The templates for the corresponding spectral types have been derived from the ISO websites². No atmospheric corrections have been applied, because the effects in the mid-infrared are negligible with exception of the ozone band and very high airmasses. Since even the ozone band is corrected with a high accuracy in Fig. 9.41, the atmospheric extinction is indeed very low.

The green line is the sum of the blue and the average of the red lines, i.e. the quasi spectrum of the complete system. The shape of the summed up spectrum is in very good agreement with the result presented in Przygodda (2004) that has been obtained with TIMMI 2. The spectrum of the total system shows if any only a moderate sign of absorption. The reason for this moderate absorption becomes evident when looking at the individual spectra:

- The spectrum of T Tau S is dominated by a deep silicate absorption, caused by cold material in the line of sight, e.g. a disk seen under a high inclination angle. The bright inner parts are blocked from the observer by the material in front of it. This result favours the scenario describing infrared companions as a result of a special viewing geometry. Similar re-

²http://www.iso.vilspa.esa.es/users/expl_lib/ISO/wwwcal/isoprep/cohen/templates

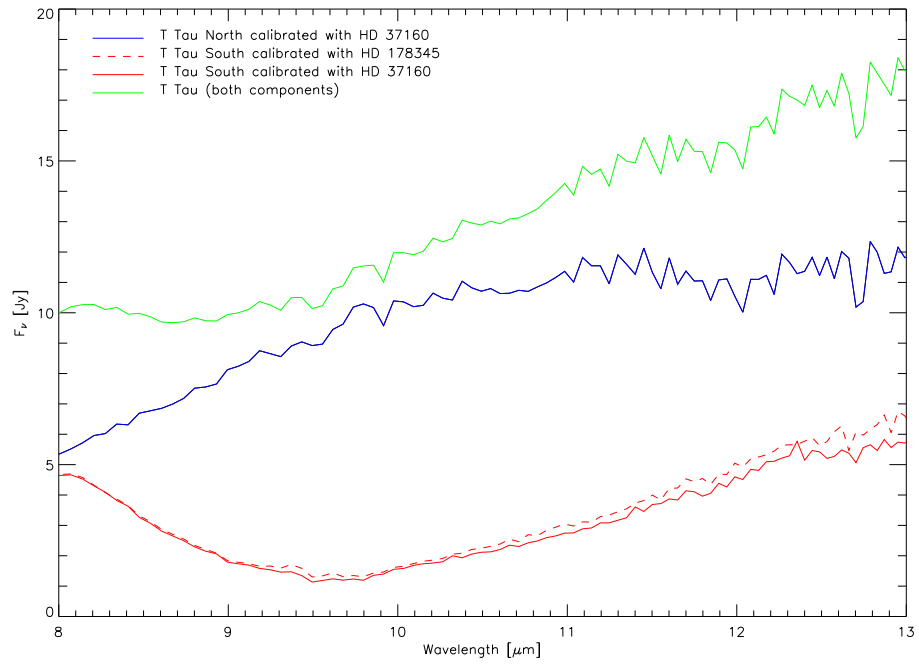


Figure 9.41: The mid-infrared spectra of T Tau (green), T Tau N (blue), and T Tau S (red) derived from the photometric measurements obtained with MIDI.

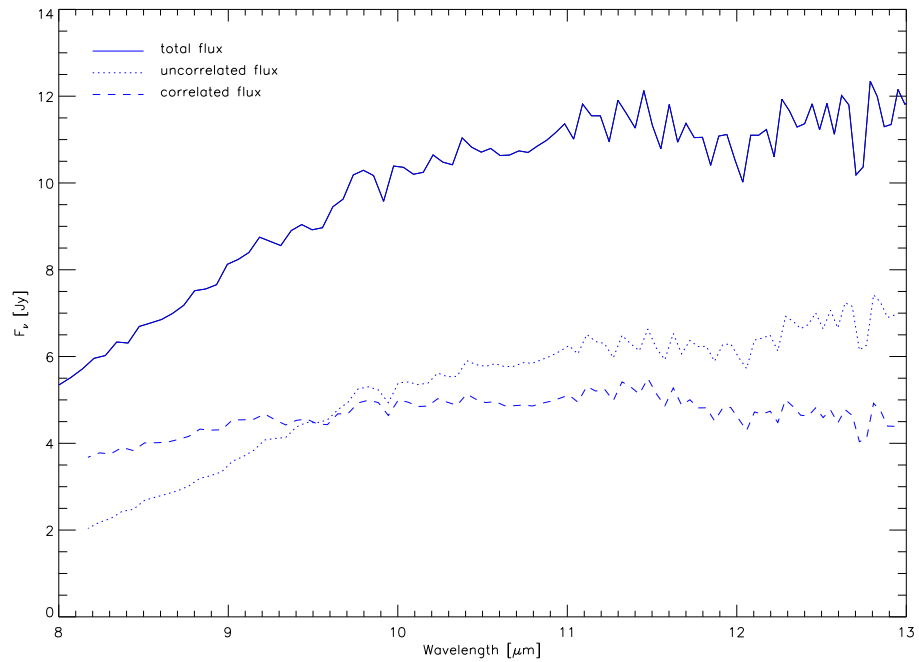


Figure 9.42: Spatially resolved spectrum of T Tau N. Plotted is the integrated (solid), the uncorrelated (dotted), and the correlated flux (dashed).

sults have been found for the infrared companion of VV CrA (Przygodda, 2004). However, one has to take into account that the southern star is a binary itself and that it is not yet clear how the single stars exactly contribute to the combined spectrum.

- This deep absorption is almost cancelled out by a emission feature of the northern component. This emission is believed to originate in thin circumstellar material, e.g. the upper layers of a disk seen under a low inclination angle.

Both the emission of the northern component and the absorption towards the southern companion appear very broad. The shape of the continuum in the spectrum of T Tau S can be probably described best by a linear approximation between the values of the absorption spectrum at $8\ \mu\text{m}$ and $13\ \mu\text{m}$.

9.5.5 Correlated Flux of T Tau N

In Fig. 9.42 the correlated flux (dashed) of T Tau N, i.e. the total flux (solid) multiplied with the visibility is plotted. The difference between the correlated and the total flux is the uncorrelated flux (dotted). The correlated flux originates in those parts of the stellar system that cannot be resolved by MIDI, while the source of the uncorrelated flux can be resolved. When again assuming a Gaussian distribution of the material around T Tau N and defining a Gaussian disk showing a visibility of 0.9 as resolved, the structures not resolved by MIDI at $8\ \mu\text{m}$ are smaller than $\sim 0.5\ \text{AU}$. According to this definition the resolution at the upper end of the wavelength range corresponds to structures of $\sim 0.8\ \text{AU}$.

The correlated flux appears to be very constant over the whole wavelength range, while the uncorrelated flux increases from shorter to longer wavelengths. The uncorrelated flux is lower than the correlated flux at short wavelengths. At $8\ \mu\text{m}$ 60% of the total flux originates in the small-scale structures. The inverse situation is realized at $13\ \mu\text{m}$. Here 40% of the total flux originates in the innermost parts of the T Tau N system.

9.6 Summary

From a technical point of view MIDI integrates several instruments:

- MIDI is an adaptive optics assisted *interferometric* instrument for the mid-infrared. It has been designed to operate at the VLTI. Spectrally resolved visibilities can be obtained within half an hour. A calibrator is required to determine the instrumental visibility.
- MIDI is also an adaptive optics assisted diffraction-limited *spectrograph* operating in the N-band. It allows to measure individual spectra of two sources down to separations of a half arcsecond.
- Last but not least, MIDI is an adaptive optics assisted diffraction-limited *imager* for the mid-infrared. Important quantities like the flux of a source, or the flux ratio of a binary can be determined from the acquisition images. Different filters can be used.

The *Fourierspectrum analysis* used by the software package MIA allows a straightforward reduction of the interferometric data obtained with MIDI. This method has been demonstrated and was applied to two objects: the binary Z CMa and the triple T Tau.

- The interferometric observations of Z CMa have been used to derive the binary parameters of this system. Although the non-linear least squares fit is simple, the position of the companion emitting only 0.155 ± 0.075 of the flux of the primary in the N-band could be derived. It is located at a position angle of $130.5^\circ \pm 0.3^\circ$ and is separated 109 ± 1 mas from the primary.
- The flux ratio between T Tau N and T Tau S could be determined in the lower N-band by analysing the acquisition images. The southern component emits 0.47 ± 0.02 of the flux of the northern component.
- The close binary T Tau Sa-Sb has been resolved. A projected separation of 124 ± 1 mas was found at a position angle of 111.4° . The flux ratio is 0.456 ± 0.021 in the N-band.
- When assuming a Gaussian symmetry of the circumstellar structure around T Tau N one finds a constant slope for the FWHM as function of the wavelength: $\Delta\sigma/\Delta\lambda = 1.97 \pm 0.05 \text{ mas } \mu\text{m}^{-1}$.
- Individual spectra show a deep silicate absorption towards T Tau S and an emission feature towards T Tau N.

These simple interpretations of the interferometric measurements only touch a small fraction of the informations contained in the data. To dig deeper more sophisticated methods like radiative transfer calculations have to be included. However, the approach shown in the last sections may give an impression of the worth of the measurements obtained with MIDI.

Chapter 10

The Future - Imaging with MIDI

Currently an international collaboration between the Observatoire de la Côte d'Azur (F), the Max-Planck-Institute for Astronomy (Heidelberg), the European Southern Observatory, the Observatoire de Lyon (F), the Observatoire de Bordeaux (F), ASTRON (NL) and the Max-Planck-Institute for Radio-

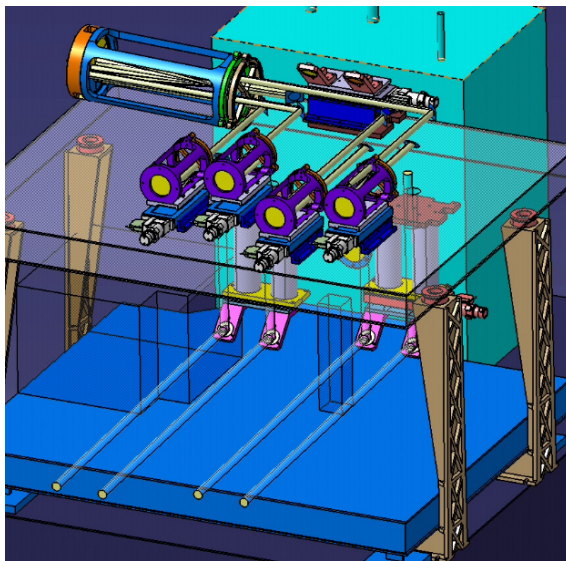


Figure 10.1: Design Study of APreS-MIDI (courtesy of Bruno Lopez, OCA, Nice).

astronomy (Bonn) develops APreS-MIDI or *APer-ture Synthesis in the mid-infrared with MIDI* (Lopez et al., 2003). This device will turn MIDI into the first interferometric imager in the mid-infrared by recombining in the pupil plane three or four telescope beams coming either from the UTs or the ATs.

APreS-MIDI is mounted on a small optical bench that will be put above the warm optical bench of MIDI (Fig. 10.1). Small pick-up mirrors will feed then the beams to the delay lines of APreS-MIDI. Here mirrors focus them on the reflecting faces of a cutted pyramidal mirror, the key element of APreS-MIDI. Afterwards, the beams are sent along the same axis into the MIDI dewar. In the imaging mode MIDI will work as mere camera. Its beamcombiner is moved out of the optical path. Since APreS-MIDI does not affect MIDI due to its modular implementation, a fast switching between imaging and 'classical' mode is possible.

The pupils coming from the different telescopes are superimposed with small tilt angles between them. This produces a set of fringes (Fig. 10.2) represented in

the Fourier space by peaks which yield the fringe contrast information with respect to the spatial frequencies sampled by the baselines. This allows an efficient coverage of the Fourier plane. Moreover, APreS-MIDI measures the so-called *closure-phase*, i.e. the sum of the phases coming from three baselines forming a triangle that is not

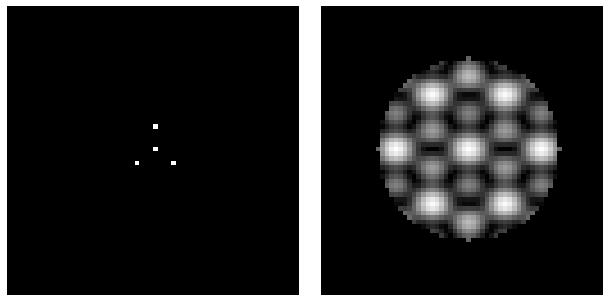


Figure 10.2: The geometry of the incoming beams (left) and the fringe signal in the image of the pupil plane (right) recorded by the detector of MIDI (courtesy of Frank Przygodda).

affected by the atmosphere. This absolute Fourier phase is necessary to reconstruct images (Fig. 10.3). The selection of appropriate image reconstruction methods previously applied to speckle or radioastronomic data will thus play a crucial role.

In Fig. 10.3 a promising example is shown. The typical T Tauri disk seen at $10\ \mu\text{m}$ in the upper left image has been calculated by Sebastian Wolf (MPIA) with his radiative transfer code *MC3D* (Wolf, 2003). The prominent double structure therein is the inner rim of the disk separated by a gap of 25 mas from the stellar source. In the upper right image the disk has been convolved with a point-spread-function corresponding to an aperture of 200 m, i.e. the longest available baseline. The result of the reconstruction of simulated data performed

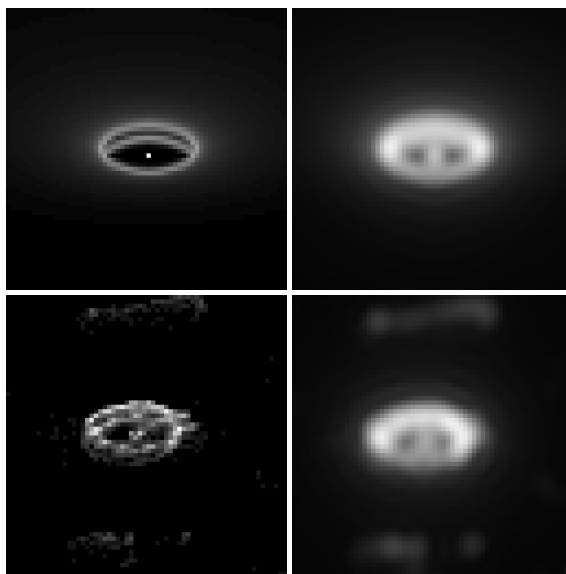


Figure 10.3: The lower left image is a reconstruction of the upper left image. The images on the right side are derived from the left images by convolving them with the PSF of a 200 m aperture.

by K. H. Hofmann and S. Kraus (both MPIFR, Bonn) by using the *Building Block Method* (Hofmann & Weigelt, 1992) is shown in the lower left image. They included 300 visibilities and 200 closure phases corresponding to five observing nights with four ATs when a sampling of ten measurements in each night is assumed. The convolution with the point-spread-function allows an easy comparison with the upper right image.

When this next generation of instruments becomes available the term resolution in optical astronomy will probably no longer be associated with the diameter of the primary mirror!

Bibliography

- Ageorges, N., Eckart, A., Monin, J.-L., & Menard, F. 1997, *A&A*, 326, 632
- Aitken, R. G. & Doolittle, E. 1932, *New General Catalogue of Double Stars within 120° of the North Pole* (Publ. 417, Carnegie Institution of Washington)
- Allen, L. E., Myers, P. C., Di Francesco, J., et al. 2002, *ApJ*, 566, 993
- Altena, W. F., van Lee, J. T., & Hoffleit, E. D. 1995, *The General Catalogue of Trigonometric Parallaxes*, 4th edn. (New Haven: Yale University Observatory)
- Anderson, J. A. 1920, *ApJ*, 51, 263
- André, P., Ward-Thompson, D., & Barsony, M. 1993, *ApJ*, 406, 122
- Barsony, M., Carlstrom, J. E., Burton, M. G., Russell, A. P. G., & Garden, R. 1989, *ApJ*, 346, L93
- Barsony, M., Kenyon, S. J., Lada, E. A., & Teuben, P. J. 1997, *ApJS*, 112, 109
- Barsony, M., Koresko, C., & Matthews, K. 2003, *ApJ*, 591, 1064
- Basri, G. & Marcy, G. W. 1995, *AJ*, 109, 762
- Beck, T. L., Schaefer, G. H., Simon, M., et al. 2004, *ApJ*, 614, 235
- Boden, A. F. 1999, in *Principles of Long-Baseline Interferometry*, ed. P. R. Lawson, *Michelson Fellowship Program*, 9–30
- Bontemps, S., André, P., Kaas, A. A., et al. 2001, *A&A*, 372, 173
- Bouvier, J. & Appenzeller, I. 1992, *A&AS*, 92, 481
- Bouvier, J., Duchêne, G., Mermilliod, J.-C., & Simon, T. 2001, *A&A*, 375, 989
- Bouvier, J., Rigaut, F., & Nadeau, D. 1997, *A&A*, 323, 139
- Brandner, W., Alcalá, J. M., Kunkel, M., Moneti, A., & Zinnecker, H. 1996, *A&A*, 307, 121
- Casanova, S., Montmerle, T., Feigelson, E. D., & André, P. 1995, *ApJ*, 439, 752

BIBLIOGRAPHY

- Cohen, M. & Kuhi, L. V. 1979, *ApJS*, 41, 743
- Costa, A., Jessop, N. E., Yun, J. L., et al. 2000, in *Birth and Evolution of Binary Stars*, ed. B. Reipurth & H. Zinnecker, Poster Proceedings of IAU Symposium No. 200, 48–50
- de Geus, E. J. 1992, *A&A*, 262, 258
- de Zeeuw, P. T., Hoogerwerf, R., de Bruijne, J. H. J., Brown, A. G. A., & Blaauw, A. 1999, *AJ*, 117, 354
- Duchêne, G. 1999, *A&A*, 341, 547
- Duchêne, G., Bouvier, J., Bontemps, S., André, P., & Motte, F. 2004, *A&A*, 427, 651
- Duchêne, G., Bouvier, J., & Simon, T. 1999, *A&A*, 343, 831
- Duchêne, G., Ghez, A. M., & McCabe, C. 2002, *ApJ*, 568, 771
- Duquennoy, A. & Mayor, M. 1991, *A&A*, 248, 485
- Durisen, R. H. & Sterzik, M. F. 1994, *A&A*, 286, 84
- Dyck, H. M., Simon, T., & Zuckerman, B. 1982, *ApJ*, 255, L103
- Elias, J. H. 1978, *ApJ*, 224, 453
- ESO. 2003, *VLT Whitebook*, Education & Public Relations Department, Karl-Schwarzschild-Strasse 2, D-85748 Garching, Germany
- Evans, N. J., Balkum, S., Levreault, R. M., Hartmann, L., & Kenyon, S. 1994, *ApJ*, 424, 793
- Fizeau, H. 1868, *C. R. Acad. Sci.*, 66, 932
- Fried, D. L. 1965, *J. Opt. Soc. Am.*, 55, 1427
- Furlan, E., Forrest, W. J., Watson, D. M., et al. 2003, *ApJ*, 596, L87
- Garcia, P. J. V., Thiébaud, E., & Bacon, R. 1999, *A&A*, 346, 892
- Genzel, R., Thatte, N., Krabbe, A., Kroker, H., & Tacconi-Garman, L. E. 1996, *ApJ*, 472, 153
- Geoffray, H. & Monin, J.-L. 2001, *A&A*, 369, 239
- Ghez, A. M., McCarthy, D. W., Patience, J. L., & Beck, T. L. 1997, *ApJ*, 481, 378
- Ghez, A. M., Neugebauer, G., Gorham, P. W., et al. 1991, *AJ*, 102, 2066
- Ghez, A. M., Neugebauer, G., & Matthews, K. 1993, *AJ*, 106, 2005
- Greene, T. P. & Meyer, M. R. 1995, *ApJ*, 450, 233
- Greene, T. P., Wilking, B. A., Andre, P., Young, E. T., & Lada, C. J. 1994, *ApJ*, 434, 614

- Greene, T. P. & Young, E. T. 1992, *ApJ*, 395, 516
- Grosso, N., Montmerle, T., Bontemps, S., André, P., & Feigelson, E. D. 2000, *A&A*, 359, 113
- Haas, M. 1989, PhD thesis, Ruprecht-Karls-Universität Heidelberg
- Haisch, Karl E., J., Barsony, M., Greene, T. P., & Ressler, M. E. 2002, *AJ*, 124, 2841
- Hartmann, L., Kenyon, S., Hewett, R., et al. 1989, *ApJ*, 338, 1001
- Hartmann, L. & Kenyon, S. J. 1996, *ARA&A*, 34, 207
- Hellemans, A. 2000, *Nature*, 408, 12
- Herbig, G. H. 1962, *AdA&A*, 1, 47
- Herbig, G. H. & Bell, K. R. 1988, *Lick Observatory Bulletin*, 1111
- Herbig, G. H. & Kameswara Rao, N. 1972, *ApJ*, 174, 401
- Herbst, T. M., Beckwith, S. V., Birk, C., et al. 1993, in *Infrared Detectors and Instrumentation*, ed. A. M. Fowler, *Proc. SPIE No. 1946*, 605–609
- Hofmann, K. H. & Weigelt, G. 1992, in *High-Resolution Imaging by Interferometry II. Ground-Based Interferometry at Visible and Infrared Wavelengths*, ed. J. M. Beckers & F. Merkle, *ESO Conference and Workshop Proceedings*, 193
- Hofmann, R., Blietz, M., Duhoux, P., et al. 1992, in *Progress in Telescope and Instrumentation Technologies*, ed. M.-H. Ulrich, *ESO Conference and Workshop Proceedings*, 617
- Houk, N. & Smith-Moore, M. 1988, *Michigan Catalogue of Two Dimensional Spectral Types for the HD*, Vol. 4
- Joy, A. H. 1945, *ApJ*, 102, 168
- Joy, A. H. & van Biesbroeck, G. 1944, *PASP*, 56, 123
- Knox, K. T. & Thompson, B. J. 1974, *ApJ*, 193, L45
- Knude, J. & Hog, E. 1998, *A&A*, 338, 897
- Köhler, R. 1997, PhD thesis, Ruprecht-Karls-Universität Heidelberg
- Köhler, R. 2001, *AJ*, 122, 3325
- Köhler, R., Kasper, M. E., & Herbst, T. M. 2000a, in *Birth and Evolution of Binary Stars*, ed. B. Reipurth & H. Zinnecker, *Poster Proceedings of IAU Symposium No. 200*, 63–64
- Köhler, R., Kunkel, M., Leinert, C., & Zinnecker, H. 2000b, *A&A*, 356, 541
- Köhler, R. & Leinert, C. 1998, *A&A*, 331, 977
- Koresko, C. D. 2000, *ApJ*, 531, L147

BIBLIOGRAPHY

- Koresko, C. D. 2002, *AJ*, 124, 1082
- Koresko, C. D., Beckwith, S. V. W., Ghez, A. M., Matthews, K., & Neugebauer, G. 1991, *AJ*, 102, 2073
- Koresko, C. D., Herbst, T. M., & Leinert, C. 1997, *ApJ*, 480, 741
- Koresko, C. D. & Leinert, C. 2001, in *Birth and Evolution of Binary Stars*, ed. B. Reipurth & H. Zinnecker, *Proceedings of IAU Symposium No. 200*, 265–274
- Kroupa, P. 1995, *MNRAS*, 277, 1491
- Labeyrie, A. 1970, *A&A*, 6, 85
- Lada, C. J. 1987, in *Star forming regions*, ed. M. Peimbert & J. Jugaku, *Proceedings of IAU Symposium No. 115*, 1–18
- Lada, E. A., Strom, K. M., & Myers, P. C. 1993, in *Protostars and Planets III*, ed. E. H. Levy & J. I. Lunine, *Space Science Series*, 245–277
- Lawrence, J. S. 2004, *PASP*, 116, 482
- Lawson, P. R. 1999, in *Principles of Long-Baseline Interferometry*, ed. P. R. Lawson, *Michelson Fellowship Program*, 325–332
- Leinert, C. 1994, in *Star Formation and Techniques in Infrared and mm-Wave Astronomy*, ed. T. P. Ray & S. V. W. Beckwith, *Lecture Notes in Physics No. 431*, 215–283
- Leinert, C., Allard, F., Richichi, A., & Hauschildt, P. H. 2000, *A&A*, 353, 691
- Leinert, C., Henry, T., Glindemann, A., & McCarthy, D. W., J. 1997, *A&A*, 325, 159
- Leinert, C., Jahreiß, H., Woitas, J., et al. 2001, *A&A*, 367, 183
- Leinert, C., Witzel, N., Richichi, A., Eckart, A., & Tacconi-Garman, L. E. 1994, *A&A*, 291, L47
- Leinert, C., Zinnecker, H., Weitzel, N., et al. 1993, *A&A*, 278, 129
- Lépine, J. R. D., Mishurov, Y. N., & Dedikov, S. Y. 2001, *ApJ*, 546, 234
- Lidman, C., Ageorges, N., Brandner, W., & Moutou, C. 2004, *NAOS-CONICA User Manual*, Doc. No. VLT-MAN-ESO-14200-2761, Issue 1.8.0, European Southern Observatory
- Lohmann, A. W., Weigelt, G., & Wirtzner, B. 1983, *Appl. Opt.*, 22, 4028
- Lopez, B., Mathias, P., Mekarnia, D., et al. 2003, in *Interferometry for Optical Astronomy II*, ed. W. A. Traub, *Proc. SPIE No. 4838*, 1011–1017
- Lord, S. D. 1992, *NASA Tech. Mem.*, 103957
- Loren, R. B. 1989, *ApJ*, 338, L902

- Luhman, K. L. & Rieke, G. H. 1999, *ApJ*, 525, 440
- Mathieu, R. D. 1994, *ARA&A*, 32, 465
- Mathieu, R. D., Walter, F. M., & Myers, P. C. 1989, *AJ*, 98, 987
- McCaughrean, M. J. & Stauffer, J. R. 1994, *AJ*, 108, 1382
- Menten, K. M., Reid, M. J., Eckart, A., & Genzel, R. 1997, *ApJ*, 475, L111
- Michelson, A. A. 1890, *Phil. Mag.*, 30, 1
- Michelson, A. A. 1891, *Nature*, 45, 160
- Michelson, A. A. & Pease, F. G. 1921, *ApJ*, 53, 249
- Millan-Gabet, R. & Monnier, J. D. 2002, *ApJ*, 580, L167
- Montmerle, T., Koch-Miramond, L., Falgarone, E., & Grindlay, J. E. 1983, *ApJ*, 182
- Noll, R. J. 1976, *J. Opt. Soc. Am.*, 66, 207
- Padgett, D. L., Strom, S. E., & Ghez, A. 1997, *ApJ*, 477, 705
- Palla, F. & Stahler, S. W. 2000, *ApJ*, 540, 255
- Perryman, M. A. C., Lindegren, L., Kovalevsky, J., et al. 1997, *A&A*, 323, L49
- Petr, M. G., Coude Du Foresto, V., Beckwith, S. V. W., Richichi, A., & McCaughrean, M. J. 1998, *ApJ*, 500, 825
- Poetzel, R., Mundt, R., & Ray, T. P. 1989, *A&A*, 224, L13
- Prosser, C. F., Stauffer, J. R., Hartmann, L., et al. 1994, *ApJ*, 421, 517
- Przygodda, F. 2004, PhD thesis, Ruprecht-Karls-Universität Heidelberg
- Quirrenbach, A. 1999, in *Principles of Long-Baseline Interferometry*, ed. P. R. Lawson, *Michelson Fellowship Program*, 71–86
- Reipurth, B. & Aspin, C. 2004, *ApJ*, 608, L65
- Reipurth, B. & Zinnecker, H. 1993, *A&A*, 278, 81
- Ressler, M. E. & Barsony, M. 2001, *AJ*, 121, 1098
- Richichi, A., Leinert, C., Jameson, R., & Zinnecker, H. 1994, *A&A*, 287, 145
- Roddier, F. 1999, *Adaptive Optics in Astronomy*, ed. F. Roddier (Cambridge University Press)
- Sartori, M. J., Lépine, J. R. D., & Dias, W. S. 2003, *A&A*, 404, 913
- Schwarzschild, K. 1896, *AN*, 139, 353
- Simon, M. 1997, *ApJ*, 482, L81
- Simon, M., Ghez, A. M., Leinert, C., et al. 1995, *ApJ*, 443, 625

- Simon, M., Howell, R. R., Longmore, A. J., et al. 1987, ApJ, 320, 344
- Simon, M., Longmore, A. J., Shure, M. A., & Smillie, A. 1996, ApJ, 456, L41
- Skinner, S. L., Brown, A., & Stewart, R. T. 1993, ApJS, 87, 217
- Stapelfeldt, K. R., Burrows, C. J., Krist, J. E., et al. 1998, ApJ, 508, 736
- Stéphan, E. 1873, C. R. Acad. Sci., 76, 1008
- Stéphan, E. 1874, C. R. Acad. Sci., 78, 1008
- Terebey, S., van Buren, D., Hancock, T., Padgett, D. L., & Brundage, M. 2001, in *From Darkness to Light: Origin and Evolution of Young Stellar Clusters*, ed. T. Montmerle & P. André, ASP Conference Proceedings No. 243, 243–252
- Traub, W. A. 1999, in *Principles of Long-Baseline Interferometry*, ed. P. R. Lawson, Michelson Fellowship Program, 31–58
- van den Ancker, M. E., Blondel, P. F. C., Tjin A Djie, H. R. E., et al. 2004, MNRAS, 349, 1516
- Wang, H., Apai, D., Henning, T., & Pascucci, I. 2004, ApJ, 601, L83
- Weigelt, G. P. 1977, Opt. Comm., 21, 55
- Wilking, B. A., Lada, C. J., & Young, E. T. 1989, ApJ, 340, 823
- Wilking, B. A., Schwartz, R. D., & Blackwell, J. H. 1987, AJ, 94, 106
- Wolf, S. 2003, Comp. Phys. Comm., 150, 99
- Zinnecker, H., McCaughrean, M. J., & Wilking, B. A. 1993, in *Protostars and Planets III*, ed. E. H. Levy & J. I. Lunine, Space Science Series, 429–495

Quotations at the beginning of the chapters 2 to 9 from J. R. R. Tolkien's 'Lord of the Rings – Translations from the Red Book'

Acknowledgments / Danksagung

Hiermit möchte ich allen danken, die mich in den letzten drei Jahren während der Entstehung dieser Dissertation unterstützt haben. All jenen, deren Name hier versehentlich nicht aufgeführt ist, möchte ich versichern, daß sie nicht vergessen sind.

Prof. Dr. Christoph Leinert danke ich für die mir gegebene Möglichkeit zur Ausarbeitung dieser Dissertation. Seine fortwährende und ermutigende Unterstützung hat mir sehr geholfen, mich auf dem Gebiet der professionellen Astronomie zurechtzufinden.

Prof. Dr. Immo Appenzeller möchte ich für die Bereitschaft danken diese Arbeit zu begutachten.

Prof. Dr. Thomas Henning und Prof. Dr. Hans-Walter Rix, den Direktoren des Max-Planck-Instituts für Astronomie danke ich für die Möglichkeit in der Astronomie mitarbeiten zu dürfen.

Der MIDI-Gruppe möchte ich für die freundliche und offene Aufnahme danken, die es mir ermöglicht hat, den Beginn eines neuen Kapitels der beobachtenden Astronomie hautnah mitzuerleben. Mein besonderer Dank gilt Uwe Graser, Olivier Chesneau, Sebastiano Ligori, Richard Mathar, Udo Neumann, Frank Przygodda und Rainer Köhler.

Für die vielen interessanten Gespräche und die gute Arbeitsatmosphäre danke ich allen (ehemaligen) Angehörigen des Instituts. Insbesondere möchte ich Daniel Apai, Wolfgang Brandner, Tom Herbst, Laszlo Mosoni, Ilaria Pascucci, Elena Puga, Sascha Quanz, Jens Rodmann, Sascha Rüger, Alexander Schegerer, Manfred Stickel, Konrad Tristram, Stefan Umbreit, Hongchi Wang und Sebastian Wolf danken.

Mein Dank gilt ebenfalls all jenen ‘guten Geistern’ aus Technik und Verwaltung ohne deren Hilfe im Hintergrund kein wissenschaftliches Arbeiten möglich gewesen wäre.

Eric Bakker, Serge Correia, Anne Dutrey, Walter Jaffe, Hartmut Jahreiß, Bruno Lopez, Jörg-Uwe Pott, Huub Röttgering, Rens Waters, Jens Woitas und Hans Zinnecker danke ich für die interessante und gute Zusammenarbeit.

Der ESO danke ich für die professionelle Durchführung diversers Beobachtungsprogramme und die Gastfreundschaft, die mir vor und während meiner vier Aufenthalte in Chile zuteil wurde. Mein besonderer Dank gilt Nancy Ageorges, Angelika Beller, Christian Hummel, Chris Lidman, Olivier Marco, Sebastien Morel, Francesco Paresce, Andrea Richichi, Markus Schöller, Markus Wittkowski und den vielen namenlosen Mitarbeitern der *User Support Group*.

Friedrich vom Stein wünsche ich auch weiterhin immer genügend Käse und Popcorn. Diese Leckereien hat er sich aufgrund der tollen Unterstützung wirklich redlich verdient. Ich hoffe, daß seine Bemühungen die 'Dummheiten der Zweibeiner' zu verhindern auch in Zukunft erfolgreich sein werden.

Meinem langjährigen Studienfreund Alexander Wagner möchte ich für viele unterhaltsame Gespräche, Spielenachmittage, Kinobesuche, und Abendessen herzlich danken. Auf das wir noch viele Gespräche über kleine kollidierende und große rotierende 'Teilchen' führen können.

Rainer Köhler, Frank Przygodda und Alexander Wagner danke ich für das schnelle und kompetente Korrekturlesen der Dissertation.

In tiefer Verbundenheit möchte ich an dieser Stelle auch meiner Mutter für die Unterstützung in jeder Lebenslage danken. Meiner Schwester, meiner Großmutter, und den 'Binders', die mir einen problemlosen Start in Heidelberg ermöglicht haben, soll hier ebenfalls herzlich gedankt sein.